Ion Beam Collimation for Future Hadron Colliders

Andrey Abramov

Department of Physics
Royal Holloway, University of London

A thesis submitted to the University of London for the degree of Doctor of Philosophy

September 2020

Declaration

I confirm that the work presented in this thesis is my own. Where information has been derived from other sources, I confirm that this has been indicated in the document.

Signed: 

Date: 9th September 2020

На майка ми, Татяна. Благодаря, че вярва в мен и ми държа небето.

Abstract

The application of integrated simulation frameworks, which include particle tracking and physical interactions, to heavy-ion beam collimation in existing and future hadron colliders is presented. The SixTrack-FLUKA coupling and Beam Delivery Simulation (BDSIM) were used and the tools and techniques developed for the simulations are presented. A simulation study of the collimation cleaning inefficiency for heavy-ion beams was performed for the Large Hadron Collider (LHC), using both frameworks, and compared to measurements taken during operation. A detailed energy deposition study of ion beam collimation in a 3D model of the entire LHC ring was performed using BDSIM. The SixTrack-FLUKA coupling was used to study heavy-ion beam collimation in the Future Circular hadron-hadron Collider (FCC-hh). An analysis of the most limiting losses and an evaluation of the collimation system performance were carried out. The performance of the High-Energy Large Hadron Collider (HE-LHC) collimation system with heavy-ion beams was also investigated. The dominant beam loss clusters were identified and possible mitigation strategies are discussed. Support for partially stripped ions (PSI), which retain some of their bound electrons, was added to BDSIM and a physics model that treats charge-changing interactions of PSI with matter was implemented. Using the newly added features in BDSIM, the collimation of PSI beams in the LHC was studied in the context of the Gamma Factory initiative.

Acknowledgements

I would like to thank my supervisors—Stewart Boogert (RHUL), Laurie Nevay (RHUL) and Roderik Bruce (CERN), for their tireless support and guidance. Stewart helped me every step of the way and he not only showed me the ropes of physics, but shaped my attitude towards work and life. Laurie gave me valuable ideas and feedback about crucial parts of my work and guided me on my journey to becoming a physicist and a software developer. Roderik gave me insights into the design and operation of the world's largest accelerators and supported me during my time at CERN. I am forever grateful for their efforts, which made this thesis possible.

I would also like to thank my friends and colleagues at RHUL and CERN. The meetings and discussions with the team at RHUL have inspired my work and ideas. Thanks to Will Shields and Stuart Walker at RHUL for the assistance with preparing and running simulations with BDSIM. Outside of work hours, the coffee breaks, ice cream walks and pub visits at RHUL have kept my spirits high throughout my PhD. The collimation team at CERN have been very welcoming during my time there and have not only helped me with my work, but also given me unforgettable memories. I am grateful to Nuria Fuster-Martínez, Alessio Mereghetti and James Molson at CERN for the help with running SixTrack-FLUKA simulations. I look back with great fondness at the coffee and cake breaks, group lunches and my unsuccessful, but enjoyable attempts at skiing while at CERN.

Finally, huge thanks to my mum Tatyana, my sisters Ivana and Kalina, my aunt Boryana, and my partner Sophie for believing in me and always supporting me.

Contents

List of Figures

List of Tables

Chapter 1

Introduction

High-energy ion colliders are large and complex installations used for particle physics research. The main purpose of heavy-ion colliders is to study strongly interacting matter in order to gain understanding of key Standard Model aspects like symmetries of nature and the origin of masses. Collisions of intense, energetic ion beams provide the opportunity to probe quark and gluon interactions, including quark-gluon plasma (QGP), strong force interactions described by Quantum Chromo-dynamics (QCD), and anti-matter states [1,2]. In the conditions of extreme temperature and pressure during heavy-ion collisions, a transition is observed between colour singlet hadronic states to a deconfined plasma of quarks and gluons. This type of matter is predicted to have existed in the first moments after the Big Bang and hence measuring and quantifying the interactions that take place in it can provide an understanding of the early universe evolution.

Currently, there are two ion colliders in operation - the Large Hadron Collider (LHC) [3] at the European Organisation for Nuclear Research (CERN) in Switzerland, and the Relativistic Heavy-Ion Collider (RHIC) [4] at the Brookhaven National Laboratory (BNL) in the USA. Those two colliders are delivering successful and complementary physics programmes and are both expected to be operational for a further two decades. Exploratory studies of future hadron collider designs are underway, including projects like the High Energy LHC (HE-LHC) [5] and the Future Circular hadron-hadron Collider (FCC-hh) [6] in Switzerland and the Super proton-proton Collider (SppC) [7] in China. As demonstrated by the LHC, a collider optimised for proton-proton collisions can successfully operate as an ion-ion and

proton-ion collider as well. The future hadron colliders can be designed from the start with interchangeable proton and ion beam operation that will increase their physics reach and improve the return on investment. To allow this, the additional challenges involved with ion beam operation must be addressed early on.

One of the challenges is machine protection. The intense, high-energy beams in future hadron colliders pose a threat to equipment in and around the accelerator beamlines. The stored energy per nominal proton beam in the LHC is 360 MJ, while a proton beam in the FCC-hh is designed to have 8.6 GJ. Only a fraction of the beam's energy can cause damage to equipment if deposited over a short period of time. An even smaller fraction can cause loss of superconductivity in the accelerator magnets (called a quench), where the thresholds are in the range of $\mathrm{mW\,cm^{-3}}$. A high-energy hadron collider must include a collimation system to protect the machine from beam losses and safely handle the large power loads involved. The collimation system is often designed and optimised for proton beam operation, but must also handle ion beams.

Ions can undergo nuclear fragmentation and electromagnetic dissociation (EMD) when interacting with the collimators, which can produce ion fragments that are within the geometrical acceptance of the machine, but with an altered charge-to-mass ratio. Such fragments can escape the collimation system and cause losses and energy deposition downstream, where their trajectories are affected by dispersion. Due to the complex interactions between beam ions and the solid material of collimators, simulation studies of ion beam collimation in accelerators are non-trivial and require particle tracking of many isotopes, as well as a comprehensive treatment of particle interactions.

Thesis structure

In this thesis, the first systematic studies of ion beam collimation at the energies and operational parameters of future hadron colliders are presented. The performance of the collimation system in ion beam operation is evaluated for the FCC-hh and HE-LHC. To achieve this, the nominal collimation configuration for protons is used as a starting point, as no dedicated ion beam collimation configuration is currently available. After selection of appropriate initial parameters and settings for the ion beam operation, simulations are per-

formed using integrated simulation tools that include particle tracking and particle-matter interactions with the appropriate physics processes. The results from the simulations are analysed to provide an estimate of the collimation system performance for nominal ion beam operation. In addition to this, the most significant loss clusters and the losses in critical sections of the machine are analysed in detail. A set of simulations is also carried out for a well-defined LHC operational scenario and compared with measured data in order to validate the simulation tools used. Finally, a study of the LHC collimation system performance with beams of partially stripped ions (PSI) is carried out. PSI have recently been proposed for use in the LHC, because their remaining bound electrons enable interactions of interest with laser beams and electro-magnetic (EM) fields, but the first operational tests have indicated a prohibitively low collimation efficiency, motivating the simulation studies performed.

This chapter covers fundamental accelerator physics concepts, particle physics interactions between high-energy ions and matter and the simulation tools and techniques used in this work.

1.1 Accelerator physics

A particle accelerator is a machine that boosts the kinetic energy of subatomic particles and contains them in a well-defined beam by the use of EM fields. First developed in the early 20^{th} century, accelerators were originally used to study the structure of the atomic nucleus. Today, accelerators have broad applications in the fields of particle physics, atomic and nuclear physics, biology, medicine and others. High-energy particle accelerators remain at the forefront of fundamental particle physics research, allowing the study of the Standard Model with precision not achievable by any other means. Numerous accelerator designs have been developed—electrostatic, betatron, cyclotron, synchrotron and others [8]. To achieve the highest energies, cascades of synchrotrons are used. A synchroton is a cyclic accelerator with separated element functions—radio-frequency (RF) cavities provide the acceleration, dipole magnets provide the bending that keeps the particles on a closed orbit, quadrupole magnets control the beam size and additional higher-order magnets correct chromatic and geometric aberrations in the beam. In a synchrotron, the orbit of the beam

particles is kept constant during acceleration by ramping the magnetic fields and the RF frequency synchronously with the beam energy.

This section covers some of the essential concepts and methods in accelerator physics. These include particle motion in EM fields, coordinate systems and beam dynamics. Detailed derivation of the concepts outlined here can be found in [8–10].

1.1.1 Equations of motion

A beam of charged particles moving through an EM field can be described by equations of motion. In the Lagrangian formalism, the equations of motion can be derived from a single function known as the Lagrangian of the system $L = L(\boldsymbol{q}, \dot{\boldsymbol{q}}, t)$, which is a function of n generalised coordinates $\boldsymbol{q} = (q_1, \cdots, q_n)^{\mathrm{T}}$ and n generalised velocities $\dot{\boldsymbol{q}} = (\dot{q}_1, \cdots, \dot{q}_n)^{\mathrm{T}}$ where the dot represents a derivative with respect to time. The time-independent form of the Lagrangian is,

$$L = T - V \ , \tag{1.1}$$

where T is the kinetic and V is the potential energy of the system.

In this formalism, n equations of motion can be derived using the Euler-Lagrange equation,

$$\frac{d}{dt}\left(\frac{\partial L}{\partial \dot{q}_i}\right) - \frac{\partial L}{\partial q_i} = 0 \ , \tag{1.2}$$

where $i = 1 \cdots n$. The resulting n second-order differential equations, together with $2n$ initial conditions $(\boldsymbol{q}(t_0),\ \dot{\boldsymbol{q}}(t_0))$ completely determine the behaviour of the system for all time.

In accelerator physics, it is often beneficial to treat beam dynamics using Hamiltonian mechanics, which is based on the Hamiltonian $H = H(\boldsymbol{q}, \boldsymbol{P}, t)$, a function of generalised coordinates $\boldsymbol{q}$ and the generalised momenta $\boldsymbol{P} = (p_1, \cdots, p_n)^{\mathrm{T}}$. If the Lagrangian of the system is known, it is straightforward to obtain the Hamiltonian. The generalised momenta

of the Hamiltonian formalism can be obtained from the Lagrangian as,

$$P_i = \frac{\partial L}{\partial \dot{q}_i} \quad \text{for} \quad i = 1, \cdots, n \ . \tag{1.3}$$

The Hamiltonian can then be obtained as the Legendre transform of the Lagrangian,

$$H = \sum_{i=1}^{n} \dot{q}_i P_i - L \ . \tag{1.4}$$

The time-independent Hamiltonian represents the full energy of the system,

$$H = T + V. \tag{1.5}$$

The equations of motions are then represented by $2n$ first-order differential equations,

$$\frac{\partial H}{\partial q_i} = -\dot{P}_i \quad \text{and} \quad \frac{\partial H}{\partial P_i} = \dot{q}_i \tag{1.6}$$

for $i = 1, \cdots, n$. There are also $2n$ initial conditions of the form $(\boldsymbol{q}(t_0),\ \boldsymbol{P}(t_0))$ required to fully describe the system. The force acting on a charged particle in an EM field is the Lorentz force,

$$\boldsymbol{F} = e(\boldsymbol{E} + \boldsymbol{v} \times \boldsymbol{B}) \ , \tag{1.7}$$

where $\boldsymbol{E}$ is the electric field, $\boldsymbol{B}$ is the magnetic field and e is the charge of the particle.

This can be derived, using Eq. (1.2), from the Lagrangian of a charged particle in an EM field,

$$L = -mc^2\sqrt{1-\beta^2} + e\boldsymbol{v}\boldsymbol{A} - e\phi \ , \tag{1.8}$$

where m and $\boldsymbol{v}$ are the particle's mass and velocity, c is the speed of light, $\beta = v/c$, $\boldsymbol{A}$ is the vector potential and ϕ is the scalar potential.

The electric $\boldsymbol{E}$ and magnetic $\boldsymbol{B}$ fields can be expressed in terms of $\boldsymbol{A}$ and ϕ as,

$$\boldsymbol{E} = -\nabla\phi - \frac{\partial \boldsymbol{A}}{\partial t}, \qquad \boldsymbol{B} = \nabla \times \boldsymbol{A}. \tag{1.9}$$

Using Eqs. (1.3) and (1.4), the Hamiltonian for a particle in an accelerator can be derived in Cartesian coordinates,

$$H = \sqrt{c^2(\boldsymbol{P} - e\boldsymbol{A})^2 + m^2c^4} + e\phi \ , \tag{1.10}$$

with (u, P_u) for $u \in \{x, y, z\}$ as the conjugate phase-space coordinates of the system.

1.1.2 Coordinate system

In Hamiltonian mechanics, the evolution of the system does not depend on the coordinate system chosen. Hamilton's equations Eq. (1.6) are invariant under canonical coordinate transforms. The lack of a universal coordinate system allows for a convenient one for the system under consideration to be chosen, provided that a canonical transform exists.

In a circular accelerator, there is a closed curve that passes through the centres of most magnetic elements by construction, which forms a convenient basis for a coordinate system. This curve is called the design orbit or reference trajectory and is the trajectory that a beam particle with nominal momentum and no offsets will follow through a sequence of idealised, perfectly aligned magnets with no fringe fields. Instead of using a fixed global Cartesian coordinate system, it is beneficial to define a local curvilinear coordinate system about the reference trajectory. The Frenet-Serret coordinate system [9], shown in Fig. 1.1, is most commonly used in accelerator physics.

The motion of a particle in this coordinate system is parameterised by the arc length s travelled along the reference trajectory, which is an independent variable of the system. At

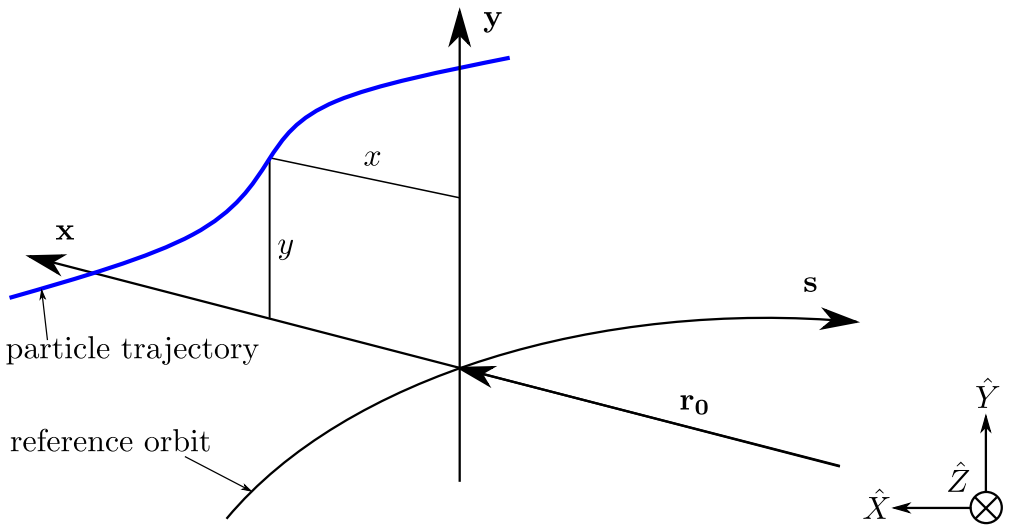

Figure 1.1: Diagram of curvilinear coordinate system used for circular accelerators, the Frenet-Serret coordinate system. Diagram based on [9].

every s position, a Cartesian coordinate system perpendicular to the reference trajectory is used to define the position of a particle. The x-axis is in the bending plane and the y-axis is perpendicular to the bending plane. The particle trajectory can be expressed as,

$$\boldsymbol{r}(s) = \boldsymbol{r_0}(s) + x\hat{\boldsymbol{x}} + y\hat{\boldsymbol{y}} \ , \tag{1.11}$$

where $\hat{\boldsymbol{s}} = \frac{d\boldsymbol{r}(s)}{ds}$, $\hat{\boldsymbol{x}}(s) = -\rho(s)\frac{d\hat{\boldsymbol{s}}(s)}{ds}$ and $\hat{\boldsymbol{y}}(s) = \hat{\boldsymbol{x}} \times \hat{\boldsymbol{s}}$. Here, ρ denotes the local radius of curvature.

A transformation of the Hamiltonian Eq. (1.10) from Cartesian coordinates to local curvilinear coordinates can be achieved using a canonical transform,

$$H(X, P_x, Y, P_y, Z, P_z; t) \rightarrow H(x, p_x, y, p_y, t, p_s; s) \tag{1.12}$$

With an appropriate choice of a transform, the conjugate canonical momenta for (x, y, s) become,

$$p_s = \left(1 + \frac{x}{\rho}\right) \boldsymbol{P} \cdot \hat{\boldsymbol{s}} \quad , \quad p_x = \boldsymbol{P} \cdot \hat{\boldsymbol{x}} \quad , \quad p_y = \boldsymbol{P} \cdot \hat{\boldsymbol{y}} \ , \tag{1.13}$$

where $\boldsymbol{P}$ is the momentum vector in the Cartesian coordinate system. This leads to the new Hamiltonian,

$$H = e\phi + c\sqrt{m^2c^2 + \frac{(p_s - eA_s)^2}{(1+x/\rho)^2} + (p_x - eA_x)^2 + (p_y - eA_y)^2}\ . \tag{1.14}$$

After a change of variable from the time t to the distance along the reference trajectory s, the final form of the Hamiltonian becomes

$$\tilde{H} = -\left(1 + \frac{x}{\rho}\right)\sqrt{\frac{(H - e\phi)^2}{c^2} - m^2c^2 - (p_x - eA_x)^2 - (p_y - eA_y)^2}\ - eA_s\ , \tag{1.15}$$

where A_x, A_y, A_s are the vector potential components in the new coordinate system. The conjugate canonical coordinate pairs are as follows,

$$(x,\ p_x), \quad (y,\ p_y), \quad (t, -H). \tag{1.16}$$

The definition of the conjugate coordinates and notations vary in literature and in practical implementations, but the underlying principles and methods are largely equivalent and therefore the choice of convention is driven by convenience.

1.1.3 Accelerator magnets

The transverse motion of the beams in an accelerator is almost exclusively controlled by magnets. The accelerator magnets are designed with specific field properties in order to achieve the desired effect on the beam particles. For example, the bending of the particle trajectories on a closed orbit is achieved by dipole fields, while the focussing is produced by quadrupole fields. In a bending magnet, the bending radius is related to magnetic field and the particle momentum by the magnetic rigidity equation,

$$B\rho = \frac{p}{e}, \tag{1.17}$$

where B is the magnetic field, ρ is the radius of curvature and p, e are the particle momentum and charge respectively. The magnetic rigidity is a key property of a charged particle beam and is widely used when designing magnets for an accelerator. A more practical expression for the magnetic rigidity is,

$$\frac{1}{\rho\,[\mathrm{m}]} = 0.29998 \frac{Z}{A} \frac{B\,[\mathrm{T}]}{\beta E\,[\mathrm{GeV/c}]} \ . \tag{1.18}$$

In addition to the dipole and quadrupole fields, there are other higher-order fields used to correct various imperfections and aberrations. For magnets used in accelerators, it is often useful to express the magnetic field seen by the beam as a series of multipoles. A general multipole expansion of a magnetic field can be expressed as [9],

$$\frac{e}{p} B_{nx} = \sum_{m=1}^{n/2} A_{n-2m+1,2m-1} \frac{x^{n-2m}}{(n-2m)\,!} \frac{y^{2m-1}}{(2m-1)\,!} \ , \tag{1.19}$$

$$\frac{e}{p} B_{ny} = \sum_{m=1}^{(n+1)/2} A_{n-2m+1,2m-1} \frac{x^{n-2m+1}}{(n-2m+1)\,!} \frac{y^{2m-2A}}{(2m-2)\,!} \ , \tag{1.20}$$

where n is the multipole order, $B_{nx,y}$ is the magnetic field, $A_{j,k}$ are the potential coefficients and e, p are charge and momentum of the design beam particle. The magnetic field is normalised by the magnetic rigidity to make calculations for different beams easier.

From Eq. (1.19), the form of the magnetic field can be derived. The magnetic field components in the horizontal and vertical planes for the most common magnets used in accelerators are shown in Table 1.1, with the symbols κ, k, m replacing the $A_{j,k}$ coefficients for the respective magnets. Example plots of these magnetic fields in the x-y plane are shown in in Fig. 1.2.

Table 1.1: Magnetic field $\boldsymbol{B}$ components in the horizontal (x) and vertical (y) plane for multipoles corresponding to the most common accelerator magnets.

Multipole	$\frac{e}{p}Bx$	$\frac{e}{p}By$
Dipole	0	$-\kappa_x$
Quadrupole	k_y	$-k_x$
Sextupole	mxy	$-\frac{1}{2}m\left(x^2-y^2\right)$

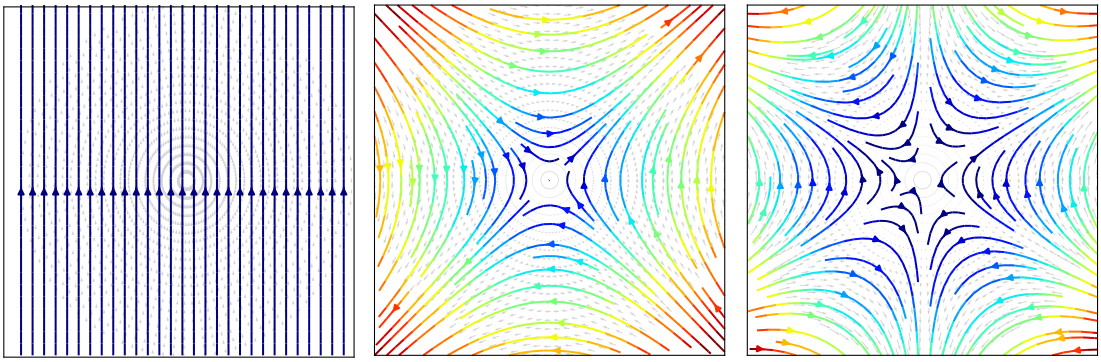

Figure 1.2: Radial magnetic field distribution for the most frequently used accelerator magnets: dipole (left), quadrupole (middle), sextupole (right). The arrows represent the direction of the field and the colour represents relative intensity.

In addition to the magnetic fields in Eq. (1.19), which are known as straight, rotated magnetic fields can be useful. For example, a rotated quadrupole field can be useful in correcting coupling between the horizontal and vertical planes. Rotated magnetic multipoles are referred to as skew multipoles. Skew components of the field can also arise from manufacturing and alignment errors in regular magnets. The strength parameters for straight and skew multipoles can be obtained in a convenient form by differentiation of the field,

$$s_n\left[\mathrm{m}^{-\mathrm{n}}\right] = \frac{C_m}{\beta E[\mathrm{GeV}]} \frac{\partial^{n-1} B_y[\mathrm{T}]}{\partial x^{n-1}(m-1)} \ , \tag{1.21}$$

$$\underline{s}_n\left[\mathrm{m}^{-\mathrm{n}}\right] = \frac{C_m}{\beta E[\mathrm{GeV}]} \frac{\partial^{n-1} B_x[\mathrm{T}]}{\partial y^{n-1}(m-1)} \ , \tag{1.22}$$

where s_n and $\underline{s}_n$ are the straight and skew strength parameters respectively, β is the normalised velocity and $C_m = 0.299\,792\,5\,\mathrm{GeV\,T^{-1}\,m^{-1}}$.

Typically, each type of accelerator magnet is designed to have a longitudinally uniform field dominated by a single multipole component.

1.1.4 Single particle dynamics

Synchrotron accelerators use the strong focussing principle [11] to control the beam size and provide beam stability. In strong focussing beam transport systems, dedicated quadrupoles

are used for beam focussing and alternating polarity quadrupoles provide focussing in both transverse planes. The sequence of elements in a beamline, including dipole magnets that provide the bending, quadrupole magnets that provide the focussing, and other magnetic elements; is referred to as the accelerator lattice. A beam particle traversing the lattice will experience transverse and longitudinal oscillations about the reference trajectory. The analytical treatment of beam dynamics is greatly simplified if the closed reference orbit is factored out of the particle motion and only the deviation from that orbit is considered. In doing so, the system can be represented as a harmonic oscillator with non-linear perturbations. The curvilinear coordinate system described in Section 1.1.2 is hence a natural choice for studying beam dynamics.

The transverse oscillations of the particles about the reference orbit are called betatron oscillations. In the transverse plane homogenous second-order differential equations can be constructed that describe particle motion without perturbations:

$$u'' + K_u(s)u = 0, \tag{1.23}$$

where $u \in \{x, y\}$, the double prime $''$ denotes double differentiation with respect to s and $K_u(s) = \kappa_{u0}^2(s) + k_0(s)$ is the restoring force, which depends on the independent variable s. The restoring force features the quadrupole strength parameter,

$$k_0(s) = \frac{p}{q}\frac{\partial B}{\partial x} \tag{1.24}$$

and $\kappa_{u0} = 1/\rho$, the local curvature due to dipole magnet bending as described in Section 1.1.1. The homogenous differential equations involve multiple approximations, like assuming a paraxial, mono-energetic beam and ignoring acceleration and chromatic effects. Furthermore, the coordinate pairs (u, u') are not canonical. This formulation is not suitable to accurately describe the full system, but it forms a basis for the analytical formulation of single particle dynamics.

In a periodic lattice, $K_u(s+L) = K_u(s)$, where L can be the circumference of the machine or the length of a repeating element sequence (cell), the differential equations are known as Hill's equations. In a typcal circular accelerator, the bending of the beam is limited to

the horizontal plane and hence after some expansion the equations become,

$$x'' + \left(k_0(s) + \frac{1}{\rho(s)^2}\right)x = 0 \ , \tag{1.25}$$

$$y'' + k_0(s) = 0. \tag{1.26}$$

In the horizontal plane, the two contributions to beam focussing are readily identified—the strong focussing due to the quadrupoles is contained in the k_0 term and the weak focussing due to the bending magnets is represented by the $\frac{1}{\rho^2}$ term in the expanded form of the restoring force $K_x(s)$. In the vertical plane only the focussing from the quadrupoles is relevant.

The general solution to the linear equations of motion can be expressed as,

$$\big[\mathcal{S}''(s) + K(s)\mathcal{S}(s)\big]u_0 + \big[\mathcal{C}''(s) + K(s)\mathcal{C}(s)\big]u_0' = 0, \tag{1.27}$$

where $(u_0,\ u_0')$ are some arbitrary initial conditions and $\mathcal{S}(s)$ and $\mathcal{C}(s)$ are sine-like and cosine-like principal solutions satisfying the boundary conditions,

$$\mathcal{C}(0) = 1 \quad , \quad \mathcal{C}'(0) = 0, \tag{1.28}$$

$$\mathcal{S}(0) = 0 \quad , \quad \mathcal{S}'(0) = 1. \tag{1.29}$$

The general solution can be expressed in terms of a matrix,

$$\begin{pmatrix} u(s) \\ u'(s) \end{pmatrix} = \begin{pmatrix} \mathcal{C}(s) & \mathcal{S}(s) \\ \mathcal{C}'(s) & \mathcal{S}'(s) \end{pmatrix} \begin{pmatrix} u_0 \\ u_0' \end{pmatrix}. \tag{1.30}$$

Solving those equations for a given configuration of the magnetic fields allows a particle's coordinates to be transported across a magnetic lattice element. The magnetic elements in

most accelerators are designed to have a constant magnetic field inside the magnet and zero field outside of it. This is not true for real magnets where the magnetic field is not perfect inside the magnet and also extends beyond the physical dimensions of the magnets in the form of fringe fields. Ignoring the imperfections and fringe fields and assuming a piece-wise constant magnetic field in all accelerator elements (the hard-edge approximation), the matrices like Eq. (1.30) for each element of an arbirary transport line can be multiplied together to produce a single transfer matrix between the start and end s-positions.

The formulation of the linear equation of motion in an accelerator does not capture all the effects that govern single particle dynamics. If non-linear effects are included as perturbations, then Eq. (1.23) becomes inhomogeneous and special treatment is required for each of those effects. One of the most important perturbations is the first order chromatic aberration in bending magnets due to the finite energy spread of the beam particles. A beam particle with a momentum deviation will follow a different trajectory in a bending magnet than the reference particle, resulting in a physical offset at the end of the bending magnet,

$$u(s) = u_\beta(s) + D_u(s)\delta \ . \tag{1.31}$$

where u_β is the coordinate due to the linear betatron motion Eq. (1.23), δ is the momentum defect of the beam particle $\frac{\Delta p}{p_0}$ and $D_u(s)$ is the dispersion function, which can also be expressed in terms of the principal solutions for the linear motion equations,

$$D(s) = \int_0^s k(\tilde{s}) \left[\mathcal{S}(s)\mathcal{C}(\tilde{s}) - \mathcal{C}(s)\mathcal{S}(\tilde{s})\right] d\tilde{s} \ , \tag{1.32}$$

1.1.5 Beam phase space

Starting from the principles outlined in Section 1.1.4, it is possible to treat the beam as a whole, rather than individual particles. A beam of particles can be represented as a distribution in a six-dimensional phase space with coordinates shown in Eq. (1.16). The distribution is most commonly assumed to be Gaussian.

An alternative formulation of the solutions to equation of linear motion [12] Eq. (1.30) is,

$$u(s) = A_u \sqrt{\beta_u(s)} \cos(\psi_u(s)) \ , \tag{1.33}$$

$$u'(s) = \frac{A_u}{\sqrt{\beta_u(s)}} [\alpha_u(s) \cos(\psi_u(s)) + \sin(\psi_u(s))] \ , \tag{1.34}$$

where ψ_u is the phase, A_u is an integration constant and

$$\alpha_u(s) = -\frac{1}{2} \frac{d\beta_u(s)}{ds} \ . \tag{1.35}$$

This is often called the phase-amplitude formulation. Any coupling between the two planes is neglected and the two planes are treated separately, meaning that u can be x or y with equal validity.

The motion of the beam particles is modulated by β_u, the amplitude function. The transverse phase space oscillations of the beam particles are known as betatron oscillations. The phase advance between $s = 0$ and $s = L$ is given by,

$$\Delta\psi_u = \int_0^L \frac{1}{\beta_u(s)} ds \ . \tag{1.36}$$

The total number of betatron oscillations per revolution in a circular accelerator is known as the tune ν,

$$\nu_u = \frac{1}{2\pi} \Delta\psi_C = \frac{1}{2\pi} \oint \frac{1}{\beta_u} ds \ , \tag{1.37}$$

where C is the circumference of the machine. The parametric equation of an ellipse can be derived from Eq. (1.33) and Eq. (1.34) as,

$$A_u^2 = \gamma_u(s) u^2 + 2\alpha_u(s) u u' + \beta_u(s) u'^2 \ , \tag{1.38}$$

with $\gamma(s) = (1 + \alpha(s)^2)/\beta(s)$. This relationship is a constant of motion and is known as the Courant-Snyder invariant. The ellipse parameters $\alpha(s), \beta(s), \gamma(s)$ are called the Twiss parameters, and the parameter A_u^2 is phase space area enclosed by the beam. The Twiss parameters are related via

$$\beta(s)\gamma(s) + \alpha(s)^2 = 1 \ . \tag{1.39}$$

The ellipse area is related to the the emittance ϵ_{sp}, $A_u^2 = \pi\epsilon_{\text{sp}}$, with the subscript used to differentiate the single particle emittance (used here) from the beam emittance (defined later). Each particle follows its own ellipse in phase space, and while the ellipse shape and orientation change during propagation in the beam transport systems, the enclosed area remains constant. This is a manifestation of Liouville's theorem [9], which states that under the effect of conservative forces, the particle density in phase space remains constant.

Similar to Eq. (1.30), a matrix can be constructed that transports the Twiss parameters across the magnetic lattice elements [9]. The Twiss parameters are functions only of the magnetic lattice and are often referred to as the lattice functions or the machine optics because of the similarity with light optics.

To describe the movement of the beam as an ensemble, a convenient particle trajectory can be chosen that encloses all (or a desirable fraction) of the other particle trajectories. This trajectory forms the beam envelope; its corresponding ellipse is often referred to as the beam phase ellipse. This allows the beam emittance ϵ to be defined. A diagram of the phase ellipse showing relevant parameter relationships can be seen in Fig. 1.3.

Different definitions of ϵ can be used. For the case of Gaussian beams, it is common to define the emittance ϵ as the root mean square (rms) emittance of all particles in the beam. If the emittance and the optical functions are known, observable physical properties of the beam such as beam size can be recovered. If dispersion is neglected, the transverse rms beam sizes can be obtained as,

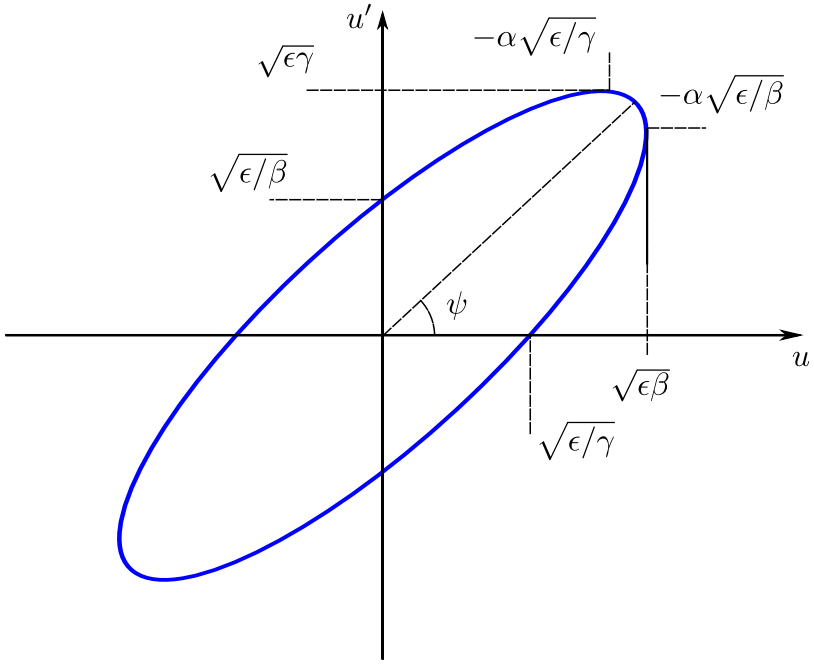

Figure 1.3: Diagram of the beam phase ellipse, where u can be x or y [9].

$$\sigma_u = \sqrt{\beta_u \epsilon_u} \ , \tag{1.40}$$

$$\sigma_{u'} = \sqrt{\gamma_u \epsilon_u} \ , \tag{1.41}$$

where the $\sigma_u, \sigma_{u'}$ contain one standard deviation σ of the beam distribution, which for a Gaussian distribution is about 68.2 %.

Acceleration is not a conservative force and during acceleration, the transverse emittance of the beam is reduced, because the radio-frequency (RF) cavities preferentially increase the longitudinal component of the beam particle's momentum. This effect is known as adiabatic damping. The normalised emittance ϵ_{N} can be defined,

$$\epsilon_{\mathrm{N}} = \beta_{\mathrm{r}} \gamma_{\mathrm{r}} \epsilon \ . \tag{1.42}$$

In this context, to avoid ambiguity with the Twiss parameters, β_{r} denotes the particle's velocity, γ_{r} denotes the relativistic factor and ϵ is the geometrical emittance discussed

previously.

1.1.6 Longitudinal motion

From Eq. (1.7), it can be derived that only electric fields in the direction of propagation of the particle can increase its energy. Modern high-energy circular accelerators use time-varying EM fields to accelerate the beam. The high-frequency accelerating field is confined to dedicated elements along the beamline, called RF cavities, which are installed in straight sections of the machine, where no other EM fields exist. In most cases, an RF cavity contains a resonant structure that is powered by a high-frequency power source to produce a standing EM wave of a specified angular frequency ω_{rf}, with an accelerating voltage V in the longitudinal direction given by [10],

$$V = V_0 \sin(\omega_{\mathrm{rf}} t + \phi_s) \ , \tag{1.43}$$

where V_0 is the amplitude of the RF voltage and ϕ_s is a phase factor.

As a particle in an accelerator gains energy, its revolution frequency f changes. The change in the revolution frequency depends on the particle's momentum p as [13],

$$\frac{\mathrm{d}f}{f} = \left(\frac{1}{\gamma_r^2} - \alpha_{\mathrm{p}} \right) \frac{\mathrm{d}p}{p} \ , \tag{1.44}$$

where γ_r is the Lorentz factor and α_{p} is known as the momentum compaction factor and it depends on the lattice. The dependence of the revolution frequency on the momentum is important for the stability of the longitudinal motion in an accelerator. At low particle energies ($\gamma_r^2 < \alpha_{\mathrm{p}}$), the revolution frequency decreases with increasing momentum, while at high particle energies ($\gamma_r^2 > \alpha_{\mathrm{p}}$) it increases. The energy corresponding to $\gamma_{\mathrm{tr}} = 1/\sqrt{\alpha_{\mathrm{p}}}$ is known as the transition energy and it delimits two different regimes. The following discussion is focussed on the regime below the transition energy.

An example of the longitudinal motion in an accelerator below the transition energy is shown in Fig. 1.4. A particle with phase $\phi = \phi_s$, momentum p_0 and a revolution period T_0

is called the synchronous-particle and is labelled as ϕ_2 in Fig. 1.4. For optimal acceleration, the angular frequencies of the RF and the synchronous particle must match,

$$\omega_{\mathrm{rf}} = h\omega_0 \ , \tag{1.45}$$

where $\omega_0 = \beta_0 c/R_0$ is the angular revolution frequency of the synchronous particle with β_0, R_0 denoting the speed and average orbit radius of the synchronous particle respectively, c is the speed of light and h is an integer called the harmonic number.

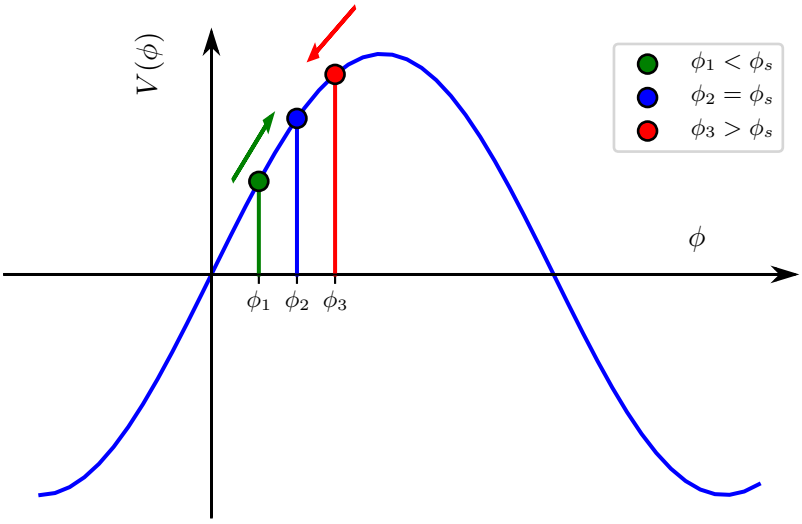

Figure 1.4: Example of the longitudinal motion below the transition energy in an accelerator. The particle with $\Delta p/p = 0$ is the synchronous particle and the RF voltage provides a restoring force to particles with momentum deviations.

The energy gain of a particle traversing the RF cavity will hence depend on the phase of that particle relative to the phase of the cavity. The synchronous particle will gain energy of $\Delta E = eV_0 \sin(\phi_s)$ per passage through the RF cavity. In a real beam there is a spread of beam particle momenta about the reference momentum and each particle will follow a different off-momentum closed orbit as described in Section 1.1.4 and therefore will have a different revolution frequency. Below transition, a higher momentum particle, ϕ_1 in Fig. 1.4, will arrive at the RF cavity ahead of the synchronous particle ($\phi < \phi_s$) and will receive less energy. Conversely, a particle with a lower momentum, ϕ_3 in Fig. 1.4, will arrive at the RF cavity behind the synchronous particle ($\phi > \phi_s$) and gain more energy. As long as the phase of the RF cavity obeys the condition $0 < \phi_s < \pi/2$, this effect provides

phase stability of the longitudinal motion.

The motion in the longitudinal plane is called synchrotron motion and the oscillations are called synchrotron oscillations. The fractional off-momentum deviation is defined as,

$$\delta = \frac{\Delta p}{p_0} = \frac{\omega_0}{\beta^2 E}\frac{\delta E}{\omega_0} \ . \tag{1.46}$$

The differential equations of motion can then be obtained,

$$\frac{d\delta}{dt} = \frac{\omega_0}{2\pi\beta^2 E} eV_0[\sin(\phi) - \sin(\phi_s)] \ , \tag{1.47}$$

$$\frac{d\phi}{dt} = h\omega_0\eta\delta \ , \tag{1.48}$$

where η is called the slip factor and has the form,

$$\eta = \frac{\Delta\omega/\omega_0}{\Delta p/p_0} \ . \tag{1.49}$$

For small oscillation amplitudes, the synchroton motion can be treated as a harmonic oscillator, with the linearised equation of motion in the variable $\Delta\phi = \phi - \phi_s$ being,

$$\frac{d^2}{dt^2}\Delta\phi - \frac{h\omega_0^2 eV\eta_0\cos(\phi_s)}{2\pi\beta^2 E}\Delta\phi = 0 \ . \tag{1.50}$$

The phase stability condition below the transition energy then takes the form,

$$\eta_0\cos(\phi_s) < 0. \tag{1.51}$$

The phase stability condition delimits different areas in phase space. The area of stable motion is called the RF bucket and the largest phase space trajectory is called the separatrix and forms the boundary between stable and unstable motion. An example of the

longitudinal beam phase space can be seen in Fig. 1.5.

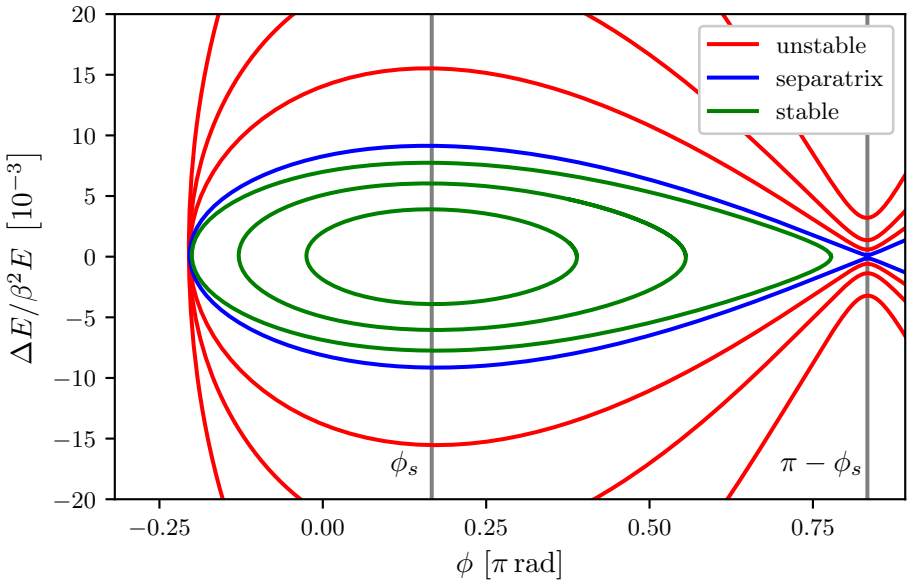

Figure 1.5: Example of the longitudinal beam phase space, showing different kinds of particle trajectories - unstable, limiting (separatrix) and stable.

1.1.7 Particle tracking

The methods described in Section 1.1.5 provide information about the movement of the beam as a whole through the magnetic lattice, which aids the design and fundamental understanding of beam dynamics in an accelerator. However, non-linear effects are present in an accelerator and there is the possibility for chaotic motion of beam particles. These effects can limit the feasibility and accuracy of analytical computations for particle motion and beam losses for an ensemble of particles. It is often of interest to track individual particle trajectories in the accelerator, instead of an ensemble. Particle tracking is used in studying long-term beam stability in the presence of non-linear effects, resonances and instabilities, as well as for beam loss studies like the one described in this work.

Considering a $2n$-dimension phase space with coordinates $q_1 \cdots q_n$ and momenta $p_1 \cdots p_n$, particle tracking can be expressed as the general transformation [14],

$$\boldsymbol{z}^{\text{fin}} = \mathcal{M}\boldsymbol{z}^{\text{in}} \ , \tag{1.52}$$

where $\boldsymbol{z} = (q_1 \cdots q_n, p_1 \cdots p_n)$, "in" denotes initial state, "fin" denotes the final state and $\mathcal{M}$ maps the phase space onto itself and is often called the transfer map. The mapping can be over a single magnetic element, a sequence of elements or even the entire circumference of the accelerator. The motion in an accelerator can be described by a Hamiltonian $H(\boldsymbol{z}, t)$ as outlined in Section 1.1.1. The relationship between phase space coordinates is given by Eq. (1.6), which can be summarised as $\dot{z} = [z, H]$, where the dot represents a time derivative and [ ] is the Poisson bracket [14].

Therefore, the transfer map $\mathcal{M}$ must necessarily arise from the integration of Hamilton's equations. Finding such a transfer map corresponds to solving the equations of motion. For transfer maps derived from Hamiltonians, the symplectic condition must hold true,

$$M(\boldsymbol{z}^{\text{in}})^{\text{T}} J M(\boldsymbol{z}^{\text{in}}) = J \ , \tag{1.53}$$

where $M(\boldsymbol{z}^{\text{in}})_{ab} = \partial z_a^{\text{fin}} / \partial z_b^{\text{in}}$ is the Jacobian matrix and

$$J = \begin{pmatrix} 0 & I \\ -I & 0 \end{pmatrix} \ , \tag{1.54}$$

is the Poisson matrix, with $0, I$ denoting the $n \times n$ null and identity matrices respectively. If the Jacobian of the transformation fulfilled by $\mathcal{M}$ satisfies Eq. (1.53), $\mathcal{M}$ is known as a symplectic map. The symplectic condition is connected to the preservation of phase space volume occupied by the particle beam as stated by Liouville's theorem and symplecticity is hence a desirable property of particle tracking algorithms.

There are multiple constraints when constructing and using transfer maps for particle tracking. Different approaches have been applied to tracking using maps, including Lie algebra methods [15] and Truncated Power Series Algebra (TPSA) [16, 17]. Suitable approximations can be made to make the problem analytically tractable. For example, in the case of linear motion, the transfer maps reduce to transfer matrices as given by Eq. (1.30), which greatly speeds up computation.

Another approach to particle tracking is numerical integration of the equations of motion

Eq. (1.6). Integration schemes such as Euler or Runge-Kutta [15, 18] can be used to track particles in arbitrary EM fields, but this is often achieved at the cost of symplecticity and computational efficiency [15].

1.1.8 Hadron colliders

The main purpose of hadron colliders is the study of fundamental particle physics interactions and the Standard Model by colliding high-energy hadron beams. The most important figures of merit for a collider are the collision energy and the luminosity.

The beam-beam collision configuration is chosen in order to maximise the energy available to produce new particles and interactions—centre-of-mass (c.o.m.) energy for the system. In considering the kinematics of a collision, the energy-momentum 4-vector $p = (E, \boldsymbol{p})$ is used, where E is the total energy and $\boldsymbol{p}$ is the three-momentum. Consider a two-particle colliding system with incoming 4-momenta p_1, p_2 and the Mandlestam variable $s = (p_1 + p_2)^2$ is used to represent the c.o.m. energy [19]. For a fixed target experiment ($|\boldsymbol{p}_1| > 0, |\boldsymbol{p}_2| = 0$),

$$\sqrt{s_{\mathrm{FT}}} = \sqrt{m_1^2 + m_2^2 + 2E_1 m_2} \approx \sqrt{2E_1 m_2}\ , \tag{1.55}$$

if the ultra-relativistic regime is considered ($p \gg m$).

If instead the colliding beams setup ($\boldsymbol{p}_2 = -\boldsymbol{p}_1$) is used,

$$\sqrt{s_{\mathrm{CB}}} = E_1 E_2\ . \tag{1.56}$$

It is obvious from Eqs. (1.55) and (1.56) that colliding beams is the optimal setup for maximising the c.o.m. energy in a collider. Equation (1.55), still has significance, as it defines the energy scale for interactions between beam particles and material in the beamline.

The second key parameter is the luminosity $\mathcal{L}$. It is related to the rate of events at the

collision point as [20],

$$\frac{dN}{dt} = \sigma_p \cdot \mathcal{L} \ , \tag{1.57}$$

with N denoting the number of events and σ_p denoting the cross-section. The total number of expected events for a period T can hence be obtained by [12],

$$N_{\text{total}} = \sigma_p \cdot \mathcal{L}_{int} \ , \tag{1.58}$$

where

$$\mathcal{L}_{\text{int}} = \int_{t=0}^{T} \mathcal{L}(t)dt \tag{1.59}$$

is the integrated luminosity. The processes of interest typically have small cross-sections and hence a high luminosity is required for achieving significant event yields. The units of luminosity are $\text{cm}^{-2}\,\text{s}^{-1}$, which is equivalent to $10^{24}\,\text{b}^{-1}\,\text{s}^{-1}$, where b is the barn - the standard unit of cross-section in particle physics. The integrated luminosity is often quoted in inverse femtobarns (fb^{-1}) or inverse attobarns (ab^{-1}).

The luminosity for colliding bunched beams in a cyclic accelerator is given by,

$$\mathcal{L} = \frac{n_b N_1 N_2}{A} f_{\text{rev}} \ , \tag{1.60}$$

where N_1, N_2 are the number of particles in the colliding bunches, n_b is the number of bunches, f_{rev} is the revolution frequency and A is the overlap area of the beams. For Gaussian beams colliding head-on, $A = 4\pi\sigma_x^*\sigma_y^*$, where σ_x^*, σ_y^* are the rms transverse beam sizes at the interaction point.

In real accelerators, the beams are collided with a crossing angle, which reduces the luminosity. For symmetric Gaussian beams colliding at an angle θ_c, the expression becomes,

$$\mathcal{L} = \frac{n_b N_1 N_2 f_{\mathrm{rev}}}{4\pi \sigma_x^* \sigma_y^*} \mathcal{F} \ , \tag{1.61}$$

where the factor $\mathcal{F} \approx 1/(1+\phi^2)^{1/2}$ includes luminosity reduction due to the crossing angle. The parameter $\phi = \theta_c \sigma_z / 2\sigma_x$ is called the Piwinski angle with σ_z denoting the longitudinal rms beam size. An additional reduction of the luminosity occurs for collisions of long bunches due to the variation of the β^* over the bunch length (hourglass effect), but this reduction is relatively small for the LHC [20].

By making the assumptions of identical round beams at the collision point ($\sigma_x^* = \sigma_y^*$) and using the definitions in Section 1.1.5, the beam size can be re-written as [21],

$$\mathcal{L} = \frac{n_b N_{\mathrm{b}}^2 f_{\mathrm{rev}} \gamma}{\epsilon_{\mathrm{N}} \beta^*} \mathcal{F} \ , \tag{1.62}$$

where ϵ_{N} is the normalised emittance, β^* is the value of the betatron function at the interaction point and γ is the Lorentz factor. It is clear from this formulation that the luminosity can be increased by reducing the normalised emittance, reducing the collision beta function or increasing the bunch intensity.

In the case of ion beams, the luminosity is sometimes given as a nucleon-nucleon luminosity,

$$\mathcal{L}_{\mathrm{NN}} = A_1 A_2 \mathcal{L} \ , \tag{1.63}$$

where A_1, A_2 are the mass numbers of the colliding nuclei. This parameter allows direct comparison for beams of different ion species and asymmetric collisions like proton-ion.

1.2 Ion interactions with matter

Relativistic heavy ions can interact with collimators and other material in the beamline via a broad range of physics processes. The interaction with collimators is key for studies of collimation cleaning efficiency because the resulting secondary ions and other particles can travel significant distances in the machine and cause delocalised energy deposition.

In the microscopic description of the interaction [21], a moving projectile ion interacts with a target, which can be an atom/nucleus of the traversed material or an ion from the counter-rotating beam. The interactions between beam ions at the interaction points are a significant source of losses during ion operation and have been extensively studied [22–24]. This work focusses only on interactions between beam ions and collimators and passive materials. Rutherford scattering, multiple scattering, target ionisation, electromagnetic dissociation (EMD) and nuclear fragmentation are key types of beam-collimator interactions and are discussed in more detail in the following.

1.2.1 Rutherford scattering

Rutherford scattering is the elastic scattering of charged particles by the Coulomb force, which for two ions can be expressed as,

$$\boldsymbol{F} = \frac{1}{4\pi\epsilon_0}\frac{z_1 z_2 e^2}{|\boldsymbol{r_{21}}|^2}\hat{\boldsymbol{r}}_{\boldsymbol{21}} \ , \tag{1.64}$$

where ϵ_0 is the vacuum permittivity, z_1, z_2 are the atomic numbers of the ions, e is the electron charge, $\boldsymbol{r_{21}} = \boldsymbol{r_1} - \boldsymbol{r_2}$ is the vector distance between the charges and $\hat{\boldsymbol{r}}_{\boldsymbol{21}} = \boldsymbol{r_{21}}/|\boldsymbol{r_{21}}|$ is a unit vector between the charges. The diagram of Rutherford scattering is shown in Fig. 1.6.

Interactions of this type can be considered in a frame of reference where one of the particles is a stationary, scattering centre (target) and the other is incident on it (projectile). At moderate and high energies, classical treatment can be applied. The system in the rest frame of the target can be fully described using the vector distance from the projectile to the target $\boldsymbol{R}(\boldsymbol{b}, t)$, where $\boldsymbol{b}$ is known as the impact parameter and t is time. The impact parameter is a general measure of the distance between the interacting nuclei and it can be used to differentiate different types of interactions.

The differential cross-section for this interaction is given by the Rutherford formula,

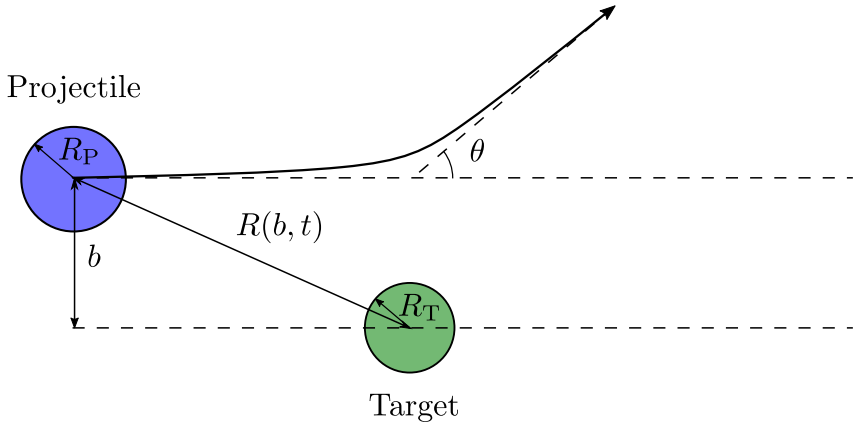

Figure 1.6: Diagram of Rutherford scattering of nuclei. The projectile ion is deflected due to the Coulomb interaction with the target.

$$\frac{d\sigma}{d\theta} = \left(\frac{1}{4\pi\epsilon_0}\right)\frac{z_1 z_2 e^2}{M^2\beta^4 c^4}\frac{1}{\sin(\theta/2)^4} \ , \tag{1.65}$$

where θ is the scattering angle, βc is the particle velocity and M is the projectile ion mass.

1.2.2 Multiple scattering

When traversing a medium, a charged particle is subject to multiple small angle deflections [12]. For a hadronic projectile, the deflection is dominated by Coulomb interactions with the target nuclei, but there are also contributions from strong force interactions. In the absence of large angle (hard) scatters, the scattering and displacement distributions are well represented by the multiple scattering (MSC) theory of Molière. The mean angle is,

$$\theta_0 = \frac{13.6\,[\text{MeV}]}{\beta cp} z \sqrt{\frac{x}{X_0}\left(1 + 0.038 \ln\left(\frac{xz^2}{X_0\beta^2}\right)\right)}, \tag{1.66}$$

where θ_0 is the rms transverse kick, βc, p and z are the projectile velocity, momentum and atomic number, x is the distance travelled in the material and X_0 is the radiation length.

The radiation length can be approximated as [25],

$$X_0 \approxeq \frac{716.4\,[\mathrm{g/cm^2A}]}{Z(Z+1)\ln\Big(287/\sqrt{Z}\Big)}, \tag{1.67}$$

where Z, A are the atomic number and the mass number of the target material.

Multiple scattering is important for collimation systems because beam ions with large offsets intercepted by the collimators can be scattered away from the main beam where they can be safely disposed of.

1.2.3 Target ionisation

Charged particles propagating through a medium made up of neutral atoms suffer collisions with bound electrons. In those collisions, part of the projectile momentum is imparted onto the electron and results in atomic and collective excitations or ionisation of target atoms.

The rate of energy loss $\frac{dE}{dx}$ due to electron collisions is often treated as a continuous process and given as a function of the projectile velocity β by the Bethe formalism [12, 26],

$$-\frac{dE}{dx} = \frac{4\pi e^4}{m_e}\frac{z^2}{c^2\beta^2}N_e L\ , \tag{1.68}$$

where e, m_e are the mass and charge of the electron, z, γ are the atomic number and relativistic factor of the projectile ion and

$$N_e = \frac{ZN_A\rho}{M}\ , \tag{1.69}$$

is the electron density, where Z, M, ρ are the target atomic number, mass and density, and N_A is the Avogadro's number. The dimensionless quantity L is called the stopping logarithm and has the standard form [26],

$$L = \ln\left(\frac{2mc^2\beta^2}{I}\right) + \ln\left(\gamma^2\right) - \beta^2 \ , \tag{1.70}$$

where I is the mean excitation energy of the target atom.

Corrections are necessary to Eq. (1.70) for ion projectiles at very high energies $\gamma \gg 1$. The first correction is known as the density effect and addresses the polarisation of the medium by the charge of the projectile. The second correction is due to the finite size of the projectile nucleus. The result is a stopping logarithm that is asymptotically constant [27],

$$L = \ln(1.6c/R\omega_{\mathrm{pl}}) \ , \tag{1.71}$$

where $R = A^{1/3}10^{-13}\,\mathrm{cm}$ is the assumed nucleus size, and $\omega_{\mathrm{pl}} = \sqrt{4\pi N_e e^2/m_e}$ is the plasma frequency of the material. Therefore, the stopping power in this regime only has a weak dependence on the parameters of the projectile or the medium.

The qualitative explanation of this observation is that the density effect causes saturation of the stopping power contribution from distant collisions ($b > R$), while the finite nucleus size limits the maximum momentum transfer in close collisions ($r < R$) and hence saturates the close collision contribution.

Equation (1.68) defines the linear stopping power, which has the units of $\mathrm{MeV\,cm^{-1}}$. The mass stopping power is often used instead,

$$-\frac{1}{\rho}\frac{dE}{dx} \ , \tag{1.72}$$

in units of $\mathrm{MeV\,cm^{-2}\,g^{-1}}$ because it is independent of the target material density ρ.

The ionisation energy loss goes as the square of the projectile charge and is hence significantly greater for ion than for proton projectiles.

1.2.4 Electromagnetic dissociation

Electromagnetic dissociation (EMD) is a photo-nuclear reaction that occurs in ultra-peripheral collisions of nuclei (no direct nuclear overlap). For relativistic ions, the electric field is Lorentz-contracted and appears transverse to the direction of motion. During interaction via those strong fields, the nuclei exchange large quantities of virtual photons and can become excited.

The magnetic field can be represented by an equivalent flux of photons using the Weisëcker–Willaims–Fermi (WWF) approximation. The cross-section can then be expressed as [28],

$$\sigma_{\mathrm{WW}} = \int dE N(E) \sigma_{\gamma}, \tag{1.73}$$

where $N(E)$ is the photon spectrum at energy E and σ_{γ} is the cross-section for the same process induced by real photons. The cross-section for EMD is given by the sum of cross-sections for electric dipole E_1 and quadrupole E_2 interactions,

$$\sigma_{\mathrm{EMD}} = \sigma_{\mathrm{E}_1} + \sigma_{\mathrm{E}_2}. \tag{1.74}$$

This can be expressed as [29],

$$\sigma_{\mathrm{EMD}} \approx N_{\mathrm{E}_1}\left(E_{\mathrm{GDR}}\right) \int \sigma_{\mathrm{E}_1}(E) dE + N_{\mathrm{E}_2}(E_{\mathrm{GQR}}) E_{\mathrm{GQR}}^2 \int \sigma_{\mathrm{E}_2}(E) \frac{dE}{E^2}, \tag{1.75}$$

where E_{GDR} is the energy peak of the giant dipole resonance (GDR) and E_{GQR} is the energy peak of the giant quadrupole resonance (GQR).

The excited nuclei decay to the ground state by emission of one or more nucleons. Neutrons, protons or even light ion fragments can be emitted, with single neutron emission having the largest probability [22]. The process of m-neutron emission from a nominal lead ion beam interacting with a carbon collimator in the LHC can be expressed with the reaction chain formula [21],

$$^{208}\mathrm{Pb}^{82+} + ^{12}\mathrm{C} \rightarrow ^{208-m}\mathrm{Pb}^{82+} + ^{12}\mathrm{C} + m\mathrm{n} \,. \tag{1.76}$$

The cross-section for EMD scales with z^2 and $\ln(\gamma)$, where z is the charge number of the projectile nucleus and γ is the relativistic factor. EMD is an important process for ion collimation because the secondary ion species emerging from the collimators have a magnetic rigidity close to nominal and can travel a significant distance away from their production point. The off-rigidity secondary ions are affected by dispersion and quickly get lost on aperture when they enter the accelerator arc. Furthermore, since EMD ions have discrete magnetic rigidity defects, they form secondary beams which can deposit sustained localised power loads on superconducting magnets.

1.2.5 Nuclear fragmentation

During heavy-ion collisions where there is a direct projectile-target spatial overlap, the nuclei can interact via the strong force. This interaction can be treated in the abrasion-ablation framework [30]. During a collision where there is an overlap of the projectile and target ions, the nucleons in both can be classified as participants and spectators. The different stages of the abrasion-ablation process are shown in Fig. 1.7.

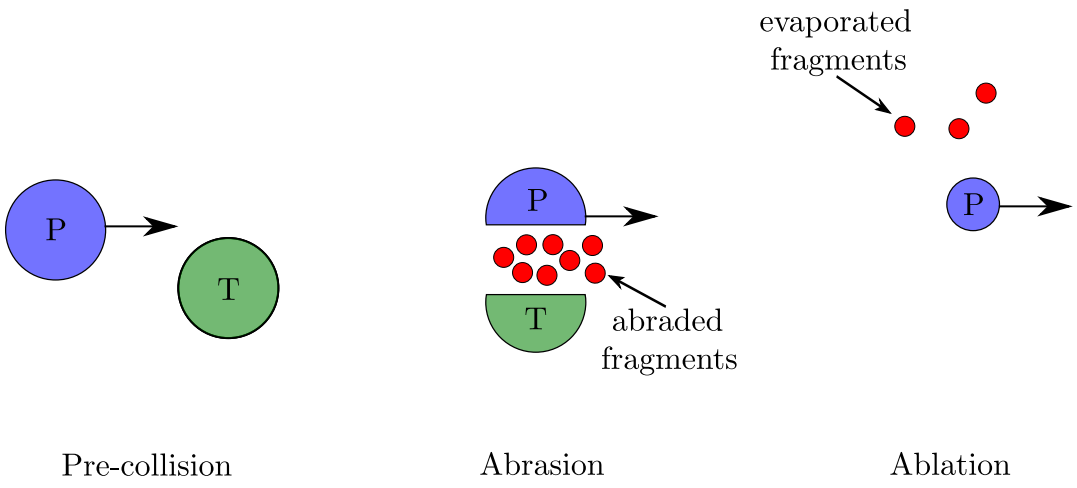

Figure 1.7: Schematic of abrasion-ablation process for nuclear fragmentation, showing projectile (P) and the target (T) in the three distinct stages of the process. Figure based on [31].

In the initial phases of the collision, momentum transfer takes place between the participants and nucleons in the overlap region are abraded. The gluon exchange that takes place involves large momentum transfers and the result is liberation of nucleons and ion fragments or production of new particles. During the abrasion phase, the spectator nucleons remain relatively undisturbed and the remaining projectile fragment continues on the pre-collision trajectory.

In the ablation phase, the projectile is in an excited state and can restore equilibrium by ejection of photons, nucleons or ion fragments. Fission is possible for some nuclei and lighter nuclei projectiles can also undergo disintegration, which can be described by the Fermi breakup model [32].

The final state products of nuclear fragmentation can consist of the full range of ion species between $A = 1 \cdots A_0$, where A_0 is the mass number of the original projectile ion, as well as baryons, mesons and other secondary products. Furthermore, secondary nuclei produced in the interaction can undergo further fragmentation.

Nuclear fragmentation in collimators results in a broad distribution of magnetic rigidity and scattering angles for fragmentation products, which leads to a spread of loss locations in the machine.

1.3 Simulation tools

Due to the complex interactions between beam ions and the collimators and the resulting broad spectrum of secondary ions, studies of ion beam collimation require advanced simulation tools. In order to enable such studies, multiple software packages are used as part of this thesis. These include tools for optical accelerator design, particle tracking and particle-matter interactions, as well as the frameworks that enable integrated studies. The main software packages used are MADX, BDSIM and the SixTrack-FLUKA coupling, which are briefly outlined in the following.

1.3.1 MADX

Methodical Accelerator Design (MADX) [33] is a FORTRAN program used for design and optimisation of accelerator optics. It is widely used in the physics community and has a mature interface. MADX supports both thick and thin lens lattice representations and produces summary tables of optical parameters in the so-called Twiss (.tfs) files, which are useful as configuration input for further, dedicated simulations like collimation or radiation transport.

1.3.2 SixTrack

SixTrack [34–36] is a 6D symplectic particle tracking code developed for long term tracking in high-energy circular accelerators and extensively used for single particle tracking studies in the LHC. SixTrack is written in FORTRAN and is compiled into a single executable. It supports thick and thin lens tracking via symplectic transfer maps for a variety of beamline elements. Following a recent update, SixTrack can handle tracking of arbitrary ion species [37]. SixTrack features an extension for proton interactions in collimators [38], which is actively used for LHC collimation studies [39].

The input for SixTrack is a set of plain-text files including the sequence of beamline elements, tracking configuration and beam distribution settings. The input is delimited in sets of related instructions knows as blocks. The output can be produced in ASCII or binary files.

1.3.3 FLUKA

FLUKA [40, 41] is an integrated, general-purpose Monte Carlo particle-matter interaction and transport code written in FORTRAN. It supports a broad range of particles and has comprehensive and extensively benchmarked models supporting hadron, lepton and heavy-ion particle interactions from energies in the order of keV to cosmic ray energies in arbitrary materials. FLUKA also provides event generators for hadron-hadron and nucleus-nucleus collisions.

The geometry modelling in FLUKA is performed using a native Combinatorial Geometry (CG) engine. Users benefit from an extensive library of detailed 3D geometry models [42] for components of the LHC, FCC-hh and other machines, as well as from a well-developed material database. The inputs to FLUKA are provided in a single plain-text file, which includes the beam parameters, physics configuration, output specification, custom routines and geometry description. The input is made up of declarations known as cards.

1.3.4 SixTrack-FLUKA coupling

SixTrack and FLUKA can be used together for studies including particle tracking and physics interactions. The interface is provided by the SixTrack-FLUKA active coupling framework [43]. The conceptual mechanism of the SixTrack-FLUKA coupling is depicted in Fig. 1.8.

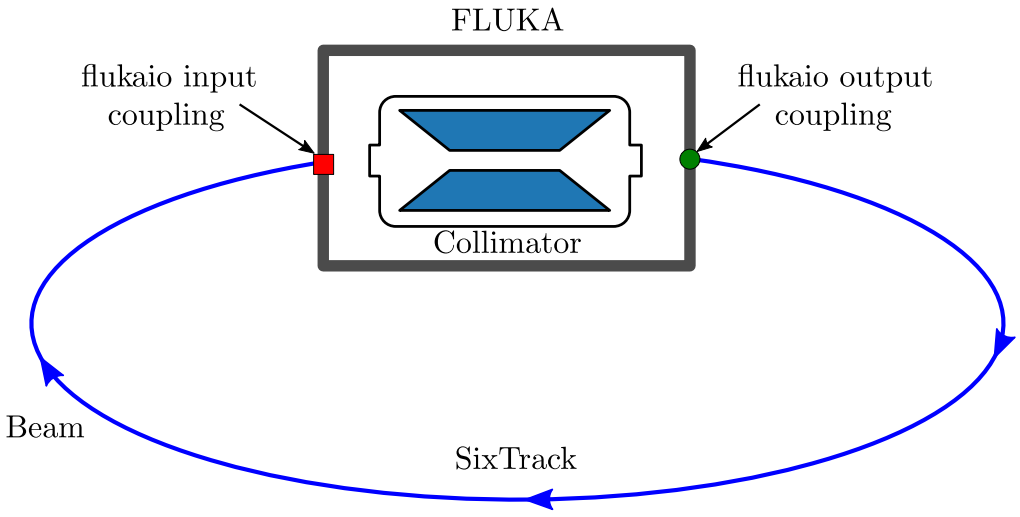

Figure 1.8: Schematic of the SixTrack-FLUKA coupling. At the entrance of every collimator the beam is transferred from SixTrack to FLUKA, where interactions with the collimator are simulated in a 3D model. The surviving particles are sent back to SixTrack for further tracking.

For a SixTrack-FLUKA coupling simulation, the accelerator model and beam distribution prepared in SixTrack and a selection of 3D radiation transport models are prepared in

FLUKA for regions of interest like collimators. Each of the insertion region contains an individual FLUKA model, surrounded by a perfect absorber (FLUKA black hole). During a run, SixTrack is used to track the particles in the accelerator lattice, until a region of interest is reached. At the boundary of the insertion region, the beam particles are transferred into the corresponding FLUKA insertion region, where a full Monte Carlo simulation of the particle interactions is executed. The surviving beam particles and newly generated secondary particles are sent back to SixTrack for further tracking. The communication between the code is performed at runtime by a specialised interface—`flukaio`. This simulation framework has been extensively developed and used for ion collimation simulation in the LHC [21, 44–46].

1.3.5 BDSIM

Beam Delivery Simulation (BDSIM) [47] is a software package for simulation of radiation transport in accelerator beam lines. BDSIM is designed for simulation of particle-matter interactions and its primary purpose is the detailed study of energy deposition and charged particle backgrounds in accelerator beam lines and collimation systems.

In BDSIM, the machine model is built using Geant4 [48–50], an object-orientated C++ library for simulation of the passage of particles through matter. Geant4 provides an extensive selection of modular Monte Carlo physics processes, including hadronic, electromagnetic and nuclear interactions, which can be combined and configured into physics lists appropriate for the case studies.

BDSIM combines dedicated accelerator tracking in the vacuum beampipe volumes with full interaction simulation for particles that leave the aperture. This approach allows for reliable tracking of both primary and secondary particles not only in the beam pipe, but also in the body of the magnet and in external absorptive volumes such as collimators and tunnel walls. BDSIM automatically builds a 3D geometry transport model from a MADX summary file input by leveraging Geant4's advanced hierarchical geometry engine. The geometry model can be customised using Geometry Description Markup Language (GDML) format input. BDSIM takes as input plain-text files formatted in the GMAD format (Geant4 + MADX) and produces output in binary ROOT [51] files.

Chapter 2

Ion beam collimation in the LHC

The Large Hadron Collider (LHC) operated at CERN is the world's largest and highest energy particle accelerator. The LHC is a hadron synchrotron that accelerates and stores counter-rotating beams of hadrons in a 27 km circumference ring before bringing them into collision at 4 points, where physics experiments are located. It provides proton–proton collisions at an unprecedented centre-of-mass energy of 13 TeV and heavy-ion collisions at 2.7 TeV per nucleon. The LHC design instantaneous luminosity is $1 \times 10^{34}\,\mathrm{cm}^{-2}\,\mathrm{s}^{-1}$ for proton beams and $1 \times 10^{27}\,\mathrm{cm}^{-2}\,\mathrm{s}^{-1}$ for ion beams [52]. The currently achieved peak luminosity surpasses the design value by a factor of 2 for proton beams [53] and a factor of 6 for heavy-ion beams [54], demonstrating excellent performance of the LHC. Data collected by the particle physics experiments since commissioning in 2008 has driven numerous important discoveries, most notably the discovery of the Higgs boson in 2012 [55, 56].

The collider long-term operation is organised into stages, known as runs, separated by periods of long shutdown (LS) during which maintenance and upgrades can be carried out. After a successful Run II (2015-2018), the LHC is currently in LS2 until 2021. Following the upcoming Run III, the LHC is scheduled to undergo a significant performance upgrade – the High Luminosity LHC (HL-LHC). With this upgrade, the physics programme at the LHC is expected continue until at least 2035.

At top energy, the design LHC proton beam stored energy is 360 MJ, the highest of any accelerator currently in operation and around 100 times larger than that of the Tevatron [57], the second highest energy accelerator in the world. The colossal stored energy, in addition to the high particle energy, presents unique challenges and requires sophisticated methods and systems to ensure safe operation. This section focusses on the collimation system, which protects the superconducting magnets and other sensitive equipment from unavoidable beam losses.

This chapter is focussed on key concepts for ion beam collimation, introduced using elements from the design and operation of LHC. Hadron collider operation, beam loss mechanisms, collimation systems and the challenges of ion beam collimation are covered in the first part of this chapter. The second part covers the ion beam collimation simulation workflows and techniques used throughout this thesis. Finally, a fully integrated simulation study for ion beam collimation in the LHC is presented. The operational configuration chosen for the simulations has not been studies in detail before. Results from the SixTrack-FLUKA coupling and BDSIM are shown alongside measured data and a discussion of the agreement between the different results is presented.

2.1 The LHC machine

2.1.1 Layout and optics

The geometrical layout of the LHC [3, 52] is comprised of 8 straight Insertion Regions (IRs) and 8 circular arc segments. A diagram of the layout can be seen in Fig. 2.1.

The main particle physics experiments are housed in IR1 (ATLAS [58]), IR2 (ALICE [59]), IR5 (CMS [60]) and IR8 (LHCb [61]). Those 4 insertions contain the experimental interaction points (IPs) where the beams interact. The RF system is installed in IR4 and IR6 features the beam extraction system. The last two straight sections, IR3 and IR7, are dedicated to the collimation system. The collimation system is described in more detail in Section 2.1.5.

The LHC IRs consist of a long straight section spanning 545 m and a transition region on

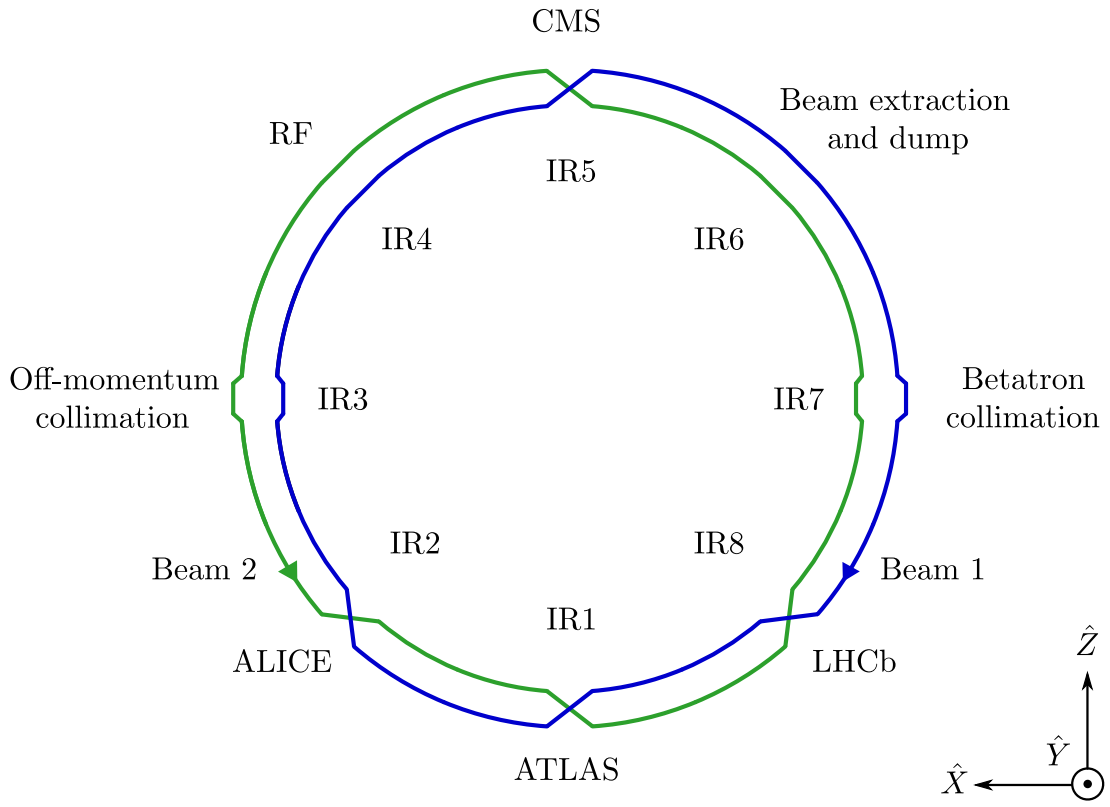

Figure 2.1: Diagram of the LHC layout. Each octant contains a long straight section with a dispersion suppressor and a half-arc on either side. Diagram based on [21].

either end called a dispersion suppressor (DS). The DS cancels out the horizontal dispersion generated in the arc and in separation dipoles and is used to match the insertion into the arc optics. The arcs separating the IRs are 2.45 km long and are made up of 23 individual FODO cells with 90° phase advance each. An arc cell contains 6 main dipole magnets, 2 main quadrupole magnets, as well as sextupole and other higher-order magnets. More details on the magnets are provided in Section 2.1.3.

The main LHC magnets have dual bores that transport both counter-rotating beams - Beam 1 (B1) an Beam 2 (B2). In the arcs, the beams are separated by 194 mm and contained in individual beam pipes. In order to provide more space for equipment in the collimation cleaning insertions IR3 and IR7, the beam separation in those sections is increased to 224 mm by specialised dipoles—the separation dipoles.

In the immediate vicinity of the IP, a single vacuum chamber is shared by the incoming and outgoing beam. Separation and recombination dipoles are used to bring the beams

in and out of the shared vacuum pipe. On approach of the IP, the beams are focussed to their smallest size for collision by a triplet of quadrupoles—the inner triplet. The optical functions and the layout of an experimental IR are shown in Fig. 2.2.

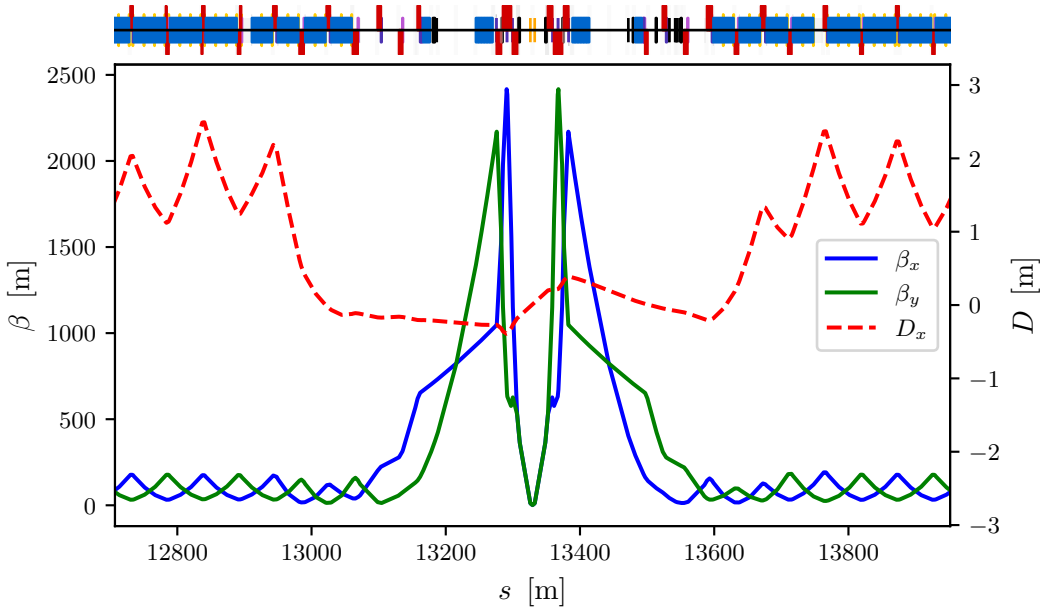

Figure 2.2: Plot of the optical functions for Beam 1 in IR5. The layout of the magnetic elements can be seen on top (blue–dipole, red–quadrupole, yellow–sextupole, black–collimator, gray–other).

In IP1 the beam crossing is in the vertical, while at IP5 the crossing is in the horizontal. The orbit of the beam through the IP, shown in figure Fig. 2.3, demonstrates the effect of the crossing. When the beams are not being collided, an orbit bump in the plane orthogonal to the crossing is used to keep them separated at the IPs.

2.1.2 Operational cycle

During nominal operation in physics mode, the LHC beams are subject to burn-off due to collisions [62]. Over time, the intensity loss becomes sufficient to compromise the luminosity and the beams must be extracted to a dedicated absorber (dump), where the beam energy is safely dissipated. A beam dump can also be triggered by a fault in the machine. Following a dump, fresh beams are injected and accelerated to top energy. The operation is divided in discrete cycles. Each operation cycle [63, 64] consists of a sequence of different machine configuration stages. The main stages of the operational cycle are shown in Fig. 2.4 and

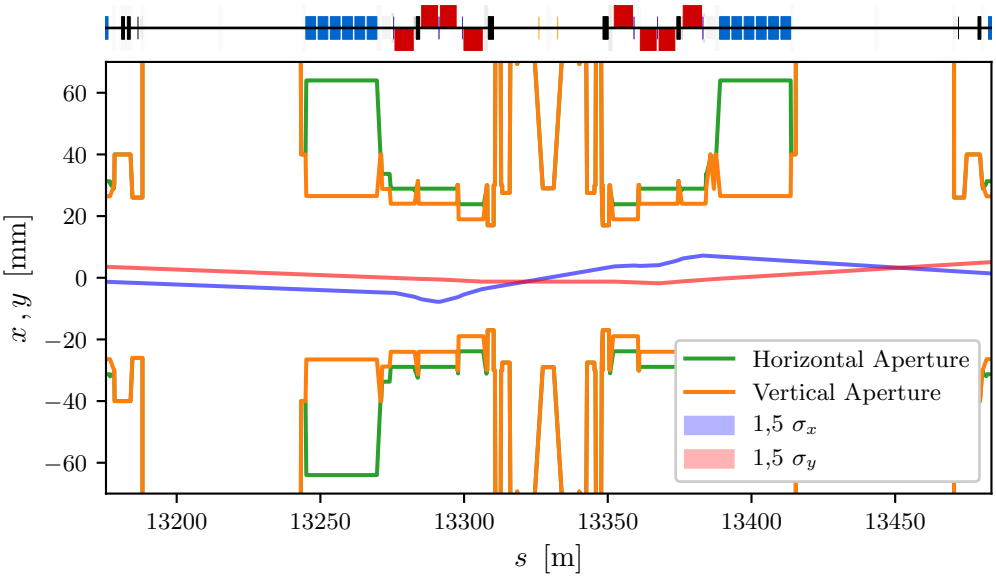

Figure 2.3: Orbit of Beam 1 in in IR5 showing the horizontal crossing and the beam focussing on approach of the IP. The beam is depicted as blue and red bands, with the darker bands showing a $1\,\sigma$ beam envelope and the lighter bands showing a $5\,\sigma$ beam envelope.

include,

1. Prepare Injection—The machine is configured to receive fresh bunches. The collimators are set to injection openings and additional injection protection collimators are deployed to guard against beam mis-steering during injection.

2. Injection—Bunches of particles are extracted from the SPS at $E = 450\,\mathrm{Z\,GeV}$ and injected into the LHC. Injection continues until the nominal beam intensity is achieved.

3. Prepare Ramp—After injection is complete, checks are performed and the RF system is prepared for acceleration. The injection protection collimators are retracted completely.

4. Ramp—The beams are accelerated by the RF system and the main magnet field is ramped up by increasing the electrical current supply to the magnets. During acceleration, the beam sizes are reduced via adiabatic cooling and the collimator gaps are synchronously reduced. During the ramp, beam particles not captured by the RF buckets or having a momentum deviation outside of the momentum acceptance are lost, creating significant and ramp rate-dependent beam losses.

5. Flat top—Upon reaching the top energy, the RF system discontinues the acceleration. The beams are prepared for squeezing.

6. Squeeze—The optics of the machine are changed from the injection configuration to achieve a squeeze of the β^* to the nominal values. The collimators are brought into the physics mode configuration in order to protect the aperture bottlenecks.

7. Adjust—The orbit bump separating the beams at the IPs is collapsed, collisions are initiated and the luminosity is optimised.

8. Stable beams—When collisions are established and the beam lifetime is in the normal range, stable beams are declared and data taking beings at the physics experiments. This mode of operation is sustained for many hours.

Since 2016, the ramp and the first part of the squeeze are performed together, as seen in Fig. 2.4, by using a Combined Ramp and Squeeze (CRS) [65] configuration to save time.

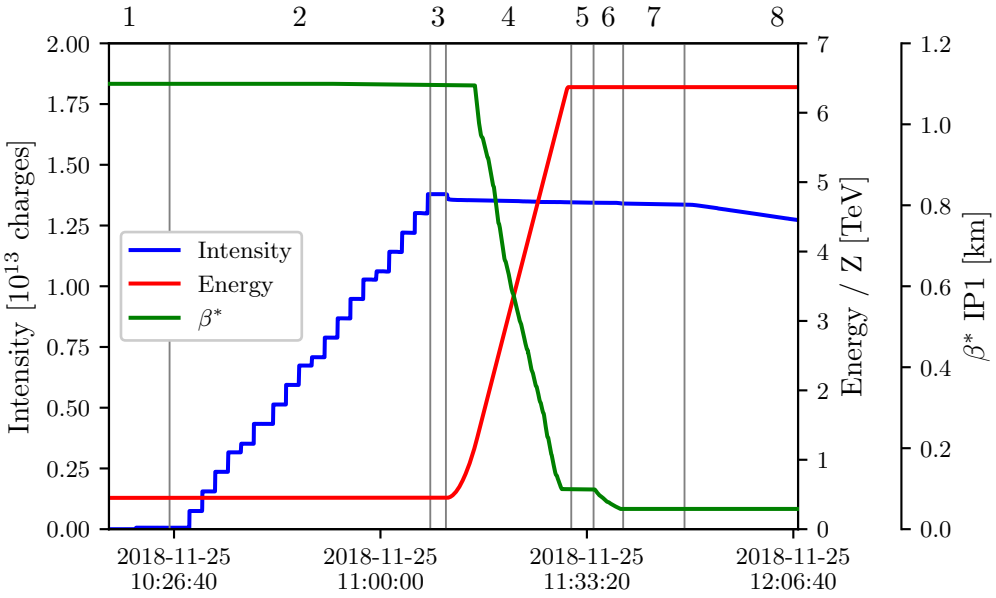

Figure 2.4: Evolution of key parameters during fill 7473 of the 2018 LHC ion run, showing the operational cycle sequence. The grey bands delimit the different operation modes and the numbers above each band denote the stage in the cycle sequence. A limited time span from the fill is shown to highlight relevant features. The entire fill lasts 12 h:17 min, with 79 % of the time spent in the stable beams mode.

2.1.3 Magnets

More than three quarters of the LHC ring is occupied by magnets. There are 1232 superconducting main dipole magnets (MB) and 392 superconducting main quadrupole magnets (MQ), as well as over 6000 other corrector magnets [66, 67]. The main dipoles are 15 m long and have a nominal magnetic field of 8.33 T. The main quadrupoles are 3 m long and have a gradient of 233 T m^{-1}. The coils of both the dipoles and the quadrupoles use niobium titanium (NbTi) Rutherford cable. The magnet cold mass assemblies are housed in cryostats and kept at a temperature of 1.9 K by means of liquid helium cooling. A cross-section diagram of an LHC dipole is depicted in Fig. 2.5.

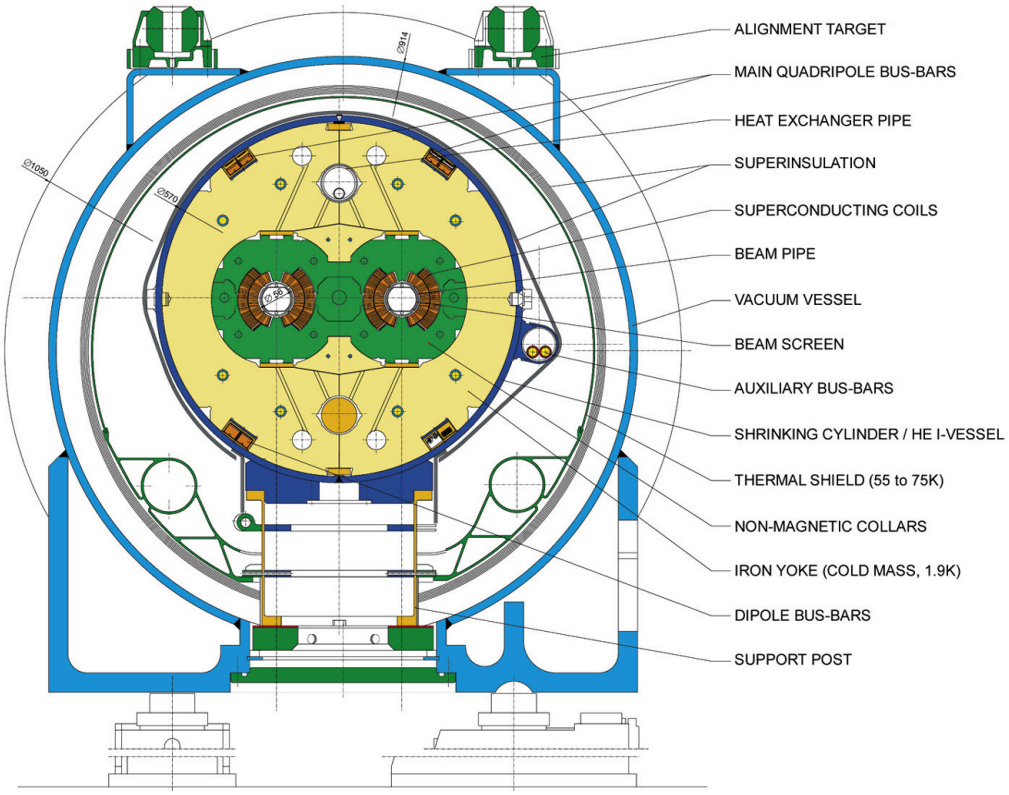

Figure 2.5: Cross-section of an LHC main dipole magnet. The main structural elements are highlighted. [68]

To remain superconducting, the magnets must be operated in narrow ranges of temperature, current and magnetic field. Local heating due to energy deposition from beam losses can cause a loss of superconductivity, or quenching, of the magnet. The quench limit depends on the time scale of the losses. During the design of the LHC, the quench limit for NbTi has been estimated as 5 mW cm^{-3} [69] for steady-state losses at the design top energy of 7 TeV. During LHC operation, quench tests performed have indicated that the

real quench limit is likely a factor 3-5 higher than the original estimate [70, 71]. If power deposition is allowed beyond this threshold, there are risks of undesired beam dumps and for even higher power loads also material damage.

A beam screen is installed in the arc magnets to protect the cold bore from synchrotron radiation and energy dissipation due to beam image currents [52]. The beam screen is a perforated tube tube that is fitted inside the bore of the arc magnets and defines the mechanical acceptance of the beampipe. The beam screen in the LHC arcs measures 22 mm half-size in the horizontal and 17 mm half-size in the vertical [3].

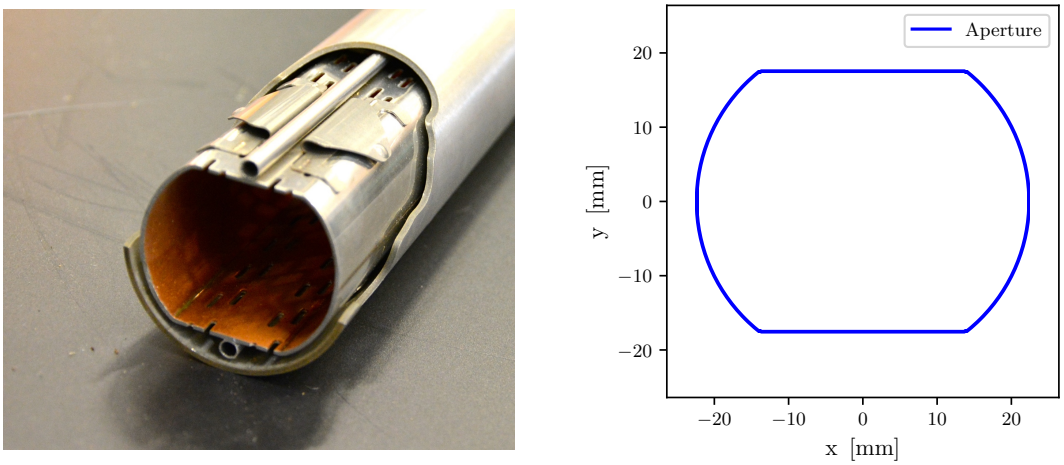

(a) (b)

Figure 2.6: Photograph of an LHC arc beampipe section with the steel pipe cut out to expose the beam screen (a) and a plot of the corresponding aperture model used in simulations (b). The dimensions of the beam screen are 22 mm half-size in the horizontal and 17 mm half-size in the vertical [3]

2.1.4 Beam losses and cleaning inefficiency

In the LHC, the design stored energy per beam is 362 MJ and the maximum achieved so far is more than 300 MJ. High-power charged particle beams can be highly destructive to material and equipment in their proximity [72, 73]. Furthermore, particles at the LHC top energy do not stop and deposit all of their energy immediately upon contact with solid material. Cascading particle interactions lead to an emission of a broad spectrum of secondary particles, often referred to as showers. Particles in the EM and hadronic showers can, in some cases, travel much further than the original impact location, spreading out

the energy deposition and creating additional risks.

By comparing the stored beam energy and the quench limit quoted in Section 2.1.3, it is clear that a fractional beam loss of as little as a few 1×10^{-9} can risk quenching the superconducting (cold) magnets. To ensure safe machine operation, the beam losses must be minimised in areas of the machine not designed to sustain losses, such as the superconducting magnets, experiments and other devices in proximity to the beam [74].

The are numerous causes for beam loss and the loss time can range from ultra-fast ($t_{\text{loss}} < 86\,\mu\text{s}$, i.e. single revolution), fast ($t_{\text{loss}} < 5\,\text{ms}$) or slow ($t_{\text{loss}} > 50\,\text{ms}$). The fast losses are usually the result of equipment failure, such as an injection kicker mis-firing, and are not considered in the following. During normal operation, some beam particles continuously diffuse outwards from the beam core due to unavoidable processes such as intra-beam scattering, beam–beam interactions, residual gas scattering, electron cloud and others [75]. These particles have large transverse amplitudes and populate the tails of the Gaussian beam distribution, called the beam halo. The halo particles eventually leave the physical acceptance of the machine and are lost, leading to potentially harmful energy deposition. In addition to this, the beam halo can penetrate the particle physics experiments and create background and noise in the experiments. It is assumed that the rate of diffusion per turn is much smaller than the rms beam size, allowing the normal diffusive losses to be represented collectively using the beam lifetime. The intensity of the circulating beam I as a function of time t can be represented as an exponential decay,

$$I(t) = I_0 e^{-t/\tau_b}, \tag{2.1}$$

where I_0 is the starting beam intensity. The time constant τ_b is the beam lifetime (BLT) and is itself a function of time $\tau_b \equiv \tau_b(t)$ as it does not stay constant during the whole operation cycle of the machine. Using this expression, the rate of beam losses can be obtained as,

$$-\frac{1}{I}\frac{dI}{dt} = \frac{1}{\tau_b}. \tag{2.2}$$

The collimation system is designed to concentrate the beam losses in the machine and dispose of the resulting power loads in a controlled manner. Perfect efficiency is not possible due to particle interaction with the collimators and production of secondary particles and hadronic showers, and some of the losses will always occur outside of the collimators. The performance of the collimation system is hence quantified by the fraction of beam losses not captured.

For ion collimation, the local cleaning inefficiency η is defined as [21],

$$\eta(s) = \frac{E_{\mathrm{loc}}}{E_{\mathrm{max}}\Delta s} \ \left[\mathrm{m}^{-1}\right] \ , \tag{2.3}$$

where E_{loc} is the energy loss in a region $[s, s + \Delta s]$ and E_{max} is the peak energy loss in the collimation system. An alternative formulation can be given as,

$$\eta(s) = \frac{E_{\mathrm{loc}}}{E_{\mathrm{tot}}\Delta s} \ \left[\mathrm{m}^{-1}\right] \ . \tag{2.4}$$

This definition differs from Eq. (2.3) in using the total energy loss around the full ring E_{tot}, instead of the peak energy lost on the collimation system E_{max}. The formulation in Eq. (2.3) is well-suited for comparison with measurements in the LHC, while Eq. (2.4) allows straightforward comparison with a quench limit estimate. The definitions are related by a linear scaling factor, meaning that the relative magnitude difference between different loss clusters is not affected by the choice of normalisation.

Some regions of the machine are tolerant of beam losses, in particular the warm magnets in the collimation insertions [76], while others like the superconducting magnets, are sensitive to losses and localised losses there can cause quenches. A comparison with a quench limit estimate can be performed to define the maximum intensity of the circulating beam that can be tolerated without quenches. The quench limit in terms of cleaning inefficiency η_{C} can be defined as [77],

$$\eta_{\mathrm{C}} = \frac{\tau_b R_q}{I_0}, \tag{2.5}$$

where R_q is the quench limit, typically quoted as a proton loss rate in units of p/m/s. For the LHC at top energy of 7 TeV, the quench limit is $R_q = 7.8 \times 10^6$ p/m/s [69].

For ion beams, Eq. (2.5) can be obtained in terms of energy instead of number of protons by using,

$$I_0 = n_b N_b E_\mathrm{i} \ , \tag{2.6}$$

$$R_q^\mathrm{ion} = R_q E_\mathrm{p} \ , \tag{2.7}$$

where n_b is the number of ions per bunch, N_b is the number of ion bunches, E_i is the nominal ion energy and E_p is the nominal proton energy.

The limit of the maximum acceptable losses at any point of the operational cycle can be obtained by defining a minimum acceptable BLT, τ_b^min. For the LHC operation at top energy this time is defined as 12 min, sustained for 10 s [78]. For proton beams of nominal intensity, this results in a cleaning inefficiency quench limit of $1.74 \times 10^{-5}\,\mathrm{m}^{-1}$.

2.1.5 Collimation system

Collimation system of the LHC

The LHC is fitted with an advanced collimation system [79, 80] to clean the beam halo, protect the machine for normal and anomalous losses [81] and reduce the background to experiments [82, 83]. The collimation system is designed to safely handle beam losses of up to 500 kW [52] and has proven successful in preventing magnet quenches with instantaneous losses of up to 1 MW [84].

The collimation system consists of more than 120 collimators. The majority of the collimators are active devices with two individually movable jaws of solid material that are brought close to the beam [85]. The jaws are straight and parallel to the beam and have a tapering on either side in the axis of the beam. The jaw assembly is contained in an outer

vacuum vessel. The distance between the start and end of the tapering, where the jaw is straight, is the active length of the collimator. Photographs of LHC collimators showing the jaws and the outer assembly can be seen in Fig. 2.7.

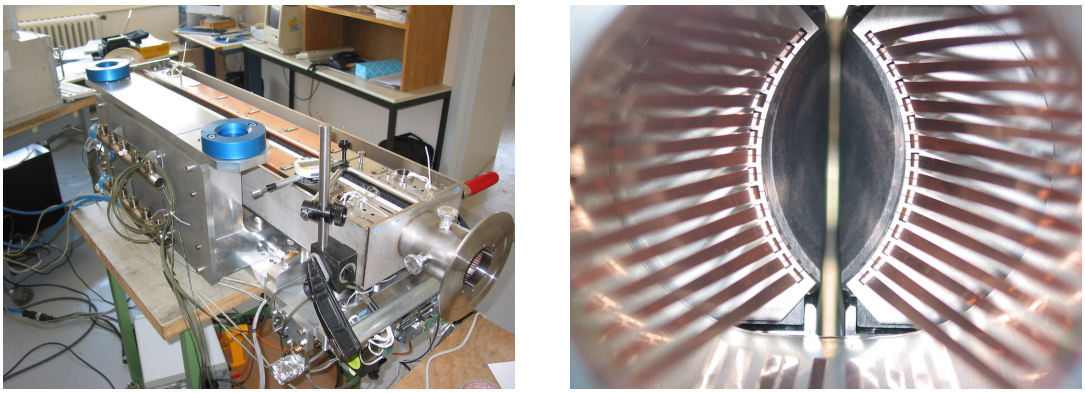

(a) (b)

Figure 2.7: Photographs of an LHC collimator. A side view of a collimator assembly, including the tank, is shown in (a), while a view of the jaws along the beam path is shown in (b) [86].

There are two insertion regions dedicated to the collimation system—IR3 and IR7. Cleaning of halo particles with large betatron excursions happens in IR7, where the optical functions are designed to provide a maximum separation for such particles. The optical functions of the betatron cleaning insertion are shown in Fig. 2.8b. The removal of halo particles with large momentum deviations happens in IR3, where additional horizontal dispersion is introduced in order to translate the momentum defect of the halo particles into a physical trajectory deviation. The optics for the off-momentum cleaning insertion can be seen in Fig. 2.8a.

The principle of the LHC multi-stage collimation system is illustrated in Fig. 2.9. The primary collimators, Target Collimator Primary (TCP), are the closest devices to the beam in the machine and form the first collimation stage. The purpose of the primary collimators is to intercept and dispose of beam halo particles. When traversing the primary collimators, particles accumulate an offset due to MSC. In addition to MSC, the halo particles can undergo elastic scattering, acquiring an angular kick, and inelastic interactions, depositing energy and producing secondary particles. Other processes that have an influence on the collimation performance are elastic scattering, single diffractive scattering for protons and nuclear fragmentation and EMD for ions. Those processes can result in particles with significant energy offsets that get lost in the downstream DS. The particles scattered by the

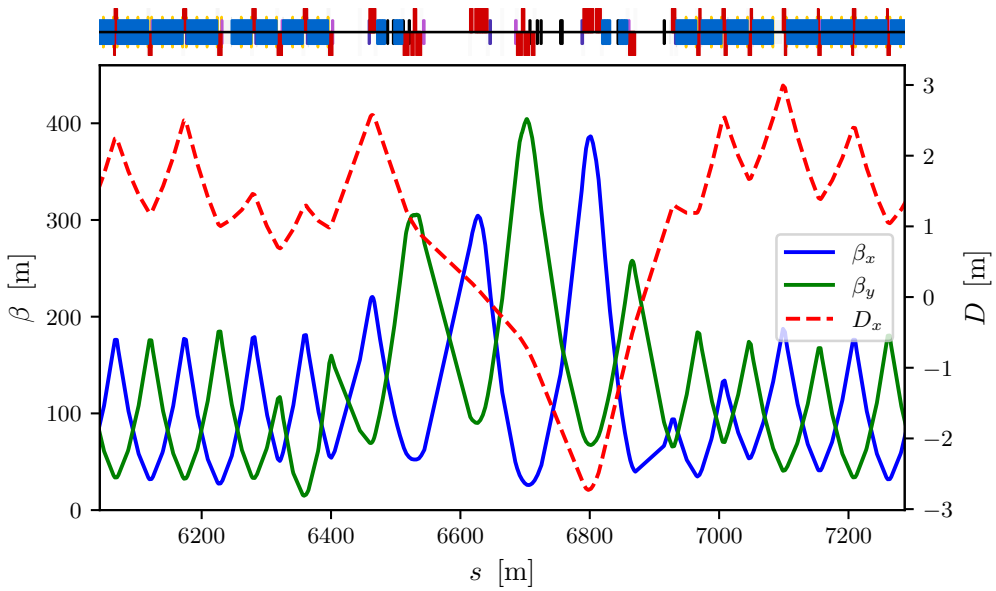

(a)

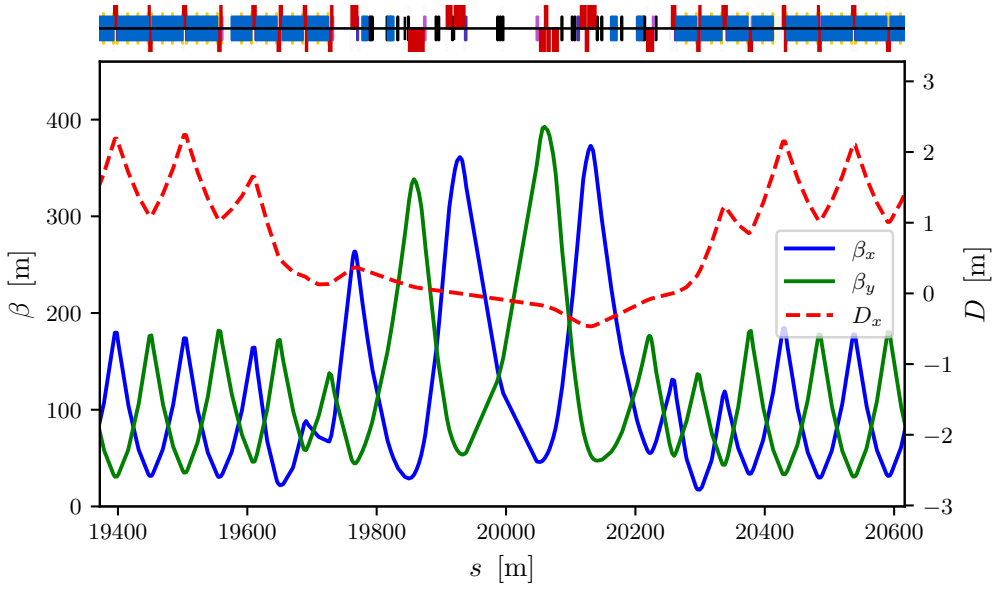

(b)

Figure 2.8: Optical functions in the LHC collimation insertions IR3 (a) and IR7 (b).

TCPs form the secondary halo. The TCPs are exposed to high sustained power loads of up to tens of kW [84] due to energy deposition from the impacting particles during operation and robustness is a crucial requirement. A low-Z, low-density material [87] is chosen to limit the energy deposition in the volume of the TCP, while maintaining good mechanical characteristics. The TCP collimators are made of carbon fibre composite (CFC), with $Z = 6$ and $\rho = 1.67\,\mathrm{g\,cm^{-3}}$. The active length of the jaw is 0.6 m.

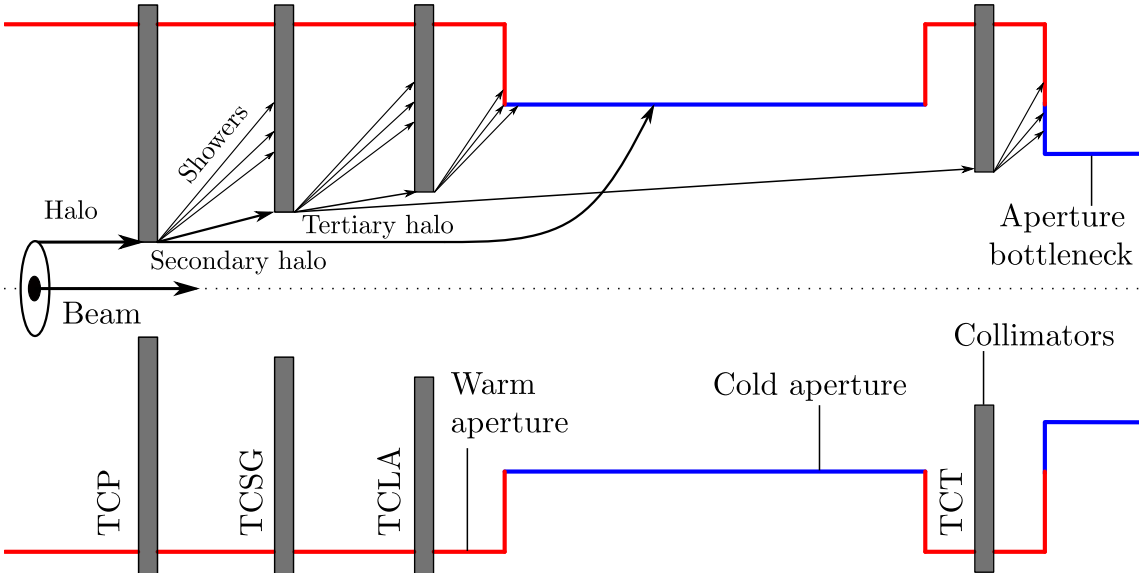

Figure 2.9: Diagram of multi-stage collimation system including primary (TCP), secondary (TCSG) and tertiary (TCT) collimators and shower absorbers (TCLA). Beam halo particles impacting the TCP are scattered to the TCSGs, hadronic showers from the TCSGs are absorbed by the TCLAs and TCTs are in place to protect the aperture bottlenecks. Particles with momentum defects that escape the collimation insertion are lost in the downstream dispersion suppressor.

The secondary collimators, Target Collimator Secondary—Graphite (TCSG), which form the second stage of the collimation system, are installed in locations where the phase advance from the primary collimator is optimal for intercepting the secondary halo and primary halo particles deflected by MSC [88,89]. In the TCSGs, the halo particles generally travel longer distances in the collimator jaw than in the TCPs, increasing the likelihood of elastic and inelastic interactions. Electro-magnetic and hadronic showers are generated in the secondary collimators and a significant fraction of the halo energy deposition occurs there. The particles leaving the collimator form the tertiary halo. The TCSGs are some of the most loaded collimators in the machine and robustness is a key requirement. They are also made of CFC and have an active length of 1 m. Starting from Run III of the LHC, TCSG collimators made of molybdebum-graphite (MoGr), coated with 5 µm of molybdenum, will be employed.

Active absorbers, Target Collimator Long Absorber (TCLA), are installed downstream of the TCSGs. Their role is to stop elements of the tertiary halo and shower products coming from the TCSGs before they reach the dispersion suppressor. The TCLAs are not exposed

to large power loads like the TCPs and TCSGs, and the main requirement is minimising the particle leakage. Because of this requirement, a high-Z, high-density material [87] that enhances the interaction cross-section and energy deposition is chosen. The TCLAs have an active length of 1 m and are made of a tungsten alloy (Inermet180), with Z = 74 for tungsten and $\rho = 18.7\,\mathrm{g\,cm^{-3}}$ for the alloy.

The betatron collimation system includes a third collimation stage that provides local protection for the aperture bottlenecks in the machine. In the LHC, the bottlenecks are the inner triplets of the experimental IRs, where the beams are focussed down to the collision size. Tertiary collimators, Target Collimator Tertiary—Pickup (TCTP), are deployed upstream of the inner triplets in IRs 1, 2, 5 and 8. The Target Collimator Tertiarys (TCTs) have an active length of 1 m and are made of Inermet180.

In IR7, there are 3 sets of collimators covering the horizontal, vertical and skew planes. In IR3, the dispersion is only in the horizontal and only one set of collimators is installed. Each experimental IR has one TCT in each of the horizontal and vertical planes upstream of the first inner triplet. The counts and distribution of the main collimators around the ring are summarised in Table 2.1. There are additional collimators installed for protecting the machine during injection and extraction, cleaning collision debris and other specific tasks. Those collimators do not affect the collimation studies presented and are not included in the table.

Table 2.1: Counts and materials for collimators per beam in the LHC. The materials are carbon-fibre composite (CFC) and tungsten heavy alloy (Inermet180).

Collimator	Count	Material
IR7 TCP	3	CFC
IR7 TCSG	11	CFC
IR7 TCLA	8	Inermet180
IR3 TCP	1	CFC
IR3 TCSG	4	CFC
IR3 TCLA	4	Inermet180
IR1, 2, 5, 8 TCT	2	Inermet180

It is critical that the collimation system maintains the design hierarchy—primary, secondary, tertiary. For example, beam halo particles should only impact the primary collimators. The phase advance between collimator stages and their gaps are optimised to maintain the hierarchy even in cases of collimator jaw flatness imperfections or orbit errors.

Collimation upgrades for High Luminosity LHC

The High Luminosity LHC (HL-LHC) [90] is a significant upgrade of the LHC, planned as part of the effort to fully exploit the machine's potential. The main goal of the upgrade is to achieve an integrated luminosity of $250\,\mathrm{fb}^{-1}$ per year, allowing to reach $3000\,\mathrm{fb}^{-1}$ over the HL-LHC lifetime, a factor of around 10 beyond what has been achieved in the first 10 years of LHC operation. Upgrades of the injector chain [91, 92] are planned to increase the beam intensity by a factor 2, relative to the current LHC. The design stored energy per beam in the HL-LHC is 678 MJ, more than double the currently achieved maximum.

In order to handle the challenges of beam collimation in the HL-LHC, the collimation system is also being upgraded [93]. One of the most significant upgrades is the introduction of dispersion suppressor collimators, Target Collimator Long Dispersion (TCLD). During the current LHC long shutdown period (LS2, in 2019–2021), it is planned to install one TCLD collimator in the DS of the outgoing beam on each side of IR7. To make space for the TCLD, one main dipole in cell 9 will be replaced by two shorter, stronger dipoles with the collimator assembly in the middle. A visual comparison of a nominal dipole and the TCLD assembly with the shorter 11 T dipoles is shown in Fig. 2.10.

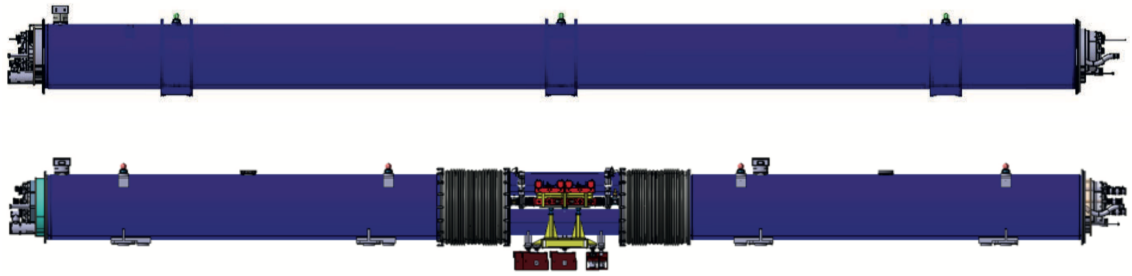

Figure 2.10: Visualisation of a nominal LHC 8 T dipole (top) and the HL-LHC 11 T dipole assembly with the TCLD collimator in the middle (bottom). The collimator unit, shown in gray, yellow and red on the bottom image, is housed inside the connection cryostat, which joins the two 11 T magnets. Image re-printed from [90].

The shorter magnets would be manufactured using niobium tin (Nb_3Sn) superconductor and have a field of 11 T and a length of 11 m, resulting in the same integrated bending of 120 T m as an LHC main dipole. The primary purpose of the TCLDs is to intercept dispersive losses from the upstream IR7 for both proton and ion beams [21, 94, 95]. The collimator is made of Inermet180 has an active length of 0.6 m. A schematic diagram of

the layout for the IR7 DS with the TCLD collimator inserted is depicted in Fig. 2.11.

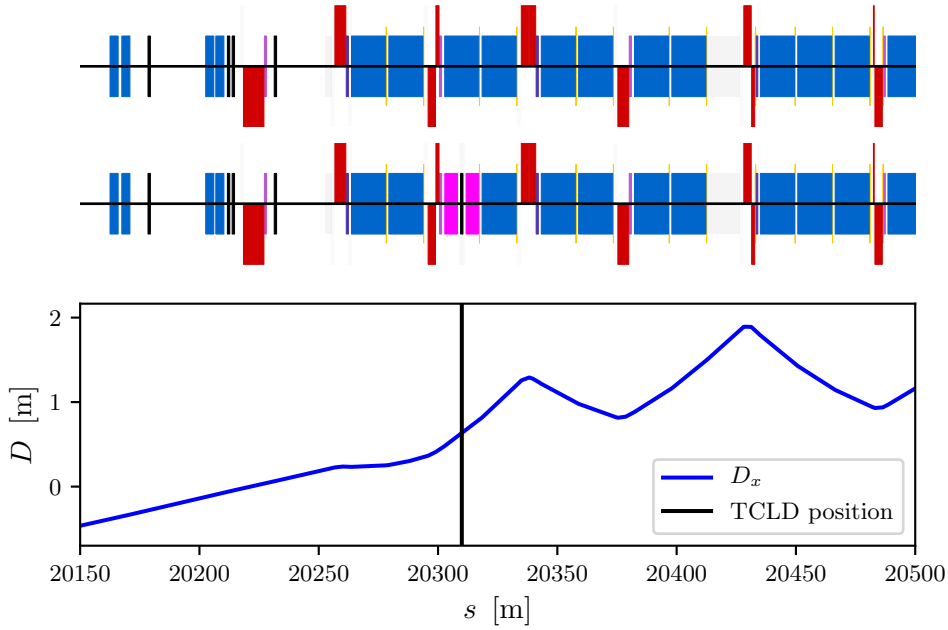

Figure 2.11: Diagram of the layout in the DS of IR7 showing the LHC configuration (top), the HL-LHC configuration with the TCLD included in cell 9 (middle), and the dispersion function (bottom). The 11 T magnets in the TCLD assembly for the HL-LHC are depicted in magenta and the collimator is depicted as a black bar. The dispersion function is taken from the HL-LHC optics.

In addition to the DS collimators, novel collimation techniques are under development for the HL-LHC, including crystal collimation and hollow electron lenses. The aim of the novel collimation techniques is to provide a better control of the beam halo and reduce the losses due to collimation in the superconducting regions of the machine.

For crystal collimation [96–98], a bent silicon crystal is used instead of the amorphous carbon primary collimator in the standard collimation setup. Halo particles impacting the crystal can enter a channeling regime, in which their trajectories are guided by the potential between crystalline planes. The achieved deflection is much larger than that from scattering in an amorphous material, and the halo particles can be directed onto a single massive absorber that can be placed at a larger aperture to avoid increasing the impedance. In addition to this, the interaction cross-sections are suppressed in the channeling regime, resulting in fewer scattered particles that can be lost in the DS. Crystal collimation has shown promise for improving the cleaning efficiency for both proton and heavy-ion beams.

Hollow electron lenses [99–101] make use of magnetically confined electron beams to clean and scrape the beam halo. In this technique, an axially-symmetric, low-energy electron beam with a torus profile is overlapped with the main hadron beam over a short region in the machine. The hadron beam core is unperturbed by the axially-symmetric electron beam, while halo particles intercepting the electron beam receive non-linear transverse kicks that enhance the halo diffusion.

2.2 Collimation of ion beams

The collimation system in the LHC is optimised for proton beam operation [74, 75]. In 2018, the maximum beam energy for proton beams achieved was 6.5 TeV and the highest achieved stored energy was around 300 MJ in 2018. In contrast, the maximum achieved stored energy for ion beams in 2018 was 13.3 MJ [54] at a maximum beam energy of 6.37 Z TeV. While significantly smaller than for proton beams, the stored ion beam energy still exceeds by around a factor 3 the design value of 3.8 MJ [52]. Despite the much lower stored energy, the performance of the collimation system is more critical for ion operation in the high-intensity regime [102, 103] than for proton operation, due to the significantly lower cleaning efficiency.

The collimation cleaning efficiency for ion beams is found to be about two orders of magnitude worse than for protons [44], since heavy ions undergo nuclear fragmentation and EMD in the collimators. These processes produce secondary ion fragments with a charge-to-mass ratio different from the nominal one [21, 44]. The fragments can emerge from the collimators within the geometric acceptance of the downstream collimators and pose a risk for the cold magnets in the DS, where the dispersion ramps up to the nominal arc values. For ion operation in the LHC, the DS losses can limit the achievable intensity [104].

2.2.1 Measured loss maps

Beam loss monitoring

Beam losses in the LHC are monitored by around 4000 beam loss monitors (BLMs) [105], installed at critical beam loss locations around the ring, most notably at quadrupole magnets, where the betatron function reaches a maximum. The purpose of the BLMs is to trigger a beam dump via the beam interlock system (BIS) in the event of losses exceeding a set threshold and to perform loss surveillance, which helps in diagnosing the cause of the losses. Most of the BLMs are parallel plate ionisation chambers, filled with nitrogen gas at a pressure of 1.1 bar. They are mounted on the outside of magnet cryostats and to other beamline elements. The signal recorded in the BLM is proportional to the number and type of charged particles traversing the BLM active volume [106]. Before reaching the BLMs, the secondary showers generated by losses on the beampipe aperture have traversed volumes of different material. Detailed simulations and measurements are used to determine the correlation between aperture impact distribution and the BLM signal [107]. The beam abort thresholds are hence set using input from Monte Carlo simulations of hadronic shower development and energy deposition in the magnets, as well as quench and material damage limits and BLM response [39, 71]. The loss signal is integrated over 12 integration times in the range between 40 µs and 82 s, with each running sum having an allocated threshold. As the hadronic shower development depends on the beam energy, the thresholds are also set for 32 energies in the range 450 GeV to 7 TeV. BLMs are installed on collimators and provide information about the performance of the collimation system, that is used during setup and validation.

Qualification loss maps

The cleaning performance of the collimation system must be evaluated before operation with nominal intensity beams. Dedicated measurement campaigns are performed during the commissioning of the LHC after technical stops and long shutdowns in order to validate the collimation settings. For this purpose, losses on the collimation system are artificially induced by exciting (blowing up) a low intensity beam of only a few bunches. During the periods of excitation, the losses in the collimation system and the rest of the ring are

recorded using the BLMs. The distribution of losses with S-position is known as a loss map and loss measurements during machine commissioning are called qualification loss maps.

Loss map measurements are performed separately for each of the two transverse planes and the longitudinal plane. The beam blow up in the transverse planes is achieved by using the transverse damper (ADT) [108], which can increase the beam emittance by introducing a white noise excitation that provides random transverse kicks to the beam particles. When the excitation is in one of the transverse planes, the loss measurement is known as a betatron loss map. In the longitudinal plane, a variation of the RF frequency is used [108] to produce both the low and the high off-momentum tails and in this case, the loss measurement is known as an off-momentum loss map. The measurements are saved under the LHC logging service [109] for offline analysis. The BLM integration time of 1.3 s is used for loss maps and the units are $\mathrm{Gy\,s^{-1}}$. As the BLM data is not continuous in s, the loss maps from measured data do not depict the cleaning inefficiency described in Section 2.1.4, but rather the normalised BLM signal. Furthermore, the cleaning inefficiency is a measure of the number of locally lost particles, while the BLMs signal is a measure the secondary shower particles, which also depend on the local geometry and the aperture impact distribution. The normalisation is done by scaling the losses recorded by the BLMs to the peak loss in the collimation system. The loss maps hence provide information about the relative distribution of losses, which is independent of beam intensity and the beam emittance.

Qualification loss maps from 2018

Loss map measurements have been performed during commissioning for the 2018 LHC run for different machine and beam configurations for both proton and ion beams [110, 111]. The scenarios of interest for this thesis are the betatron loss maps for Beam 1 horizontal (B1H) in the flat top (FT) mode with a nominal lead ($^{208}\mathrm{Pb}^{82+}$) beam. Plots of the qualification loss maps for proton and ion beams are shown in Fig. 2.12.

From Fig. 2.12 it can be observed that the losses are concentrated in the collimation cleaning insertions IR3 and IR7. The hierarchy of collimator losses in IR7 and the cold losses in the DS downstream can be seen in Fig. 2.13. For proton beams, the maximum

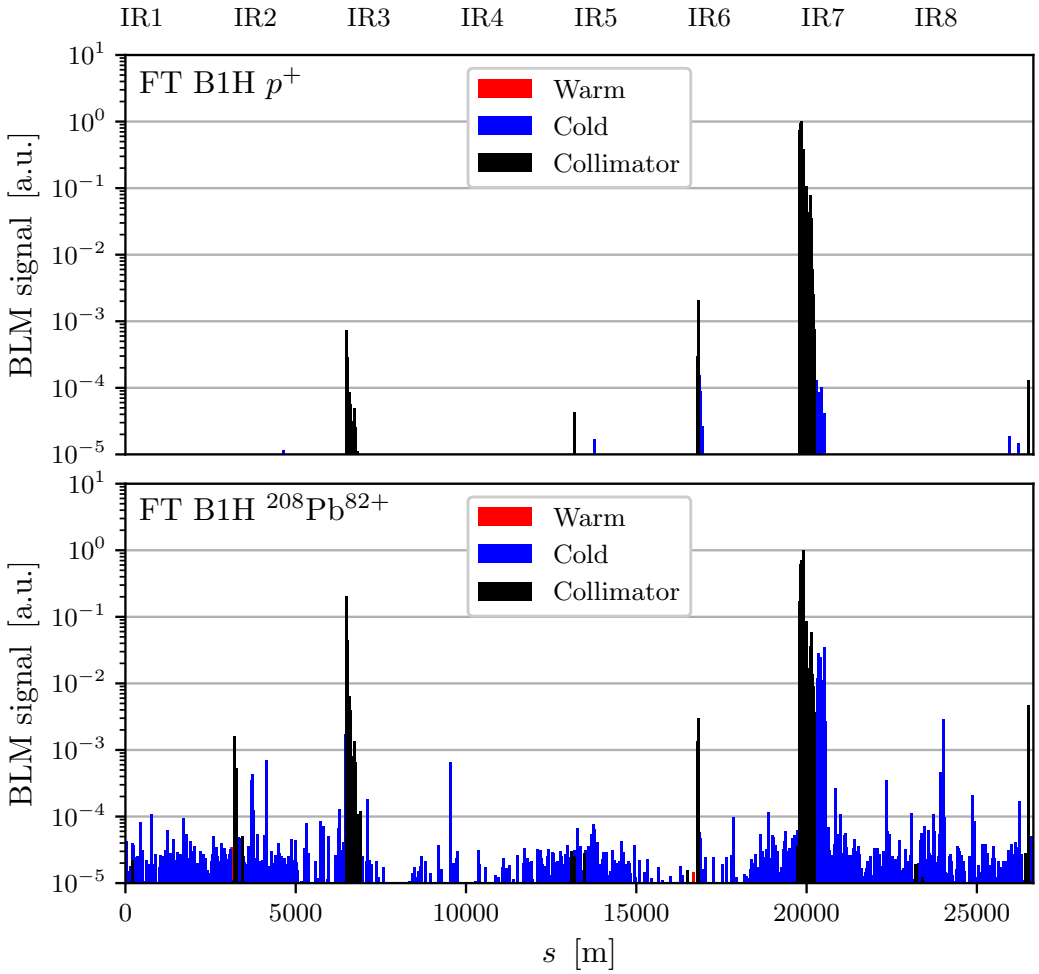

Figure 2.12: Qualification loss maps recorded during RunII proton and ion beams commissioning in 2018. The full loss map for B1H in FT mode for a 6.5 TeV proton beam (top) and for a 6.5 Z TeV lead ion beam (bottom). It can be observed that the collimation cleaning efficiency for ion beams is lower than for proton beams.

local cleaning inefficiency is around 1×10^{-4} and notable cold losses are observed only around the insertion regions.

For the ion case, the collimator hierarchy in IR7 appears broken, with the most loaded collimators being the horizontal TCSGs downstream of the TCP. The hierarchy is not actually broken, as the TCSGs collimator is not directly impacted by the halo, but they are subject to significant energy deposition from the secondary particles and hadronic showers generated in the TCP [103]. Considerable losses on collimators are also observed in the TCTs in IR1, IR2 and IR5. The DS of IR7 is the most critical place for cold losses

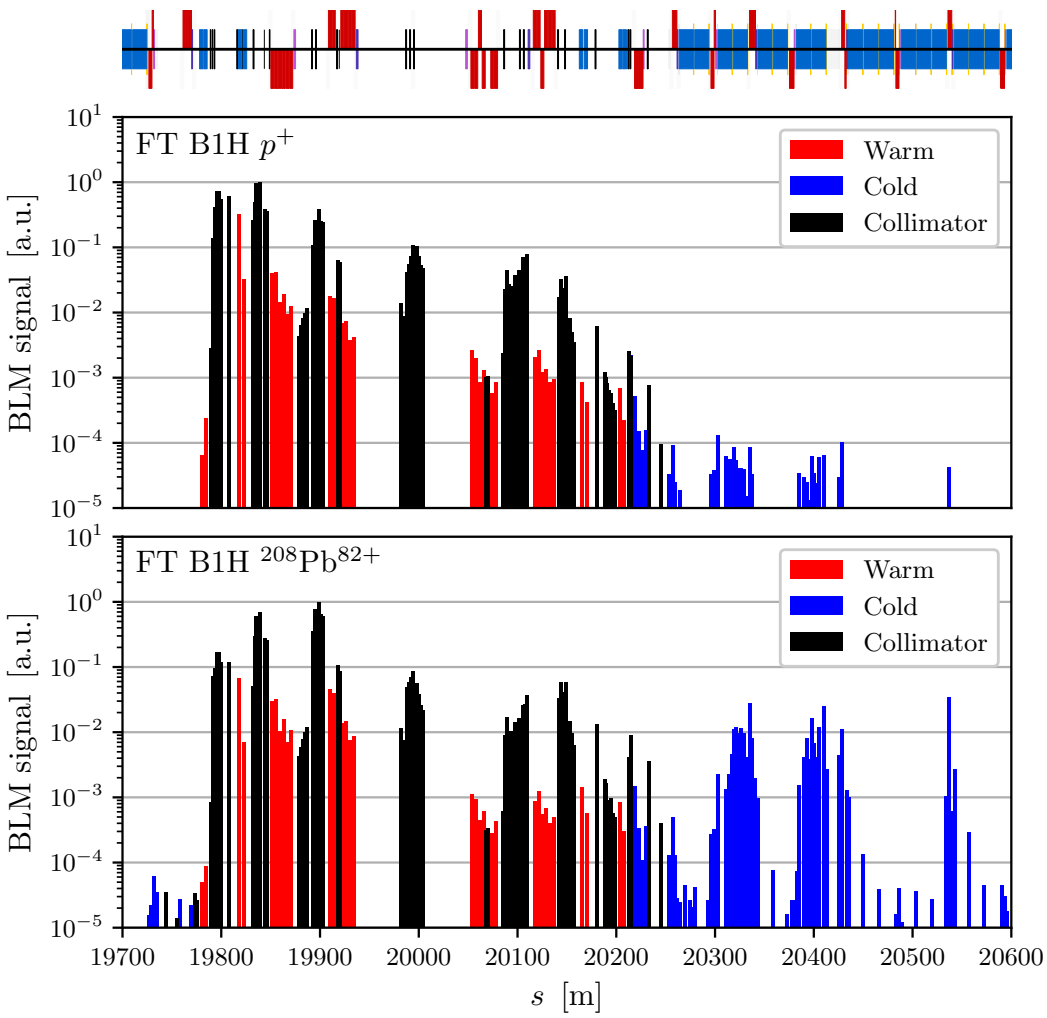

Figure 2.13: Zoomed-in view of the qualification loss maps in Fig. 2.12, showing in detail the losses in IR7 for proton (top) and ion beams (bottom). The three large cold loss clusters seen in the DS downstream of IR7 are the bottlenecks for ion collimation.

in the LHC during ion operation. Figure 2.13 clearly shows the large cold loss clusters observed downstream of the warm collimation section around $S = 19\,400 - 20\,600\,\text{m}$, where the maximum local cleaning inefficiency is around 1×10^{-2}. The discrete loss clusters correspond to the peaks in dispersion in the DS as shown in Fig. 2.8b. Additional cold loss spikes appear in the arcs downstream of IR7, while lower intensity cold and warm losses are observed around the majority of the ring.

2.3 Cleaning inefficiency simulation

A simulation study of ion collimation in the LHC is performed for the purpose of comparing with the measured loss maps from Section 2.2.1. The operational scenario of betatron collimation for B1H in FT mode has not been investigated in detail in previous simulation studies.

2.3.1 Machine configuration

The machine and beam configurations are of key importance for ion collimation simulations for the LHC. To facilitate comparison with measurements, the machine optics, the aperture model and the collimator settings used are selected to reflect as closely as possible the operational conditions during the measurement. The ion beam parameters are the nominal for Run II.

Table 2.2: Summary of simulation parameters for LHC ion operation [54, 111].

Parameter	Value
Optics	Flat top, pre-squeeze
β^* IP1/2/5/8 [m]	1/1/1/1.5
Crossing angle IP1/5 $\theta_{1/5}$ [mrad]	160
No. of bunches k_b	733
Ions per bunch N_b	2.2×10^8
Beam particle	$^{208}Pb^{82+}$
Ion normalised emittance (ϵ_N) [µm]	1.39
Equivalent proton normalised emittance (ϵ_{Np}) [µm]	3.5
Energy (E) [TeV]	522
Equivalent proton energy [TeV]	6.37
Energy / Nucleon (E / A) [TeV]	2.51
Impact parameter [µm]	1

The collimator settings are FT settings reported for the qualification loss map measurements. The settings of the main collimators for the key operation cycle stages are summarised in Table 2.3.

Table 2.3: Collimator settings for the LHC RunII ion operation [111]. The σ denotes the betatron beam size in the plane of the collimator. Not all collimators are listed.

Collimator	Opening [σ]		
	Injection	Flat top	Collision
TCP IR7	5.7	5	5
TCSG IR7	6.7	6.5	6.5
TCLA IR7	10	10	10
TCP IR3	8	15	15
TCSG IR3	9.3	18	18
TCLA IR3	10	20	20
TCT IR1, 5	13	15	9
TCT IR2	13	15	9
TCT IR8	13	15	15

2.3.2 Impact parameter

The impact parameter b is used to describe interactions between the halo particles and collimators. It is the distance from a particle's impact location to the longitudinal collimator edge. The impact parameter is used to define the beam distribution for collimation studies. A schematic of the collimator impact parameter can be seen in Fig. 2.14.

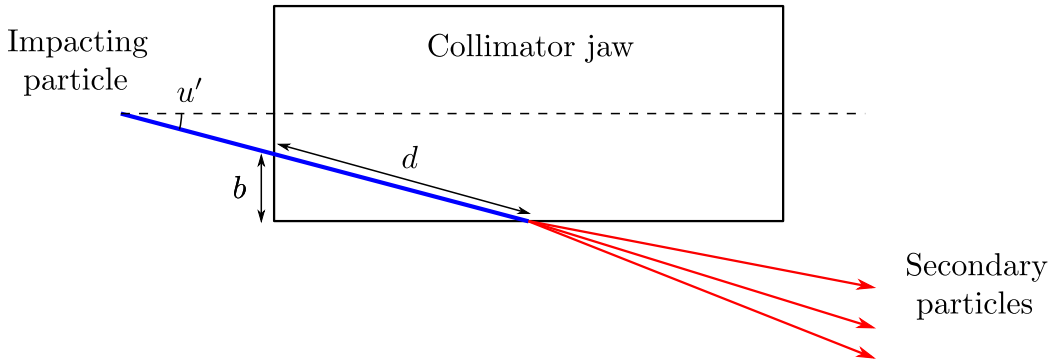

Figure 2.14: The impact parameter b is the distance between the longitudinal edge of the collimator jaw and the impacting particle. The angle u' is fixed by the optics at the collimator entrance and therefore b alone determines the distance d, travelled inside the collimator.

The assumption is made that halo particles impact the collimator close to the maximum

amplitude in phase-space, which means that the coordinates of the incident particle are determined by optics at the TCP location as,

$$u = \pm N_p \sqrt{\epsilon_u \beta_u} \ , \tag{2.8}$$

$$u' = \mp N_p \alpha_u \sqrt{\epsilon_u / \beta_u} \ , \tag{2.9}$$

where,

$$N_p = \frac{g + b}{\sigma_u} \ , \tag{2.10}$$

is the normalised amplitude of an impacting particle with g denoting the physical half-gap of the collimator and $\sigma_u = \sqrt{\epsilon_u \beta_u}$ denoting the betatron beam size at edge of the collimator. The tapering of the collimator jaw is disregarded and the edge of the collimator is taken to be the edge of the active length of the collimator.

The jaws of the LHC collimators are straight and do not follow the divergence of the beam. The physical gaps of the collimators are therefore set using the betatron beam size at the s location of the collimator centre $\sigma_{u,\mathrm{c}} = \sqrt{\epsilon_u \beta_u(s_\mathrm{c})}$, where the subscript c is used to denote the location of the collimator centre. The normalised collimator gap $N = g/\sigma_u$ is used to quote collimator settings.

The effects of dispersion are not considered when setting the collimator gaps or generating a beam distribution for the betatron collimation simulations presented. Furthermore, in the typical collimation simulation, the particle interactions happen over a period of several turns, which is significantly shorter than the period of a synchrotron oscillation in the LHC—about 500 turns. This allows for the effects due to the beam energy spread and the RF system to be disregarded.

As the collimator gaps are set at the beginning of a run, the emittance used to set them is taken as a pre-determined value [39]. The actual beam emittance varies from fill to fill, but the collimator physical gaps are not adjusted. Instead, the effective sigma openings

of the collimators are allowed to vary. For proton simulations, a reference value for the normalised emittance $\epsilon_{\mathrm{N}} = \beta\gamma\epsilon$, where β, γ are the relativistic parameters, is typically used in simulations. This allows for the performance of the collimation to be readily benchmarked against previous results.

For ion beams, the normalised emittance differs from the proton one due to the different mass and energy and the different injector chain stages for an ion beam. If the assumption is made that the physical emittances for both beams are the same, it is possible to calculate the reference ion beam normalised emittance for ion beams from reference proton beam normalised emittance as,

$$\epsilon_{\mathrm{N,ion}} = \epsilon_{\mathrm{N,proton}} \frac{(\beta\gamma)_{\mathrm{ion}}}{(\beta\gamma)_{\mathrm{proton}}} \ . \tag{2.11}$$

For the LHC, this assumption is justified because the ion beams undergo additional stages of cooling in the injector chain [21]. The design normalised emittance for proton beams is 3.75 µm, while for ion beams the normalised emittance is 1.5 µm [112], yielding a similar geometrical emittance over the whole LHC operational cycle.

The impact parameter determines the distance the halo particles will travel through the collimator. The performance of the collimation system has been shown to have a strong dependence on the impact parameter of halo ions on the TCP [21]. The representation shown in Fig. 2.14 is valid for collimators where the beam envelope is converging. For collimators where the beam envelope is diverging, the impact parameter is usually defined at the outgoing edge of the collimator to ensure that it still represents the distance travelled in the collimator in the same way as for the converging case. In this case, the maximum betatron amplitude as per Eq. (2.8) is assumed to be reached at the outgoing edge and the optical functions there are used to define the normalised amplitude, Eq. (2.10).

As the DS of IR7 is the most critical region for losses in the LHC ring, the average and peak energy losses there determine the collimation cleaning performance. The impact parameter value that results in the worst collimation efficiency is selected for ion collimation studies. For the LHC, this value is found to be $b = 1\,\mu\mathrm{m}$ [21], which corresponds to around 4.6 cm of material travelled by halo particles in the TCP. The longer distance travelled inside

the TCP for large impact parameters ($b \gg 1\,\mu m$) enables multiple nuclear fragmentation interactions and suppresses the production of the heaviest ion fragments, which dominate the large losses in the DS. The predominantly light ion fragments scattering out of the TCP for large impact parameters generally have a sufficient magetic rigidity offset to be intercepted in the straight section, resulting in an improved collimation cleaning efficiency. On the other hand, smaller impact parameters ($b < 1\,\mu m$) increase the probability of the ion remaining intact, while receiving a transverse kick due to MSC. Unfragmented ions scattered from the TCP can complete a full revolution and be lost on the next turn with a larger impact parameter, resulting again in improved cleaning efficiency.

2.3.3 Beam distribution

In normal beam operation, halo particles will gradually drift further from the beam core as a result of diffusion and eventually impact the collimator. Halo diffusion is a complex phenomenon, involving multiple physical effects and is typically not included in beam collimation simulations. Because diffusion is slow (few nm/turn [77]) and collimation simulations are normally performed over just several hundred turns, the exclusion of diffusion from the simulations does not have a significant impact on the results obtained. However, it means that particles with phase space trajectories not intercepting a collimator will continue circulating in the simulation indefinitely. On the other hand, halo particles impacting deep into the TCP will traverse more of the collimator material. The increased interaction with the collimator and larger energy deposition lead to an improved collimation cleaning efficiency, which is not representative of the real machine. Therefore, only particles in a narrow range of impact parameters are of interest for collimation simulations. These particles populate an annulus in phase space. This type of beam distribution is referred to as an annular halo [39]. Betatron motion will eventually bring particles that start at smaller spatial amplitudes in the annulus onto the collimator, but the additional turns performed cost computing time, while not contributing additional information. In the interest of efficiency, it is typical to simulate only a small area of the annular halo directly impacting the TCP. This is known as direct halo distribution [39]. For standard proton collimation simulations, the direct halo distribution involves a segment of the annular halo impacting the collimator, which includes a range of impact parameters. For ion collimation simulations, the cleaning efficiency has a strong dependence on the impact parameter and

a more restrictive selection is applied to the beam distribution. Only particles impacting the collimator with the desired impact parameter are simulated, as shown in Fig. 2.15.

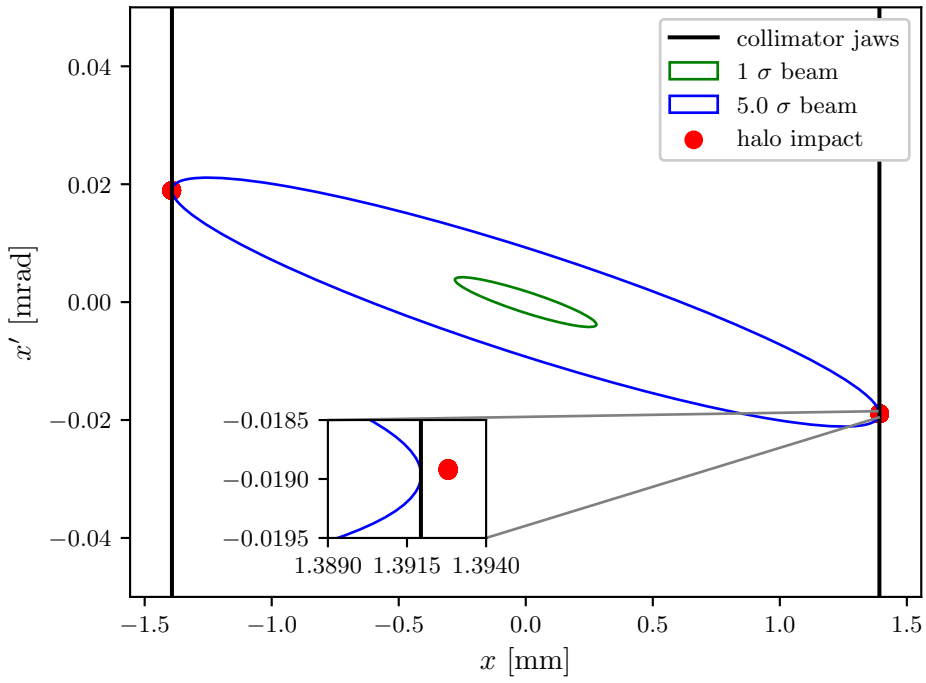

Figure 2.15: Direct halo beam distribution used for ion collimation simulations. The beam envelopes at the entrance of the LHC horizontal primary collimator (TCP.C6L7.B1) are shown for the nominal 1σ beam and a halo $N\sigma$ beam, where $N = 5$ is the normalised opening of the collimator. Only particles impacting the collimator with a desired impact parameter are simulated.

2.3.4 SixTrack-FLUKA coupling simulation

The input for the SixTrack-FLUKA coupling involves separate sets of input files for the lattice used by SixTrack for tracking and the collimator models used by FLUKA for Monte Carlo simulations. Because multiple software packages, libraries and tools are used, the preparation of the inputs is a sequential process with multiple distinct steps. A flowchart of the model preparation can be seen in Fig. 2.16. The model preparation starts with a MADX model of the magnetic lattice. The FLUKA geometry model preparation extracts the optical functions at collimators from the MADX output and makes use of additional inputs, including a mapping of collimator settings to collimator names, and beam parameters, such as energy and emittance. The SixTrack lattice specification is prepared based on the output from MADX, with the addition of special markers for the FLUKA collimators and

aperture definition markers from an user-supplied aperture model. After the lattice and the collimators are prepared, the run configuration, including the beam parameter definition and particle transfer conditions, is supplied individually to FLUKA and SixTrack. Code-specific parameters like interaction cuts or tracking settings are also provided at this stage. Finally, the optical functions from MADX and user-provided beam distribution settings to prepare the input for an external distribution generation program (gpdist), which is part of the SixTrack-FLUKA coupling software bundle. Each of the key input preparation steps is covered in more detail in the following paragraphs.

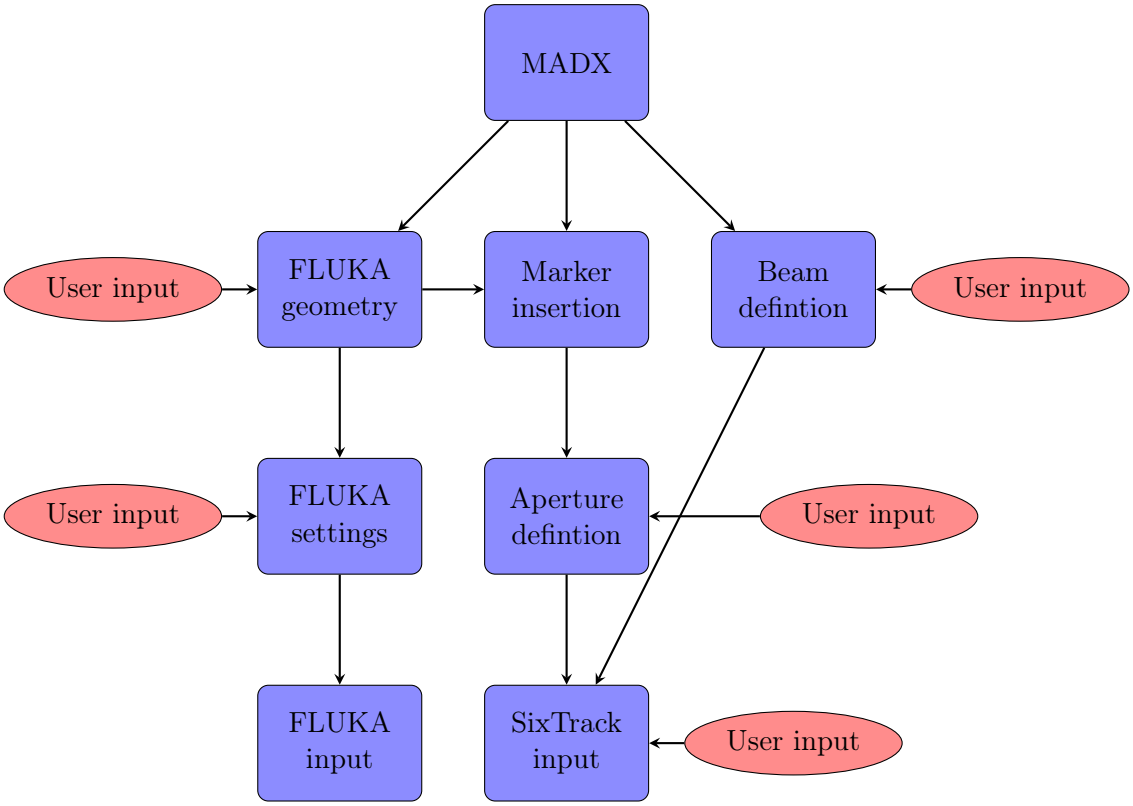

Figure 2.16: Workflow for the SixTrack-FLUKA coupling input preparation. Each node in blue represents a processing step performed by a separate script/program. The nodes in red indicate places where the user must provide parameters and settings. Transactions between blocks in blue do not require user input.

FLUKA

The collimator settings are provided using a collimator database file, which includes information about the type, length, material and opening of all collimators in the beamline. The FLUKA input is built in a semi-automated fashion by using the information in the col-

limation database and an additional specification of collimator prototypes— parameterised geometry models of the FLUKA element database (FEDB). Collimators are prepared as detailed 3D geometry models, placed in a compact sequence in the FLUKA main geometry specification file. Each of the collimators is surrounded by a perfect absorber (FLUKA black hole) to prevent cross-talk, and coordinate transformations at the collimator model entrance and exit are stored. A segment of the full FLUKA geometry model that highlights the main features is shown in Fig. 2.17.

In addition to geometry, user-configurable template files are used to provide the beam and physics settings. The physics processes used include ion fragmentation, evaporation, coalescence and EMD, as well as hadronic elastic and inelastic interactions. Other electromagnetic processes are switched off and a tracking cut of 1 TeV is applied to all particles (1 TeV/nucleon for ions). These settings help control and optimise the use of computing resources. Furthermore, for the LHC ion collimation simulation, only ion particles are passed back to SixTrack for further tracking. It is expected that protons and neutrons escaping the collimators will significantly contribute to energy deposition only in the warm elements of collimation insertions, which are not the primary focus of the collimation studies presented. The geometry prototypes, physics, beam settings and other configurations are combined into a single input file for FLUKA.

SixTrack

The lattice description used by SixTrack is produced in MADX and exported as a Table File System (TFS) file. It includes the positions and parameters of all beamline elements. SixTrack uses thin-lens tracking, where the magnetic elements are represented by a sequence of drifts and zero-length magnetic lenses that provide kicks to the particle's angular coordinates. The conversion of the lattice to a thin-lens representation is also done by MADX. The aperture model is provided separately as a set of markers describing aperture limitations at different s-positions. Collimators are represented in MADX as thin markers at the centre of the element. A dedicated script is used to expand the collimators into entrance and exit markers in the SixTrack lattice. In combination with the set of FLUKA transforms mentioned earlier, this allows the transfer of particles between SixTrack and FLUKA during the simulation.

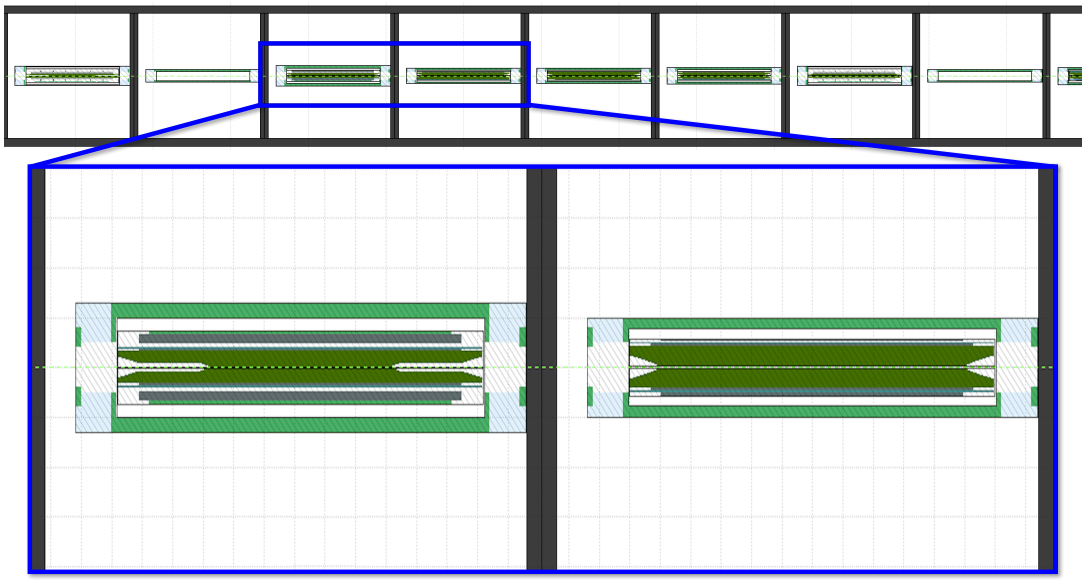

Figure 2.17: View of a segment of the FLUKA collimator model showing the compact insertion cell layout (top). The zoomed-in view of two of the collimators (bottom) shows the collimator jaws, assembly elements and outer tank. The gray bands separating the two collimators are part of a perfect absorber bounding box that enables particle transfer between SixTrack and FLUKA and prevents cross-talk between the collimators.

In previous versions of SixTrack, the beam losses on the aperture have been addressed by storing all of the particle trajectories in a file and applying the aperture limitation filtering as a post-processing step [38]. The latest version of SixTrack, used for the simulations presented, includes an online aperture check. The aperture limitations provided by the user are linearly interpolated in s to provide aperture markers at desired intervals, 10 cm for the current studies. During tracking, the particle coordinates are compared with the aperture limitation at all aperture markers. If a particle is found outside of the aperture limitation, the coordinates are back-propagated using drift tracking to the point where the particle left the beampipe and the s-location of the aperture intersection is recorded. Drift tracking is used for the back-propagation because SixTrack performs thin-lens tracking and the aperture defintion markers are located in the drift spaces between the lenses. The particle is considered as lost if it leaves the aperture and its total energy is counted towards the energy deposition at the loss location. This is not physically accurate, as in reality, a high-energy charged particle can deposit only a portion of its energy and continue to propagate further, undergoing further interactions and producing hadronic and electromagnetic showers. The SixTrack-FLUKA coupling simulations are intended to help

identify patterns and coarse features in the losses, meaning that the physical inaccuracy of the aperture energy deposition can be tolerated. For areas of the machine where energy deposition is crucial, the particle aperture loss location obtained from tracking in SixTrack can be used in comprehensive FLUKA energy deposition studies [71,76] to obtain accurate results.

The energy deposition, E_{dep}, in a collimator is calculated by SixTrack as the difference between the total energy going into a FLUKA insertion and the total energy coming out. In the standard simulation configuration, protons escaping the collimator are not tracked further, but they are recorded in order to correct the energy deposition at the collimator. This can be expressed as,

$$E_{\text{dep}} = \sum_i E_i - \sum_j E_j - \sum_k E_k \ , \tag{2.12}$$

where the indices i denote particles entering FLUKA, j—particles passed back to SixTrack for tracking and k—particles escaping, but not tracked further. It is possible to also track protons further, as done for the FCC-hh simulations discussed in Chapter 3, but this is not done for the LHC simulations. The energy deposition in the collimator is normalised to the active length of the collimator, in accordance with Eq. (2.3).

Beam distribution

Previously, to achieve a beam distribution with the desired impact parameter at the TCP, particle trajectories originating at IP1 have been used [21]. Because of the effect of sextupoles and other non-linear effects, the halo distribution is diluted and skewed by the time it reaches the TCP. The correct impact parameter on the TCP can be ensured by performing a preliminary SixTrack run, where particles are tracked from IP1 to the TCP and the ones with the correct impact parameter are selected as input for the main simulation [21]. For the studies presented, a new approach was developed, which allows generation of a direct halo distribution with an arbitrary impact parameter at the collimator itself, by using the gpdist distribution generator.

The Twiss parameters at the edge of the collimator can be readily acquired by drift propagation from the centre, where they are defined in MADX,

$$\beta_{\mathrm{e}} = \beta_{\mathrm{c}} \pm L^2\gamma_{\mathrm{c}} \mp 2L\alpha_{\mathrm{c}} \ , \tag{2.13}$$

$$\alpha_{\mathrm{e}} = \alpha_{\mathrm{c}} \mp L\gamma_{\mathrm{c}} \ , \tag{2.14}$$

$$\gamma_{\mathrm{e}} = (1 + \alpha_{\mathrm{e}}^2)/\beta_{\mathrm{e}} \ , \tag{2.15}$$

where L is the half-length of the collimator, the subscript e denotes the edge of the collimator, the subscript c denotes the centre of the collimator, and the subscript u has been dropped for clarity. The upper set of signs denotes an end point upstream of the centre and the lower set denotes an end point downstream of the centre. Knowledge of the optics and the desired impact parameter allows computation of N_p, the effective size of the impacting distribution in units of sigma. The distribution is then specified as an annular halo in the plane of the collimator and a Gaussian distribution up to $3\,\sigma$. Cuts in the transverse particle coordinates are used to produce the direct halo. Because the FLUKA insertion markers are on the boundary of the collimator tank, an additional drift back-propagation transformation is applied to shift the generated particle coordinates to the FLUKA insertion marker position. This ensures that the achieved impact parameter is exact. A diagram of a collimator model in FLUKA, highlighting the relevant planes for the beam distribution, is shown in Fig. 2.18. For the LHC TCP, the active length is 60 cm, while the total FLUKA insertion region length is 1.42 m

Simulation execution

The simulation includes 3×10^6 primary ions being tracked for 700 turns. The total number of particles are split in multiple individual jobs running a fraction of the primary particles each and executed on the HTCondor batch job processing service at CERN. Each of the individual jobs has its own random number seed to ensure unique, yet reproducible, results are obtained. The output from all jobs is collected and analysed together to obtain the final results.

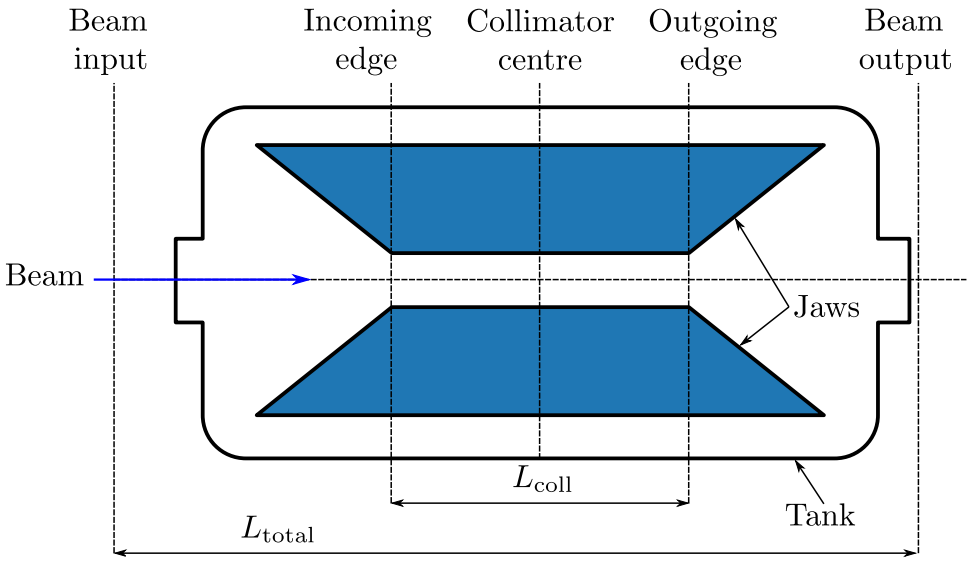

Figure 2.18: Diagram of a FLUKA collimator model showing the planes where particles enter the model and the planes marking the longitudinal edges of the collimator. The active length of a collimator L_{coll} is used for setting up the beam, while the total length of the FLUKA model is L_{total}, which includes the jaw tapering and the collimator tank. The start of the model region is slightly upstream of the beginning of the collimator tank, while the end is immediately downstream of the end of the tank.

2.3.5 BDSIM simulation

The input for BDSIM includes the layout of and strengths of the magnetic lattice elements, the aperture model and the collimator settings. There is a Python input conversion tool that loads a thick-lens lattice description from MADX in the form of a TFS table file and produces a set of inputs for BDSIM. The entire beamline is built as a 3D geometry model in Geant4, including the beampipe, magnets and collimators. The geometry model is in a global Cartesian coordinate system. A flowchart of the input preparation for BDSIM can be seen in Fig. 2.19. Because input is prepared for one program and there is a single input preparation tool, the input preparation process requires fewer steps than the one for the SixTrack-FLUKA simulation, shown in Fig. 2.16.

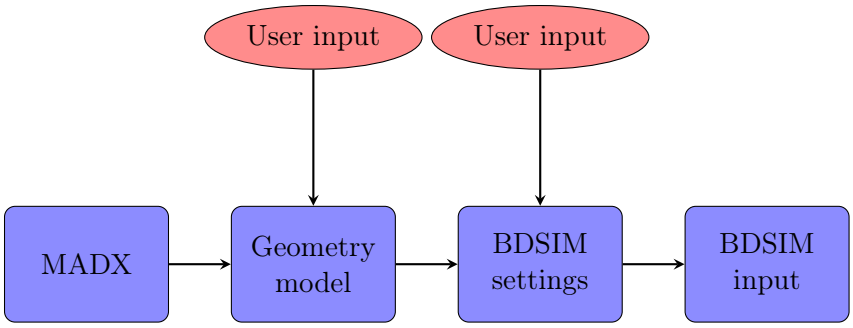

Figure 2.19: Workflow for BDSIM input preparation. Each node in blue represents a processing step performed by a separate script/program. The nodes in red indicate places where the user must provide parameters and settings. Transactions between blocks in blue do not require user input.

Geometry model

BDSIM supports a number of different generic geometry models of accelerator components, which can be combined in different ways and mapped to the MADX beamline elements. Parameters of the geometry components can be customised for specific elements, such as the openings of collimators. The collimator model in BDSIM is simplified and includes parallel rectangular blocks placed around the beam. The jaw tapering, the jaw assembly and the collimator tank are not implemented in the BDSIM model. In the LHC model, the arc lattice is built using dual-aperture LHC-style dipole and quadrupole magnet models. In the insertion regions, warm magnets are represented by single-aperture magnet models. Examples of the different types of magnet geometry used in the BDSIM model can be seen in Fig. 2.20.

The aperture is supplied as a set of aperture description markers at different s-locations. A physical beampipe is built between each pair of consecutive aperture markers. The beampipe is built from straight segments of constant transverse cross-section between aperture markers. This allows for the aperture intersection of a lost particle's trajectory to be determined accurately, but it also makes possible for gaps in the beampipe to occur if there is a large aperture extent change between two markers. Particles can escape through such gaps without interacting, but this is not expected to be a problem for a sufficiently dense aperture model. To ensure consistency with the SixTrack-FLUKA simulations, BDSIM loads the aperture model from a SixTrack aperture summary table file. For the LHC collimation simulation, a tunnel is programmatically built around the accelerator beamline.

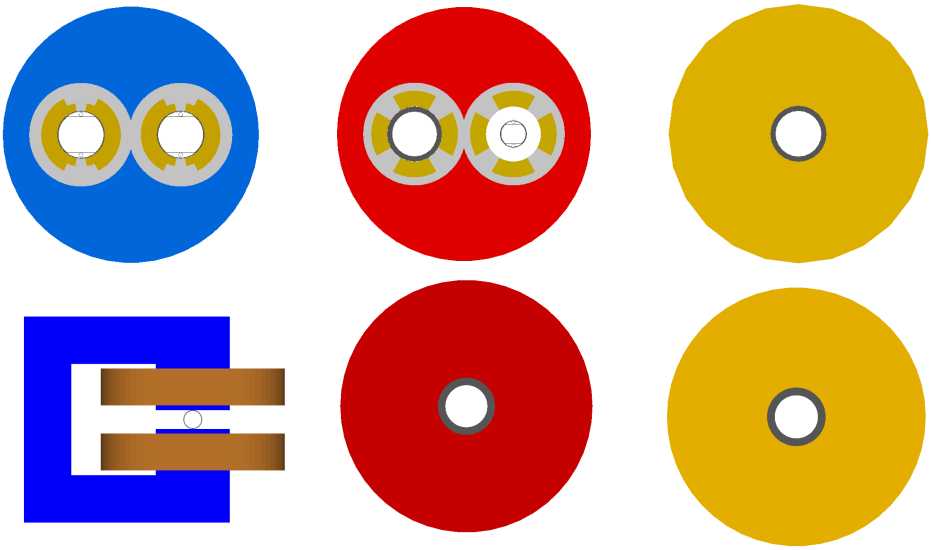

Figure 2.20: Cross-section view of the magnet geometry models used for LHC simulations. The LHC-specific geometry types used for superconducting magnets in the arcs are shown on the top row, including the dual-aperture dipole (top left), quadrupole (top middle), as well as a single-aperture sextupoles (top right). The geometry models used for warm magnets in the LHC insertions are shown in the bottom row and also include dipole (bottom left), quadrupole (bottom middle) and sextupole (bottom right) magnets.

The tunnel has the approximate transverse cross-section of the real one and follows the reference orbit of the particles. The tunnel, as well as the beamline placement in it, is not an accurate representation of the real machine, but it is intended to prevent cross-talk between remote machine regions via secondary particles propagating in air. A view of a section of the BDSIM LHC model can be seen in Fig. 2.21.

Particle tracking

BDSIM can track arbitrary primary and secondary particles in the whole accelerator beamline and in adjacent absorbent volumes such as beampipe, magnet bodies and the tunnel. Magnetic fields are attached to each magnet geometry model in order to track charged particles. The tracking is performed by integrating the equations of motion of the particles for the field in the magnet being traversed. The full ring geometry model is in global Cartesian coordinates and transforms are provided to local curvilinear coordinates for beamline elements, in order to enable tracking algorithms in the standard accelerator curvilinear coordinate system (see Fig. 1.1). Because of the use of global Cartesian coordinates in models

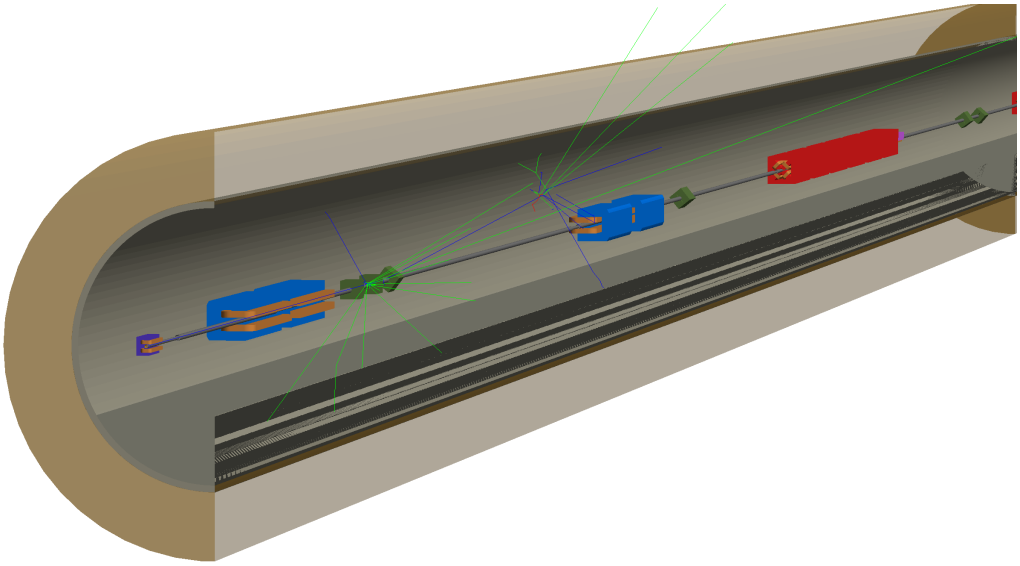

Figure 2.21: View of a section of the BDSIM LHC model showing the start of IR7, including the beamline and the tunnel. Collimators are shown in green, dipoles in blue and quadrupoles in red. A beam particle is shown interacting with the horizontal primary collimator (TCP.C6L7.B1) and producing secondary particles, which are subject to further interactions.

on the scale of the LHC, numerical significance loss (truncation) is possible in some calculations due to scale differences (µm beam particle motion vs. km accelerator ring size). A mixture of analytical and dedicated numerical integrators are used for primary particles on paraxial trajectories to improve accuracy and reduce the simulation run time. Primary particles with large transverse momenta and secondary particles are tracked using general-purpose, 4^{th} order Runge-Kutta numerical integrators from Geant4. The tracking routines used for primary particles inside the beampipe are generally symplectic. However, small geometrical gaps in the 3D model and therefore integration errors, as well as the nature of converging the integration to intersect a surface with a given tolerance, lead to an effective lack of symplecticity.

The tracking has been shown to result in an effective emittance growth of 13 % over 200 turns for proton beams in the LHC [113], which is considered acceptable for collimation simulations. For Pb ion beams at top energy in the LHC, it was found that the single-turn offset acquired by a particle on the reference trajectory due to the imperfect tracking remains below 0.2 µm in the transverse spatial coordinates. As the primary beam ion distribution is started at the TCP with exact parameters and interaction occurs immediately,

the tracking can only affect the impact parameter for secondary interactions with the TCP on subsequent turns. Previous studies have shown that the secondary impact parameters span a broad range of up to 200 µm [21] and hence the µm-level offsets due to tracking are not expected to be a serious concern for ion beam collimation in BDSIM. This assumption should be tested in the future with a detailed study of the multi-turn impact parameter on the TCP and comparison with the SixTrack-FLUKA coupling. It should be noted that the tracking will likely be significantly worse for larger accelerators, like the FCC-hh, because it relies on repeated transforms between global Cartesian and local curvilinear coordinates. The computations involved in the transforms are expected to exhibit numerical loss of precision when processing µm-level beam particle movement in a 100 km-long accelerator model.

To demonstrate the tracking in BDSIM, the trajectories of several different ion species starting at IP1 in the LHC in BDSIM and the SixTrack-FLUKA coupling are shown in Fig. 2.22.

The geometry model and the associated magnetic fields in BDSIM are constructed programatically from the MADX lattice description and any inaccuracies can result in tracking problems. One of the most robust methods to validate the geometry model is to compare the resulting optical functions to the ones expected in MADX. BDSIM performs single particle tracking and, unlike MADX, does not directly compute the optical functions of the lattice model used. Instead, the optical functions in BDSIM are reconstructed from the tracking data, with routines implemented to extract the optical functions from the beam distribution at a particular s-plane. The parameters calculated from the beam distribution include the emittance ϵ, the Twiss parameters α, $\beta\,\gamma$, beam centroids $\bar{x}$, $\bar{y}$ and dispersion functions D, D'. Because the parameters are calculated from a finite beam sample, they have associated statistical uncertainties. The methodology and routines implemented in BDSIM to perform calculations of optical functions and their statistical uncertainties from a beam distribution can be found in Appendix A. A comparison of the horizontal beta function between BDSIM and MADX for IR5 of the LHC is shown in Fig. 2.23. Similar agreement is observed for the other optical functions calculated from the beam distribution in BDISM.

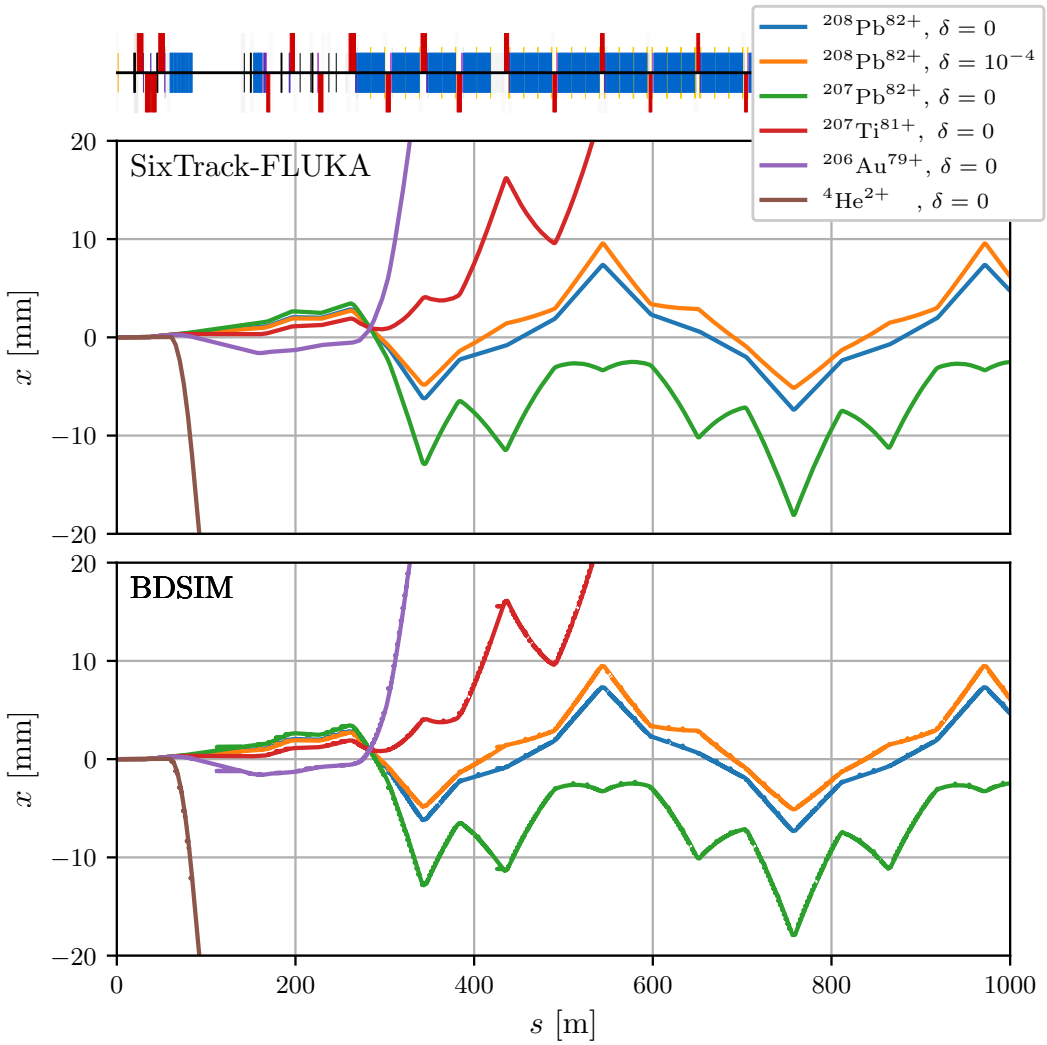

Figure 2.22: Tracking of different ion species, starting from IP1 in the LHC, in the SixTrack-FLUKA coupling (top) and BDSIM (bottom). The tracked particles are unmatched to the magnetic lattice and have the same energy per nucleon as the primary beam ions. The trajectories appear jagged at some points in BDSIM because of a bug with recording of trajectory coordinates, which does not affect the actual tracking.

Physical interactions

The physical interactions in BDSIM are provided by Geant4. The required physics processes can be specified using modular physics lists, or a Geant4 reference physics list can be enabled, which includes a variety of related processes [114]. For ion beam collimation studies, the enabled physics processes include ion nuclear interactions, EMD, hadronic elastic and inelastic interactions and EM interactions. All secondary particles species produced in interactions, including ions, baryons, mesons and leptons, are tracked further. By default,

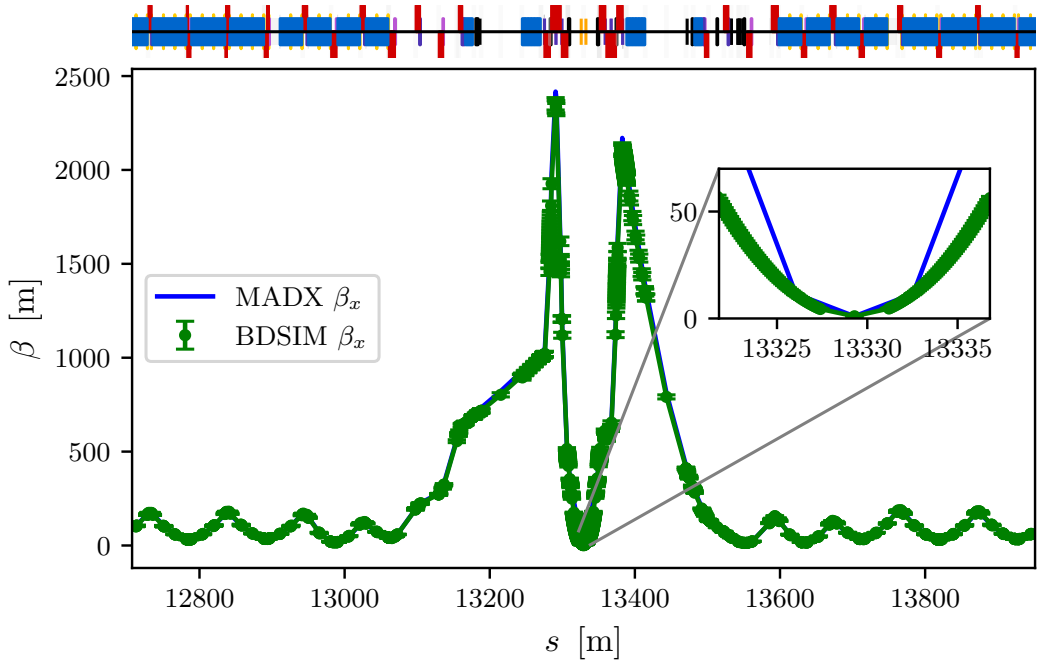

Figure 2.23: Comparison of the beta function in the LHC IR5 between MADX and BDSIM, showing good agreement. The beta function and the other optical functions are calculated in BDSIM from the beam distribution. The error bars represent the statistical uncertainty due to the finite beam population used, 5000 particles in this case. The high density of BDSIM plot points close to the IP is due to the detailed aperture model in this region.

Geant4 uses range cuts to control the computing resource usage and avoid the infrared divergence of EM processes. Range cuts are used to suppress the production of particles that would not travel a specified minimum distance. The distance travelled by a particle depends on the particle type, energy, and the material it traverses and hence range cuts result in different effective production cuts in energy for different materials. As a rule of thumb, the range cut in BDSIM should not be longer than the typical geometry element size and hence the range cut value used for the LHC simulations is 0.5 m. In addition to range cuts, a tracking cut of 1 TeV is applied, similar to the SixTrack-FLUKA coupling simulation.

The BDSIM simulations in this thesis are using updated versions of BDSIM and Geant4, which have introduced improvements to the handling of heavy-ion interactions, relative to versions used for the first study of ion collimation for the LHC using BDSIM [115]. Geant4 has not previously been used in simulation studies of heavy-ion beam collimation at the top energy of the LHC. Because of this, adjustments were necessary to the physics processes to

enable the studies presented. The applicable energy range of the nucleon-nucleon elastic scattering process in Geant4 is limited to 1 TeV/n in the version used (Geant4 10.04.p03). This limit was increased to 5 TeV/n to cover the LHC top ion energy of 2.51 TeV/n, while allowing a margin for lighter fragments produced at a higher energy per nucleon. In addition to this, an error was discovered in the Geant4 implementation of the EMD process. The error was due to the simplified treatment of the virtual photon energy transfer and caused energy non-conservation for high-energy heavy-ions undergoing EMD, ultimately resulting in complete suppression of EMD fragment yields at high energies. The error was corrected by applying a source code patch to the Geant4 version used.

Collimators are designed to be the only elements in the LHC that intercept primary particles and losses on the aperture necessarily occur after interaction with the collimators. The physical interactions that occur inside collimators hence define the loss distribution in the whole ring. The spectrum of primary and secondary particles escaping the TCP (collimator leakage) is of particular importance in ion collimation simulations. The halo particles interacting with the TCP receive a transverse kick due to MSC, which defines their future trajectories. Some of the primary particles also undergo inelastic interactions like fragmentation and EMD. Secondary particles produced in inelastic interactions can be lost on the collimators downstream, or escape from the collimation insertion with an altered magnetic rigidity.

For $^{208}Pb^{82+}$ beams at top energy, the energy spectrum of the particles leaking out of the LHC TCP in BDSIM is dominated by a sharp peak for energies below 10 TeV, corresponding to light ions, as well as protons, neutrons and EM shower products. Another sharp peak is observed above 515 TeV, close to the nominal energy of 522 TeV, corresponding to intact primary ions and heavy-ion fragments. There is a continuum between the two peaks, corresponding to a broad range of ion fragments. A hard cut-off is present at 1 TeV, which is the value of the energy cut used in the simulation. The collimator leakage is concentrated in the forward direction, with the majority of particles escaping with a transverse deflection of less than 1 mm and an angle of less than 1 mrad.

The TCP collimator leakage in BDSIM is compared to the one in SixTrack-FLUKA. This is achieved by recording the distribution of particles at the exit plane of the collimator on the first pass. In BDSIM, the exit plane is the outgoing edge of the simplified parallel

block geometry, while in SixTrack-FLUKA, it is the outgoing edge of the collimator tank as shown in Fig. 2.18. Only the ion part of the leakage is compared, as SixTrack-FLUKA is not configured to track other particles. The comparison between the energy fraction of ion species in the TCP leakage is shown in Fig. 2.24

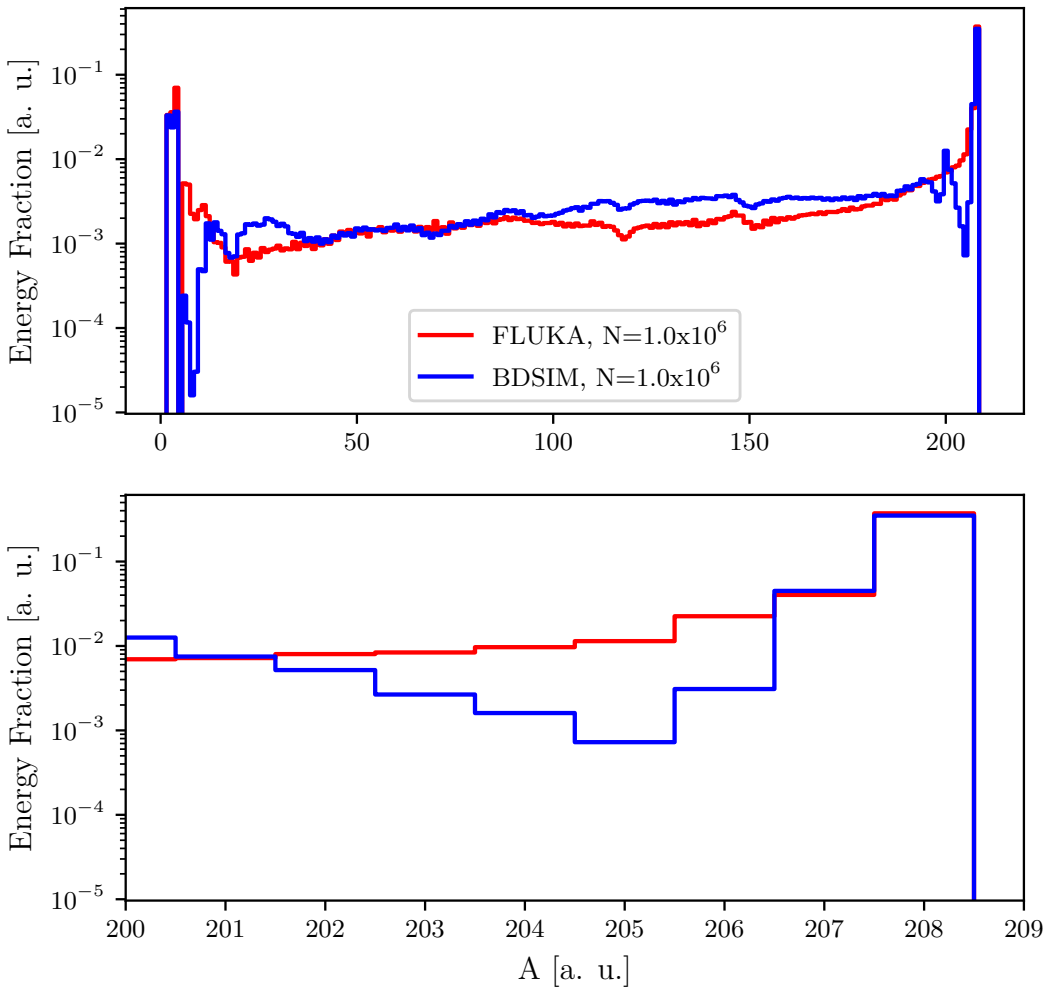

Figure 2.24: Energy fraction of different ion species escaping the TCP. The plots show histograms of the ion mass number (A), weighted by the total ion energy and normalised to unity. The full range of A is shown on top and a zoomed-in view of the large A region is shown on the bottom.

The energy spectrum of the different ion species exhibits similar features in SixTrack-FLUKA and BDSIM. The largest energy fractions are heavy ion species with $Z > 70$, close to nominal lead, and light ion species with $Z < 6$, mainly hydrogen and helium isotopes. Between the peaks at the extremities of the spectrum is continuum of ion isotopes with lower energy contributions. There are some discrepancies observed between the two simulations. The lightest and the heaviest fragments have similar yields in FLUKA and

BDSIM, with the differences mainly observed in the rest of the spectrum. The distribution recorded in FLUKA is characterised by a smooth variation across the whole range, while the distribution in BDSIM exhibits sharper variation in the ranges $A = 4 - 40$ and $A = 190 - 206$. There are also differences in the mid-range continuum, with BDSIM reporting higher energy yields. The regions of higher and lower yield in the two simulations are broadly balanced. In FLUKA, 65.6 % of the total energy incident on the TCP is carried away by ion fragments escaping the collimator, while in BDSIM this fraction is 61.2 %. The rest of the energy is accounted for by energy deposition in the collimator and shower production.

Detailed investigation of the reasons for the discrepancies observed is required. Benchmarking of the EMD process for nominal ion projectiles at top LHC energy is one of the possible avenues of investigation, as the associated cross-sections are significant in this regime. Preliminary analysis shows that other inelastic processes like nuclear fragmentation also contribute to the discrepancies, but rigorous studies and benchmarking are necessary to confirm those findings.

In BDSIM there is no fundamental distinction between losses on the collimators and the losses on the rest of the beamline. However, for the purposes of the LHC ion collimation cleaning inefficiency simulations, the output in BDSIM is prepared to match the one from the SixTrack-FLUKA coupling, where losses on the collimators and on the aperture are treated differently (see Section 2.3.4). Energy deposition is recorded inside the collimators, while for losses on the aperture, the s-location of the loss is recorded, weighted by the lost particle's energy and binned into a histogram. The histogram bin width is set to 10 cm. In the simulation, lost particles are not stopped when they reach the aperture, but the information from any physical interactions is disregarded for the loss maps. Furthermore, only ion impacts on the aperture are selected at the analysis stage. Other secondary particles and shower products escaping the collimators are still tracked and treated in the simulation, but they only contribute to the energy deposition in the collimators and not to the losses on the aperture. The loss maps are produced by scaling the per-event average energy of ions impacting the aperture by the bin width and normalising to the peak lost energy as per Eq. (2.3). For the collimators, the energy deposition is summed over the whole collimator and normalised to the collimator active length to ensure consistency with the SixTrack-FLUKA loss map plots. The s-location is used to distinguish cold and

warm aperture losses. Information in BDSIM is recorded per primary particle (event) and averaged over all primary particles to achieve the full results. This approach allows for the statistical uncertainties in the final quantities to be estimated. The statistical fluctuations in energy deposition can be significant for loss clusters in the machine that result from only a few lost particles.

The beam distribution is prepared using the same method as described in Section 2.3.4 and the impact parameter is 1 µm, the same as the one used in the SixTrack-FLUKA simulations, but the actual procedure is simplified. In the MADX thick-lens lattice representation the optical functions are by default defined at the end of the element. Because the BDSIM collimators are rectangular blocks with extent equivalent to the active length of the collimator, it is possible to define the beam distribution using the optical function values from the preceding drift, avoiding the need for optical function or particle coordinate back-propagation.

Simulation execution

The simulation includes 3×10^6 primary ions being tracked for 200 turns. The total number of particles are split in multiple individual jobs running a fraction of the primary particles each and executed on the computing cluster at Royal Holloway University of London (RHUL). To reduce computing time, the relevant results are binned into histograms on the cluster nodes and the individual histogram files are later merged, while preserving the statistical uncertainties.

2.3.6 Interpreting a loss map comparison

One of the most frequent types of analysis in this thesis is the comparison of cleaning inefficiency loss maps from measurements and simulations, or from different simulation tools. Because the loss maps are affected by a large number of variables, which are difficult to control, there is no general, rigid methodology for comparing loss maps. Instead, qualitative criteria are often employed for the comparison, with quantitative analysis limited to critical regions of the machine and key parameters of interest. The procedure used for interpreting the agreement between different loss maps is outlined in the following.

The comparison of loss maps is based on observations of losses on collimators and losses on the aperture. To illustrate the principle, an idealised distribution of losses in a collimation insertion is shown in Fig. 2.25. A multi-stage collimation system is designed to shield the sensitive superconducting magnets from beam losses. As a result, there is generally a trend of loss magnitude reduction from the primary collimator, impacted by the beam halo, to the DS and arcs downstream of the warm collimation insertion. The distribution of collimator losses in the insertion is related to the collimation system hierarchy discussed in Section 2.1.5.

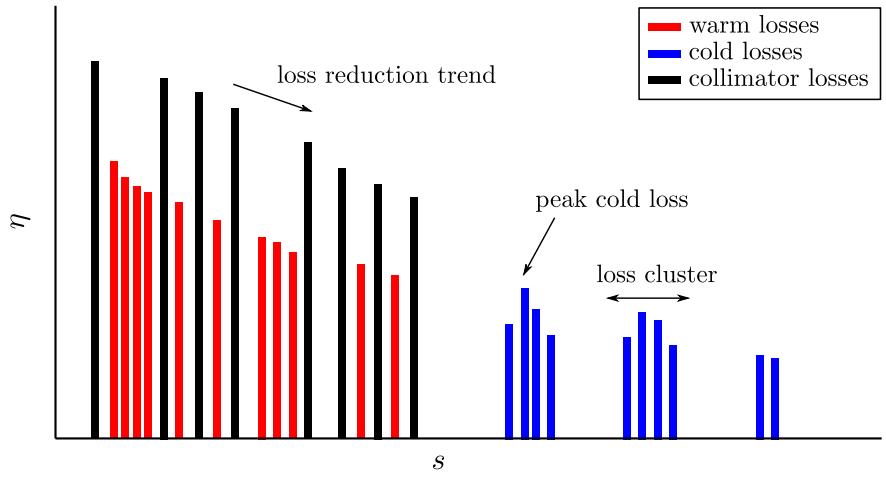

Figure 2.25: Diagram of an idealised loss distribution for a loss map in a collimation insertion. The bars represent loss spikes and the colour identifies the type of loss. In reality, loss maps rarely exhibit the clear trends depicted, due to the effects of the optical functions, the beam particle type, etc.

It should be noted that in realistic scenarios, the losses do not follow exactly the trend expected from the collimator hierarchy. For heavy-ion beams in the LHC for example, the secondary collimators are exposed to larger power loads than the primary collimators, as shown in Fig. 2.13. Nevertheless, the loss trends form an important basis for loss map comparison. Within the scope of this thesis, an agreement within one order of magnitude for collimator losses is generally expected.

The other important criterion in the comparison is the location and magnitude of the cold loss clusters. The peak cleaning inefficiency in the cold regions of the machine is a quantity of particular interest, as it is the bottleneck for losses in the machine. The peak cold loss is expected to match within metres in s-location and about an order of magnitude in value.

The distribution of relative cold loss spike magnitudes and overall size of the cold loss clusters is also important when comparing loss maps.

Finally, the warm losses in the collimation insertions are considered. The warm losses are dominated by showers of low-energy particles with large transverse offsets, leaking from the collimators. Such particles are generally neglected in cleaning inefficiency simulations, in order to optimise the simulation execution, leading to large observed discrepancies with measurements. Any discrepancies in the warm losses are considered acceptable, as the warm losses do not pose a quench risk and hence do not constitute a bottleneck for the collimation efficiency.

2.3.7 Simulation results

Simulations are performed of betatron collimation of $^{208}Pb^{82+}$ beams for B1H in the LHC. The results from the simulations are compared to the measured data. The simulated full-ring loss maps from the SixTrack-FLUKA coupling and BDSIM are shown alongside the qualification loss map measurements in Fig. 2.26 and a zoomed-in view of IR7 is shown in Fig. 2.27. Both simulated loss maps show full energy deposition in the collimators and only ion losses on the aperture.

It should be noted that the difference of the peak values in measured and simulated loss maps is due to the quantities and units used and not due to a real discrepancy. The measured loss maps show peak-normalised BLM signal and do not, by definition, exceed unity. While the simulated loss maps are normalised to peak energy loss as per Eq. (2.3), the peak occurs in the TCP that is 60 cm long, resulting in the cleaning inefficiency in units of m^{-1} exceeding unity.

The main features of the measured losses are represented well in both simulations. These include the concentrations of collimator losses in the collimation insertions IR7 and IR3, as well as prominent cold loss clusters in the DS or IR7 and the rest of the ring. While the distribution of the notable losses is predicted by the simulations, the magnitude of the losses is underestimated by up to an order of magnitude. The measured loss map is recorded by BLMs on the outside of beamline elements, that are only sensitive to the showers developed as a result of losses on the aperture. Because of this, discrepancies are

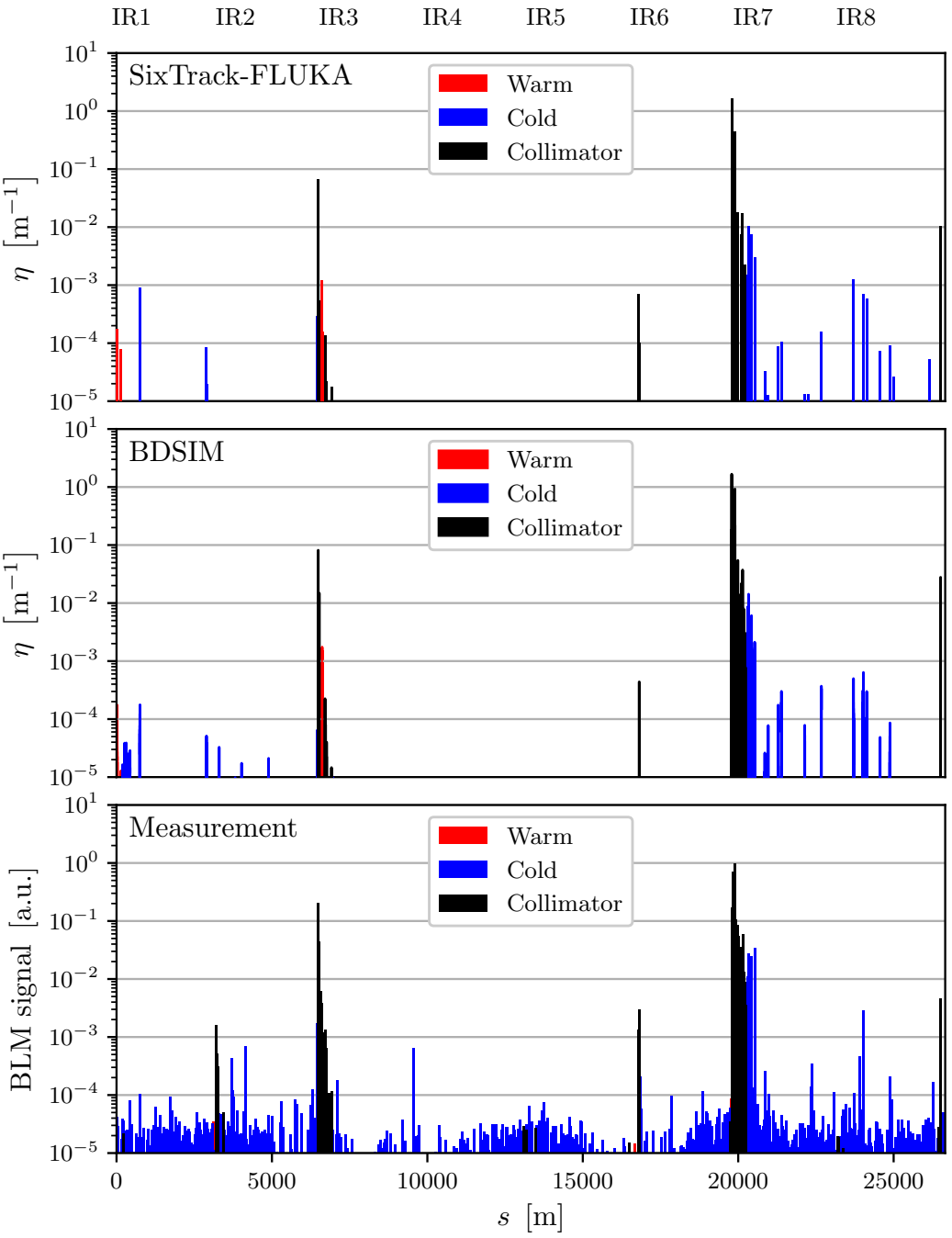

Figure 2.26: Comparison of loss maps simulated with the SixTrack-FLUKA coupling (top) and BDSIM (middle) with the measured loss map (bottom).

expected with the simulations. Furthermore, in both simulations, the significant tracking energy cuts contribute to a more pronounced collimator hierarchy and a comparatively sparser distribution of the aperture losses.

The predicted locations and magnitudes of cold loss spikes in the arc between IR7 and IR8 are similar between SixTrack-FLUKA and BDSIM, but the measured loss maps show the losses occurring in locations slightly different from the predicted ones. Aperture and closed orbit imperfections are a likely explanation of the slight discrepancies.

In the SixTrack-FLUKA coupling, the hadronic showers produced in aperture impacts are not tracked, resulting in more discrete energy deposition spikes around the ring relative to measured loss map. Furthermore, protons, neutrons and other shower particles produced in the collimators are not tracked further, leading to reduced energy deposition in the warm sections of the collimation insertions. BDSIM tracks all particles escaping the collimators. Only ion particles are considered for the aperture losses in the BDSIM loss maps shown in Fig. 2.26 and Fig. 2.27, but showers from collimators can impact the downstream collimators, which is reflected in better agreement with measurements in the IR7 collimator losses. The most notable differences between the collimator losses in BDSIM and SixTrack-FLUKA is seen in the first set of TCSGs and some of the TCLAs in IR7.

The structure observed in the IR7 DS cold loss clusters (DS1, DS2, DS3), which are critical for machine operation, include broad regions of continuous losses and intermittent large loss spikes. The magnitude of losses observed in the SixTrack-FLUKA simulations is lower than in the measured loss map, but the loss distribution in the clusters and their magnitude relative to each other are well reproduced. In the BDSIM simulation, the bulk of the losses is in agreement with the ones predicted by SixTrack-FLUKA, with some small differences, mostly at the beginning of the DS1 loss cluster. Those differences are likely due to differences in the distribution of secondary particles escaping the TCP, discussed in Section 2.3.5. Both simulations show a trend of sequential loss magnitude reduction in the DS1, DS2 and DS3 clusters, while the measured losses show equivalent magnitudes in DS1 and DS2 and a slightly larger loss in DS3. This can possibly be explained by orbit and aperture imperfections, which can cause local bottlenecks in the losses. Furthermore, the DS3 loss cluster is dominated by a single BLM with a large signal, which is sensitive to secondary particles from aperture losses occurring over some distance upstream. Increasing the bin width for the loss map from 10 cm to 1 m can potentially improve the agreement. Taking into account the shower propagation from the aperture impact location to the BLMs would also be helpful in understanding the differences.

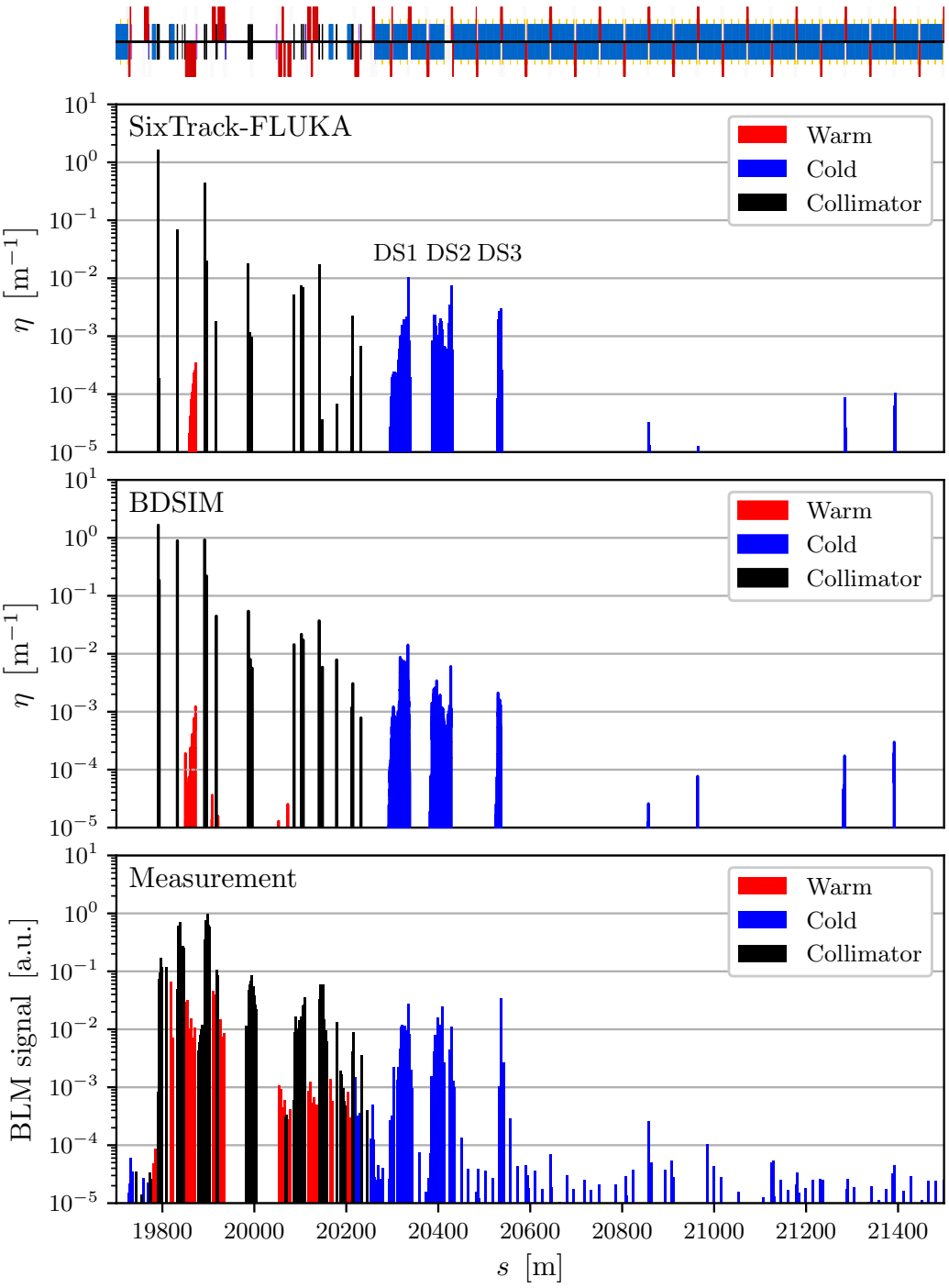

Figure 2.27: Zoomed-in view of the loss maps in Fig. 2.26, showing the losses in IR7 in detail. The loss maps shown include SixTrack-FLUKA (top), BDSIM (middle) and measured (bottom). The three dominating loss clusters are marked with labels above them.

Neither of the simulations predicts the collimator losses on the IR2 TCTs and the warm and cold loss spikes in the downstream arc. This is indicative of operational conditions in the

real machine that are not represented in the simulations, such as orbit errors or collimator opening or alignment errors. The highest losses in IR2 are recorded on the vertical tertiary collimator (TCTPV.4L2.B1), which is not generally expected when betatron collimation in the horizontal plane is considered. At the time the loss map measurements were taken, there was a fault in the local coupling correction in IR2, which was identified and corrected later in the 2018 ion run [54,116], but there is currently no evidence that this error is related to the collimation losses in this region.

The errors or imperfections are not necessarily occurring at the location of the loss. Due to the complex interactions between the different collimator stages and the machine optics, orbit errors or element misalignments can result in delocalised losses.

2.3.8 Conclusion

The approach of using simulations that include physics interactions in the collimators and secondary ion tracking in the rest of the machine has been shown to be effective in predicting the distribution of losses from collimation for ion beams in the LHC. This type of simulation is particularly useful for predicting loss hotspots and validating collimator settings, due to the broad scope and relative computational efficiency. The locations and magnitudes of the dominating cold losses is reproduced with reasonable accuracy. Good agreement is observed between the results from the SixTrack-FLUKA coupling and BDSIM.

There are discrepancies observed between the simulated and measured loss maps, most notably in IR2 where measured losses on the TCTs and the downstream aperture are not observed in simulations. This is expected to be a limitation of the machine settings and parameters used, rather than of the simulation tools themselves. Detailed energy deposition studies are required in order to quantify the quench risk in critical sections, calibrate BLM thresholds and estimate material activation, especially in the warm collimation insertions.

2.4 Energy deposition simulation in BDSIM

The simulation techniques described in Section 2.3 have been shown to effectively predict the key features of collimation beam losses in the LHC. However, because of the large kinetic energy cuts and simplified treatment of losses on the aperture, the results obtained with those techniques are not suitable for accurate prediction of energy deposition or direct comparison with measurements. Dedicated FLUKA simulations are used to correlate the losses on the aperture, the energy deposition in beamline components and the signals recorded in the BLMs in the most critical regions of the machine, like IR7 [39, 70, 71]. Those studies use input from tracking simulations and include detailed geometry models of full sections of beamline, field maps for the beampipe and the external magnet geometry and fine-tuned physical interaction models. The quantitative agreement of the latest simulation with measurements is excellent, with discrepancies not exceeding a factor of 3 over the whole IR7 region. The combination of tracking and energy deposition studies has proven to have a significant predictive power and has been successfully used to guide LHC operation [39]. Some of the limitations of the energy-deposition simulations are that they require significant human and computational resources and that models are not readily available for the whole machine.

As discussed in Section 2.3.5, BDSIM is an integrated simulation tool that performs primary and secondary particle propagation in a full 3D geometry model of LHC. In this section, the model used is developed further, with the goal of providing a more direct comparison of simulated collimation losses with measurements around the full ring. For a quantitative comparison of results, the radiation resulting from particles lost on the aperture must be propagated through the absorptive mass of beamline elements to the BLMs attached on the outside of those elements. This requires an accurate representation of the beamline elements and the inclusion of dedicated BLM instruments with the appropriate response to radiation.

Previous studies of proton beam collimation for the LHC using BDSIM [113, 117] have included the first implementation of BLMs. In those studies, the loss maps are constructed from energy deposition in aluminium cylinders at the locations of the BLMs. For this thesis, the BLM simulation techniques are improved by including accurate BLM geometry,

refining the placements of the instruments in the ring and adjusting the physics interaction cuts in order to optimise the signal in the BLM for LHC nominal ion beams.

2.4.1 BLM geometry model

Geometry models for radiation transport simulations are subject to many requirements, such as being water-tight, having non-overlapping features, having complexity optimised for the study, and conforming to the geometry description language of the simulation framework used. Those requirements have historically made the models difficult to prepare, debug and transfer to different frameworks. Part of the time of this PhD project has been dedicated to developing a software kit to alleviate some of the difficulties associated with geometry model preparation and manipulation. Pyg4ometry [118] is a Python package that uses classes to represent the fundamental geometrical entities (geometry primitives) and the Constructive Solid Geometry (CSG) operations required to build complex geometry models for radiation transport. An interactive visualiser, an automated overlap checking and other debugging tools are included in the package. At the time of writing, pyg4ometry has full support of Geant4 geometry features, including primitive solids, volume hierarchies, materials and more advanced functionality. Support has also been added for FLUKA geometry and Computer-Aided Design (CAD) formats (STL, STEP). Conversion between Geant4 and FLUKA formats is also possible. When preparing geometry for Geant4, a GDML format file is produced, which can be readily loaded in BDSIM.

The BLM geometry model for BDSIM is designed to capture the relevant features, while omitting excessive detail like screws and cabling in order to reduce the model complexity. The geometry is prepared from scratch using the specifications for an LHC ionisation chamber BLM [119]. The BLM consists of a cylindrical outer tank with a length of 48.9 cm and a diameter of 8.89 cm and an inner chamber with 61 aluminium electrodes supported by steel rods and spacers. The electrodes are 0.5 mm thick and are separated by 5.8 mm, with aluminium oxide insulators on either end of the electrode assembly. The potential difference between electrodes is 1.5 kV and the chamber is filled with nitrogen gas at an over-pressure of 100 mbar.

The geometry model includes the outer tank, the electrodes, support rods, spacers, the

insulators and the gas; and is shown in Fig. 2.28.

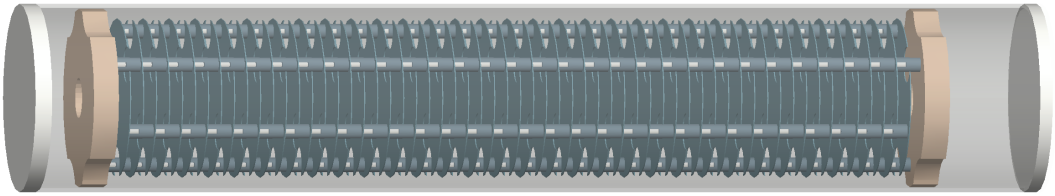

Figure 2.28: Geometry model for an LHC ionisation chamber BLM. The outer tank is made semi-transparent to highlight the electrodes, support rods, spacers and insulators inside. The model is coloured by material: steel—gray, aluminium—blue, aluminium oxide—beige.

2.4.2 BLM response to radiation

The signal recorded by a BLM depends on the radiation flux and the BLM response to the radiation. The charged particle flux and composition depend on the BLM position in the ring and the operational conditions. Previous studies include Geant4 and FLUKA simulations of the BLM response to radiation [106, 120, 121].

Charged particles traversing the BLM chamber ionise the gas, liberating charges that are collected by the electrodes. The number of charges produced is a function of the projectile particle species and energy. Not all of the charges produced in the chamber are collected by the electrodes, the sensitive gas volume is about 1.5 l and includes a slightly larger volume than the one contained between the electrodes. The number of electron-ion pairs produced in the sensitive gas region is proportional to the energy deposition there. The proportionality factor has a weak dependence on the particle energy and type and is taken as a constant, $W = 35\,\mathrm{eV/pair}$ [106]. In the simulation presented, energy deposition is scored in the sensitive gas region and scaled with the factor W to obtain the BLM response.

In order to validate the BLM geometry model, tests of the response are performed using beams of different particles over a range of beam incidence angles and energies. The procedure and setup follow previous Geant4 simulations. The Geant4 reference physics list used is the *FTFP_BERT*, however, the range cuts are set to 10 µm. In order to mitigate the systematic effects due to the internal structure, the beam is prepared to provide a

uniform irradiation at every orientation tested. For an incidence angle of 0° (beam parallel to BLM axis), the beam distribution is a circle, while for non-zero angles, the distribution is a rectangle with dimensions equivalent to the BLM projection onto the beam starting plane. For the range 0° < angle < 90°, this approach results in imperfect coverage of the curving BLM edges, but the systematic is only few percent in beam overlap area.

There are 9 particle species tested for 6 angles between 0 – 90 deg and 50 beam energies over the range 10 keV to 10 TeV. A total of 2700 individual runs are performed, each with 10 000 primary particles. The results for the incidence angle of 0 deg are shown in Fig. 2.29.

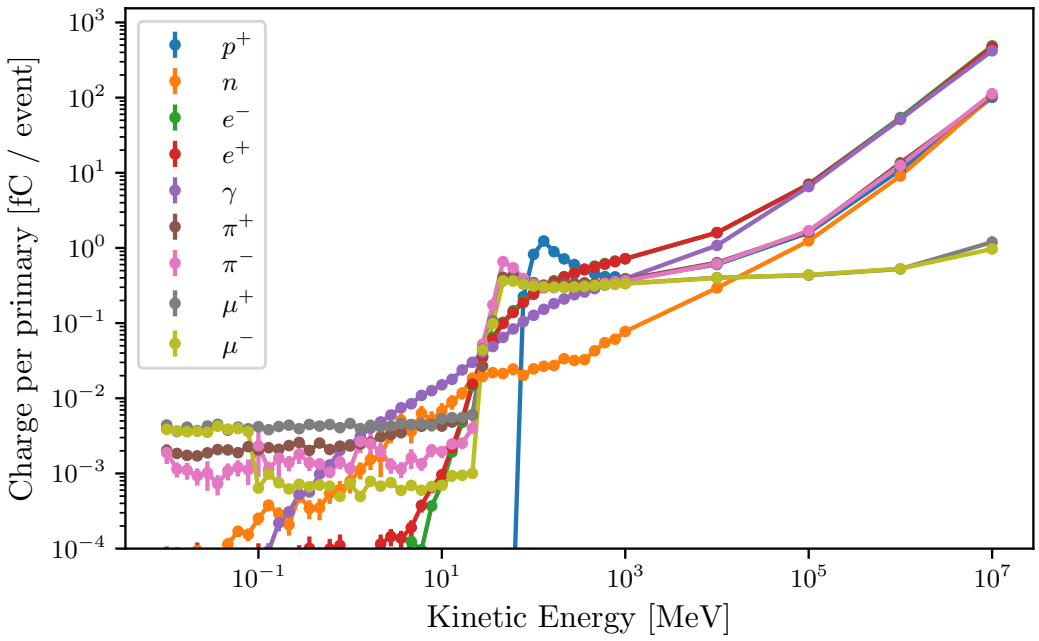

Figure 2.29: Radiation response of an LHC BLM for different incident radiation (beam along BLM axis).

The results are in good agreement with the previous studies [120]. At low energies, some of the particle species are not able to penetrate the steel tank and do not produce a significant response. For protons, a cutoff in response is observed around 50 MeV, while for electrons and positrons the cutoff is at the level of 1 MeV. Other particles, such as muons, produce a response over the whole energy range.

As expected, the BLM exhibits a strong response to radiation at high energies. This effect is attributed to the internal structure of the BLM and is reduced when the angle is increased. The difference of material traversed in the interior of the BLM for different

incidence angles hence results in a strong dependence of the BLM signal on the angle. The BLM response for a proton beam at different angles can be seen in Fig. 2.30.

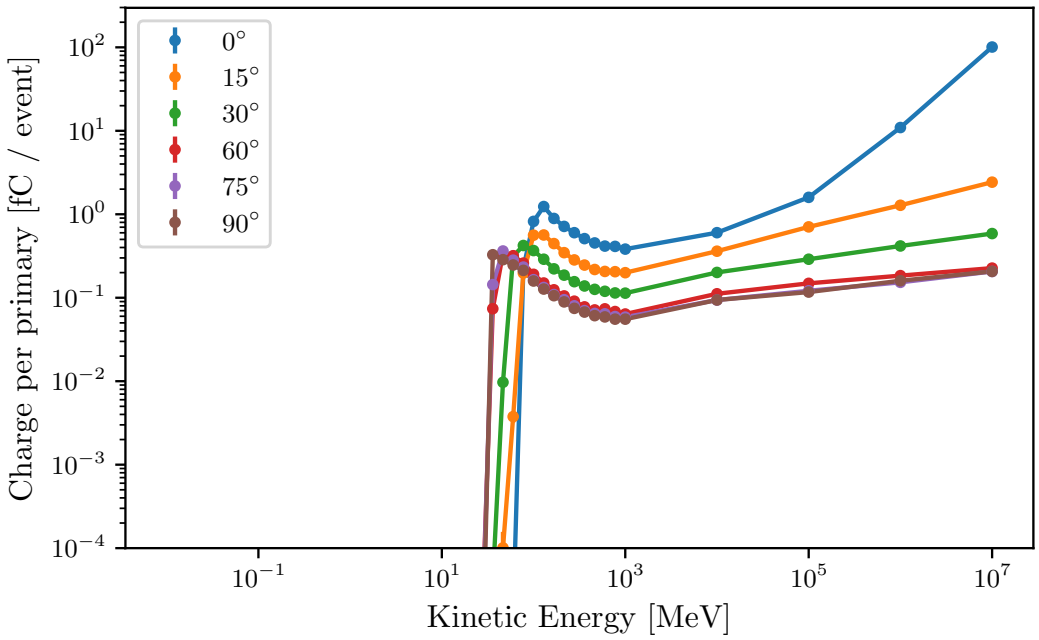

Figure 2.30: Dependence of the BLM radiation response on the angle of incidence. The data is for a proton beam at angles between 0° (longitudinal impact) to 90° (transverse impact)

The results from the BLM response tests validate the prepared geometry model and the model is used in simulations of the full LHC machine without further adjustments.

2.4.3 Simulation setup

BDSIM tracks both primary and secondary particles, allows scoring of energy deposition in any of the 3D geometry model volumes and supports outer magnetic fields. The outer magnetic fields are the fields outside of the beampipe in magnetic elements and can affect the trajectories of secondary particles produced from collimator and aperture losses.

By default, the outer magnetic fields in BDSIM are defined as a multipole field distribution, calculated as a vector sum of the fields from infinitely long (in z) current-carrying wires placed half way between each pole. The radial field distribution for outer magnetic fields for common LHC magnets is shown in Fig. 2.31. The magnitude of the outer field is normalised to the magnitude of the pure field in the beampipe at the pole tip radius. The

outer field is only applied outside the beampipe and does not take into account material effects. It is possible to override the default outer fields with more accurate field maps, but this is not done for the studies here.

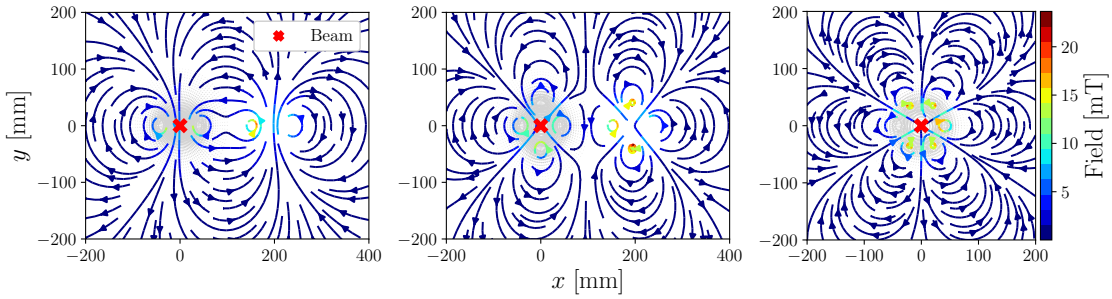

Figure 2.31: Outer magnetic field distribution in most common LHC lattice magnet: dipole (left), quadrupole (middle), sextupole (right). The arrows represent the direction of the field and the colour represents field magnitude. The beam is at the (0,0) position, marked by a red cross. For the dual-aperture magnet assemblies, the field is the sum of fields of the magnets for each aperture. The outer magnetic fields are only defined outside the beampipe and do not affect the core beam. The field values depicted are arbitrary and used for visualisation purposes only.

The capabilities of BDSIM allow detailed energy deposition simulations in the LHC, including the BLMs. One of the benefits of performing such studies in BDSIM is that the base inputs are the same as the ones described in Section 2.3.5. The required changes from the base set of inputs are the addition of the BLMs objects and the adjustment of the physical interaction cuts.

The geometry specification, placements and physical quantity scoring of the BLMs in the 3D BDSIM model of the LHC are specified using a single additional file. The file is prepared by an external Python tool by parsing information from an ASCII file specifying the BLM name, location and type. As done for the measured loss maps, only ionisation chamber BLMs in the LHC ring are selected. Further selection is done for BLM suitable for the BDSIM simulation, excluding BLMs corresponding to passive absorbers around the experimental IPs and other special equipment. In the configuration used for this study, 3380 BLMs are included in the BDSIM model, while the measured loss map includes readings from 3596 BLMs. The placement for the BLM in BDSIM is determined based on the extent of the adjacent beamline element and the placement side is extracted from the BLM name. The BLMs associated with collimators in IR3 and IR7 are placed with the detector axis transverse to the beam, while in the rest of the ring, the placement is parallel to the beam.

The other key aspect of the energy deposition simulation are the physical interaction cuts. As discussed in Section 2.3, the cuts are in place to control the computational resource usage. In simulations, cuts affect both the radiation reaching a BLM detector and its response. Reducing the cuts improves the accuracy of the simulation, but exponentially increases the number of secondary particles that must be processed. For individual components or short sections of beamline, tracking cuts in kinetic energy can be reduced to keV levels. However, for a multi-turn energy deposition studies of the entire LHC machine with ion beams at top energy, lowering the cuts make simulations impractical to run. From initial investigations, not presented here, a cut value of 1 GeV was chosen as a balance between between BLM signal and tolerable execution speed. In the future, options for physical interaction biasing can be considered to speed up the simulation execution.

2.4.4 Simulation results

The simulation is performed for 2×10^5 particles for 200 turns. Even with relatively large cuts for an energy-deposition simulation, the run time and resource usage are significant. The average run time per primary ion is about 15 min and the estimated total output size is in the multi-TB range. To manage the large volume of data, analysis is performed on the computing worker nodes following the execution of the job and the full output files are not held in persistent storage. There is the possibility for significant performance gains from optimising the run configuration and reducing the output to strictly information of interest. In addition to this, an estimation can be made of the total number of primary particles required for a given cuts configuration, in order to achieve a satisfactory statistical uncertainty in critical regions like the IR7 DS.

The loss maps from the simulated BLM energy deposition data are produced by normalising the BLM signals to the peak value, as done for the measured loss maps. The loss maps are compared against the previous BDSIM simulation results presented in Section 2.3.7 and measurements. The comparison for the full ring is shown in Fig. 2.32.

The loss map from simulated BLM signal shown a similar overall loss distribution to the measurement and the previous simulation. The collimator losses in IR6 and IR7 show a better agreement with the measurements than the BDSIM loss map from energy-weighted

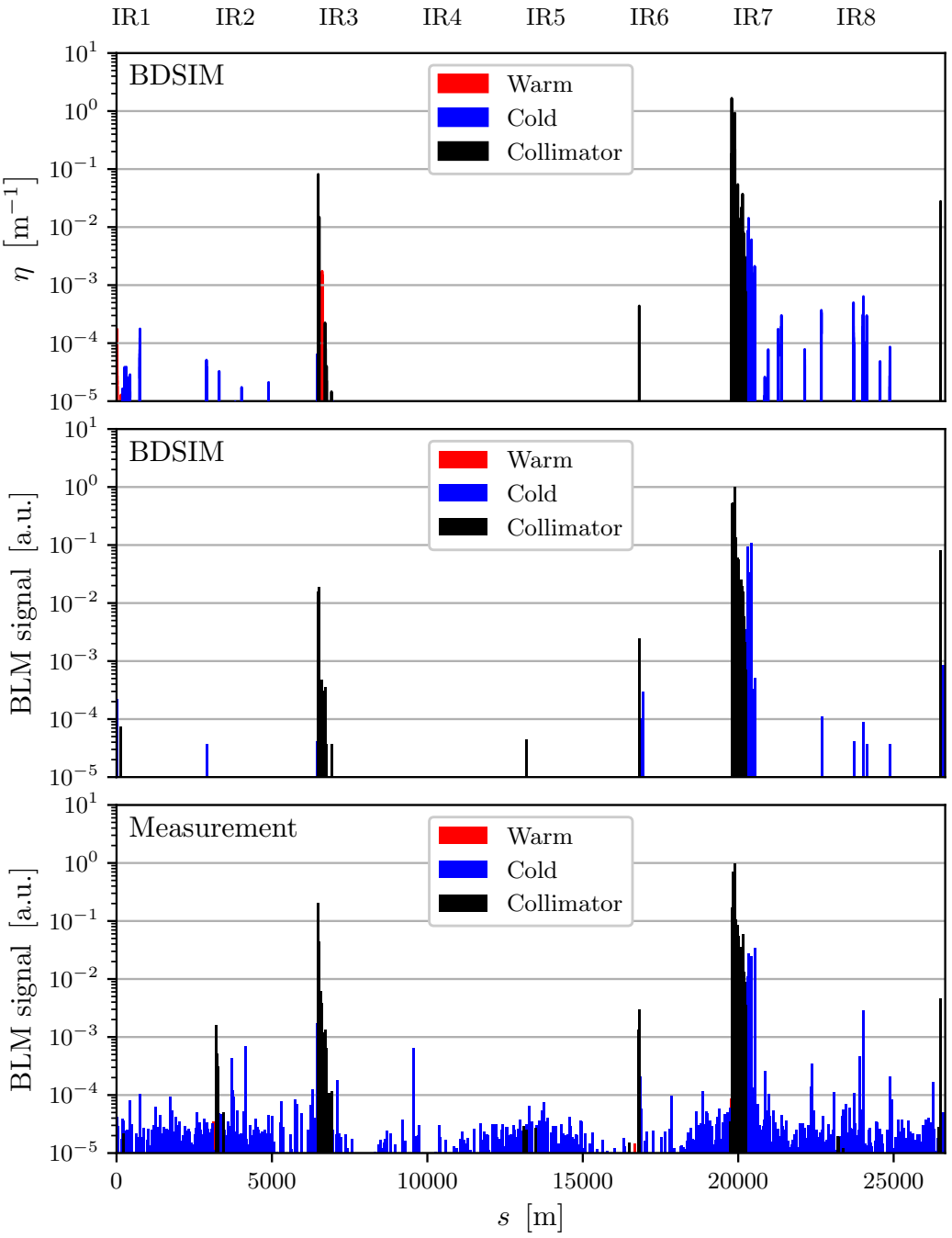

Figure 2.32: Comparison of loss maps from BDSIM simulation of energy-weighted ion aperture impacts (top, see Section 2.3.7), simulated BLM signal in BDSIM (middle) and measured BLM signal (bottom)

ion aperture impacts. The losses on TCTs in IR1 are overestimated by about one order of magnitude, while the losses in IR3 are underestimated by a similar amount relative to the measurement. This discrepancy is also found in the previous simulation and is likely

the result of the aperture loss distribution rather than the shower development. The cold losses in the arcs of IR7 and IR8 have lower magnitude than both the previous simulation and the measurement.

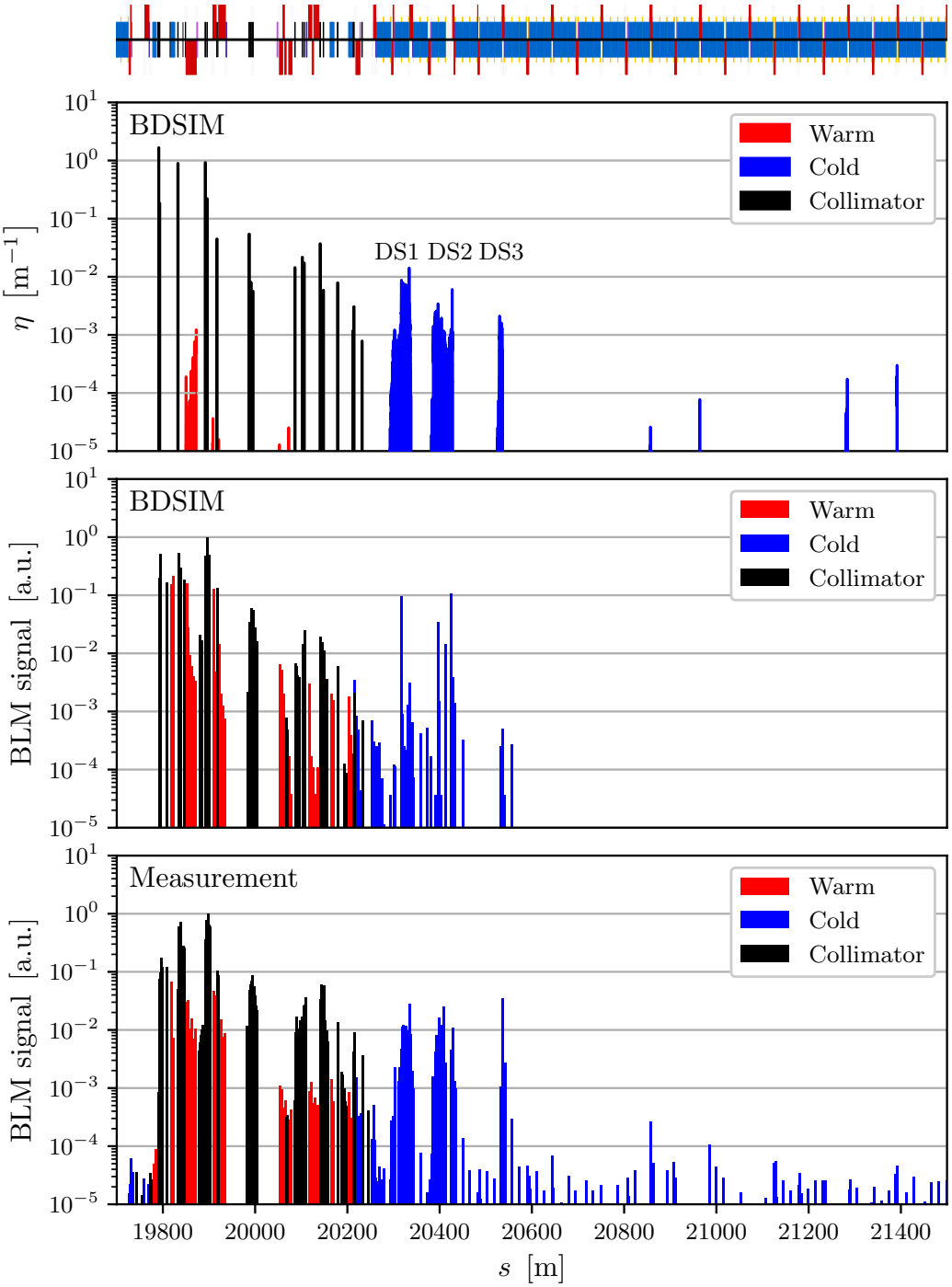

Figure 2.33: Zoomed-in view of the loss maps in Fig. 2.26, showing the losses in IR7 in detail. The loss maps shown include BDSIM loss map from energy-weighted ion aperture impacts (top, see Section 2.3.7), simulated BLM signal in BDSIM (middle) and measured BLM signal (bottom)

The betatron cleaning insertion is shown in detail in Fig. 2.33. The losses on the collimators and the aperture in the warm insertion, recorded in the simulated BLM loss map, show a good agreement with the measurements and exhibit the altered collimator loss hierarchy characteristic for ion beam collimation. The losses in the dispersion suppressor in the simulated BLM loss map show lower-intensity loss spikes immediately downstream of the warm section, which are not captured by the aperture loss simulation, but overall exhibit a worse agreement with measurement for the main DS cold loss clusters. Relative to both the previous simulation results and the measurement, the losses in the DS1 and DS2 clusters in the simulated BLM data show sharp peaks that overestimate peak losses, while the DS3 loss cluster magnitude is underestimated. This is also seen in Fig. 2.34, which shows a more detailed comparison of the measured and simulated BLM signals in IR7. The comparison is qualitative, as the BLM signals are individually normalised, but nevertheless provides important information. The peak cold losses in the DS1 and DS2 loss clusters are overestimated by about a factor 7, while the peak loss in DS3 is underestimated by about a factor 50 in the simulation, but it should also be noted that the peaks also have a discrepancy in the same s-location. The simulated collimator loss peaks in the straight section of IR7 generally agree with measurements within a factor of a few. Another observation from Fig. 2.34 is that the statistical uncertainty in the simulated results does not appear to be significant, despite the relatively low number of 2×10^5 primary particles simulated, compared to the 3×10^6 particles used in the cleaning inefficiency simulations shown in Section 2.3.7. The current estimate of the uncertainty in the simulation should be reviewed and benchmarked against results from previous energy deposition studies in future.

Absorptive volumes in the vicinity of the beampipe in IR7, such as passive absorbers or the transverse separation wall are not modelled in BDSIM. Such elements can influence the BLM signals in the IR7 DS as they affect secondary particle propagation outside of the beampipe. Furthermore, magnet cryostats are not modelled in BDSIM. As the BLM placement in BDSIM is prepared relative to the extent of the beamline element they are attached to, the lack of the cryostats affects the position of the BLMs relative to the beam, as well as the radiation flux reaching the BLM.

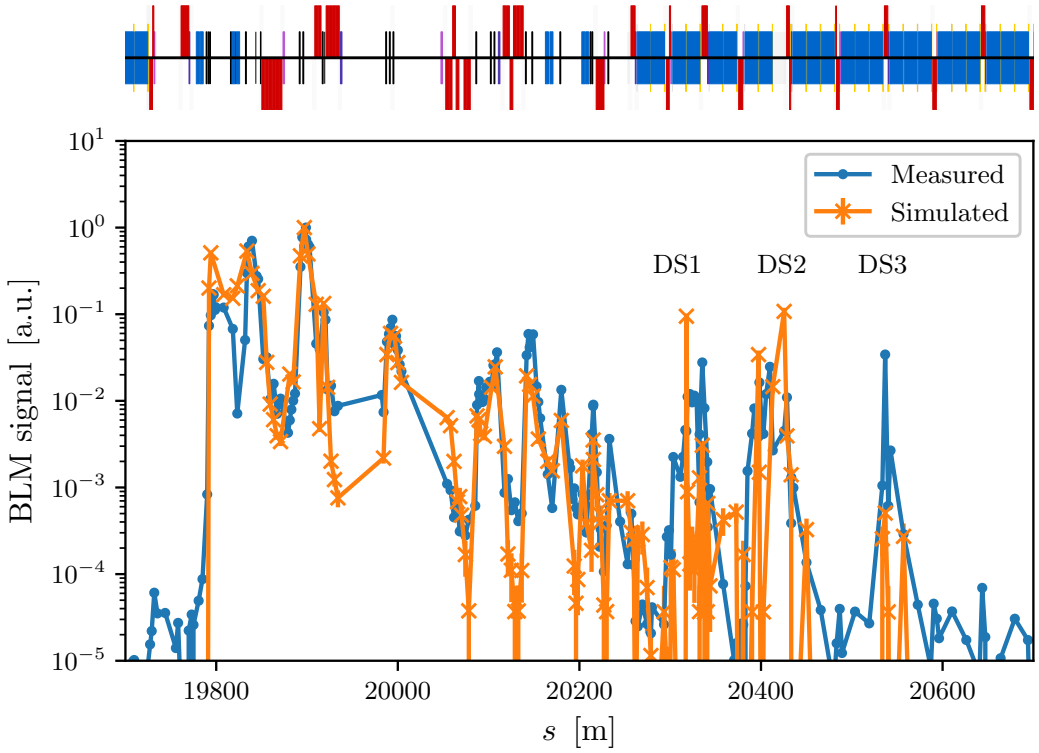

Figure 2.34: Comparison of the measured and simulated BLM signals in IR7. The two data sets are individually normalised to the peak value, as done for the measured loss maps. The simulated plot shows statistical uncertainties calculated using the per-event standard deviation in the simulated BLM signals.

2.4.5 Conclusion

The addition of a full complement of BLMs to the BDSIM 3D LHC model opens up the possibilities of a variety of studies. In this thesis, the setup has been used for collimation studies, but it can also be used to study delocalised or multi-turn loss effects due to secondary particles in scenarios such as physics debris from collisions, background to detectors, crystal collimation or beam loss due to unidentified falling object (UFO) in the beampipe.

Combining the tracking of primary and secondary beam particles in the beampipe, hadronic shower propagation from the aperture impact points, and a realistic BLM response allow for simulations to be directly compared with measurements and helps bridge the gap between the established collimation study workflows and the detailed energy deposition studies. One of benefits of using BDSIM is that the same base model can be used for more computationally-efficient loss map simulations as described in Section 2.3, as well as for

the more detailed loss studies discussed in this section.

The simulated BLM data does not currently match the measured data well overall, but the proof-of-principle study shows that detailed simulations of the full LHC machine with BLMs included are feasible, even for computationally-intensive studies like ion beam collimation at top energy. Multiple potential improvements have been identified. One of the priorities for future studies is the addition of cryostats for beamline elements, as the cryostats influence both the placement of the BLMs in BDSIM and the radiation reaching the detector. The inclusion of the collimator tanks and dense volumes in the vicinity of the beampipe, such as passive absorbers and separation walls, is also seen as a priority. Magnet and collimator supports should also be considered. In addition to introducing additional detail to the geometry model, manual adjustments of the positions for some BLMs will likely be necessary to achieve the best possible agreement, due to the sensitivity of the BLM signal to the BLM position relative to the closed orbit.

Further benchmarking and validation of the physical interaction models in Geant4 are also necessary. The EMD interaction is particularly important for losses in the DS and testing and development of the associated interaction model in Geant4 is considered essential. Another avenue for improvement is optimising the physical interaction settings in order to improve accuracy and reduce the required computing resources. The minimum kinetic energy cut for the simulation should be investigated in detail. As an additional improvement, instead of using the detailed BLM geometry model, a custom scoring routine that uses pre-calculated BLM response functions as shown in Fig. 2.29 can be used. This will reduce the overall model complexity, speed up the propagation of particles in the BLMs and reduce the dependence of BLM signal on the particle type and energy and the kinetic energy cuts used. Preliminary tests show that using this approach, a reduction of simulation time of multiple orders of magnitude can be achieved for transport of particles in the BLM volume, but further validation of the accuracy is required before using this method in studies.

Chapter 3

Ion beam collimation in the FCC-hh

The FCC project is an exploratory study focussed on developing the design and technology for a post-LHC collider that can be built at CERN. The study has recently produced a conceptual design report (CDR), which includes the proposed designs of three options for a new collider—a lepton-lepton collider (FCC-ee) [122]; hadron-hadron collider (FCC-hh) [6] and a lepton-hadron collider (FCC-he), as well as an LHC upgrade option (HE-LHC), which is discussed in Chapter 4. While the lepton and hadron collider options can be built and operated independently, an integrated approach [123] is favoured, with the lepton collider built first and later replaced with the hadron one, allowing both machines to use the same infrastructure. This sequential approach has proven successful in managing the cost and delivering a diverse particle physics research programme at CERN, with the Large Electon-Positron collider (LEP) and the LHC machine.

The integrated FCC programme is aimed at achieving an extensive understanding of the Standard Model and electroweak (EW) symmetry breaking, measuring the properties of Higgs boson with high precision and maximising the potential for discovering new physics beyond the Standard Model. The combination of a luminosity-frontier, highest-energy lepton collider and an energy-frontier hadron collider allows for increased direct particle discovery reach at the highest masses and a greatly improved sensitivity to deviations from the Standard Model via precision measurements for low masses.

The project duration is expected to be about 70 years, with operation beginning following

the completion of HL-LHC operation. If the project is approved, work on the infrastructure and machine construction for the FCC-ee is planned to begin in 2028 and take 10 years to complete. The FCC-ee is intended to operate for 15 years, until 2055. After this, following a 10-year construction period, the FCC-hh is proposed to be launched in the late 2060s and continue operation for 25 years. The 25-30 years of FCC-ee construction and exploitation allow for a focussed R&D campaign for the FCC-hh, aimed at reducing the cost and solving the challenges identified at present.

The design stored energy per proton beam in the FCC-hh is 8.3 GJ, over 20 times larger than for the LHC. For Pb ion beams, the design stored energy is 362 MJ, a factor of more than 70 larger than the design value for the LHC and a factor of more than 25 larger than the maximum value achieved in the LHC. This unprecedented energy places unique challenges on the collimation system. The loss of even a tiny fraction of the beam can result in catastrophic damage to the superconducting magnets. Furthermore, the large power contained in the beam halo poses a threat to the collimators themselves and the collimation system must be able to safely absorb and dissipate the incident power during different operational scenarios.

The FCC-hh is also designed to operate as a nucleus-nucleus collider, colliding beams of heavy or light ions. Experience from the LHC shows that ion operation requires additional considerations and the achievable intensity is significantly lower than for proton beams. The combination of the large beam energy, novel superconducting magnets and reduced collimation efficiency requires detailed investigation to establish the feasibility of ion beam operation in the FCC-hh and the associated limitations. The first systematic study of collimation for nominal ion beams in the FCC-hh is presented in this chapter, including an impact parameter scan, cleaning inefficiency simulation at injection and top energy and an analysis of the losses in critical locations.

3.1 The FCC-hh machine

The FCC-hh is designed to deliver proton-proton collisions at a c.o.m. energy of 100 TeV, a factor 7 larger than for the LHC. The peak luminosity is expected to reach $1 \times 10^{35}\,\mathrm{cm}^{-2}\,\mathrm{s}^{-1}$, with integrated luminosity in each of the two main experiments of about $20\,\mathrm{ab}^{-1}$.

3.1.1 Layout and optics

The fundamental design of the FCC-hh layout and optics is based on the LHC, with scaling to account for the increased beam energy. The layout of the accelerator is a ring with a circumference of 97.75 km. There are 8 straight insertion regions (IRs), with 6 of the insertions having a length of 1.4 km and 2 having a length of 2.8 km. The IRs are separated by short arc regions (SARs) or long arc regions (LARs). The arc cell in the FCC-hh is 213 m long, with a phase advance of 90° in both planes. A SAR contains 20 arc cells, while a LAR contains 78. The total length of the arcs is 83.75 km and the dipole fill factor is 0.8.

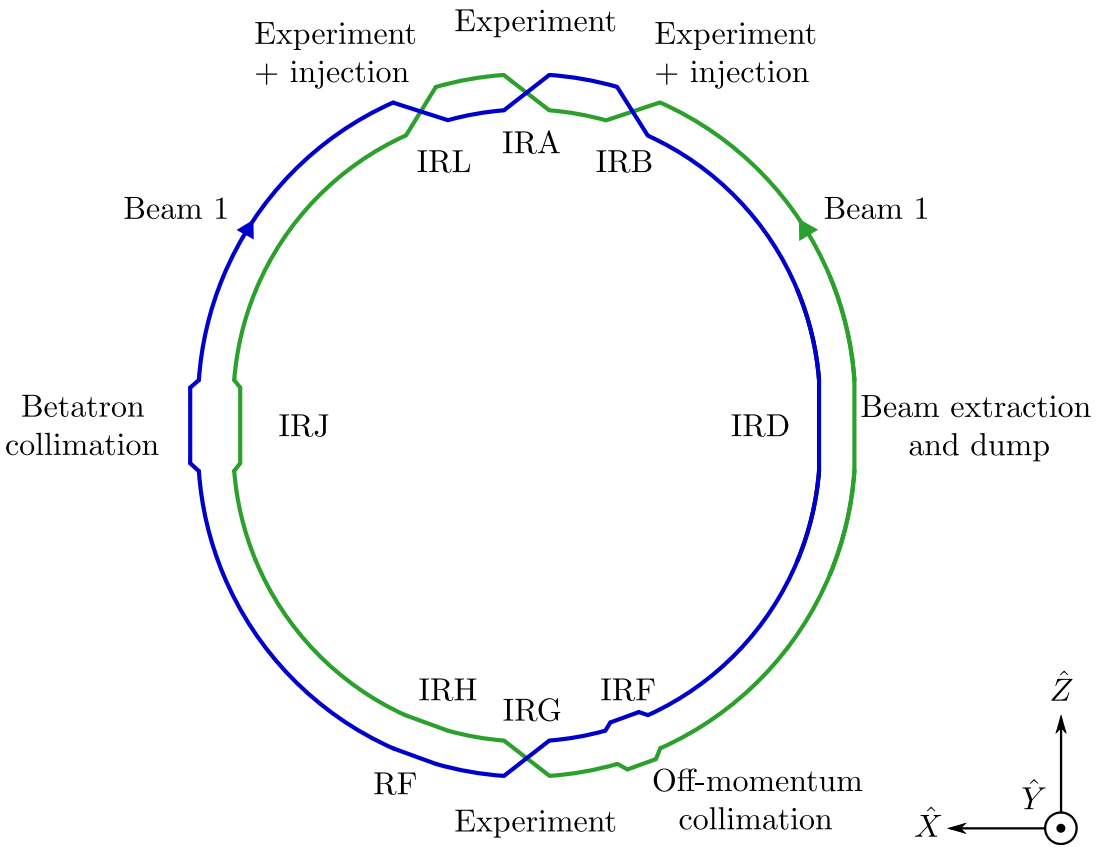

Figure 3.1: Diagram of the conceptual FCC-hh layout. Diagram based on [6].

The FCC-hh ring positioning is aligned relative to the existing CERN accelerator complex, such that injection can be performed from either the LHC or an upgraded Super Proton Synchrotron (SPS). Like in the LHC, the two main high-luminosity experiments are placed in diametrically opposite locations, IRA and IRG. IRL and IRB are located on either side of IRA and house the secondary experiments, as well as the injection systems. The secondary

experimental IRs are separated from IRA by SARs to protect the secondary experiments from physics debris emerging from IPA and prevent detector cross-talk. Unlike the LHC, where the secondary physics experiments are centered in their IRs, the FCC-hh secondary experiments are located at the IR extremity away from IPA, to make room for the injection systems and improve the protection of the experiments during injection. The betatron collimation system is housed in IRJ, which has a length of 2.8 km in order to alleviate the problems associated with the high beam energy and large stored energy. The off-momentum collimation is located in IRF, the RF system in IRH, and the beam extraction systems in IRD, which is the second insertion with length of 2.8 km.

The layout differences, relative to the LHC, are driven by robustness considerations. In normal proton beam operation, each of the high-luminosity experiments emits around 500 kW of power in the form of collision debris, while the collimation system can generate large quantities of radiation under some operational scenarios. In ion beam operation, the power emitted from the IP can reach 100 kW, with most the power concentrated in secondary beams from EMD and bound-free pair production (BFPP) interactions [124]. The secondary beams lead to highly localised losses, which are already a problem in the LHC, where the emitted power is around 3 orders of magnitude lower [24].

The most sensitive equipment, the extraction kickers and the RF systems, is placed in areas with lower radiation levels, away from the collimation system and the experiments.

3.1.2 Magnets

Given the dipole fill factor of 0.8, the dipole field required to keep the beam on the closed in the FCC-hh is 16 T. This is nearly twice the nominal field of the LHC dipoles and is well beyond the reach of the currently established superconductor technology. An extensive R&D campaign is underway to study novel superconducting materials and magnet designs that meet the requirements. The superconductor included in the baseline design of the FCC-hh lattice magnets is Nb_3Sn. The first dipole and quadrupole magnets based on this material are currently being prepared for the HL-LHC project, with peak fields of 11 – 12 T.

The main dipole design for the FCC-hh builds upon the experience of the LHC cryo-magnets and features a twin-aperture magnet assembly, enclosed in a cryostat and cooled by

liquid helium to 1.9 K. The coils have a cosine-theta layout and are made from Rutherford cable. The magnetic length of the dipole is 14 m and separation between the aperture central axes is 250 mm. Due to the mechanical characteristics of Nb_3Sn, the dipole magnets are straight, unlike the LHC dipole magnets. The straight dipoles introduce an offset (sagitta) between the magnetic axis and the closed orbit in the dipole magnets. The sagitta manifests as a reduction of the available aperture. For the FCC-hh, the assumed sagitta is 2.524 mm and its impact on the aperture is pessimistically modelled as a constant mechanical aperture constriction along the full length of the magnet.

The lattice quadrupoles also have a twin-aperture design and use Nb_3Sn. The nominal gradient is $367\,\mathrm{T\,m^{-1}}$, with a peak field of 10.51 T. The magnetic length of the quadrupole is 6.4 m and the separation is 250 mm, like in the dipoles. The majority of the other superconducting magnets in the machine, like the lattice sextupoles and dipole correctors, rely on the NbTi superconductor material used in the LHC.

Preliminary analysis shows that Nb_3Sn has a larger margin for beam losses than NbTi [125]. The currently used value for the quench limit is $70\,\mathrm{mW\,cm^{-3}}$ [126]. This value is likely conservative, with further studies pending.

One of the challenges for FCC-hh operation is the beam-induced heating of the magnet cold bores. Due to the increased energy, the linear power density in synchrotron radiation (SR) emission from a nominal proton beam in the FCC-hh can reach $35.4\,\mathrm{W\,m^{-1}}$, a factor 160 larger than for the LHC [6]. In order to reduce the heating of the cold bore, a special beam screen has been developed for the FCC-hh, which involves longitudinal slits in plane of the SR fan [127]. The slits allow for the photons to be extracted to an antechamber, where the power is dissipated with minimal heat transfer to the cold bore. An early prototype for the FCC-hh beam screen is shown in Fig. 3.2a, with the corresponding aperture model, used for simulations, shown in Fig. 3.2b. The specialised beam screen is not considered necessary for the straight sections, where a scaled, LHC-like beam screen is envisaged.

3.1.3 Collimation system

The stored energy per proton beam for the FCC-hh is 8.3 GJ, a factor 24 larger than the LHC design stored energy, which creates additional challenges for the collimation system.

(a)

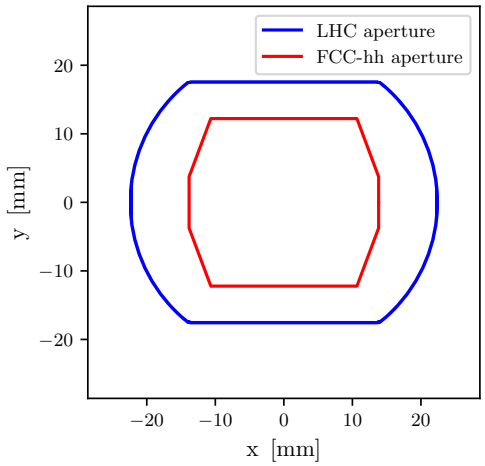

(b)

Figure 3.2: Photograph of an early prototype FCC-hh beam screen [128](a) and a plot of the aperture model used in simulations, compared with the one used for the LHC (b). The dimensions of the beam screen are 13.8 mm half-size in the horizontal and 12.2 mm half-size in the vertical [6].

The design of the FCC-hh collimation system [129, 130] is based on that of the LHC and HL-LHC, discussed in Section 2.1.5. The two collimation insertions are IRJ for betatron cleaning and IRF for off-momentum cleaning. A multi-stage collimator hierarchy is present in each of the collimation insertions, with TCPs intercepting the beam halo, TCSGs interacting with the out-scattered particles and TCLAs absorbing the secondary showers generated in the upstream collimators. There are also TCTs foreseen for the experimental insertions, as well as TCLDs for the dispersion suppressors of the experimental and collimation insertions. The β-functions and the length of the collimation insertions are scaled by a factor 5 to make the physical collimator apertures similar to ones in the LHC. This ensures the mechanical stability and reduces the collimator impact on impedance. The optical functions in the collimation insertions are depicted in Fig. 3.3.

The collimation system must be able to sustain a BLT of 12 min for 10 s, the same criterion used for the LHC. This corresponds to an instantaneous power of 11.6 MW for proton beams and 0.5 MW for heavy-ion beams. In order to safely dispose of this power, several changes have been implemented in the collimator design, relative to the LHC. The length of the horizontal and vertical TCP has been reduced from 60 cm to 30 cm. The skew TCP has been removed, because it would be exposed to an unsustainable power load of 260 kW due hadronic showers from the upstream TCPs. The collimator suffering the largest total

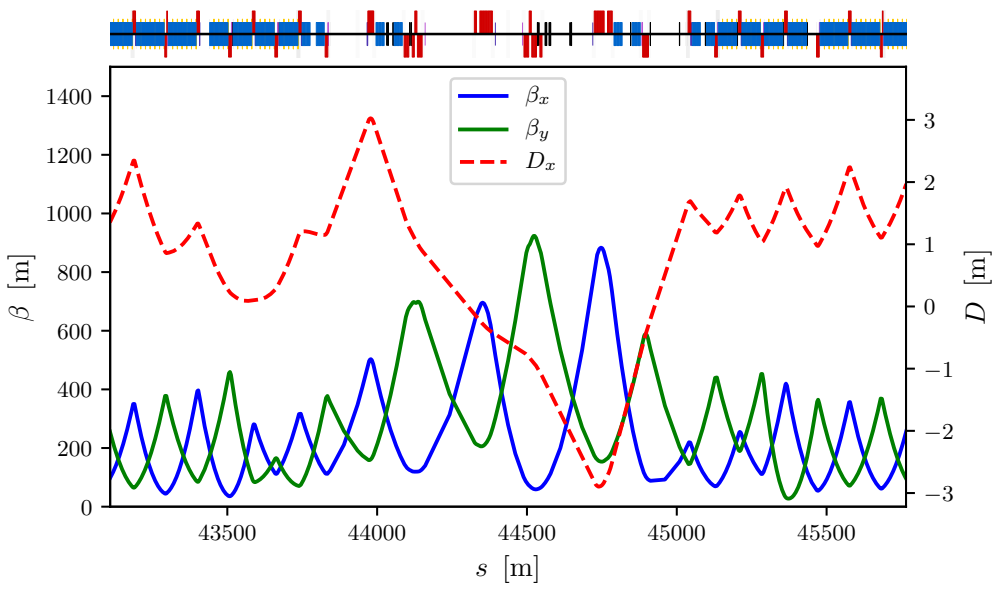

(a)

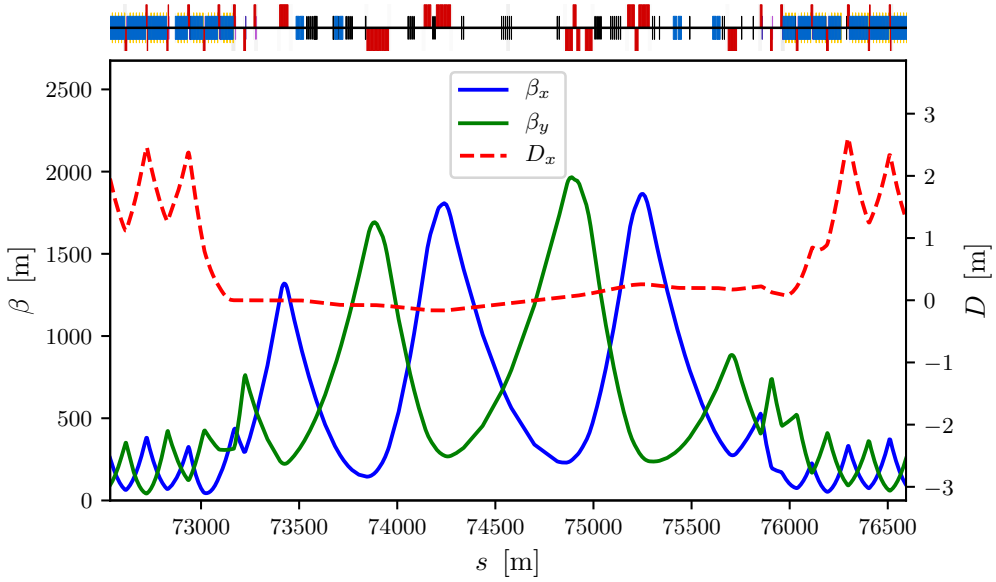

(b)

Figure 3.3: Optical functions in the FCC-hh collimation insertions—IRF for off-momentum cleaning (a) and IRJ for betatron cleaning (b).

power load (up to 92 kW) is the first TCSG. In order to safely absorb the losses, the thickness of the TCSG jaws is increased from 2.5 cm to 3.5 cm for the TCPs and from 2.5 cm to 4.5 cm for the TCSGs.

The collimators contribute significantly to the FCC-hh impedance budget [131]. In order to reduce the impedance, the majority of the TCSGs are made from MoGr. The collimators

experiencing the largest power loads, the TCPs and the first TCSG in IRJ are made from CFC, like in the LHC. The TCTs, TCLAs and TCLDs are made from tungsten.

Protons that have undergone single diffractive scattering and ions that have undergone EMD and fragmentation in the TCP can have a magnetic rigidity different than the nominal, but without sufficient transverse deflection to be intercepted by downstream collimators. As discussed in Section 2.2, such particles can be lost in the downstream DS, where the dispersion ramps up. To protect the superconducting magnets in the DS, TCLD collimators are to be installed in the collimation cleaning insertions, like for the HL-LHC. A diagram of the collimation system hierarchy for the FCC-hh is shown in Fig. 3.4.

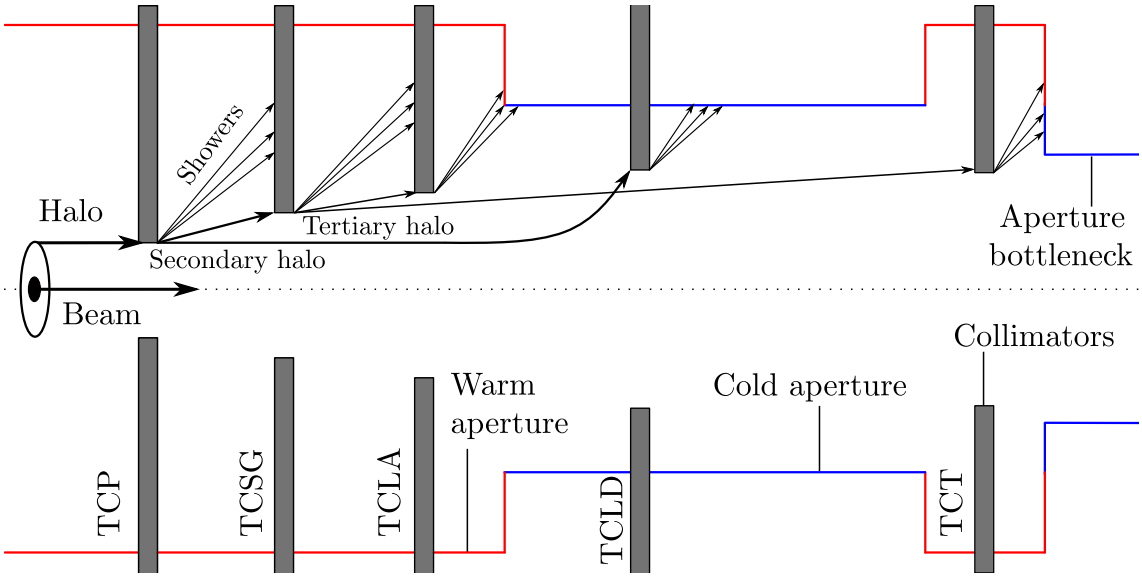

Figure 3.4: Diagram of the multi-stage collimation system in the FCC-hh. The collimation hierarchy includes primary (TCP), secondary (TCSG) and tertiary (TCT) collimators and shower absorbers (TCLA), as shown in Fig. 2.9. Relative to the LHC, there are additional TCLD collimators installed in the DS to mitigate losses from off-momentum particles. See Fig. 3.5 for the actual collimation system.

Unlike the HL-LHC lattice, where a nominal dipole must be replaced with 2 shorter and stronger dipoles to accommodate the TCLD assembly, the FCC-hh lattice spacing is larger and allows the installation of additional collimators without modification of existing beamline elements. Furthermore, unlike the HL-LHC, the FCC-hh design features multiple TCLD collimators in the collimation insertions, with 3 foreseen for IRJ and 4 for IRF. The collimation system in IRJ is shown in more detail in Fig. 3.5

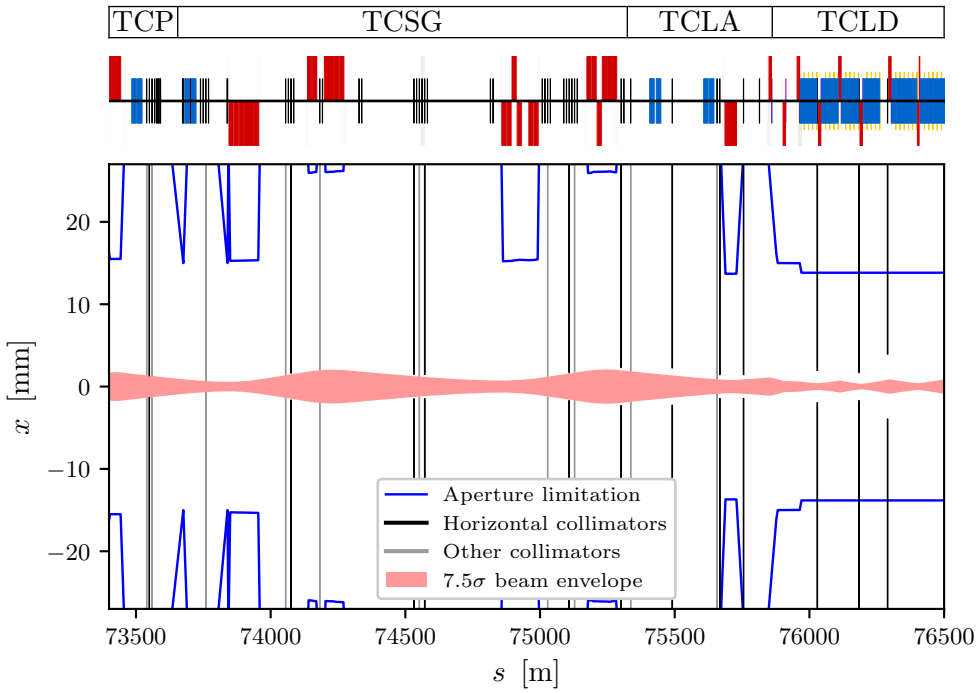

Figure 3.5: Layout of the collimators in IRJ of the FCC-hh, showing the placement and physical openings in the horizontal plane. Labels are shown for the regions housing the collimators of the different stages in the collimation hierarchy. The vertical and skew collimators are shown as continuous grey bars. The horizontal aperture limitation is overlaid and a beam betatron envelope touching the TCP is depicted to show the optical function evolution across the insertion.

There are also TCLD collimators in every experimental IR. A summary of the collimators per beam with their preliminary settings can be seen in table Table 3.1.

3.2 Simulation setup

The goal of the simulations presented here is to test the performance of the collimation system for FCC-hh operation with nominal ion beams and to investigate the effect of the TCLDs collimators on the losses in the DS downstream of the warm collimation insertions. The most demanding collimation scenarios are identified as betatron cleaning at top energy and off-momentum cleaning at injection energy (see Section 2.1.2 for the operational cycle). During normal operation at top energy, the collimation system sustains significant, continuous losses due the beam halo, with the majority of losses concentrated in IRJ. In

Table 3.1: Counts, materials and settings for collimators per beam in the FCC-hh [130]. The sigma settings are for nominal proton beam operation and are based on the normalised emittance of 2.2 µm. The materials are carbon-fibre composite (CFC) and tungsten heavy alloy (Inermet180) and molybdenum-graphite (MoGr).

Collimator	Count	Material	Injection (σ)	Collision (σ)
IRJ TCP	2	CFC	7.6	7.6
IRJ TCSG	11	CFC/MoGr	8.8	8.8
IRJ TCLA	5	Inermet180	12.6	12.6
IRJ TCLD	3	Inermet180	21	35.1
IRF TCP	1	CFC	10.8	18.7
IRF TCSG	8	MoGr	13	21.7
IRF TCLA	5	Inermet180	14.4	24.1
IRF TCLD	4	Inermet180	21	35.1
TCT	12	Inermet180	14	10.5
experimental TCLD	8	Inermet180	21	35.1
extraction TCLA	2	Inermet180	11.8	11.8
extraction TCLD	1	Inermet180	21	35.1

the second critical scenario, at the start of the ramp, the losses can also be significant, as particles with momentum outside of the RF bucket acceptance are lost during acceleration (see Section 1.1.6). The largest losses in this case occur in IRF.

For betatron collimation studies at top energy, an impact parameter scan is performed first to establish the value, which results in the worst collimation system performance. The results are shown in Section 3.3.1. For momentum collimation at injection energy, a beam with no transverse or longitudinal distribution (pencil beam) on the reference orbit is used, starting at IPA. The beam has a fixed momentum offset that ensures impact on the off-momentum TCP in IRF. The beam is started at IPA because the interaction points are dispersion free, which allows for precise control of the impact parameter at the off-momentum TCP by tuning the momentum offset of the beam.

The lattice model used for the collimation studies is the one featured in the collimation chapter of the long CDR. The nominal proton beam optical configuration is used for the simulations, as dedicated ion beam settings were not available. The key parameters for the simulation are listed in Table 3.2. All simulations presented are performed for an ideal machine with no optical or collimator imperfections.

As for the LHC, the physical emittance of the ion beam is taken to be the same as the

Table 3.2: Summary of simulation parameters for FCC ion operation [6].

Parameter	Unit	Value	
		Injection	Collision
Beam particle	-	$^{208}Pb^{82+}$	
Ion normalised emittance (ϵ_N)	µm	0.837	
Equivalent proton normalised emittance (ϵ_{Np})	µm	2.2	
No. of bunches	-	2760	
Ions per bunch	10^8	2	
Crossing angle	µrad	0	100
β^*	m	4.6	0.3
Energy / Nucleon (E / A)	TeV	1.3	19.7

physical emittance of the proton beam, from which an ion beam normalised emittance is calculated, as listed in Table 3.2. In the case of the LHC, this assumption is justified by the superior cooling of ion beams in the injector chain, but in the FCC-hh it results in an ion normalised emittance that is around 40 % smaller than the baseline value quoted in [6]. Tolerating the inconsistent emittance value allows for the proton beam collimator settings (listed in Table 3.1) to be taken directly in terms of sigma settings and mechanical openings and enables direct comparison. The physical outcomes of the simulations are not affected by the choice of normalised emittance and using the baseline normalised emittance value instead would only change the effective sigma settings of the collimators for ion beam operation.

The collimation studies are performed using the SixTrack-FLUKA coupling framework, using the procedure described in Section 2.3.4. The kinetic energy cuts are set at 1 TeV/nucleon, the same as for the LHC simulations, but protons emerging from the collimators are also tracked in the ring. As this is the first set of ion collimation simulations using the SixTrack-FLUKA coupling at this model scale and beam energy, further optimisation of the settings is necessary to improve performance.

For the FCC-hh loss maps, all losses around the ring are normalised to total energy lost in the simulation as per Eq. (2.4), instead of peak energy lost in the collimation system, see Section 2.1.4 for details. This notation allows for a straightforward comparison with the estimated quench limit. For beam collimation at top energy, the estimated quench limit in terms of cleaning inefficiency for Pb beams is $\eta_{max} = 2 \times 10^{-5}\,\mathrm{m}^{-1}$. The value is based on

the energy deposition quench limit for Nb_3Sn, quoted in Section 3.1.2, the beam energy and intensity from Table 3.2, and a BLT of 12 min.

3.3 Results

3.3.1 Impact parameter scan

In preparation for the main collimation simulations, an impact parameter (see Section 2.3) scan is performed. The beam used is a Pb beam at top energy, incident on the horizontal TCP. The lattice and collimator configuration used for the scan is an earlier iteration than the one used for the main collimation simulations, described in Section 3.2.

The impact parameter value that results in the worst collimation system efficiency is selected. For the selection, the figure of interest chosen is the integral of losses in the DS of IRJ. The DS is taken as the region $s = 76\,000 - 77\,000$ m. The TCLDs collimators are removed for the scan, in order to lessen the impact of the collimator settings on the results. Furthermore, it allows a comparison with the LHC, where TCLD collimators are not present. The scan is performed for 8 impact parameter values over the range between 10 nm and 10 µm, with 1.2×10^6 primary ions simulated at every point. The results from the scan are shown in Fig. 3.6.

The integrated DS losses show a peak at the impact parameter value of 0.1 µm, indicating the worst cleaning inefficiency. This is in contrast with the LHC, where the worst cleaning inefficiency is found at an impact parameter of 1 µm. The value of 0.1 µm is used for the simulations presented in the next section, but should be considered preliminary. The FCC-hh design is still evolving and it is essential to repeat the parameter scan for the current and future lattice and collimator configurations. To fully characterise the dependence of the losses on the impact parameter, the scan should also be performed in both transverse planes for Beam 2.

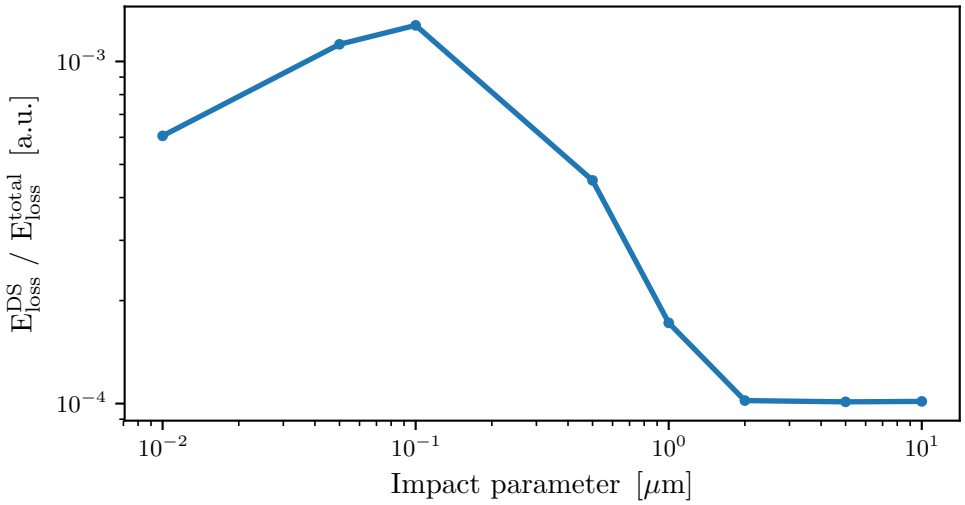

Figure 3.6: Impact parameter scan for an ion beam at top energy incident on the horizontal primary collimator. The aperture losses are integrated over the IRJ DS region, $s = 76\,000 - 77\,000$ m and normalised to the total energy lost in the simulation.

3.3.2 Betatron cleaning at top energy

There are two cases considered for the betatron loss maps at top energy. The lattice model used in this case is the baseline collision configuration, with $\beta^* = 0.3$ m and the crossing scheme on (version tag *fcc_hh_dev_0300_cross_thin* [132]). The first case is the nominal collimator configuration and the second is the case with the TCLDs collimators removed. The second case is included in order to provide a measure of the ability of the TCLD collimators to protect the cold aperture in the dispersion suppressors and also to allow a direct comparison with the LHC, where those collimators are not present. The simulations are performed for 1×10^6 primary ions, tracked for 700 turns, with an identical primary beam distribution for both simulation cases.

Betatron loss maps for B1H at top energy with and without TCLDs are shown in Fig. 3.7 top and bottom, respectively. The corresponding zooms into the betatron cleaning insertion, IRJ, are shown in Fig. 3.8. The loss distribution around the ring exhibits the expected concentration of losses in IRJ and IRF, with notable losses also being recorded on the TCTs of the experimental insertions and in IRD. For the nominal collimation configuration (with TCLDs), the losses in the DS of IR are comfortably below the estimated quench limit. No significant cold loss clusters are observed in the rest of the ring.

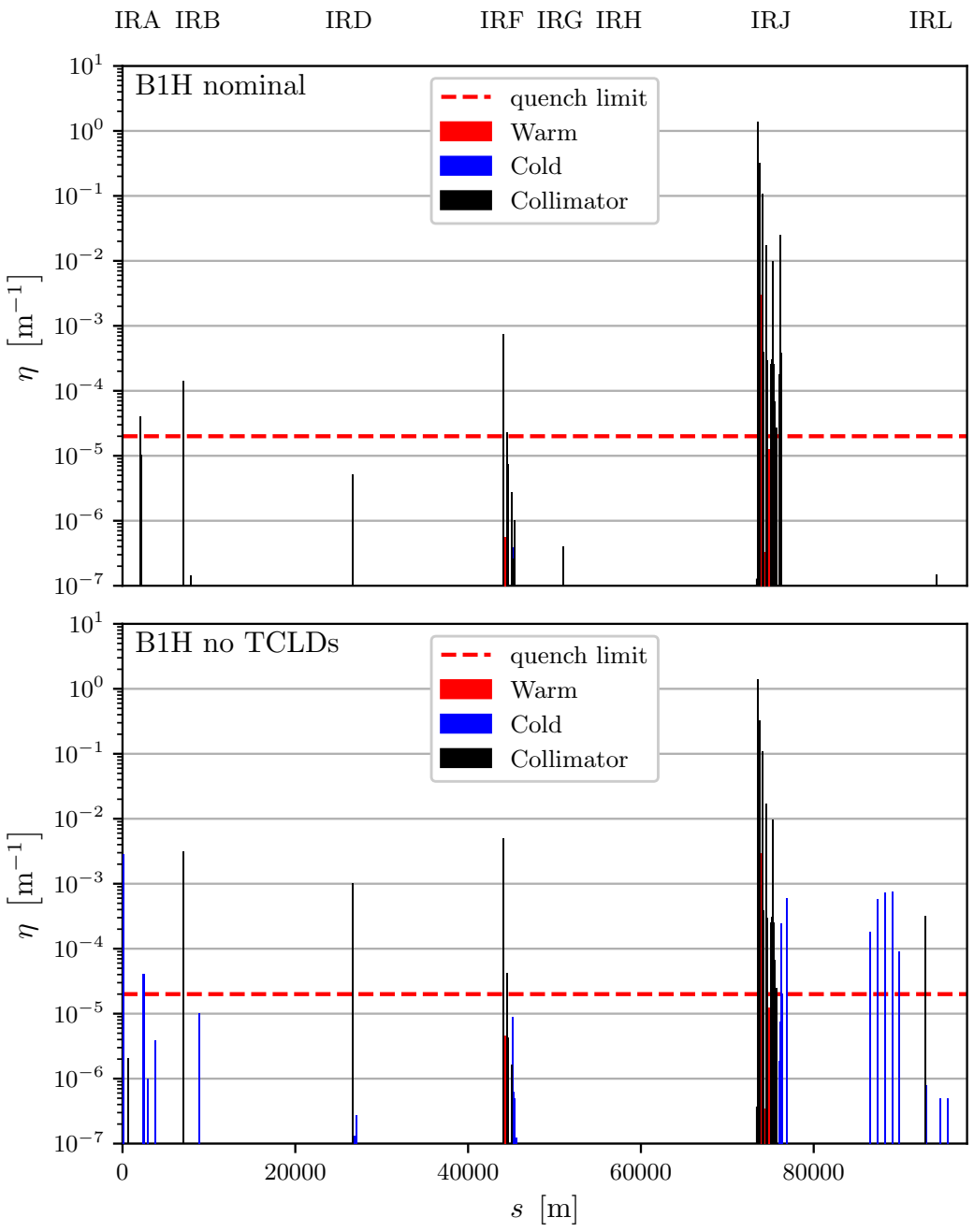

Figure 3.7: Comparison of FCC-hh betatron loss maps for B1H with $^{208}Pb^{82+}$ ions at top energy with the nominal collimator configuration (top) and with the TCLD collimators removed (bottom).

In the nominal case, the 3 TCLDs are exposed to large losses, with the second one being one of the most loaded collimators in the machine. A quantitative evaluation of the power loads on collimators is not possible with the current setup, because the method

for computing collimator energy deposition relies on the difference between total incoming and total outgoing energy (see Eq. (2.12)). Due to the large energy cuts and omission of EM processes, energy that would normally escape a collimator in the form of low-energy secondary particle showers is instead counted as deposited in the collimator. Furthermore, because secondary showers are not present in the collimator leakage, the energy deposition for collimators downstream of the impacted one is also affected. It is likely possible to obtain a set of scaling factors from energy deposition simulations that can relate collimator losses in the SixTrack-FLUKA simulation to realistic power loads, but no energy deposition simulations for ion beams are currently available.

The simulation without TCLDs (see bottom plots of Fig. 3.7 and Fig. 3.8) shows numerous cold loss peaks with a magnitude well above the quench limit, both in the DS of IRJ and in the rest of the ring. This demonstrates that TCLDs installed at the nominal locations and with settings, optimised for protons, are also effective in intercepting ion losses. Those collimators are essential for operation at nominal ion beam intensity.

While the cold losses without TCLD collimators are likely not tolerable for operation, the relative magnitude of the largest cold loss clusters is lower than in the LHC (see Section 2.3.7). For a similar operational scenario, the peak cold loss in the LHC found from both simulations and measurements corresponds to a cleaning inefficiency of around 1×10^{-2}, while the worst cleaning inefficiency from the simulations of the FCC-hh without TCLDs is around 5×10^{-4}, more than an order of magnitude lower. Another notable difference is that for the FCC-hh, the peak cold losses are found in a collection of loss clusters deep into the arc downstream from IRJ, close to IRL. Those differences are interesting, as the lattice and collimation system of the FCC-hh (disregarding the TCLDs) are scaled-up versions of the ones in the LHC. The explanation for those differences is not clear at this time. Further studies are required to investigate separately the contributions to the relatively better ion beam collimation performance in the FCC-hh from the larger beam energy and scaled up optics and layout.

A further analysis is carried out for the losses on the cold aperture in the DS of IRJ in order to establish the particle species and the energy scale of the losses. Only particles impacting on the aperture in the region $s = 76\,000 - 77\,000\,\mathrm{m}$ are selected, disregarding losses on the TCLDs. The phase space distribution of the losses in shown in Fig. 3.9. The transverse

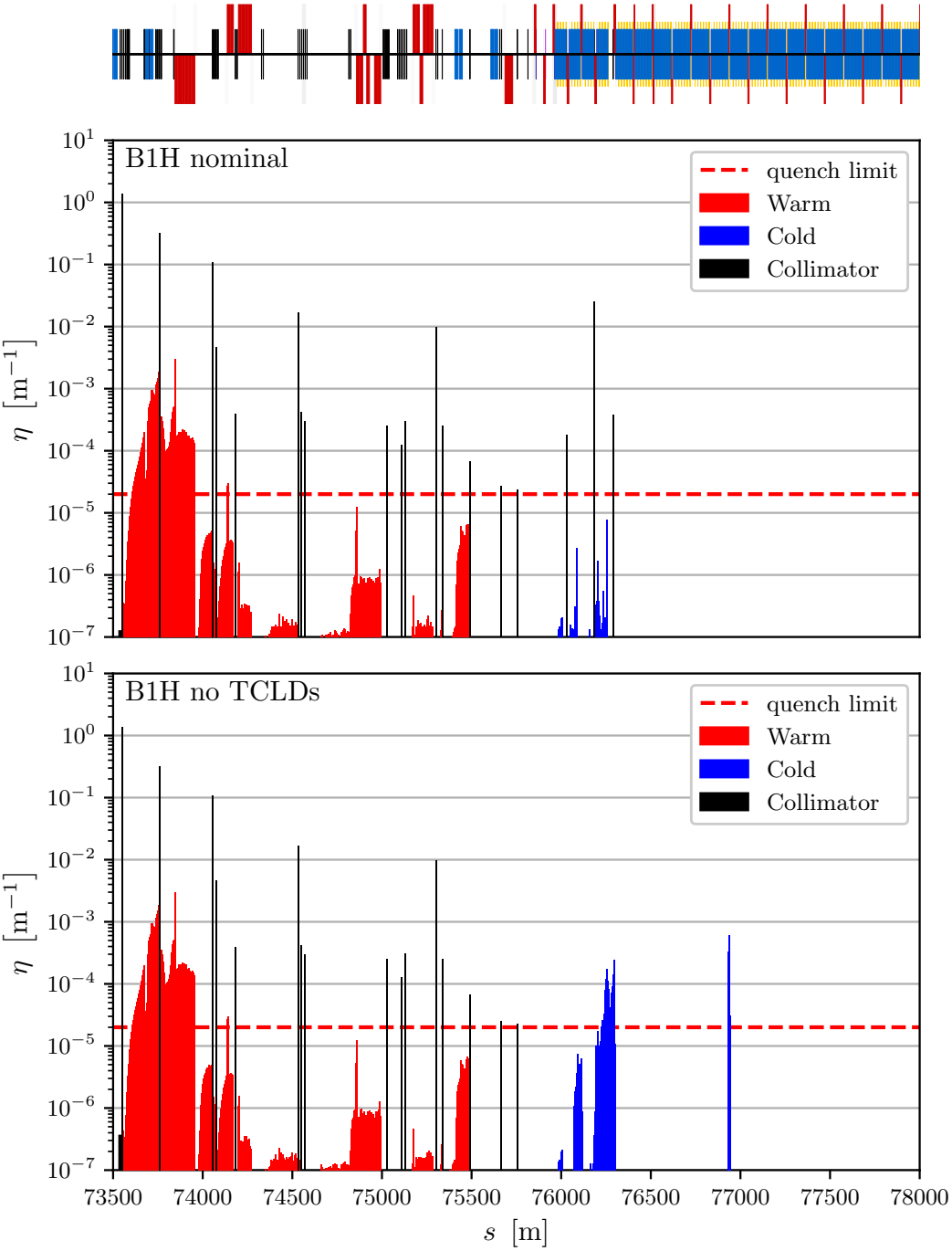

Figure 3.8: Zoomed-in view of the loss maps in Fig. 3.7, showing the losses in IRJ in detail. The plots shown are FCC-hh betatron loss maps for B1H at top energy with the nominal collimator configuration (top) and with the TCLD collimators removed (bottom).

loss coordinate distribution, depicted in the bottom left plot of Fig. 3.9a, shows that losses occur on all sides of the beampipe and an outline of the octagon aperture profile, discussed in Section 3.1.2, is visible. It is characteristic for ion beams that secondary particles, produced in interaction with the collimators, can have both a lower or a higher magnetic

rigidity than that of the nominal particles. This is in contrast to protons, where only a lower magnetic rigidity is possible for the secondary particles. The spread in magnetic rigidity is manifested as losses on both the inside (negative x) and the outside of the aperture (positive x) as a result of dispersion.

It is clear from Fig. 3.9b that only secondary particles impact the aperture in the DS. No fragments with A $>$ 160 are recorded, indicating that the collimation system with the nominal configuration for proton beams has a good performance for ion beams as well. Furthermore, it is found that nearly all the particles reaching the aperture in the DS originate at one of the TCLD collimators, indicating that they successfully intercept the heavy-ion losses coming from the warm collimation insertion. Light ions with A $<$ 6 emerging from the TCLDs account for over 86 % of the energy lost on the aperture in the DS, while protons alone account for around 75 %. Secondary protons escaping the collimators lead to significant warm losses in IRJ, which are not relevant for the current study. However, protons also dominate the cold losses in IRJ DS, meaning that they cannot be omitted from tracking in order to optimise the simulation execution, as done for the LHC. While simulations indicate that the losses are below the quench limit, the showers leaking out of the collimators impose a quench risk. Energy deposition studies must be performed to evaluate the power deposition in the coils of the most critical magnets and assess whether additional masks are required to protect them further.

Betatron collimation at top energy was also studied for Beam 1 vertical (B1V) in the FCC. The results are shown in Fig. 3.10. In this case, the starting beam is incident on the vertical TCP, with the same 0.1 µm impact parameter as the B1H case. The loss distribution around the ring, shown in the top plot of Fig. 3.10 is similar to the B1H case, with the majority of losses concentrated in the collimation insertions and no significant cold loss clusters observed. In IRJ, shown in the bottom plot of Fig. 3.10, the losses are also similar to the horizontal case. There are comparatively fewer losses occurring on the TCSG and TCLA collimators, and there are slightly fewer cold losses observed in the downstream DS. The magnitude of the cold losses recorded is far below the estimated quench limit.

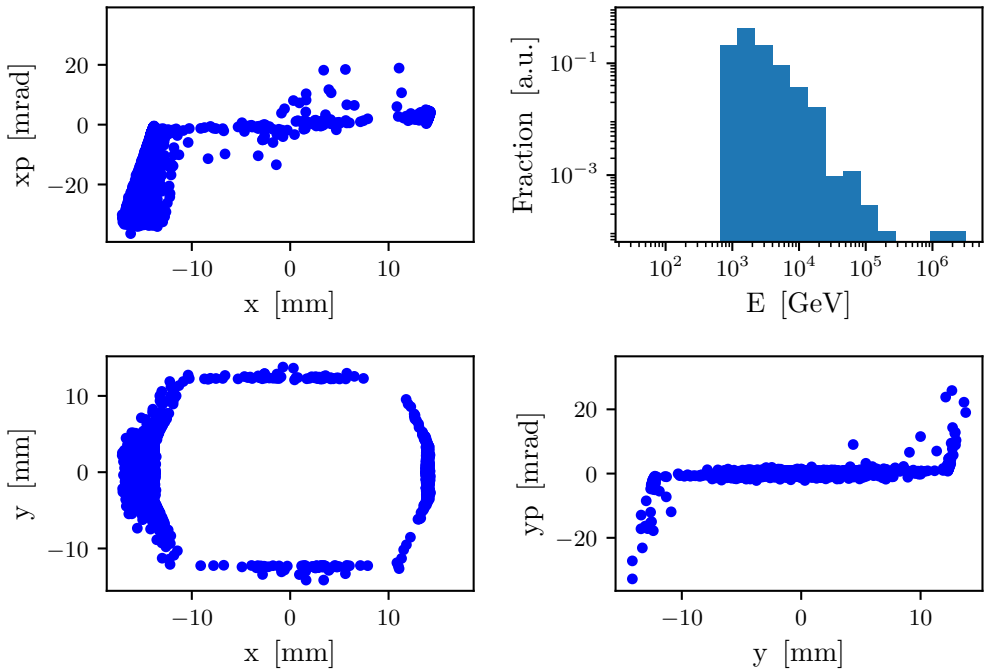

(a)

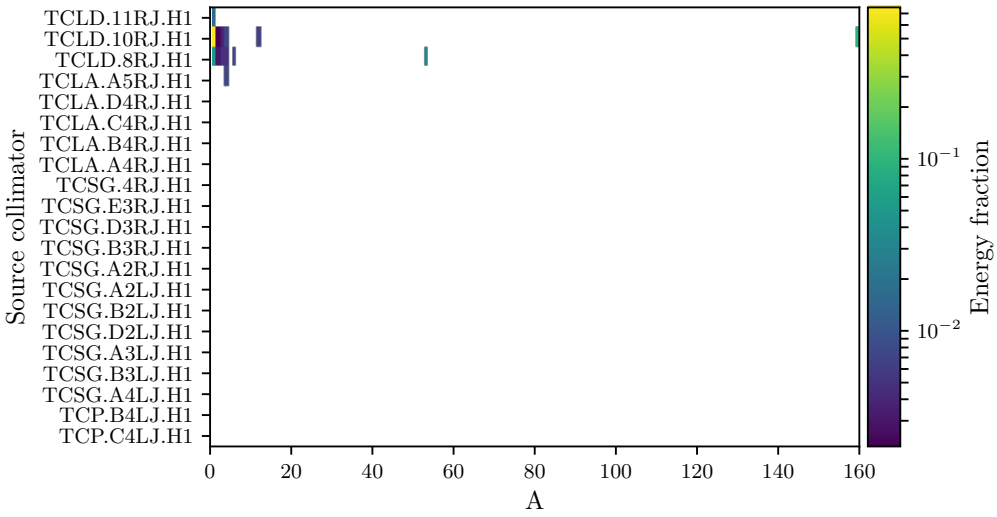

(b)

Figure 3.9: Distribution of aperture losses in the DS of IRJ ($s = 76\,000 - 77\,000\,\mathrm{m}$) for FCC-hh B1H betatron collimation at top energy. Losses on collimators are not included. The top set of plots (a) show the phase-space distribution of the losses (positive x is towards the outside of the ring). The bottom plot (b) shows the distribution of energy between the different isotope species in the losses and the collimator where the lost particle was produced. All the collimators in IRJ are listed on the y-axis in the sequence they are reached by the beam (bottom to top). The histogram of A for the aperture losses is weighted by the energy of the lost particle, normalised to the total energy lost in the DS, to get the colour scale.

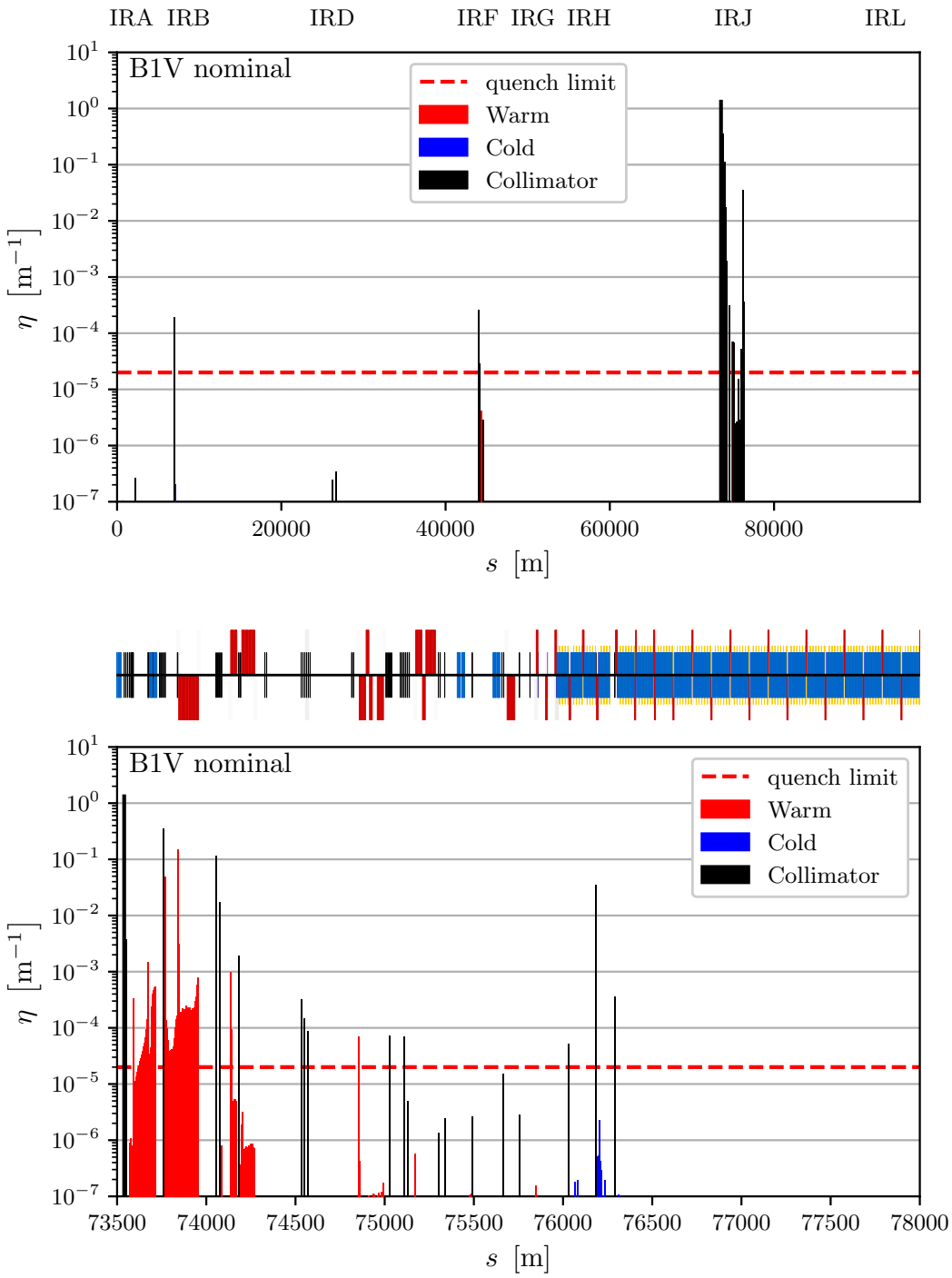

Figure 3.10: Betatron loss map for the FCC-hh B1V with $^{208}Pb^{82+}$ ions at collision energy, showing the full ring (top) and a zoomed-in view of the betatron cleaning insertion IRJ (bottom).

3.3.3 Off-momentum collimation at injection energy

The off-momentum collimation study is performed for injection energy with the injection parameters from Table 3.2 and the injection collimator settings from Table 3.1. The lattice model used in this case in the baseline injection configuration, with $\beta^* = 4.6\,\mathrm{m}$ (version tag *fcc_hh_dev_4600_thin* [132]). The pencil beam is started at IPA, on the reference orbit, with a relative energy offset of $\delta E/E = -1.5 \times 10^{-3}$. Particles impact the off-momentum TCP in the off-momentum cleaning insertion (IRF) on the first turn. Like for the betatron collimation simulations, 1×10^6 primary particles are tracked over 700 turns. The loss maps for the full ring and the zoom to IRF are shown in Fig. 3.11.

As expected, the worst cold losses are observed in the DS downstream of IRF. While the TCLDs absorb a significant fraction of the losses, three extensive cold-loss clusters are observed in the DS and one additional smaller cluster in the downstream arc. A comparison is made with an assumed quench limit of $\eta_{\mathrm{max}} = 1 \times 10^{-3}\,\mathrm{m}^{-1}$ [133], which is based on the LHC injection quench limit and ramp loss rate. This quench limit value is approximate and carries a significant uncertainty, but is nevertheless useful for an initial evaluation of the collimation performance at injection. All of the cold losses recorded remain more than an order of magnitude below the estimated quench limit and no areas of immediate concern are identified. As the rate of losses during the ramp determines the BLT, further studies are required to establish the loss rate and define the limits of safe operation. Should the losses prove limiting, an increase of the ramp time or other mitigation strategies can be considered.

3.3.4 Conclusion

The first detailed study of ion beam collimation for the FCC-hh has been performed. The study covers the most challenging collimation scenarios—betatron cleaning at top energy and off-momentum cleaning at injection energy. For betatron cleaning at top energy, an impact parameter scan has been performed, identifying a preliminary impact parameter value that results in the worst cleaning inefficiency as 0.1 µm. The impact parameter scan should be repeated for the latest machine configuration. Betatron cleaning simulations have been performed at top energy for both the nominal proton beam collimator configuration

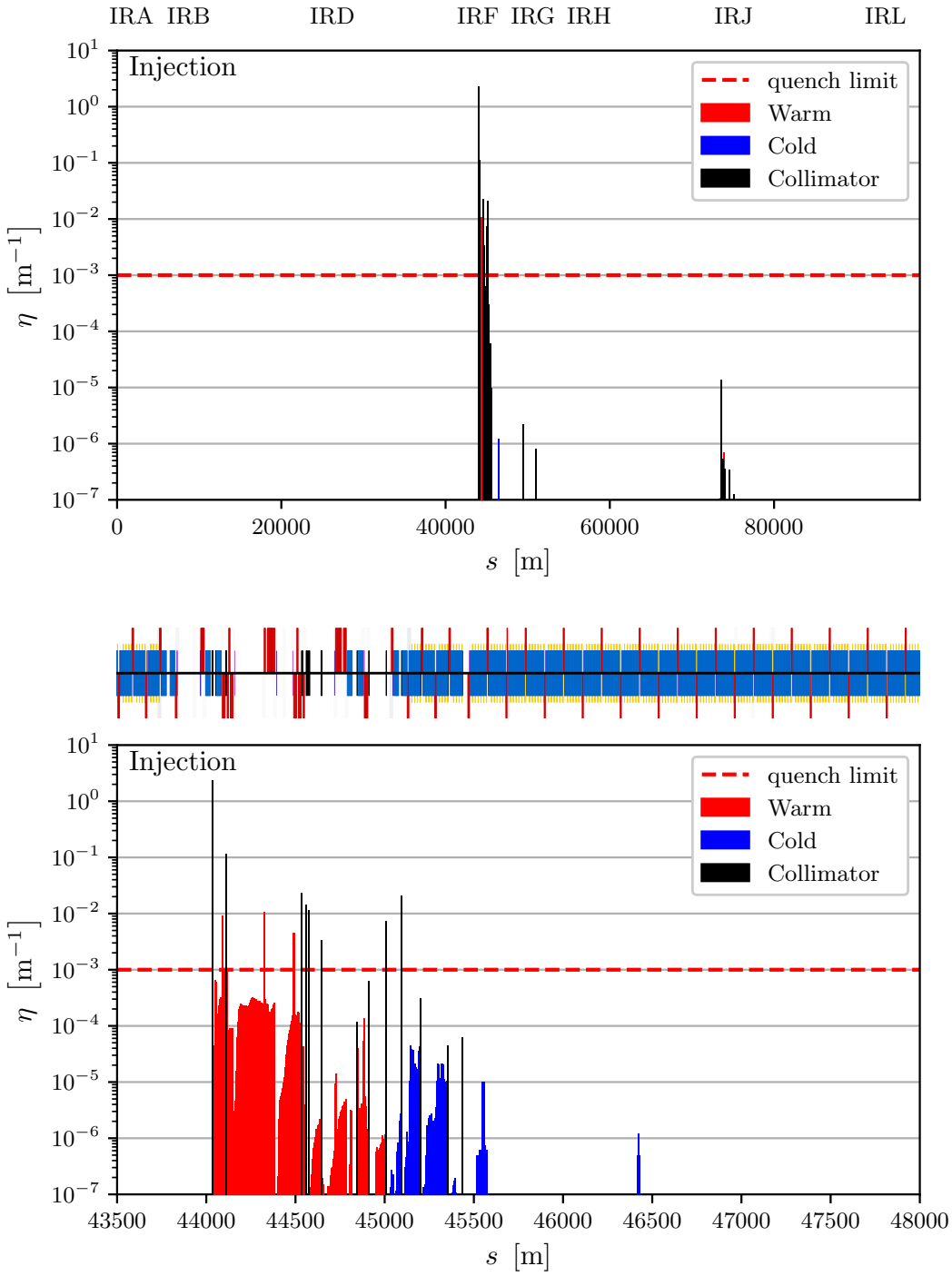

Figure 3.11: Off-momentum loss map for the FCC-hh B1H with $^{208}Pb^{82+}$ ions injection energy, showing the full ring (top) and a zoomed-in view of the IRF, the off-momentum cleaning insertion (bottom).

and in a configuration without the TCLD collimators. In addition to this, off-momentum cleaning simulations have been performed at injection energy, with no loss peaks found above the estimated quench limit.

The results of the simulations, within the scope of this study, suggest that the collimation system designed and configured for proton beams is also adequate for Pb ion operation with baseline parameters. For betatron collimation at top energy, the TCLDs have been found to be crucial for operation, keeping the losses in the DS of IRF below the estimated quench limit. With the TCLDs at their nominal settings, no ion fragments with $A > 160$ were found in the DS aperture losses. Up to 86 % of the cold aperture losses in the DS were found to originate from ions with $A < 6$ leaking out of the TCLDs themselves. Detailed energy deposition studies are required to quantify the risk to the most critical superconducting magnets due to the showers escaping the collimators, and determine if additional protection is necessary. To fully characterise the range of potential losses, studies should be performed for collimation cleaning using optical and collimator imperfections. Given the emerging interest in FCC-hh operation with lighter ions such as argon (Ar) or calcium (Ca) at the FCC-hh [124], evaluations of ion beam collimation performance should also be carried for light-ion beams.

Chapter 4

Ion beam collimation in the HE-LHC

The High Energy LHC (HE-LHC) [134–137] is a design study for a future hadron collider that would utilise the existing LHC tunnel and infrastructure. The collider is proposed to use the 16 T magnet technology, developed for the FCC-hh, to achieve a c.o.m. energy for proton-proton collisions of 27 TeV, a factor 2 larger than for the LHC. If the project is approved, the construction can begin following the decommissioning of the HL-LHC, with physics operation starting around the mid-2040s. The target integrated luminosity is $15\,\mathrm{ab}^{-1}$ over the expected project lifetime of 20 years.

The main motivation for the project is delivering a significantly improved physics reach over the HL-LHC, without incurring the large costs associated with the FCC-hh. The potential benefits of the HE-LHC are extending the energy reach in direct searches by approximately a factor 2 and improving the precision of studies in the EW and flavour sectors, thus providing a better direct and indirect sensitivity to new physics, and exploring in detail the properties of potential future LHC discoveries. Those benefits are in line with the ones for the FCC-hh, adjusted to the smaller scale of the HE-LHC.

The HE-LHC design and operational parameters are based on those of the LHC and the HL-LHC. Because of the novel magnet technology envisaged and the tight space constraints in the existing LHC tunnel, the optics and layout of the magnetic lattice in some regions differ from those of the LHC, which is discussed in Section 4.1. Furthermore, the stored beam energy for proton beams is 1.4 GJ, a factor of 4 larger than in the LHC. The combination

of the large stored energy and the changes to the lattice create a unique operational regime for collimation, which requires detailed investigation.

An ion collider mode of operation is foreseen for the HE-LHC, with $^{208}Pb^{82+}$ ion collisions at an energy of 5.32 TeV/nucleon. As discussed in Chapter 2, collimation for ion beams is associated with additional challenges. With a total stored beam energy of almost 50 MJ, far beyond what has been achieved operationally with lead ion beams in the LHC [54], ion collimation becomes extremely challenging in the HE-LHC and dedicated studies are necessary.

In this chapter, the first evaluation of collimation performance for the Pb beams is presented. This includes an impact parameter scan and simulations for B1H at top energy for two cases, a collimation configuration with settings identical to the ones used for proton beams and a configuration with no DS collimators. Comparison of the simulated cold losses with an estimate for the quench limit and a detailed analysis of the most critical cold loss clusters are also presented, together with a discussion of potential mitigation strategies.

4.1 Machine overview

4.1.1 Layout and optics

The HE-LHC is designed to fit in the existing LHC tunnel. This design fixes the locations of the straight section IRs and places constraints on the lattice layout. The ring dimensions and layout are the same as shown in Fig. 2.1, with 2 high-luminosity physics experiments in IR1 and IR5 and two secondary experiments in IR2 and IR8. The collimation systems are located in IR3 (off-momentum) and IR7 (betatron). The RF system is installed in IR4 and the beam extraction and dump systems are installed in IR6. Injection options are considered at 450 Z GeV from the existing SPS or at 900 Z GeV or 1.3 Z TeV from an upgraded superconducting Super Proton Synchrotron (scSPS). The different injection options have different challenges associated with them. Currently, the 1.3 TeV injection option is the baseline.

To achieve the design proton beam top energy of 13.5 TeV with the 16 T magnets, a

similar dipole fill factor is required as for the LHC. There are two alternative arc design concepts considered, with pending evaluation of the trade-off between maximising the collision energy reach or maximising the available aperture at injection energy [134, 138, 139]. Both concepts have a 90° phase advance, with one using 18 FODO cells per arc ('18x90' design) and the other one using 23 shorter cells per arc ('23x90' design). The latter is similar to the LHC arc design and offers an improved available aperture for injection from the current SPS at 450 GeV, but with the downside of the collision energy being lower by more than 1 TeV. For proton collisions, the design c.o.m. energy, assuming 16 T magnets, is 25.83 TeV for the '23x90' option and 27.24 TeV for the '18x90' option. For the studies in this chapter, the '23x90' arc design is assumed.

The arc dipole magnet design and dimensions are similar to the ones for the LHC (see Section 2.1.3) for both arc concepts, with the magnetic length being around 14 m. The main dipoles have the LHC two-aperture design and are cooled to 1.9 K by liquid helium. The same Nb_3Sn superconductor as the FCC-hh is planned to be used to achieve the required 16 T field (see Section 3.1.2). Unlike the FCC-hh dipoles, which are straight, the HE-LHC dipoles are assumed to be curved, with a bending radius of 2800 m, but the feasibility of this design is still pending validation. The baseline beam separation in the arcs of 250 mm is the same as in the FCC-hh and significantly larger than the 194 mm separation in the LHC.

While the beam energy in the HE-LHC is not as high as in the FCC-hh, SR emission is still a concern, with linear power of up to 5.5 $W\,m^{-1}$, compared to about 0.2 $W\,m^{-1}$ in the LHC [140]. To dissipate the power, the same beam screen design as the FCC-hh is used (see Fig. 3.2).

Thanks to the experience gained during the HL-LHC study [141], TCLDs were also foreseen early on in the HE-LHCs design process to protect the DS of the betatron collimation insertion from off-momentum losses coming from the warm straight sections. As covered in Section 2.1.5, the space required for the TCLD collimators that protect the DS of IR7 in the HL-LHC is achieved by replacing a nominal main dipole magnet with two shorter and stronger dipoles. For the HE-LHC, the dipole field is already at the foreseeable maximum, meaning that this strategy is not viable. In the HE-LHCs, the space for the TCLDs is instead achieved by moving magnets around and optimising the layout in the DS of the

collimation insertion [134, 142].

The baseline beam parameters such as emittance for the HE-LHC are taken to be the same as for HL-LHC, with suitable beams delivered by the injector chain following the LHC injector upgrade (LIU) [143]. The parameters are listed in Table 4.1.

Table 4.1: Summary of parameters for HE-LHC ion operation. The emittance and bunch populations are based on the HL-LHC [143].

Parameter	Value
Optics	Flat top
β^* [m]	10
No. of bunches k_b	1248
Ions per bunch N_b $[10^8]$	2.1
Beam particle	$^{208}Pb^{82+}$
Ion normalised emittance (ϵ_N) [µm]	0.993
Equivalent proton normalised emittance (ϵ_{Np}) [µm]	2.5
Energy (E) [TeV]	1107.0
Equivalent proton energy [TeV]	13.5
Energy / Nucleon (E / A) [TeV]	5.32

4.1.2 Collimation system

Like the injection options and arc optical configuration, the design of the HE-LHC collimation system is an active topic of study. The collimation system design is based on that of the LHC and the HL-LHC (see Section 2.1.5), with some key differences. As in the LHC, collimators are housed in two dedicated IRs, IR7 for betatron collimation and IR3 for off-momentum collimation. Each of these IRs includes a 3-stage collimation system - TCPs to intercept halo particles, TCSGs to capture particles out-scattered by the TCPs and TCLAs to stop the showers generated in collimators upstream. As in the LHC, there are also the TCTs foreseen to protect the experimental insertions and other collimators to absorb physics debris and protect against anomalous beam loss scenarios. There are two TCLDs collimators per beam foreseen for the IR7 DS to absorb off-momentum losses, as opposed to the single TCLD in the HL-LHC. For nominal proton beam operation, the collimation system must be able to safely handle a BLT of 12 min, which results in power loads of up to 1.8 MW, placing stringent requirements on the collimation system performance and robustness. The collimator design and the low-impedance collimator materials

would likely be the ones being developed for the HL-LHC [144, 145].

The optical functions in the collimation insertions are designed to be similar to the ones in the LHC (see Fig. 2.8), in order to preserve the collimator placements and phase advance between collimators. As element length scaling like in the FCC-hh is not possible due to the LEP/LHC tunnel constraints, making the optical functions the same would require roughly doubling the strength of magnets and hence would require superconducting magnets. With multi-MW power loads on the collimation system in IR7, this solution would be particularly challenging. Different options are currently being studied to optimise the optical functions and the magnetic element parameters and layout in the collimation insertions. The current optical functions, which are scaled from the LHC, for IR3 and IR7 are shown in Fig. 4.1.

The collimator sigma settings are also adopted from the HL-LHC [146]. At top energy, the HE-LHC TCP physical opening is 0.81 mm, smaller than the 1.1 mm opening of the HL-LHC TCP. Keeping the HL-LHC sigma settings for the TCLD collimators will result in a prohibitively small physical opening of ~ 0.8 mm , versus ~ 1.7 mm in the HL-LHC, and those settings are increased, without an impact on the cleaning efficiency [134]. The collimator settings are summarised in Table 4.2. Injection settings are not listed as multiple injection scenarios exist and collimation at injection is not studied. The materials listed are adopted from the LHC and used for the simulations presented, they may not correspond exactly to the materials that will ultimately be selected.

Table 4.2: Counts, materials and settings for collimators per beam in the HE-LHC [134]. The settings are for nominal proton beam operation at top energy and are based on the HL-LHC [146]. The sigma settings are hence expressed in the proton beam reference sigma, based on the normalised emittance of 2.5 µm. The materials are carbon-fibre composite (CFC) and tungsten heavy alloy (Inermet180).

Collimator	Count	Material	Setting (σ)
IR7 TCP	3	CFC	6.7
IR7 TCSG	11	CFC	9.1
IR7 TCLA	8	Inermet180	11.5
IR7 TCLD 1	2	Inermet180	18.1
IR7 TCLD 2	2	Inermet180	22.2
IR3 TCP	1	CFC	17.7
IR3 TCSG	4	CFC	21.3
IR3 TCLA	4	Inermet180	23.0
TCT	8	Inermet180	10.5

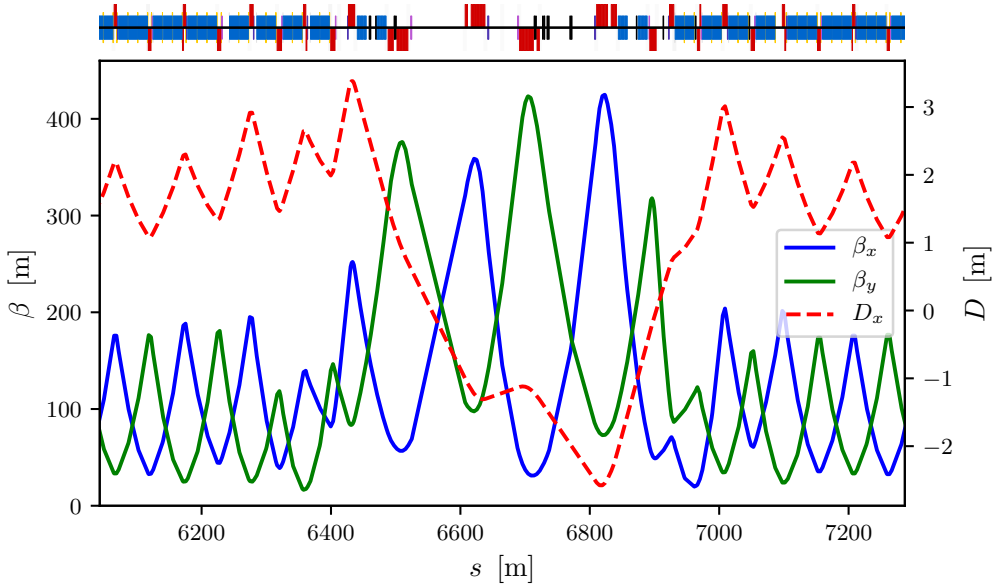

(a)

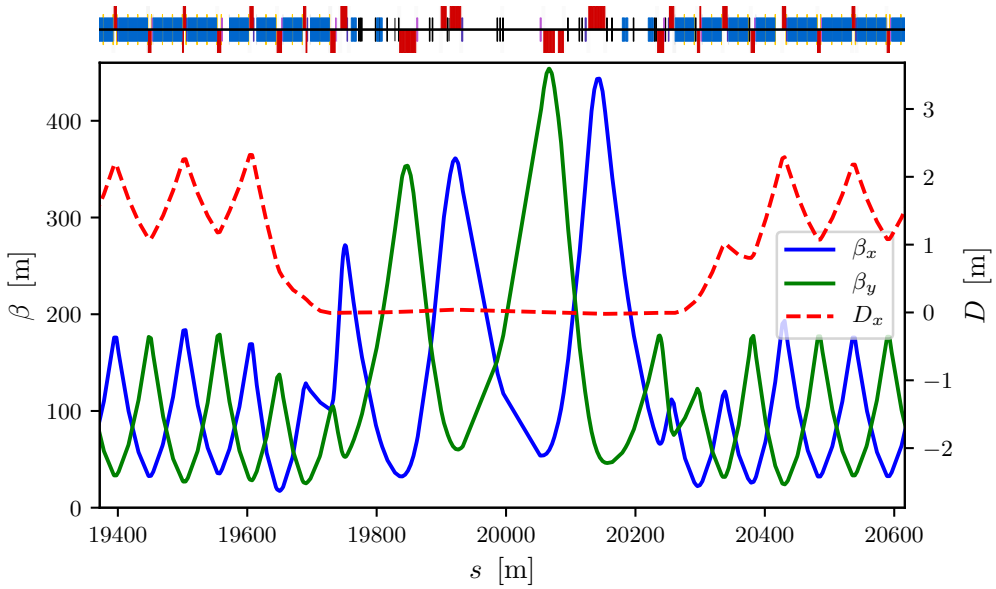

(b)

Figure 4.1: Optical functions in the HE-LHC collimation insertions—IR3 for off-momentum cleaning (a) and and IR7 for betatron cleaning (b). The plots depict the flat top regime for the 23x90 lattice option with integrated TCLD collimators.

The impact of the different optical functions, the different layout and the addition of the two TCLDs on the collimation cleaning efficiency must be carefully assessed.

4.2 Simulation setup

The goal of the HE-LHC studies herein is to characterise the collimation system performance for ion beams and quantify the benefits from the addition of TCLD collimators. The results presented in this chapter expand on the previous reports on the topic [147]. Only betatron collimation for B1H at top energy is studied. Two collimation configurations are considered, the nominal one and one without the TCLDs collimators included.

The workflow for the simulations follows the one employed for the FCC-hh ion collimation studies presented in Chapter 3. An impact parameter scan is performed first. The betatron cleaning studies are performed with the impact parameter value that results in the worst collimation performance.

The lattice model used is version 0.4 of the 23x90 design [148]. This lattice version does not feature a collision configuration and the studies presented are performed for the flat top configuration. Furthermore, the separation in the arcs is 204 mm (increased to 224 mm in IR7 by normal-conducting dog-leg dipoles), as opposed to the nominal 250 mm arc separation in the baseline HE-LHC design. The lattice includes the two TCLD collimators in the DS of IR7 and the associated layout changes.

The parameters used for the simulations are listed in Table 4.1. The crossing angle is set to zero in the simulations for simplicity, because it does not affect the local cleaning inefficiency in IR7.

The collimation settings for the simulations are the same as for the nominal proton beam settings listed in Table 4.2. Both the sigma settings and the physical openings are taken directly, under the assumption that geometric emittance is the same for the proton and ion beams. This assumption comes from the LHC and is discussed in Section 2.3. The normalised emittance used for ion beams is hence 0.993 µm, around 25 % lower than the baseline value of 1.3 µm. This choice of ion emittance simplifies the comparison between proton and ion collimation. The physical outcomes of the simulations depend on the mechanical openings of the collimators and changing the notation to using the baseline ion normalised emittance can be achieved by simply scaling the sigma settings of the collimators for ion beam operation.

The simulation model is an early prototype, used mainly to study the collimation efficiency in IR7 following the addition of TCLDs, and is lacking some collimation features in the full ring. It includes all of the collimators in IR3 and IR7, but does not include all of the TCT collimators or the collimators in the extraction region IR6. The only TCT collimators included are the horizontal and vertical ones in IR2 and the horizontal one in IR8. The layout and physical openings of the collimators in IR7 is depicted in Fig. 4.2. For detail on the betatron collimation stages, including TCLDs, see the FCC-hh collimation system diagram in Fig. 3.4.

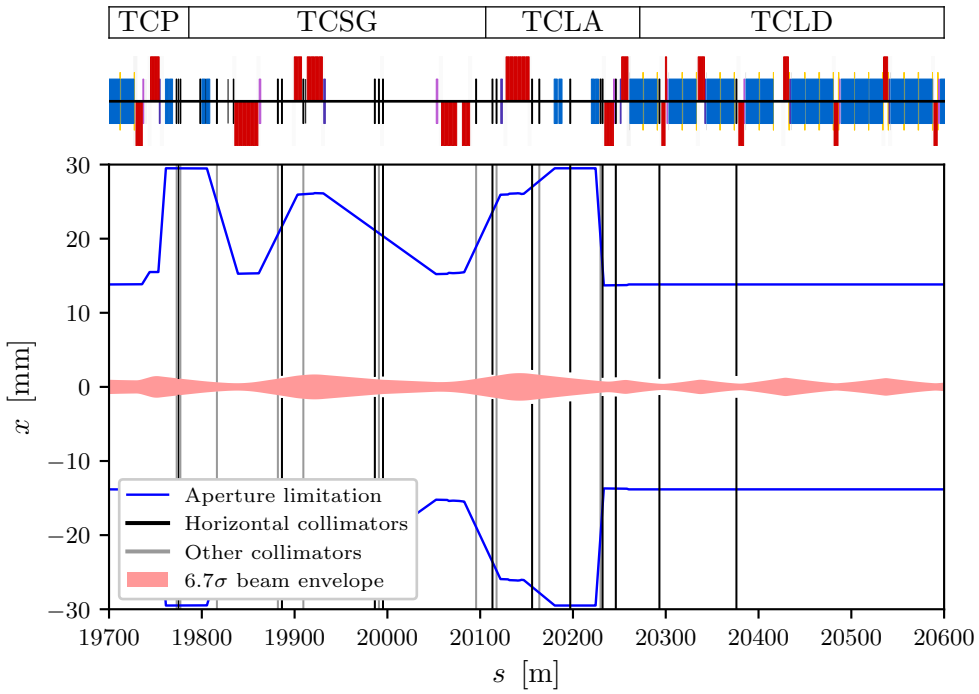

Figure 4.2: Layout of the collimators in the horizontal plane of the HE-LHC IR7 showing the placement and physical opening. The regions corresponding to the different stages in the collimation hierarchy are labelled. The vertical and skew collimators are shown as continuous grey bars. The horizontal aperture limitation is overlaid (blue) and a beam betatron envelope touching the TCP is depicted (red).

The collimation studies are performed using the SixTrack-FLUKA coupling framework, using the procedure described in Section 2.3.4. The simulations are performed for an ideal machine with no optical or collimator imperfections. The kinetic energy cuts are 1 TeV/nucleon, and only proton and ion fragments are tracked in the ring, like for the FCC-hh simulations in Chapter 3. The cleaning inefficiency notation is also the same as for the FCC-hh, with the loss maps normalised to total energy lost in the ring, as per

Eq. (2.4).

For collimation at top energy, the estimated quench limit in terms of cleaning inefficiency for Pb-ion beams is $\eta_{\max} = 2 \times 10^{-4}\,\mathrm{m}^{-1}$. The value is based on the preliminary energy deposition quench limit for Nb_3Sn of $70\,\mathrm{mW\,cm}^{-3}$ (see Section 3.1.2); the beam energy and intensity from Table 4.1; a BLT of 12 min; and the energy deposition per lost ion.

4.3 Results

4.3.1 Impact parameter scan

Ion collimation simulations are sensitive to the choice of impact parameter, as discussed in Section 2.3. An impact parameter scan is performed for B1H betatron collimation at top energy to determine the value, which results in the worst collimation cleaning efficiency. The selection criteria are the losses on the cold aperture in the IR7 DS in the region $s = 20\,250 - 20\,550\,\mathrm{m}$. Unlike for the FCC-hh impact parameter scan discussed in Section 3.3.1, the TCLD collimators are not removed for the scan. This choice does not allow for a direct comparison of the impact parameter with the LHC, where TCLD collimators are not present, but provides a better picture for the performance of the nominal HE-LHC collimation system.

For the scan, 6 impact parameter values in the range 100 nm to 5 µm are tested, with 1.2×10^6 primary ions simulated at every step for 200 turns. The results are shown in Fig. 4.3.

The impact parameter that results in the maximum integrated losses in the IR7 DS is 1 µm, which is the same as for the LHC and larger than the 0.1 µm value found for the FCC-hh. This value is used for the betatron collimation simulations at top energy. For future studies, it is suggested that the impact parameter scan is repeated without the TCLDs to investigate the differences and compare with the LHC on equal footing. The scan should also be repeated for the vertical plane and for Beam 2.

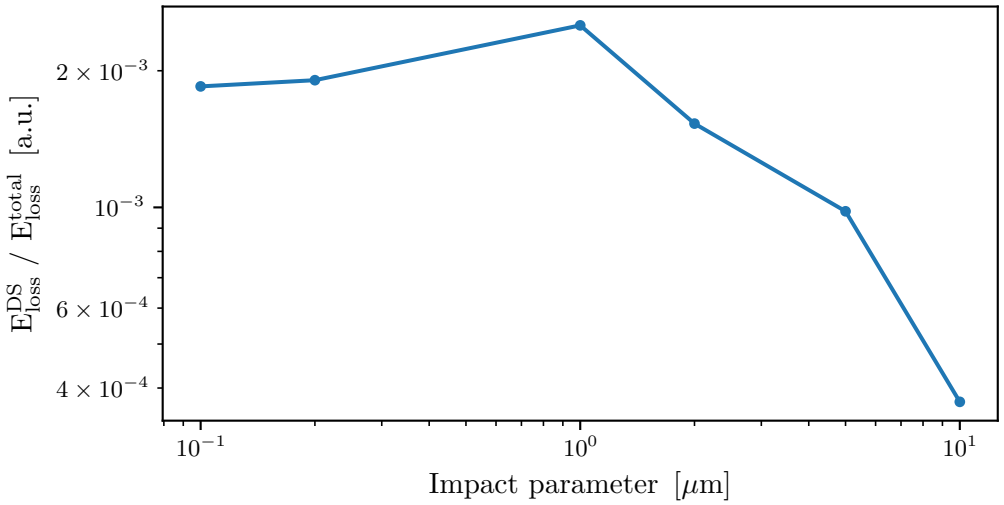

Figure 4.3: Impact parameter scan for a $^{208}Pb^{82+}$ ion beam at top energy incident on the horizontal primary collimator. The aperture losses are integrated over the IR7 DS region, $s = 20\,250 - 20\,550$ m and normalised to the total energy lost in the simulation.

4.3.2 Betatron cleaning at top energy

The betatron cleaning simulations are performed for B1H at top energy. Two collimation configurations are considered, one including and one excluding the TCLD collimators. For each case, 1.2×10^6 primary ions are tracked for 200 turns. The simulated loss maps for the full ring are shown in Fig. 4.4 and IR7 is shown in detail in Fig. 4.5.

Results for the nominal collimator configuration, with the TCLDs included, are shown in the top plot of Fig. 4.4. The majority of recorded losses appear on collimators in IR3 and IR7, with some collimator losses on the TCT in IR2. Compared with the loss maps for the LHC in Fig. 2.26 and the FCC-hh in Fig. 3.7, the collimator loss cluster in the extraction region IR6 (IRD for the FCC-hh) is missing. This is because the TCDQ collimator is not included in the HE-LHC model. Furthermore, not all TCT collimators are included in the model, resulting in a lack of losses around the experimental insertions.

The cold losses are mostly concentrated in the DS downstream of the collimation insertions IR3 and IR7, with no notable loss peaks appearing in the rest of the ring, which is a promising result. The losses in the DS in IR3 are well below the estimated quench limit and are considered tolerable, but the losses in IR7 (top plot of Fig. 4.5) are more significant.

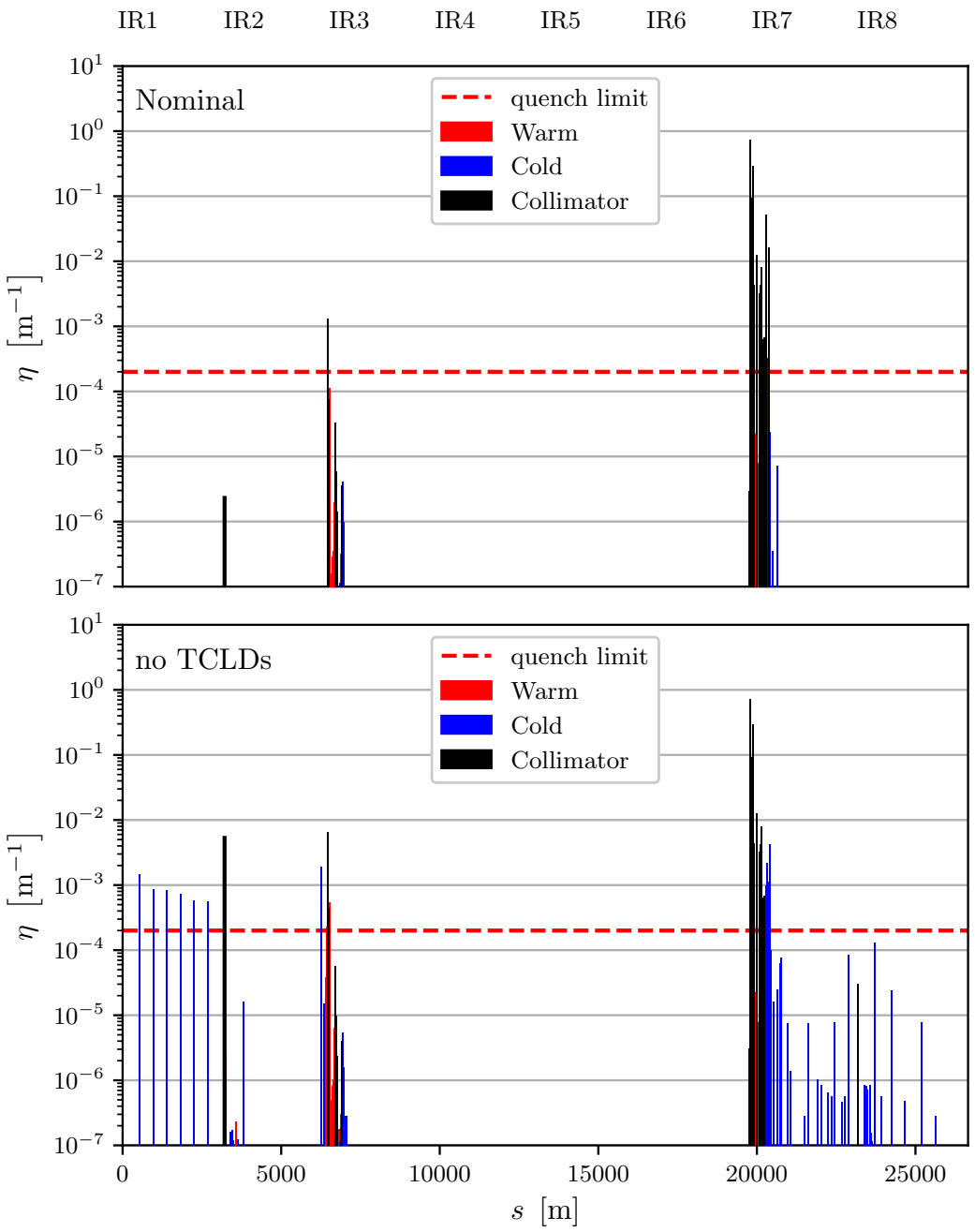

Figure 4.4: Comparison of HE-LHC betatron loss maps for B1H at top energy with the nominal collimator configuration (top) and with the TCLD collimators removed (bottom). The estimated quench limit is depicted on both plots as a horizontal red line.

The two TCLD collimators successfully intercept the majority of the fragments coming from the warm section and suffer some of the largest power loads as a result, with losses exceeding those in the TCLAs and some of the TCSGs.

Despite the good TCLD performance, there are two cold loss clusters appearing slightly above the estimated quench limit, one upstream of the first TCLD and one downstream. The maximum cleaning inefficiency for the cold losses is $3.2 \times 10^{-4}\,\mathrm{m}^{-1}$, occurring in cell 9 of the IR7 DS, while the quench limit is estimated as $2 \times 10^{-4}\,\mathrm{m}^{-1}$. A detailed analysis of the losses in the DS of IR7 is presented in Section 4.3.3.

The simulation results for the case where the TCLDs are removed are shown in the bottom plots of Fig. 4.4 and Fig. 4.5. In this configuration, there is a dramatic increase in losses around the full ring. Numerous loss clusters, exceeding the estimated quench limit by approximately an order of magnitude, are found not only in the DS of IR7, but also in the arc upstream of IR2 and immediately upstream of IR3. The relative magnitude and structure of the cold loss clusters in the IR7 DS are similar to the LHC and significantly larger than for the FCC-hh without TCLDs. The beam energy in the HE-LHC is nearly double that of the LHC, but the optical functions in the collimation insertions are similar, as covered in Section 4.1.2, indicating a possible explanation of the similar loss profiles observed. Further studies are required to explore the connection between the beam energy, the optical functions and the distribution of losses from collimation.

4.3.3 Analysis of the IR7 DS losses

The losses on superconducting elements in the DS of IR7 are analysed in detail to determine the distribution, composition and origin of the lost particles. The goal is to identify potential mitigation strategies. Only losses in the region $s = 22\,250 - 22\,500\,\mathrm{m}$ are considered for the analysis. The loss map for this region is shown in Fig. 4.6.

There are three main loss clusters observed, DS1 in cell 8, DS2 in cell 9 and DS3 in cell 11. Two of the clusters are found to be above the estimated quench limit, DS1 exceeding it by 25 % and DS2 exceeding it by 50 %. The DS1 cluster is of particular concern, as it appears upstream of the first TCLD and will not be affected by changing the settings of that collimator. The phase space distribution of the particles lost on the aperture, their particle species fractions and the collimators where they were produced are shown Fig. 4.7.

From Fig. 4.7a, it can be observed that losses have a broad range of energies and occur on all sides of the aperture in the DS. The majority of impacts occur on the inside of the ring

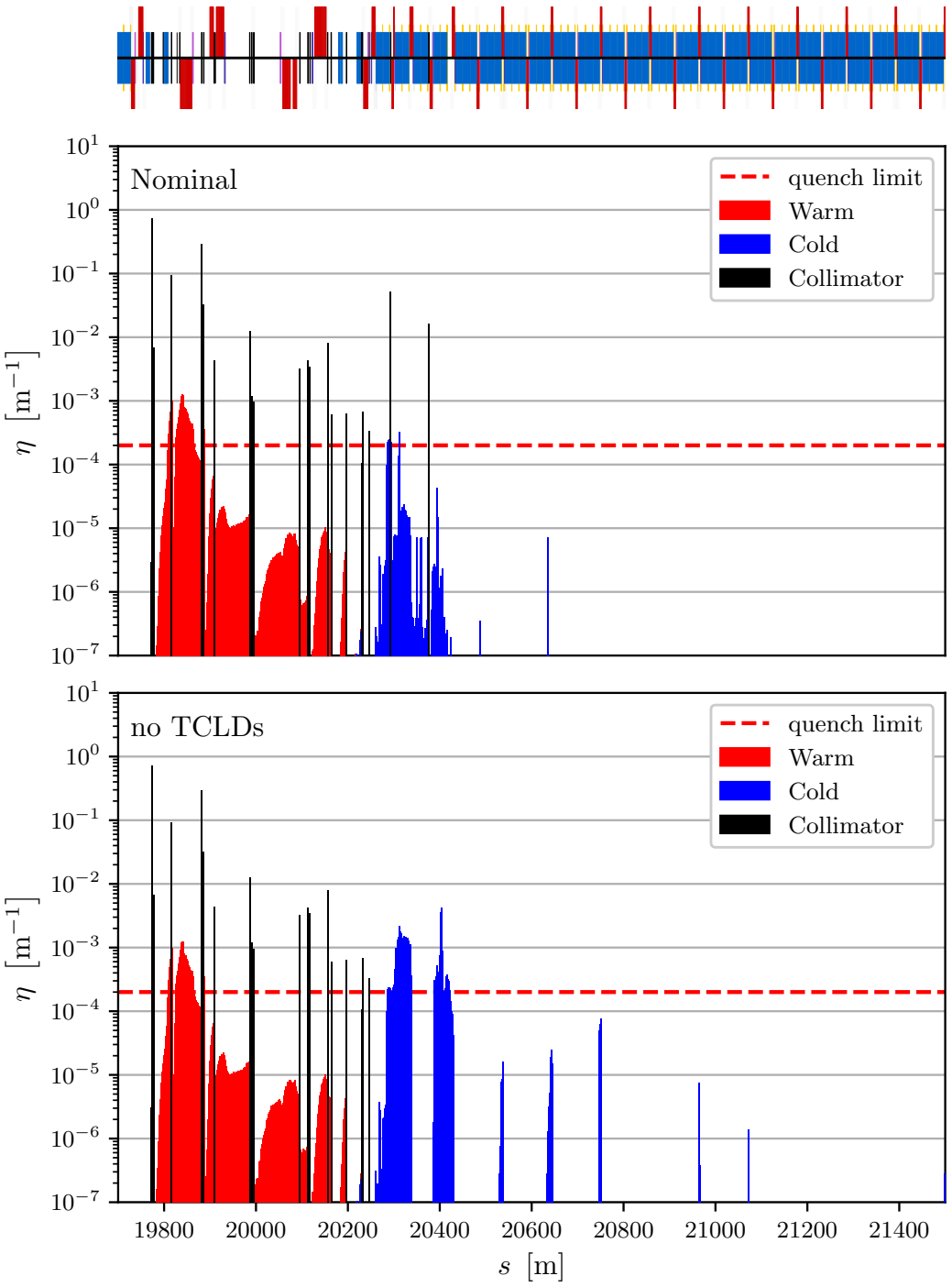

Figure 4.5: Zoomed-in view of the loss maps in Fig. 4.4, showing the losses in IR7 in detail. The top simulation includes the TCLD collimators, while the bottom one excludes them.

(negative x), indicating the magnetic rigidity of the particles lost there is predominantly lower than the nominal. A broad distribution of ion species in the DS losses can be observed in Fig. 4.7b, covering the range $A = 2-203$. Light ion species have the largest contribution to the losses, with fragments having $A < 6$ accounting for 76 % of the deposited energy.

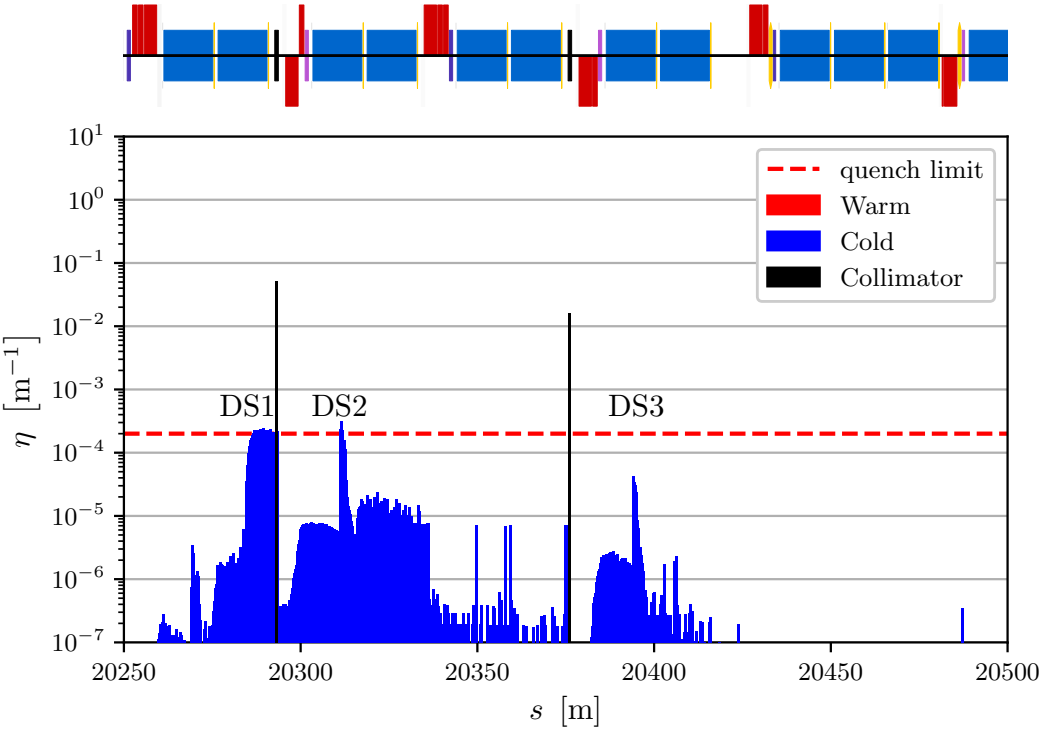

Figure 4.6: Extract from the loss map in Fig. 4.4, showing the IR7 dispersion suppressor region. The three main cold loss clusters are marked as DS1, DS2 and DS3. The two black bars are the TCLDs

It can also be observed that the fragments lost on the aperture in the DS originate in collimators across the whole hierarchy. The losses are dominated by fragments coming from the primary collimator (TCP.C6L7.B1) and the first DS collimator (TCLD.8R7.B1). This is in contrast with the FCC-hh, where only fragments from the TCLD collimators contribute to the losses in the DS, as observed in Fig. 3.9b. Further analysis reveals that the DS1 cluster is dominated by light ion fragments coming from the horizontal TCP and the DS2 cluster is dominated by secondary ions and protons out-scattered by the upstream TCLD.

The results indicate that the collimation system, with settings optimised for protons, is generally effective, with no cold loss hot spots identified outside of the DS of IR7. The betatron collimation system in IR7 successfully prevents the nominal $^{208}\mathrm{Pb}^{82+}$ ions in the halo, as well as the heaviest EMD fragments, namely $^{207}\mathrm{Pb}^{82+}$ and $^{206}\mathrm{Pb}^{82+}$, from reaching the aperture in the DS. However, it does not absorb the lighter ion fragments produced in the warm section, and two cold loss clusters are found that exceed the quench limit. This is not expected to be a critical limitation for heavy-ion operation in the HE-LHC, because

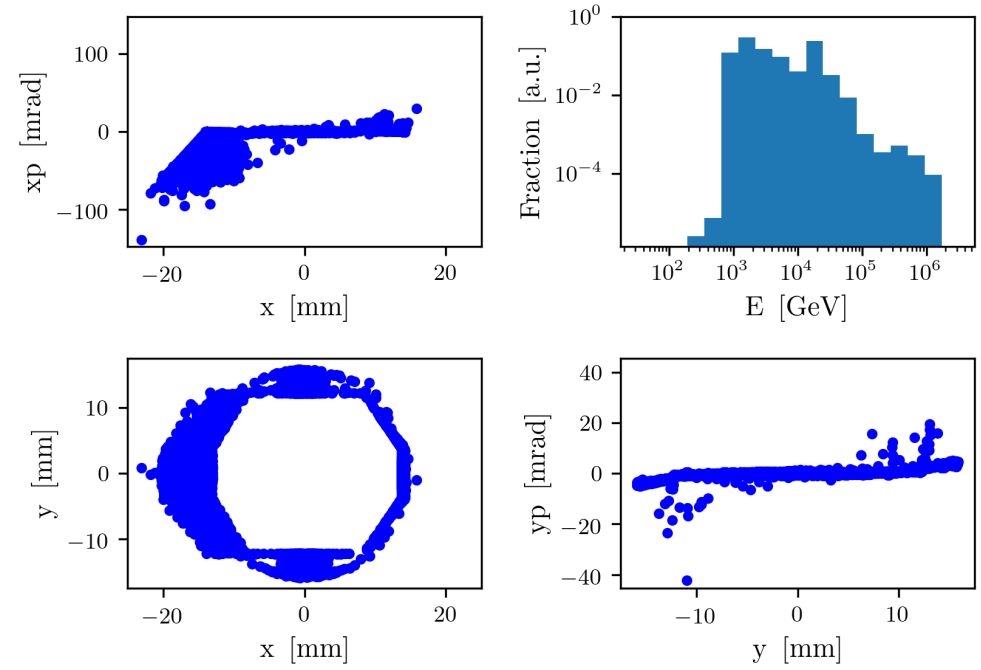

(a)

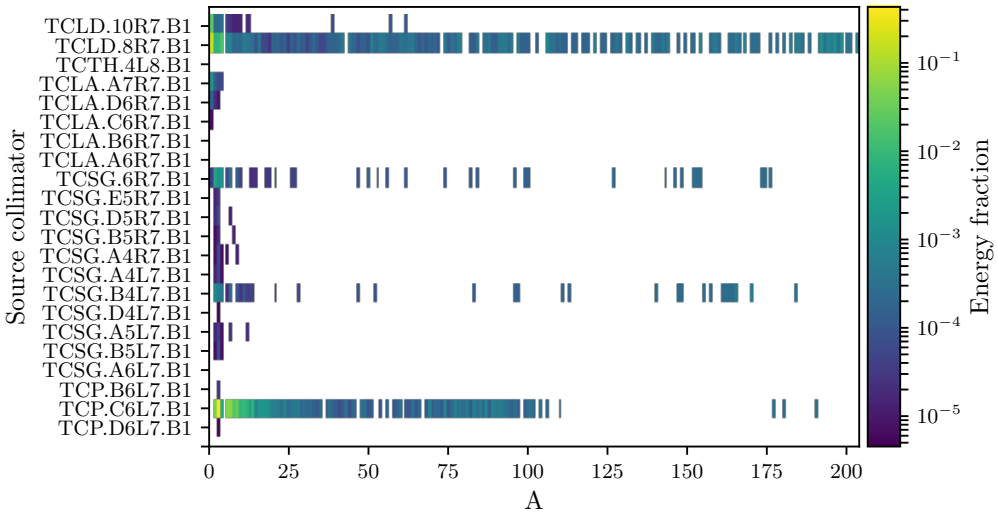

(b)

Figure 4.7: Distribution of aperture losses in the DS of IR7 ($s = 20\,250 - 20\,500\,\mathrm{m}$) for HE-LHC B1H betatron collimation at top energy. Losses on collimators are not included. The top 4 plots (a) show the phase-space distribution of the losses. The bottom plot (b) shows the distribution of energy between the different isotope species in the losses and the collimator where the lost particle was produced. Collimators in IR7 are listed in (b) in the order they are reached by the beam. The histogram of A for the aperture losses is weighted by the energy of the lost particle, normalised to the total energy lost in the DS for the colour scale.

the observed excess of losses is not significant, even though the collimation configuration has not been optimised for ion beams. Future studies including optical and collimator imperfections are required to gain better understanding of the collimation beam losses. In addition to this, energy deposition studies are also necessary, in order to assess the quench risk to the superconducting magnets from the beam losses and the showers leaking from TCLD collimators. Furthermore, the quench limit assumed is preliminary and likely pessimistic, with further studies ongoing to establish a more realistic value.

4.3.4 Loss mitigation strategies

Depending on the outcome of the energy deposition studies and the estimates of the quench limit, it may be necessary to implement mitigation strategies to reduce the losses in the DS of IR7. There are several loss mitigation strategies being considered.

Since it is found that the losses in the DS have large contributions from fragments produced in the TCP, an optimisation of the openings for the TCSG and TCLA collimators is being considered. Tightening the collimator hierarchy may intercept more of the secondary particles before they escape the warm section. Reducing the retraction of the collimators requires an investigation of what the allowed limits are, because of the impedance limit and the sensitivity to orbit and optical function drifts, as well as the finite alignment precision of the collimators. There must be a minimum relative retraction between the different collimation stages to ensure that the TCPs are the first impacted stage, even in the case of orbit fluctuations or collimator misalignments [149,150]. In addition to this, the impedance budget must also be considered, as reducing the collimator gaps increases the impedance and the collimators are already have the largest contribution to the impedance at top energy in the HE-LHC [134].

For the DS1 cluster, upstream of the first TCLD, future studies should establish from which jaw of the TCP the lost particles originate. If the losses are dominated by only one of the jaws, that jaw can be retracted further, making the TCP opening asymmetric. Such asymmetric TCP settings were used in the 2018 LHC heavy-ion operation to alleviate a loss hot spot in IR2 [102].

Another potential mitigation strategy for the DS1 cluster is implementing an orbit bump

in IR7 to move the losses from the aperture onto the TCLD. Orbit bumps are used in the LHC experimental IRs, during heavy-ion operation, to direct secondary beams from EMD and BFPP interactions at the IP onto the missing dipoles connection cryostat in the DS, away from the superconducting magnet coils [24]. Unlike the EMD and BFPP losses in the LHC, the losses in the HE-LHC IR7 DS are not secondary beams of identical particles, which complicates the orbit bump approach. A study for a potential orbit bump loss mitigation for the LHC IR7 has not been found promising, due to the broad spectrum of the losses there [21]. The HE-LHC has the TCLDs and this is a potential benefit for the orbit bump approach as losses can potentially be shifted from the aperture onto the collimators. Preliminary investigation suggest that an orbit bump of around 3 mm may be sufficient to reduce the losses in the problematic DS1 cluster to below the quench limit, but a more detailed analysis should be carried out to confirm the effect and feasibility of such a bump. As seen in Fig. 4.7a, losses occur on both sides of the horizontal aperture and it must also be investigated if moving the losses away from one side of the aperture will be negated by an increase in losses on the other.

The DS2 cluster is found to be dominated by secondary ions and protons out-scattered by the upstream TCLD and can potentially be influenced by changing the settings of the TCLD. The incidence angle and impact parameter of lost particles on the TCLD must be recorded in order to determine if reducing the retraction will reduce the secondary particle leakage. Alternatively, an increase of the active length of the collimator can be considered. The power load on the collimator and the space constraints of the lattice are the key considerations for this approach.

Finally, if the other mitigation strategies do not prove effective, a change of the TCLD locations can be considered. Due to the impact on the layout and the optical functions, this approach should be considered a last resort.

4.3.5 Conclusion

The first studies of collimation system performance for Pb ion beam operation in the HE-LHC have been carried out. For betatron collimation at top energy, the collimation system designed and optimised for protons was found to be generally effective and almost no losses

occur outside of the collimation insertions. In particular, the aperture of the arcs and the experimental insertions was not found to suffer any significant losses, in spite of the very challenging conditions with almost 50 MJ of stored beam energy and a much lower cleaning efficiency than for proton beams.

The only part of the ring that sustains notable cold losses was observed to be the DS of the betatron collimation insertion. Two large loss clusters on either side of a TCLD collimator in cell 8 have been identified with magnitudes exceeding estimated quench limit by up to 50 %. The upstream cluster is found to be dominated by light fragments originating in the horizontal TCP, while the peak of the downstream cluster results from secondary ion fragments protons out-scattered by the TCLD collimator itself. A comprehensive energy deposition study is needed to fully evaluate the quench risk from those losses. An investigation of mitigation strategies that can reduce the losses is currently ongoing, with a tighter collimation hierarchy, an orbit bump, and a longer TCLD collimator being considered.

Chapter 5

Partially stripped ion beam collimation

One of the topics of increasing interest in accelerator physics are partially stripped ions (PSI). In contrast to the fully stripped ions that have been used in nucleus-nucleus colliders and in other applications, PSI are incompletely ionised and retain some of their bound electrons. The presence of the bound electrons alters the way PSI interact with matter and EM-fields, which has interesting applications.

Ions with intermediate ionisation states have been used in accelerators for a long time [151] and are essential in the ion injector chains for the LHC [152] and RHIC [153]. The ionisation state defines an important quantity for ion beams, the charge-to-mass ratio $(Q/A)^{\dagger}$, which is related to the magnetic rigidity $(B\rho)$ of the beam. In general, ions with a lower Q/A allow for a higher source intensity, but also require stronger magnetic fields to steer. The selection of the Q/A ratio for an acceleration stage is hence driven by the compromise between the available intensity from the ion source and the achievable magnetic field in the accelerator [154]. The charge state is often modified in the transfer lines between the different accelerator stages in the injector chain by using stripping foils to remove electrons, at the cost of intensity. This approach allows for fully stripped ions at the appropriate energy to be injected into the final stage for use in collisions.

In recent years, projects such as the Facility for Antiproton and Ion Research (FAIR) at GSI (Germany) [155, 156] and the Gamma Factory initiative at CERN (Switzerland) [157]

[†]The charge $Q = Z - n$, where Z is the atomic number and n is the number of bound electrons

have motivated further studies into the aspects of accelerating and storing of PSI beams. The FAIR facility features a complex chain of acceleration and storage stages that cover 10 orders of magnitude in kinetic energy and allow for a variety of beam particles, from antiprotons to highly-charged heavy-ions. Some of the stages, such as the High Energy Storage Ring (HESR) are envisaged to operate with PSI beams in the energy range 400 MeV/u[‡] to 5 GeV/u. On the other hand, the Gamma Factory, covered in more detail in Section 5.3, proposes using PSI in the LHC as a driver for a new type of high-energy, high-intensity light source, with expected performance surpassing the one of the available free electron laser (FEL) light sources.

While the bound electrons in PSI enable interactions of interest, it also makes them more difficult to accelerate and store. In particular, interactions of the PSI with residual gas in an accelerator can change their charge state, while leaving an intact ion with a minimal change in the total energy. This leads to beam losses due to the altered magnetic rigidity of the resulting fully stripped ions. For example, in the CERN SPS, the lifetime of PSI is mainly limited by electron stripping in residual gas interactions [158]. Interactions of PSI with solid material in the beamline, such as collimators, can also have a profound effect on the beam losses, as discussed in Section 5.3.

Accurate predictions of the lifetime of PSI beam are essential for characterising the available intensity and the beam losses in an accelerator. Estimates of the beam lifetime and the performance of stripping foils are generally performed using dedicated simulation tools [159–161]. Interactions involving PSI particles are not readily handled by the established Monte Carlo physical interaction simulation frameworks, Geant4 and FLUKA in particular. Some studies of interest, like beam collimation, require a combination of tracking and in-flight interactions of the beam particles. Additional developments are hence required to allow such studies for PSI beams.

This chapter covers the first attempt of including comprehensive support for PSI in BDSIM and Geant4, thus enabling integrated radiation transport studies for PSI beams. The physical interactions of PSI with matter are discussed in Section 5.1.1. The implementation of a physical process that handles electron stripping for PSI in BDSIM is presented in Section 5.1. Finally, a study of PSI beam collimation in the LHC, in the context of the

[‡]Where u is the atomic mass unit

Gamma Factory initiative, is presented in Section 5.3.

5.1 Ion charge-changing interaction model in BDSIM

5.1.1 Ion charge-changing interaction model

The ions in a beam, traversing a medium made of neutral atoms, can undergo a broad range of ion-atom and electron-ion interactions. The material ionisation, projectile scattering, nuclear and photo-nuclear interactions are discussed in Section 1.2. In addition to those, the projectile ions can undergo charge-changing interactions, namely electron loss and electron capture. Electron loss processes include single or multiple ionisation of the projectile ion, while electron capture processes include single or multiple recombination. Both types of processes lead to a discrete change in the charge state Q of the projectile ion.

During the passage of a heavy-ion beam with a certain charge state through matter, beam ions interact with the target atoms, resulting in the formation of charge-state ion fractions $F_{\mathrm{Q}}(x)$ with different charge states Q and individual evolutions as a function of the penetration depth (target thickness) x. For very large x, a balance between the electron loss and electron capture processes is achieved and the charge-state fractions become independent of x. The charge state fractions at the equilibrium are known as equilibrium ion fractions [26].

The charge-changing processes are complex interactions that depend on the species, energy and charge state of the projectile ion, as well as on the traversed medium composition, parameters and density. The theoretical framework of these processes is still under development and for interactions like electron loss, there is no single theoretical model that covers the full kinetic energy range. The evaluation of charge-changing cross-sections and equilibrium ion fractions hence requires complex and computationally challenging calculations with different software tools, depending on the specific configuration [162].

The inclusion of the complete charge-changing cross-section calculations into a Monte Carlo physics library like Geant4 is not feasible, due to their computational complexity, and simplified models are sought for this purpose. Semi-empirical models are a good candidate

for integration in the Monte Carlo tools, because they provide a parameterised formulation of the cross-section, which can be efficiently and repeatedly evaluated during the simulation execution.

A semi-empirical formula for single electron loss cross-section is available as [163]:

$$\sigma\left[\frac{\mathrm{cm}^2}{\mathrm{atom}}\right] = 0.88\times10^{-16}(Z_T+1)^2\frac{u}{u^2+3.5}\left(\frac{Ry}{I_1}\right)^{1+0.01\mathrm{Q}}\left(4+\frac{1.31}{n_0}\ln\left(4u+1\right)\right), \tag{5.1}$$

$$u = \frac{(\beta c)^2}{I_1/Ry},$$

where Q and β are the projectile charge and relativistic factor, $c = 137$ is the speed of light in atomic units, I_1 is the projectile first ionisation energy in units of Ry, u is the reduced projectile energy, n_0 is the principal quantum number of the outermost shell and Z_T is the atomic number of the target.

As discussed in [163], the formula Eq. (5.1) is valid for heavy, many-electron ions and arbitrary target materials and is applicable over a broad energy range, including the relativistic domain, with the expected accuracy being around factor 2 for high projectile energies ($u > 2$). This study is primarily interested in the ultra-relativistic regime ($E > 10\,\mathrm{GeV/u}$), where the electron capture and multi-electron processes are suppressed [162], meaning that the equilibrium charge state is a bare nucleus and the dominant charge-changing process is single electron loss. Because of this, Eq. (5.1) alone is expected to provide an adequate treatment for in-flight interactions of PSI in this regime.

It should be noted that in solid targets, the electron loss cross-section is further enhanced by the so-called target density effect. The increase can be of up to a factor 1.5-2 [26], but is not taken into account by Eq. (5.1). Future developments should aim to introduce the density effect correction in the electron loss cross-section calculations.

In the future, it would also be of interest to add semi-empirical models for single electron capture, as well as multi-electron interactions, which would improve the accuracy of the charge-changing interaction model for intermediate and low energies. For specific cases that

are outside of the validity range of the model, or for cases where high accuracy is required, it is possible to also extend the model with tabulated cross-section data, calculated with the advanced tools mentioned previously.

5.2 Model implementation in BDSIM

The aim of the work presented in this chapter is to introduce support for PSI beams in integrated radiation transport simulations. There are several key ingredients for achieving this goal:

- Capability of defining beam ion particles with bound electrons.
- Correct tracking based on the charge state of the ion.
- Physical interactions models that deal with the bound electrons.
- Integration with the other physical interaction models.

The first two requirements are already fulfilled by the Geant4 physics library. Geant4 allows PSI beams to be defined, provides facilities to manipulate the electron occupancy of individual particles and performs tracking based on the charge state. However, it does not currently include physical interaction models that handle in-flight interactions involving the bound electrons.

Because of the modular, open-source, object-oriented design of Geant4, it is possible for users to implement additional interaction models and use them alongside the existing ones. A physics process that handles single electron stripping for PSI, herein the 'PSI stripping process', is implemented as an extension to Geant4. BDSIM is chosen for the process implementation because it provides a full integration with the Geant4 class library and offers some additional benefits. BDSIM features a build system, modular physics lists and model design utilities that help the development and testing of new physics processes. The PSI stripping process is built upon the Geant4's physics processes interfaces, ensuring that the implementation is consistent and the model can potentially be a candidate feature for a later Geant4 release.

The process is implemented in a BDSIM class `BDSProcessIonStripping`, which is derived from the `G4VDiscreteProcess` base class in Geant4. The BDSIM class implements the `GetMeanFreePath` method to compute the electron stripping cross-section and determine a physical interaction length, and the `PostStepDoIt` method to handle electron removal from the projectile ion when the process is triggered. The process is registered with the `G4ProcessManager` for particles in the `G4Ions` group, including `G4GenericIon`.

The cross-section computation uses the semi-empirical formula Eq. (5.1) to compute the electron stripping cross-section for eligible beam particles and target materials. The criterion for process activation is a projectile ion with at least one bound electron. At the input stage, the beam particle definition requires the atomic number Z, the mass number A and the charge Q. The difference between the Z and Q is used to determine the electron occupancy. Ion parameters such as mass, ionisation energy and electron shell configuration are dynamically evaluated using internal tables in Geant4. The ion is assumed to be in the ground state when populating the electron shells. It should be noted that all bound electrons are neglected and discarded during any inelastic interaction of the beam ion. The stripping cross-section is evaluated for every material traversed by the beam, with the material parameters taken from the Geant4 defintion. In the case of mixture material, the Bragg additivity rule [164] is used to combine the cross-sections for the different elements in the mixture. An example of the cross-section calculated by the process is shown in Fig. 5.1.

A mean free path (MFP) for the beam ion in the material is calculated from the cross-section,

$$\lambda = \frac{1}{n\sigma}, \tag{5.2}$$

with n denoting the number density of the medium and σ denoting the process cross-section. The Geant4 Monte-Carlo routines use the MFP to compute interaction distances for individual particles. For the interaction distance, Geant4 uses the number of MFPs traversed in the medium [165],

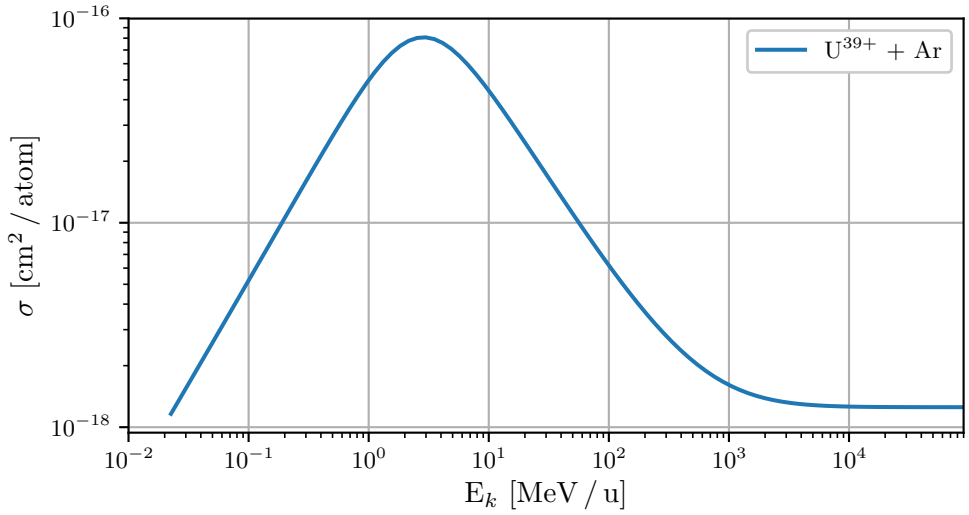

Figure 5.1: Cross-section of uranium ions with 53 electrons on an argon gas target obtained from the electron stripping physics process in BDSIM. The ion parameters such as charge, mass and electron binding energies are obtained from the internal tables in Geant4. The material is from the Geant4 predefined material database. The cross-section estimation agrees well with published results for the semi-empirical stripping model [163]

$$n_\lambda = \int_{x1}^{x2} \frac{dx}{\lambda x}, \tag{5.3}$$

where x is the distance traversed in the medium and λ is the MFP. This formulation is used because it is independent of the material being traversed. The number of mean free paths travelled, n_r, is a random variable obeying the distribution,

$$P(n_r < n_\lambda) = 1 - e^{-n_\lambda}. \tag{5.4}$$

For every particle and process, the number of mean free paths is initialised as $n_\lambda = -\log(\eta)$, where $\eta = \text{unif}(0, 1)$. During the processing of an individual particle in the simulation, the interaction distances for all registered processes are evaluated, the process with the smallest n_λ is triggered and the particle is advanced by this distance. After each step Δx taken, n_λ is updated as,

$$n'_\lambda = n_\lambda - \Delta x. \tag{5.5}$$

This ensures that processes with a shorter MFP will not prevent processes with longer MFP from being triggered.

When the PSI stripping process is triggered, a single electron is removed from the outermost populated shell. In the scope of this work, only the charge change of the projectile ion is of interest and the process is simplified by disregarding the kinematics of the interaction. The interacted ion is emitted with the same momentum as the incident ion and no secondary electron is produced. In future developments, the kinematics will be included in order to ensure momentum conservation and enable studies involving the secondary electrons.

The final requirement is the integration of the PSI stripping process into the existing Geant4 physics process framework. The evaluation order of processes at every step is important. For example, transportation (no physical interaction) should occur last, and MSC should occur second to last. The stripping process is registered with the Geant4 processes manager, which governs multi-process simulations. The integration of the process into Geant4 also enables the application of the Geant4 process biasing mechanics. This can be beneficial for study cases with low rates for interactions of interest, such as beam-gas studies.

In order to ensure full compatibility with the existing physics process, an additional step was necessary. Currently, the target ionisation model in Geant4 enforces a charge equilibrium between the projectile ion and the traversed medium by re-setting the electron occupancy of the projectile ion. In order to retain the electron occupancy when target ionisation is enabled, the responsible physics process in Geant4, `G4IonIonisation`, was wrapped in a BDSIM process, `BDSProcessIonIonisation`, that re-assigns the electrons in the final state. This approach solves the problem of erroneous electron removal and does not involve any changes in the Geant4 code base, improving the PSI stripping process portability. However, the electrons will normally contribute to the effective charge of the ion traversing a medium and may impact the outcomes of the target ionisation. In the future, it would be of interest to explore more advanced methods of handling target ionisation for PSI beam particles in Geant4.

In order to test the stripping process, a simple toy-model beamline made up of two 3 m long, 1 rad bending angle dipoles, separated by a 1 m-long drift is prepared. In the middle of the drift is a 50 µm-thick carbon foil ($\rho = 2\,\mathrm{g\,cm^{-3}}$). A beam of 450 GeV/Q $^{208}\mathrm{Pb}^{79+}$ ions, with

no transverse or longitudinal distribution , on the reference orbit is used. A visualisation of the ion trajectories before and after the stripping foil, with only the stripping process activated, can be seen in Fig. 5.2. The action of the foil produces a distribution of charge states in the emerging beam. The different charge states have different magnetic rigidities and the downstream dipole separates out their trajectories, demonstrating the tracking of different PSI species.

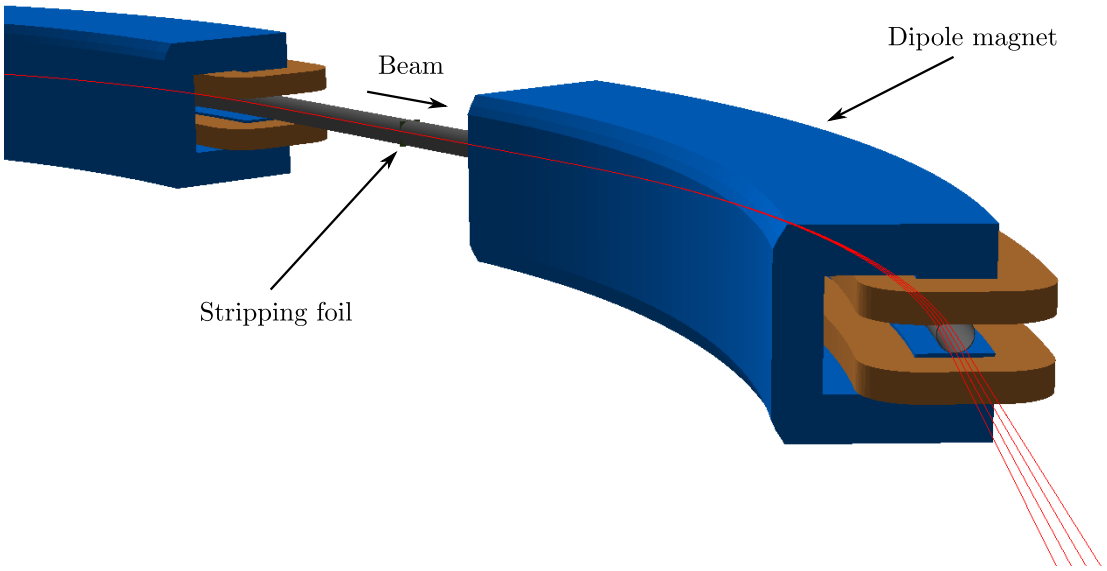

Figure 5.2: Visualisation of PSI tracking in bending magnets before and after a stripping foil in BDSIM. The trajectories of the tracked ions are depicted as red lines. It can be observed that after the stripping foil, the trajectories of ions with different charge states are separated out by the second dipole. The stripping process is the only enabled physics process for this case.

The distribution of secondary particles after the foil was also compared between the case of only stripping processes and the case of a complete set of physics processes, in order to test the compatibility of the stripping process with the existing processes in Geant4. For this case, the standard set of physics processes for ion beams, including hadronic elastic, hadronic inelastic, EM and EMD interactions was enabled.

In both cases, 4 different charge states of the primary ion can be observed, from nominal to fully ionised, and their recorded fractions are similar. In the multi-process case, a variety of other particle species are also found in the spectrum of secondary particles escaping the foil, as a result of elastic and inelastic interactions. The results show that the stripping process can function on its own, as well as in combination with other processes. A summary of

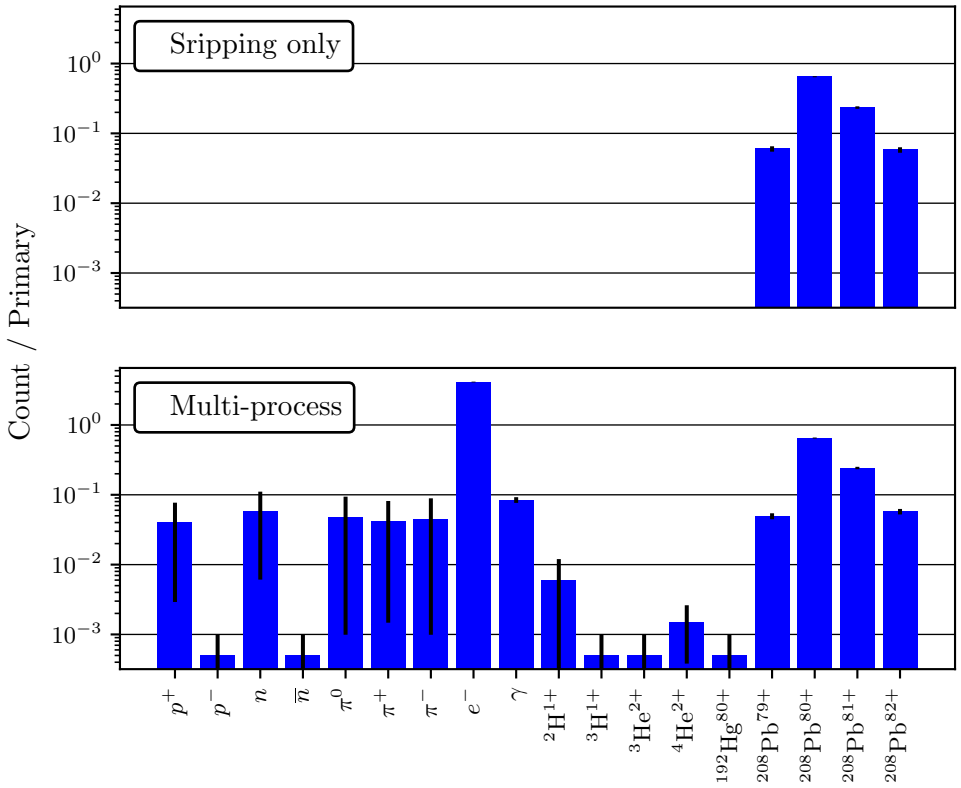

Figure 5.3: Populations of secondary particle species coming from a beam of $^{208}Pb^{79+}$ impinging on a carbon foil. The top plot shows the secondary particles produced when only the stripping process is enabled, while the bottom plot includes a comprehensive set of physics processes, as shown by the variety of secondary particle species produced. A beam of 2000 primary ions on the reference orbit was used in both cases.

calculated stripping mean free paths in the foil material and fractional yield for the different charge states can be found in Table 5.1.

Table 5.1: Summary of stripping mean free paths and fractional yield for the different charge state resulting from a 450 GeV/Q $^{208}Pb^{79+}$ beam impinging on a 50 µm thick carbon foil.

Charge state	Mean free path [µm]	Fraction [%]
$^{208}Pb^{79+}$	172	6.00
$^{208}Pb^{80+}$	93	64.75
$^{208}Pb^{81+}$	102	23.45
$^{208}Pb^{82+}$	n/a	5.80

The results from initial tests with a simple toy-model demonstrate the functionality of the PSI stripping processes. However, it is necessary to benchmark the physical outcomes against existing charge-changing interaction simulations and measured data for different

scenarios. The impact of omitting electron capture, multi-electron processes and the target density effect must be evaluated and further developments should be aimed at extending the support for different PSI charge-changing processes.

5.3 PSI beam collimation in the LHC

5.3.1 The Gamma Factory initiative

The Gamma Factory initiative [157, 166] is part of the Physics Beyond Colliders (PBC) research campaign at CERN, which is focussed on exploring opportunities for exploiting CERN's accelerator infrastructure in novel ways after the end of the physics programme at the LHC. The goal of the Gamma Factory is to study the possibility of creating high-intensity, high-energy photon beams using the LHC. For this purpose, PSI are chosen as the beam particle because the presence of the bound electrons enables resonant interactions with photons of the correct wavelength. The main proposal is to accelerate incompletely ionised heavy-ion beams to the LHC top energy and excite their atomic degrees of freedom using a laser. During the subsequent spontaneous atomic-transition emission, the emitted photon would be boosted by a factor $4\gamma_{\mathrm{L}}^2$, where γ_{L} is Lorentz factor of the carrier ion. The photons emitted during the PSI de-excitation can hence reach energies of up to 400 MeV in the LHC.

In addition to the high, tuneable, photon energy, a PSI-based light source at the LHC would be capable of providing unprecedented photon beam intensities, reaching 1×10^{17} photons/s, some 7 orders of magnitude higher than the intensity of currently available light sources. The availability of photon beams with those parameters can provide opportunities for experiments involving the primary photon beams, as well as high-intensity secondary beams of polarised electrons, positrons or muons and tertiary beams of neutrinos.

In addition to this, the ability to reliably accelerate and store PSI beams in the LHC also provides opportunities for other novel applications [167]. One of those application is an electron-hadron collider mode for the LHC, referred to as Parasitic Ion Electron Collider (PIE). In this mode, the bound electrons in PSI can participate in electron-proton collisions, with potential c.o.m. energy of 200 GeV and luminosity of up to $1 \times 10^{29}\,\mathrm{cm}^{-2}\,\mathrm{s}^{-1}$. Further

possibilities are related to the possibility of using a laser to perform Doppler cooling on PSI beams. The reduced ion beam emittance that can be achieved through cooling will be beneficial for experiments such as plasma wake-field acceleration and precision EW measurements using isoscalar ions, and can even potentially increase the nucleon-nucleon luminosity in nominal ion collisions at the LHC.

The studies for the Gamma Factory are ongoing, with a proof-of-principle (PoP) experiment proposed for the SPS [168]. The PoP experiment will aim to provide the first evaluation of photon production in collisions between an ultra-relativistic PSI beam and a laser beam. If approved, commissioning activities are planned to begin in 2021/2022. In addition to this, the PSI beams have been successfully accelerated and stored in the LHC for the first time in 2018. The experience of operating the LHC with PSI beams is discussed in detail in the following Section 5.3.2.

5.3.2 First PSI beams in the LHC

During a machine Development (MD) experiment in 2018, PSI beams were injected, accelerated and stored in the LHC for the first time, with the goal of studying the beam lifetime and characterising the beam losses [169]. During the test, $^{208}Pb^{81+}$ ions with one electron were injected and stored in the LHC (Beam 1 only). As part of the MD, loss maps were measured at injection (450 GeV/Q) and at flat-top (6.5 TeV/Q).

In both cases severe losses were observed in the DS of IR7. These losses turned out to be a real operational limitation, when a beam dump was triggered at top energy by regular losses on the collimation system, with only 24 low-intensity bunches (1.1×10^{10} charges/bunch) in the machine, causing an unusually high-loss leakage to cell 11 in the DS of IR7. The loss maps at flat-top were taken during a subsequent fill with only 6 bunches of even lower intensity (0.75×10^{10} charges/bunch). Despite the low stored intensity, the losses in the DS of IR7 still reached around 60 % of the dump threshold. As the design total ion intensity for Pb beams in the LHC is 1.3×10^{13} charges (see Section 2.3), a factor 300 larger than the one used during the MD, the collimation losses were identified as a potential critical obstruction for LHC operation with PSI beams. It should be noted that it is currently assumed that the intensity for PSI operation would be the same as for fully stripped ion

operation, but it has not been demonstrated that the injectors can provide PSI beams of this intensity.

Following the MD, the first dedicated collimation studies have revealed that the explanation of the unusually poor collimation system performance for PSI beams is the stripping action of the TCP collimator [170,171]. During nominal ion beam operation, when fully stripped ions in the beam halo impact the TCP, a fraction of them undergo inelastic interactions such as nuclear fragmentation or EMD, while the rest remain intact and acquire a transverse deflection from elastic interactions, as covered in Section 2.2. Depending on the deflection, the intact ions are intercepted by the downstream collimation stages or complete further revolutions around the ring. However, when a partially stripped ion interacts with the TCP, any bound electrons are quickly removed, resulting in a discrete change of the ion charge state. Because of the change in charge, the magnetic rigidity of all the intact, fully stripped ions emerging from the TCP is no longer matched to the magnetic lattice, with a fractional offset of about 1.2 % for the case of $^{208}Pb^{81+}$ beams. When the off-rigidity ions enter the DS downstream of the collimation, the rising dispersion diverts their trajectories onto the cold aperture there. In the case of a $^{208}Pb^{81+}$ beam, the stripping action of the TCP produces a secondary beam of $^{208}Pb^{82+}$ ions, which impact the aperture in a narrow region, giving rise to the large loss spike of the collimation losses in cell 11, observed during the PSI MD. This loss mechanism is supported by analytical arguments, tracking of off-rigidity trajectories in MADX and simulations of PSI collimation with the SixTrack-FLUKA coupling framework. The measurements and simulations of PSI collimation are covered in more detail in Section 5.3.3.

The previous studies have also identified promising mitigation strategies that can alleviate the problematic losses. Simulations performed for the HL-LHC show that the TCLD collimator, which will be installed in the DS of IR7 as part of the upgrade (see Section 2.1.5), is likely to intercept the PSI losses. The preliminary value estimated for the PSI beam intensity reach with the TCLD collimator installed is 3×10^{11} Pb ions (2.46×10^{13} charges) [170], which is beyond the baseline Pb total intensity for the ion operation in the HL-LHC [90]. Other potential loss mitigation strategies considered are an orbit bump in IR7 and the crystal collimation technique, outlined in Section 2.1.5.

Because of the latest inclusion of PSI support, in addition to the existing tracking and

physics processes in a 3D model of the full LHC ring, it is expected that studies of PSI collimation in BDSIM can complement the existing studies and provide further understanding of the losses and their mitigation. This motivates the simulations presented in Section 5.3.3, which are aimed at reproducing the loss pattern observed during the PSI beam tests in the LHC.

5.3.3 Simulations of PSI beam collimation in BDSIM

Due to the complex nature of the involved interactions, collimation simulations for ion beams require integrated tools that include particle tracking and physical interactions. Section 2.2 covers two of the simulation frameworks that satisfy the criteria—the SixTrack-FLUKA coupling and BDSIM, along with results from their application to ion beam collimation in the LHC. Those frameworks are a natural choice for simulations of PSI beam collimation, due to the significant overlap with fully stripped ion beam collimation. However, the presence of bound electrons in PSI is a complication for simulation studies. As discussed in Section 5.1.1, PSI can undergo charge-changing interactions, which means that simulation tools must have the means to keep track of the electron occupancy and have physics processes that modify it as appropriate in order to treat PSI beam particles correctly. At the time of the first studies, outlined in Section 5.3.2, neither of the simulation frameworks had support for PSI beam particles. Currently, FLUKA still does not support PSI, while SixTrack has been extended to track arbitrary ion charge states. The inclusion of PSI support in BDSIM is discussed in this thesis.

In order to perform the first PSI collimation studies with the SixTrack-FLUKA coupling, the assumption has been made that all PSI particles are stripped by the TCP collimator. The simulations have been carried out at top energy by tracking fully stripped $^{208}\mathrm{Pb}^{82+}$ ions with the energy of the nominal $^{208}\mathrm{Pb}^{81+}$ ions, starting at the TCP with an impact parameter of 1 µm. The initial distribution of off-rigidity ions is then processed as normal, with physics interaction simulation in the collimators and tracking of the secondary ion fragments in the ring. The assumption of complete stripping by the TCP is supported by the large stripping cross-section in solid materials. Using approximate formulas for electron stripping of ultra-relativistic PSI [26], the MFP for $^{208}\mathrm{Pb}^{81+}$ traversing the CFC material of the TCP is estimated as 0.4 mm. For an impact parameter of 1 µm, the distance travelled

by ions in the TCP is about 5 cm, two orders of magnitude larger than the stripping MFP.

With the addition of the semi-empirical electron stripping interaction in BDSIM, it is possible to evaluate the stripping efficiency for different ions and materials. The first test performed in BDSIM is sending a pencil beam of $^{208}Pb^{81+}$ at the LHC top energy of 6.5 TeV/Q onto a slab target of CFC and scanning the thickness of the target. Since the distance traversed by a particle in the TCP is a function of the impact parameter, as discussed in Section 2.3, the target thickness scan is used as an approximation of the ions hitting the LHC TCP at different impact parameters. For the scan, only the stripping physics process in BDSIM is enabled and 50 values for the thickness in the range 5 µm to 50 cm are used, with 10 000 primary ions simulated at every step. The results from the scan are shown in Fig. 5.4.

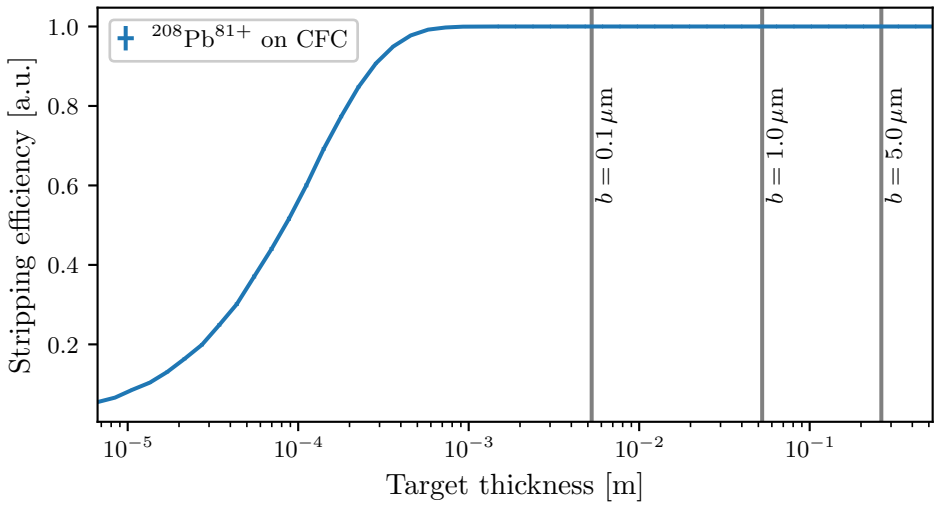

Figure 5.4: Stripping efficiency as a function of target thickness for $^{208}Pb^{81+}$ at E = 6.5 TeV/Q incident on a CFC target in BDSIM. Only the stripping physics process is enabled in BDSIM and 50 runs 10 000 primary particles are performed over the thickness range depicted. The vertical gray lines denote the material thickness travelled by particles impinging on the LHC TCP collimator with the quoted impact parameter, b.

It can be observed from the scan that for a thickness equivalent to the impact parameter value of 1 µm, the stripping efficiency recorded in BDSIM is 100 % for the number of primary particles simulated. This conclusion is in agreement with the assumptions made in the original simulations. The stripping efficiency observed is above 99 % down to a small target thickness, corresponding to impact parameters as small as 0.01 µm. This observation has implications for the selection of an impact parameter for the collimation simulations.

The value of 1 µm has been selected, as it produces the worst cleaning inefficiency for fully stripped ion collimation (see Section 2.3.2). For the case of PSI, however, a smaller impact parameter would reduce the nuclear interaction rates and increase the likelihood of intact, stripped ions escaping the TCP, which can potentially exacerbate the losses in the DS of IR7. A dedicated impact parameter scan should be performed for PSI beams in the LHC to determine the value, which results in the worst collimation cleaning inefficiency.

Following the stripping efficiency test, a full BDSIM collimation simulation is performed for PSI beams in the LHC. The simulation scenario is betatron collimation of $^{208}Pb^{81+}$ at top energy for B1H. The BDSIM model setup is the same as the one used for fully stripped ion collimation in the LHC, described in Section 2.3.5, with the addition of the PSI stripping process. The simulation parameters are the same as quoted in Table 2.2, with the difference that the beam particle is $^{208}Pb^{81+}$ and the total particle energy is $E = 515.97\,\text{TeV}$. The collimator settings are unchanged from the ones listed in Table 2.3. It should be noted that this machine configuration differs slightly from the one used for the loss map measurements during the PSI MD, outlined in Section 5.3.2, and for the initial SixTrack-FLUKA collimation simulations. During the measurements, the proton beam flat top optics and collimator settings were used. The differences between the ion and proton beam settings are mostly concentrated in the experimental IRs and do not significantly affect IR7, which is the main focus of this study. The impact parameter is kept as 1 µm for consistency with the SixTrack-FLUKA simulations. The simulation is performed with 1×10^6 primary ions, tracked for 200 turns. The loss maps recorded in the simulation are shown in Fig. 5.5 and Fig. 5.6, together with loss maps from the SixTrack-FLUKA coupling and the measurements.

The loss map simulated with BDSIM shows good agreement with the measurements. The distribution of the losses around the ring follows the pattern observed in the measured loss map, with the majority of the losses occurring in IR7. Notable loss spikes are also found in the arcs downstream of IR7, IR8 and IR1, as well as in the off-momentum cleaning insertion IR3 and in the extraction region IR6. The most prominent feature of the loss map, the large cold loss spike in the DS of IR7, is well replicated in terms of location and magnitude. The cleaning inefficiency recorded in the offending loss spike is $3.734\,\text{m}^{-1}$, a factor 4 larger that the peak cleaning inefficiency in the collimation system. This level of losses is extreme, exceeding the peak cleaning inefficiency for nominal ion operation by two

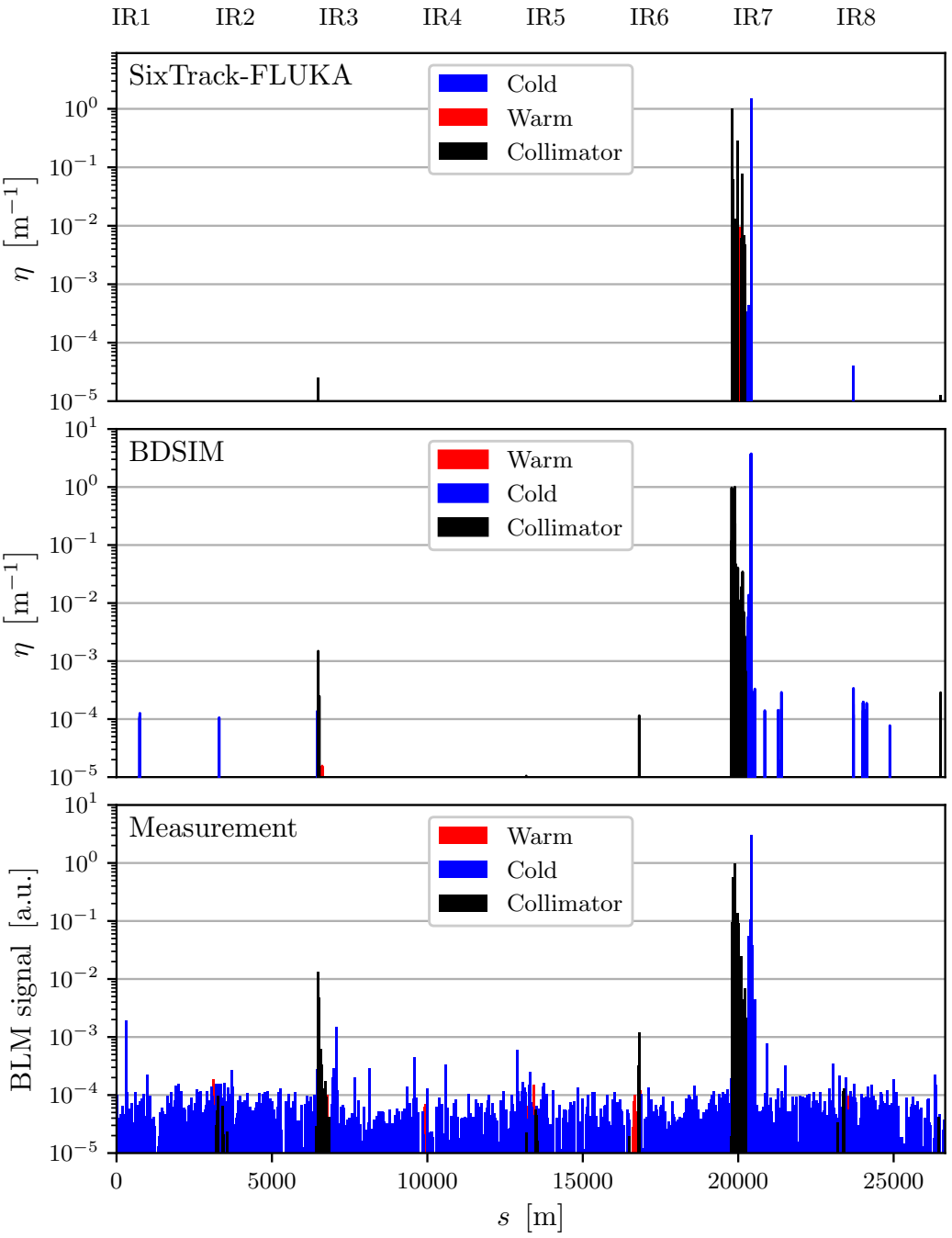

Figure 5.5: Comparison of loss maps for betatron collimation of $^{208}Pb^{81+}$ PSI beams the top energy for the LHC B1H. The top plot shows the first SixTrack-FLUKA simulation of PSI collimation, courtesy of A. Gorzawski. The middle plot shows the BDSIM simulation discussed in this chapter. The bottom plot shows the loss map measured during the PSI beam tests in the LHC, courtesy of N. Fuster-Martínez.

orders of magnitude, and for nominal proton operation by four orders of magnitude (see Fig. 2.12).

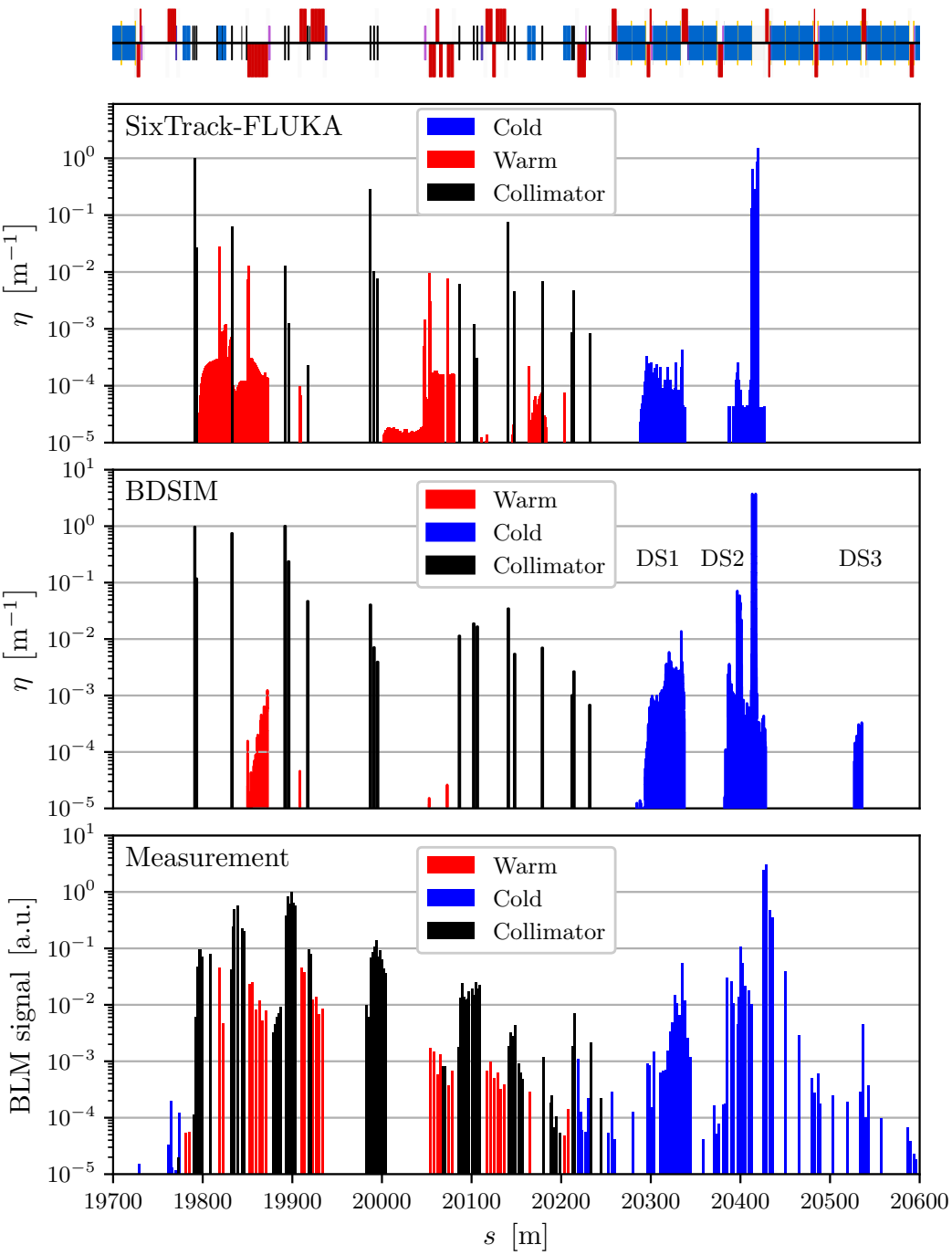

Figure 5.6: Extract from the loss maps for betatron collimation of $^{208}Pb^{81+}$ PSI beams the top energy for the LHC B1H in Fig. 5.5, showing the IR7 region in detail. The top plot shows the SixTrack-FLUKA simulation, courtesy of A. Gorzawski. The middle plot shows the BDSIM simulation. The bottom plot shows the loss map measured during the PSI operation of the LHC, courtesy of N. Fuster-Martínez.

Good agreement is also evident from the zoomed-in view of IR7, shown in Fig. 5.6. The highest losses in the simulated loss map occur in cell 11, as part of the extended DS2 cold

loss cluster, about 5 m upstream of the location of the highest measured losses. In the setup used, BDSIM only counts ion particles lost on the aperture towards the loss maps, while the measured BLM signal represents signal in the BLMs due to secondary particles leaking outside of the beamline elements, which explains the differences in loss location. The BDSIM results also reproduce the DS1 loss cluster in the DS and the smaller DS2 with good accuracy. The losses on the collimators in IR7 generally follow the measured loss pattern, with some discrepancies, mainly in the primary and secondary stages. Those discrepancies can again be attributed to the loss map recording, with results shown in Section 2.4.4 demonstrating that using simulated BLM signals instead of ion aperture losses for the loss maps significantly improves the agreement in collimator losses between BDSIM and measurements.

The observed agreement with measurements is better for the BDSIM results than for the SixTrack-FLUKA results. In the SixTrack-FLUKA results, the location and magnitude of the main loss spike in cell 11 is well reproduced, but there are some notable discrepancies observed in the IR7 collimator losses, the broader cold loss clusters in the DS of IR7 and the losses outside of IR7, relative to both the BDSIM results and the measurements. Given that the assumption of perfect stripping efficiency of the TCP has been shown to be valid and the two simulation frameworks have produced broadly compatible results for fully stripped ion collimation in the LHC (see Section 2.3.7), it is not clear at this time what is the explanation for the discrepancies. The effect of the differences between the optical and collimator settings used in the two simulations should be investigated and a BDSIM simulation with the proton beam flat top settings, as used in SixTrack-FLUKA, is suggested as a next step.

The main aim of future studies of PSI collimation using BDSIM should be to perform a quantitative analysis of the collimation losses for PSI beam operation in the LHC and evaluate the performance of the proposed loss mitigation strategies. The model used for the study presented can readily be configured for energy deposition studies, in order to provide direct estimates of peak and integrated power load due to PSI losses in the most impacted beamline elements. Furthermore, if a model of the HL-LHC is prepared, the power load on the TCLD collimator and the secondary leakage to the downstream 11 T dipole can be evaluated, in order to provide and estimate intensity reach with PSI beams. It would be of interest to compare the intensity reach estimate with the currently available

value and the value from potential future dedicated energy deposition studies in FLUKA.

Further developments of the model can include the addition of BLM monitors, as discussed in Section 2.4. This, coupled with the stripping physics process, can enable studies of beam losses and material activation due to beam-gas interaction. As a more distant prospect, the stripping model can be included in the ion crystal channeling framework in BDSIM, which is currently under development. Such an extension will likely require a considerable effort, but it can provide an opportunity to study crystal collimation efficiency for PSI beams, which is currently well beyond the reach of existing simulation tools.

5.4 Conclusion

An electron stripping physics process for PSI, based on a semi-empirical cross-section model, has been implemented in BDSIM. The model covers single ionisation of one-electron and multi-electron PSI interacting with neutral atoms in arbitrary material mixtures. In the ultra-relativistic regime, this process alone is expected to be a good approximation to the all charge-changing interactions of PSI. The process is fully integrated into the Geant4's tracking and physics interaction frameworks and is capable of operating on its own or in conjunction with other physics processes. The results from the initial tests of the process are promising, with the stripping action, the tracking for PSI with different electron occupancies and the integration with a comprehensive physics process list for ion beams successfully demonstrated. Preliminary investigation shows that the cross-section calculation is consistent with published results for the semi-empirical model employed, but further validation and benchmarking of the process is necessary. Proposed future developments are integration of the target density effect, including correct kinematics with secondary electron emission and adding a semi-empirical model of electron capture.

Using the newly-added features, a study of PSI beam collimation in the LHC has been conducted. The study includes an evaluation of stripping efficiency of the TCP as a function of the impact parameter and a simulation of betatron collimation for $^{208}Pb^{81+}$ beams in the LHC. The simulated loss maps reproduce the loss pattern measured during the first operational tests of PSI in the LHC with good accuracy. The results from the BDSIM simulation are found to be in better agreement with the measurements than the

results from the first studies of PSI collimation, performed with the SixTrack-FLUKA coupling. Because of its capacity for detailed energy deposition simulations, BDSIM is proposed for use in further studies of PSI collimation. An evaluation of the HL-LHC TCLD performance in intercepting PSI beam losses and the associated power loads and secondary particle leakage are suggested as an immediate next step. In the future, following additional developments, the possibility is identified of studying more specialised scenarios for PSI beams, such as beam-gas interactions and crystal collimation.

Chapter 6

Conclusion

6.0.1 Summary of collimation studies

Ion beams are becoming an increasingly important part of fundamental particle physics research. The LHC at CERN, designed mainly as a proton-proton collider, also operates in an ion collider mode for a limited period during every physics run. In this mode, it is one of only 2 ion colliders currently in operation and it delivers $^{208}Pb^{82+}$ collisions at 6.37 Z TeV, the highest heavy-ion collision energy ever achieved. During the 2018 ion run, the delivered Pb-Pb luminosity exceeded the design value by around a factor 6. The excellent performance of the LHC as an ion collider is the result of the experience gained, in the 9 years since the first ion collisions took place, and of extensive studies into the challenges associated with ion beam operation. One of those challenges is the collimation system performance. The LHC is fitted with an advanced multi-stage collimation system to protect the machine and clean the beam halo. The collimation system is optimised for proton beams and has shown excellent performance in the nominal p-p collider operation. For operation with ion beams, the LHC collimation system exhibits a significantly worse performance, with peak cold losses of up to 2 orders of magnitude larger than for proton beams. The collimation performance is one of the factors limiting the achievable ion beam intensity in the LHC.

Ions in the beam halo can undergo nuclear fragmentation and EMD interactions in the primary collimator. Those interactions result in a broad distribution of secondary ions

escaping the collimator. Some of the secondary ions can have a magnetic rigidity close to the nominal and remain inside the mechanical acceptance of the warm collimation insertion. Upon entering the downstream DS, the dispersion deflects their trajectories onto the aperture of the superconducting magnets there, resulting in significant beam losses. Ion collimation hence requires dedicated studies for both the current LHC and its planned upgrade, the HL-LHC. In addition to this, exploratory studies are ongoing for the design of a new hadron collider, which can begin operation after the end of the physics programme at the LHC and its upgrades. The FCC-hh and the HE-LHC are two post-LHC collider designs currently under development. Both designs include nucleus-nucleus collider operation in the baseline design. With the increased energy and intensity envisaged for the future hadron colliders, it is important for ion beam collimation to be studied early on in the design process.

The study of ion beam collimation, especially for future accelerator designs, requires dedicated simulation tools. The complex interactions undergone by ion particles in a collimator and the broad range of secondary ions produced make collimation simulations challenging. Integrated simulation tools are necessary for this purpose, which include Monte Carlo simulation of particle interactions in the collimators and tracking of different ion species in the magnetic lattice of the accelerator. Several different tools have been developed at CERN, with the latest and most advanced one being the SixTrack-FLUKA active coupling. In the coupling, FLUKA is used to simulate the interaction and energy deposition inside collimators, while SixTrack is used to track the resulting secondary particles in the ring. Previous studies have demonstrated the predictive power of the SixTrack-FLUKA coupling and studies, performed with it, have helped in understanding the ion losses in the LHC and optimising the settings of the collimation system for ion beam operation. The SixTrack-FLUKA coupling is the standard tool for ion collimation studies at CERN. Another integrated simulation tool, which fulfils the criteria for ion collimation studies, is BDSIM. It is developed at RHUL for studies of radiation transport in accelerator beamlines and it combines particle tracking physics interactions in a full 3D model of an accelerator. A key feature of BDSIM is the capability to perform energy-deposition studies in the entire beamline, including the collimators and the magnetic elements. Both of those simulation tools are used in different scenarios throughout this thesis.

The main aim of this thesis is to evaluate the ion beam collimation performance of future

hadron colliders. The simulation tools and techniques employed for this purpose were first applied to ion collimation in the LHC and the results were benchmarked against measurements. Simulations of ion collimation in the LHC were performed using the SixTrack-FLUKA coupling and BDSIM for a machine configuration, which has not been covered by previous studies. Loss maps for $^{208}Pb^{82+}$ ion for B1H FT have been recorded in the simulation. The loss maps from the SixTrack-FLUKA coupling and BDSIM both show a good agreement with the measurements. The simulations are shown to successfully reproduce the cold losses in the most critical region of the machine, the DS of the betatron collimation insertion, IR7. The largest discrepancies found were in the IR2 region, where the simulation did not reproduce some of the measured losses. This is expected to be due to operational conditions like beam orbit fluctuations, which are not represented in the simulation input. This is a possible explanation for the observed discrepancies between the simulated and measured loss maps. In addition to cleaning inefficiency simulations, the first energy-deposition study of ion collimation in the full LHC ring was performed in BDSIM. For this purpose, a detailed geometry model of the LHC BLM was developed and a set of 3380 such monitors were added to the 3D LHC model used in BDSIM. The results from the simulation showed an improved agreement with measurements for the warm losses in IR7, but overall a worse agreement for aperture losses, relative to the standard collimation simulations performed. The reason for the worse agreement in the aperture losses is likely to be the lack of cryostats in the magnet geometry models used in BDSIM, as the BLMs are sensitive to showers of secondary particles developing after an aperture impact that the steel cryostat would normally affect. Furthermore, as BLMs are placed based on the extents of the magnet, the lack of the cryostat affects the placement of the BLM monitors in BDSIM.

Following the LHC studies, the same simulation techniques are applied to the FCC-hh, a design concept for a 100 km-long hadron collider, which can provide heavy-ion collisions at an energy a factor of 7 larger than the LHC. The first comprehensive studies of the collimation performance for heavy-ion beams are performed for the most challenging scenarios, betatron collimation at top energy and off-momentum collimation at injection energy. The goal of the studies is to establish the feasibility of ion beam operation in the FCC-hh and evaluate the benefits of the TCLD collimators, installed in the DS of the collimation insertions. The SixTrack-FLUKA coupling is used for the simulation performed, as the

physical scale of the FCC-hh is too large for BDSIM to reliably handle at this time. For betatron collimation at top energy, an impact parameter scan is performed and the value of 0.1 µm is selected for the cleaning inefficiency studies, as it results in the worst cleaning inefficiency. Betatron cleaning simulations are performed with $^{208}Pb^{82+}$ ions beams for B1H at top energy in two collimation configurations, one with and one without the TCLD collimators. In both cases, a comparison is made with an estimate of the quench limit. The results show that with collimator settings taken over directly from the configuration envisaged for proton operation, the collimation system successfully intercepts ion losses. No cold loss peaks occur above the estimated quench limit and only secondary particles, out-scattered by the TCLDs, are found to reach the aperture in the DS of the betatron cleaning insertion, IRJ. It is also revealed that the TCLDs play a crucial role in the collimation performance, with their removal resulting in numerous cold loss clusters exceeding the quench limit in the IRJ DS and the rest of the ring. Despite the large losses for the case without the TCLDs, the collimation cleaning observed is comparatively better than for the LHC, where TCLDs are not present. The peak cold losses in the LHC correspond to a cleaning inefficiency of around 1×10^{-2}, while for the FCC-hh without TCLDs, the peak is only around 5×10^{-4}. The optical functions and the collimation IR layout in the FCC-hh are scaled from the LHC, with the mechanical collimator gaps remaining similar. Therefore, the better performance of the FCC-hh ion collimation can be due to the optical function scaling or the effect of the higher beam energy on the physical interactions in collimators, with further studies needed to differentiate between the two. The off-momentum loss maps for injection energy do not show cold loss clusters of immediate concern. Simulations with optical and collimator imperfections and energy-deposition studies are identified as necessary studies for the future.

A first evaluation of the collimation system performance for heavy-ion beam operation was also performed for the HE-LHC. The HE-LHC is a concept for a hadron collider, based on magnet technology developed for the FCC-hh and envisaged to be installed in the existing LHC tunnel. Simulations were performed for $^{208}Pb^{82+}$ ions beams for B1H at top energy using the SixTrack-FLUKA coupling. An impact parameter scan was used to select the value of 1 µm for the main cleaning inefficiency simulations. Loss maps were recorded with and without the TCLD collimators and compared with an estimate of the quench limit. The results show a generally good performance of the collimation system in the nominal

proton beam configuration, with no notable cold loss clusters recorded outside of the DS of IR7. In the DS of IR7, two cold loss peaks were recorded with magnitudes up to 50 % above the estimated quench limit. Analysis of the aperture losses in the DS reveals that the lost particles originate from the different collimation stages in the collimation system, including the TCP, and the TCLD collimators themselves. Energy deposition studies are required to asses the quench risk for the most impacted magnets. An optimisation of the collimator settings, a longer TCLD collimator and an orbit bump are some of the potential loss mitigation strategies. In the configuration with the TCLD collimators removed, the loss maps appear broadly similar to the ones from the LHC, with the losses in the IR7 DS having a comparable distribution and magnitude. The optical functions and layout in IR7 are similar between the LHC and HE-LHC. Without the TCLDs, the most significant difference is the beam energy, which is a factor 2 higher in the HE-LHC. Given the similarities in the loss maps between the LHC and the HE-LHC, the higher beam energy is unlikely to be the sole explanation for the improved heavy-ion collimation efficiency observed in the FCC-hh. Future studies should hence explore the effect of optical functions in the collimation insertions on the cleaning performance.

The last set of studies performed is focussed on PSI, a novel type of beam particle, proposed for use in the LHC as a driver for a new type of high-intensity light source as part of the Gamma Factory initiative at CERN. The bound electrons carried by PSI enable interactions of interest with a laser beam, but also make PSI more difficult to accelerate and store. Previous studies have identified electron stripping in interactions with collimators as a limiting factor for the achievable PSI beam intensity in the LHC. As part of this thesis, support for PSI beams was added to BDSIM. An electron stripping model for PSI, based on a semi-empirical cross-section model, has been implemented. It handles stripping of electrons from relativistic PSI, interacting with targets made up of neutral atoms. Using the newly-added features, a study of PSI beam collimation in the LHC was carried out in BDSIM. The results show good agreement with measurements taken during operational tests in the LHC. Proposed future BDSIM studies for PSI include a detailed energy deposition study for the LHC and an evaluation of potential loss mitigation strategies in the context of the HL-LHC.

6.0.2 Discussion of the simulation tools

In a broader scope, this thesis has covered the preparation, execution and analysis of ion beam collimation simulations for most of the existing and future energy-frontier hadron colliders, using multiple simulation tools. This experience has revealed some general issues related to ion collimation simulations and potential improvements to the simulation tools, which can address them.

The major issue identified is the difference in scale associated with ion beams in the largest hadron colliders. The latest collider designs inherently combine two scales, a very small one and a very large one. This is evident when considering mm beam movement versus the multi-km accelerator length or the mJ energy, capable of quenching a superconducting magnet, versus the energy of order GJ stored in the beams. This difference in scale is propagated to the simulations, with the accuracy of the simulation results correlated with the complexity of the model and the associated computational load. For the LHC, this scale problem is addressed by a set of control measures, like only tracking ion fragments and applying stringent TeV energy cuts to the physical interactions. At present, it is not clear if those measures are also valid for cases like the FCC-hh, where the total beam ion energy is already much higher, leading to more secondary particles produced and a longer simulation. If the stringent control measures have to be relaxed, the effect on the simulations can be dramatic. The most prominent example of this are the energy deposition simulations for the full LHC ring, performed as part of this thesis. Lowering the interaction cuts and tracking all fragments produced, in order to ensure a sufficient BLM response, resulted in a significant increase in the resource usage. The pilot simulation consumed an average of 15 min of CPU time per primary ion and produced a total of roughly 7 TB of data. Compared with the sub-minute running time per primary and the GB-level data sets for the normal collimation simulations, without further optimisation, full energy deposition simulations would be generally impractical. Even for the standard collimation simulations, the data sets for the FCC-hh studies are five times larger than for the LHC and their analysis is already at the limit of what is achievable on a personal computer. For the FCC-hh and HE-LHC, it should be studied which particles contribute to losses of interest and what the optimal control measures are. In addition to this, scalable output formats and optimised analysis tools can be employed to improve the processing of the simulation

results.

Related with the scale problem is the problem of obtaining a sufficient quantity of data in the regions of interest to overcome the statistical fluctuations. The regions of interest for losses in a collider are typically the superconducting magnets, where the losses pose a quench risk. By design, the superconducting magnets are shielded from normal beam losses by the collimation system and passive protection devices. For example, for the FCC-hh, the cleaning inefficiency quench limit is estimated to be $2 \times 10^{-5}\,\mathrm{m}^{-1}$, which roughly sets the scale for the ratio between peak losses per metre on the collimators and the cold aperture. In the integrated simulation of the full FCC-hh ring, the resource usage is hence dominated by the processing of warm losses in the collimation insertions. In order to optimise the simulation execution, a statistical analysis of the losses should be performed, in order to estimate the total number of primary particles required to achieve a given limit on the statistical uncertainty for the losses of interest. It is suggested that the output data should be organised per primary particle, in order to simplify data processing. In simulations that include physical interactions, one primary particle can lead to numerous secondary particles and delocalised energy deposition. Storing the data in a per-primary output structure allows a straightforward reconstruction of the physical interaction history for all lost particles and enables statistical variance calculations, which can help optimise the number of particles required for a simulation. Additional measures such as physical process biasing for interactions leading to losses of interest can also be investigated.

The other issue identified is technical in nature. The simulation models for ion collimation studies are complex and include a variety of inputs, like the optical configuration, aperture description and simulation execution settings. Furthermore, the simulation tools used are under constant development, often including backwards-incompatible changes. Because of this, the preparation of ion collimation models and their maintenance is time-consuming, often dominating the overall time required to perform a study. Having a shared database of complete models, including top-level inputs, has the potential to alleviate some of the difficulties in setting studies up. The overhead associated with modifying an existing model for a given study is expected to be much lower than preparing the full model from scratch. Version control systems, which have been employed to manage the code base for simulations, can also be applied to simulation models and the associated analysis tools. This can provide a ready access to functioning models, as well as records of previous versions

of those models, which can be useful in the recreation of studies for example. As an added benefit, the models can be used for regression testing of the simulation tools, ensuring that core functionality remains unaffected during continuous development. Version control systems for simulation models are used as part of the broader BDSIM tool chain and, to a lesser extent, as part of SixTrack and SixTrack-FLUKA studies for the LHC. A wider adoption of this approach would be associated with additional curation and maintenance efforts, but it is expected that the benefits can be significant enough to consider it.

In terms of the software tools used, the SixTrack-FLUKA was found to be the most versatile framework for ion collimation simulations. It was successfully used for the LHC, HE-LHC and the FCC-hh as part of the studies presented. It benefits from the fast, symplectic tracking in SixTrack and the advanced physics interaction modelling in FLUKA. Both SixTrack and FLUKA have been widely used at CERN and have a proven capability. The coupling between them has been extensively benchmarked against measurements for the LHC, with the good agreement also demonstrated in the studies presented. For these reasons, the SixTrack-FLUKA coupling is expected to be the main tool used for ion collimation simulations for both existing and future hadron colliders. The main design limitation of the SixTrack-FLUKA coupling is that physical interactions are only treated in the collimators, while losses on the aperture are treated in a simplified manner. In addition to this, secondary particles like neutrons or short-lived particles, which are produced in the collimators, are not suitable for tracking in SixTrack. This limitation is not considered concerning, as follow-up energy deposition studies using FLUKA are typically performed for key areas of the machine. A more practical limitation of the coupling is the complexity of the simulation models. Because the simulations rely on up to 4 different code bases (SixTrack, FLUKA, flukaio, gpdist) and a variety of model preparation scripts, the process of preparing the inputs is not straightforward and involves multiple distinct steps and file formats. Some of the steps include transient executable options, duplication of input parameters or pre-determined sequences of user actions. It is suggested that the procedure for preparing simulations can be simplified by having an additional tool to manage the process and act a single user interface. Such a tool can collect all necessary input files and parameters and automatically execute the model preparation sequence, while also enforcing naming conventions and maintaining a complete record of all the steps. Another issue is that the output from the simulation is provided separately by the different codes

running in the simulation, mainly as multiple ASCII-format files. As many as 10 individual output files per run have been used in the simulations presented in this thesis. This output configuration does not scale well to large data volumes and creates difficulties when processing the data from multiple runs on a batch processing system, as information about the evolution of the state and position for particles in the simulation is spread out across multiple files. Providing the output information in a limited number of binary output files can alleviate this issue. Alternatively, a separate executable can be used to process and organise the data upon the conclusion of each run on the batch processing system. A Python package has been developed as part of this thesis, which combines existing and new tools for interaction with the SixTrack-FLUKA framework. It provides utilities for input preparation, simulation execution and output analysis. It features prototype implementations of the concepts outlined in this paragraph, which can be developed further if proven to be useful.

BDSIM is an alternative framework for collimation simulations. It combines tracking and physics processes in a single simulation model, which allows an equal treatment of beam losses from arbitrary particle species in any part of the accelerator. The 3D beamline model employed by BDSIM and the physics process configuration can be adjusted for a given study, allowing both standard cleaning inefficiency simulations and detailed energy deposition simulations. It also benefits from a software ecosystem, which includes input preparation and output analysis tools. One of the highlight features of BDSIM is the per-primary, histogram-based output analysis tool chain, which readily scales to very large data sets and provides an integrated treatment of statistical uncertainties. BDSIM is adaptable and extendable, which enables a variety studies involving novel concepts or technologies. For example, developments of BDSIM have been performed, as part of this thesis, that provide support for fully stripped and partially stripped ion beams at the LHC. The results from the first heavy-ion collimation collimation simulations in BDSIM show a good agreement with both SixTrack-FLUKA simulations and measurements. BDSIM is a promising tool that can complement SixTrack-FLUKA coupling studies for the LHC and the HL-LHC. It can also be useful for studies involving specialised scenarios like PSI beam collimation or crystal collimation. The main technical limitation in BDSIM is the particle tracking.

The tracking routines in BDSIM are generally symplectic, but by necessity there are small

geometrical gaps in the 3D model, which lead to an accrual of tracking errors. Furthermore, the Geant4 tracking algorithms perform numerical integration, which converges to a surface intersection with finite precision for curved tracks, leading again to small tracking errors. Those effects lead to an effective lack of symplecticity in the tracking and make BDSIM unsuitable for long-term tracking or for the largest-scale accelerators, like the FCC-hh. In addition to this, the tracking takes much longer in BDSIM than in SixTrack, increasing the overall running time for the simulations. For ion collimation simulations, the imperfect tracking in BDSIM is not expected to be a critical concern, because in this particular case the tracked particles interact immediately and do not survive for many turns in the machine. Furthermore, the simulation running time is found to be dominated by the processing of the physical interactions, limiting the impact of the slower tracking. Additional studies are necessary to quantify the distribution of computation time between tracking and physical interactions. In the future, both the accuracy and the execution speed of tracking can be improved by the addition of a dedicated, symplectic tracker for particles inside the beampipe. Alternatively, a coupling to an existing symplectic tracker, like SixTrack, can also be considered. In addition to this, the physics processes, covering interactions of ultra-relativistic ions with matter, require further developments and validation. Some key interaction models for ion beams, like EMD, are not as sophisticated as the models provided by FLUKA, and also suffer code implementation problems. Extensive benchmarking against established simulations tools and measurements is essential to evaluate the accuracy of the physical interaction models used in BDSIM.

The two frameworks have fundamentally different approaches to collimation simulations. Each is associated with unique advantages and unique limitations. There is a significant overlap between the strong points of one and the limitations of the other. Complementary studies can hence be of interest for cross-validating simulation models and gaining further understanding of different beam loss aspects. Furthermore, the workflows and analysis tools associated with each framework also have different features. A comparative analysis of the practical and technical aspects of both frameworks can be used to guide their future developments, with the goal of improving ion collimation simulations for future hadron colliders.

6.0.3 Future prospects

There are several avenues identified for the continuation of the studies presented in this thesis and a road map is proposed for the near future. As an immediate next step, the studies of heavy-ion beam collimation for the FCC-hh are proposed to be formulated into a peer-reviewed publication. In addition to this, studying the effects of optical and collimator imperfections on the ion collimation efficiency is considered a high-priority task.

Following this, the next proposed step is the development and improvement of the BDSIM workflow for ion collimation simulations. For the case of heavy-ion collimation in the LHC, this includes refining the BLM model, optimising the parameters for energy deposition studies and benchmarking the results against previous simulations and measurements. It is proposed to develop a parameterised model of the BLMs, using pre-calculated data of aperture impacts location and BLM location. Such a parameterised model can potentially reduce the need to simulate in detail the shower propagation from the aperture impact location to the BLM, and alleviate the problems associated with the energy scale difference between the beam particles and the low-energy secondary particles that the BLMs are sensitive to.

The scope of the studies with PSI beams in BDSIM is also proposed to be extended. A study of PSI beam cleaning inefficiency for the HL-LHC can be performed immediately. Further refinements of the PSI interaction model will also enable studies of losses due to residual gas interactions and studies for PSI in the SPS, which can be of interest to the Gamma Factory initiative.

In parallel with studies suggested, development of the model preparation and output analysis should be performed. The highest priority tasks are considered to be the development of a simplified input preparation framework and an optimised output analysis framework, including treatment of statistical uncertainties, for the SixTrack-FLUKA coupling.

Acronyms

ADT transverse damper.

B1H Beam 1 horizontal.

B1V Beam 1 vertical.

BFPP bound-free pair production.

BIS beam interlock system.

BLM beam loss monitor.

BLT beam lifetime.

BNL Brookhaven National Laboratory.

c.o.m. centre-of-mass.

CAD Computer-Aided Design.

CDR conceptual design report.

CERN European Organisation for Nuclear Research.

CFC carbon fibre composite.

CG Combinatorial Geometry.

CSG Constructive Solid Geometry.

DS dispersion suppressor.

EM electro-magnetic.

EMD electromagnetic dissociation.

EW electroweak.

FAIR Facility for Antiproton and Ion Research.

FCC-hh Future Circular hadron-hadron Collider.

FEL free electron laser.

FT flat top.

GDML Geometry Description Markup Language.

GDR giant dipole resonance.

GQR giant quadrupole resonance.

HE-LHC High Energy LHC.

HESR High Energy Storage Ring.

HL-LHC High Luminosity LHC.

IP interaction point.

IR insertion region.

LAR long arc region.

LEP Large Electon-Positron collider.

LHC Large Hadron Collider.

LIU LHC injector upgrade.

LS long shutdown.

MD machine Development.

MFP mean free path.

MoGr molybdebum-graphite.

MSC multiple scattering.

PBC Physics Beyond Colliders.

PIE Parasitic Ion Electron Collider.

PoP proof-of-principle.

PSI partially stripped ions.

QCD Quantum Chromo-dynamics.

QGP quark-gluon plasma.

RF radio-frequency.

RHIC Relativistic Heavy-Ion Collider.

RHUL Royal Holloway University of London.

rms root mean square.

SAR short arc region.

scSPS superconducting Super Proton Synchrotron.

SppC Super proton-proton Collider.

SPS Super Proton Synchrotron.

SR synchrotron radiation.

TCLA Target Collimator Long Absorber.

TCLD Target Collimator Long Dispersion.

TCP Target Collimator Primary.

TCSG Target Collimator Secondary—Graphite.

TCT Target Collimator Tertiary.

TCTP Target Collimator Tertiary—Pickup.

TFS Table File System.

UFO unidentified falling object.

Appendix A

Optical functions from a beam distribution

Tools like MAD-X are often used to design an accelerator lattice by computing optical solutions from parameterised representation of the particle motion and the magnetic fields [172]. The tracking of optical fuctions in a beamline is possible by using transfer matrices for the mangetic elements.

BDSIM is a code that performs single particle tracking in an accelerator beamline, but lacks the facilities to perform dedicated tracking of optical functions. A procedure for calculating optical functions directly from a 6D beam distribution has been implemented in BDSIM.

The calculation of the optical functions follows the well-established procedure described in [9].
For one degree of freedom the sigma matrix of a beam is expressed as

$$\mathbf{\Sigma} = \begin{pmatrix} \langle x^2 \rangle & \langle xx' \rangle \\ \langle x'x \rangle & \langle x'^2 \rangle \end{pmatrix} = \epsilon_x \begin{pmatrix} \beta_x & -\alpha_x \\ -\alpha_x & \gamma_x \end{pmatrix} . \tag{A.1}$$

The equations for individual parameters are,

$$\epsilon_x = \sqrt{\langle x^2 \rangle \langle x'^2 \rangle + \langle xx' \rangle^2}, \tag{A.2}$$

$$\beta_x = \frac{\langle x^2 \rangle}{\epsilon_x}, \tag{A.3}$$

$$\alpha_x = \frac{\langle x x' \rangle}{\epsilon_x}, \tag{A.4}$$

with the quantities in angle brackets representing the sigmas of the horizontal distribution.

In order to estimate the values and uncertainties in the parameters calculated in Eqs. (A.1), (A.2) and (A.4) the vectors can be constructed [12]:

$$\vec{a} = \begin{pmatrix} \langle x^2 \rangle \\ \langle x x' \rangle \\ \langle x'^2 \rangle \end{pmatrix}, \tag{A.5}$$

$$\vec{f} = \begin{pmatrix} \beta_x \\ \alpha_x \\ \epsilon_x \end{pmatrix} = \begin{pmatrix} a_1/\sqrt{a_1 a_3 - a_2^2} \\ -a_2/\sqrt{a_1 a_3 - a_2^2} \\ \sqrt{a_1 a_3 - a_2^2} \end{pmatrix}. \tag{A.6}$$

For the uncertainty in the general formula is used,

$$U_{ij} \approx \sum_{k,l} \frac{\partial f_i}{\partial a_k} \frac{\partial f_j}{\partial a_l}\bigg|_{\hat{a}} V_{kl}, \tag{A.7}$$

where $U_{ij} = cov[f_i, f_j]$ is the covariance matrix element for the estimated quantities and $V_{kl} = cov[a_k, a_l]$ is the covariance matrix element for the parameters. In particular the diagonal elements U are a measure of the uncertainty in the estimated values. The expanded form of Eq. (A.7) is:

$$\begin{aligned} \sigma_{\vec{f}}^2 = &\left(\frac{\partial \vec{f}}{\partial a_1}\right)^2 cov[a_1, a_1] + \left(\frac{\partial \vec{f}}{\partial a_2}\right)^2 cov[a_2, a_2] + \left(\frac{\partial \vec{f}}{\partial a_3}\right)^2 cov[a_3, a_3] + \\ &+ 2\left(\frac{\partial \vec{f}}{\partial a_1}\frac{\partial \vec{f}}{\partial a_2}\right) cov[a_1, a_2] + 2\left(\frac{\partial \vec{f}}{\partial a_1}\frac{\partial \vec{f}}{\partial a_3}\right) cov[a_1, a_3] + 2\left(\frac{\partial \vec{f}}{\partial a_2}\frac{\partial \vec{f}}{\partial a_3}\right) cov[a_2, a_3]. \end{aligned} \tag{A.8}$$

Finding the matrix elements of V is non-trivial because the parameters in $\vec{a}$ are not coordinates, but rather moments of a bivariate distribution. The expressions for these matrix elements are obtained from *mathStatica*, a statistics package for *Mathematica*. The methods `HStatistic` followed by `CentralMomentToCentral` can be used in *mathStatica* in order

to obtain the covariances of $\vec{a}$ elements. The expressions for these covariances are obtained as

$$
\begin{aligned}
cov[a_1, a_1] &= -\frac{(-3+n)\mu_{2,0}^2}{(-1+n)n} + \frac{\mu_{4,0}}{n}, \\
cov[a_2, a_2] &= -\frac{(-3+n)\mu_{0,2}^2}{(-1+n)n} + \frac{\mu_{0,4}}{n}, \\
cov[a_3, a_3] &= -\frac{(-2+n)\mu_{1,1}^2}{(-1+n)n} + \frac{\mu_{0,2}\mu_{2,0}}{(-1+n)n} + \frac{\mu_{2,2}}{n}, \\
cov[a_1, a_2] &= -\frac{(-3+n)\mu_{1,1}\mu_{2,0}}{(-1+n)n} + \frac{\mu_{3,1}}{n}, \\
cov[a_1, a_3] &= \frac{2\mu_{1,1}^2}{(-1+n)n} - \frac{\mu_{0,2}\mu_{2,0}}{n} + \frac{\mu_{2,2}}{n}, \\
cov[a_2, a_3] &= -\frac{(-3+n)\mu_{0,2}\mu_{1,1}}{(-1+n)n} + \frac{\mu_{1,3}}{n},
\end{aligned}
\tag{A.9}
$$

where $\mu_{a,b}$ is an estimator for the central moment of the bivariate distribution $\mu_{a,b} = E[(x-\mu_x)^a(x'-\mu_{x'})^b] = \sum_{i=1}^{n}(x_i-\mu_x)^a(x_i'-\mu_{x'})^b$. μ_x and $\mu_{x'}$ are the means of the corresponding distributions.

Finally, by carrying out the calculations in Eqs. (A.5) and (A.6) the optical functions in the horizontal plane can be obtained and by plugging Eq. (A.9) into Eq. (A.8) and their statistical uncertainty can be estimated. By analogy the same procedure is then applied in the vertical plane to achieve the final results.

Bibliography

[1] W. Fischer and J. M. Jowett, "Ion Colliders", Rev. Accel. Sci. Technol. **7**, 49 (2015).

[2] P. Foka, "Overview of heavy-ion physics at the SPS and RHIC", Rev. Mex. Fis. **49S4**, 114 (2003).

[3] L. Evans and P. Bryant (editors), "LHC machine", J. Instrum. **3**, S08001 (2008).

[4] H. Hahn *et al.*, "The RHIC design overview", Nucl. Instrum. Methods Phys. Res., Sect. A **499**, 245 (2003).

[5] A. Abada *et al.*, "HE-LHC: The High-Energy Large Hadron Collider", Eur. Phys. J. ST **228**, 1109 (2019).

[6] FCC Collaboration, A. Abada *et al.*, "FCC-hh: The Hadron Collider", Eur. Phys. J. ST **228**, 755 (2019).

[7] J. Tang *et al.*, "Concept for a future super proton-proton collider", 2015, arXiv:1507.03224 [physics.acc-ph].

[8] A.W. Chao, M. Tigner (editors), *Handbook of Accelerator Physics and Engineering* (World Scientific, 1998).

[9] H. Wiedemann, *Particle Accelerator Physics*, Third ed. (Springer, 2007).

[10] S. Y. Lee, *Accelerator Physics* (World Scientific, 1999).

[11] E. Courant and H. Snyder, "Theory of the alternating-gradient synchrotron", Ann Phys (N Y) **281**, 360 (2000).

[12] Particle Data Group, M. Tanabashi *et al.*, "Review of particle physics", Phys. Rev. D **98**, 030001 (2018).

[13] B. Holzer, "Introduction to Longitudinal Beam Dynamics", in *CERN Accelerator School: Course on Superconductivity for Accelerators*, pp. 41–56, 2014.

[14] A. Dragt, "An overview of Lie methods for accelerator physics", in *Proc. of the Particle Accelerator Conf. 2013, Pasadena, USA*, p. 1134, 2005.

[15] A. J. Dragt, *Lie methods for nonlinear dynamics with applications to accelerator physics* (University of Maryland, Center for Theoretical Physics, Department of Physics, 2011).

[16] R. H. Kleiss, F. Schmidt, and F. Zimmermann, "The use of truncated Taylor maps in dynamic aperture studies", Part. Accel. **41**, 117 (1993).

[17] L. Deniau and C. Tomoiagă, "Generalised Truncated Power Series Algebra for Fast Particle Accelerator Transport Maps", in *Proceedings, 6th Int. Particle Accelerator Conf., Richmond, USA*, p. MOPJE039, 2015.

[18] M. Hann-Shin and R. Wirz, "Comparison of charged particle tracking methods for non-uniform magnetic fields", in *Proc. 42nd AIAA Plasmadynamics and Lasers Conference*, p. 3739, 2011.

[19] D. H. Perkins, *Introduction to High Energy Physics*, 4 ed. (Cambridge University Press, 2000).

[20] W. Herr, "Concept of luminosity", in *CERN Accelerator School: Intermidiate accelerator physics*, 2006.

[21] P. Hermes, "Heavy-Ion Collimation at the Large Hadron Collider : Simulations and Measurements", PhD thesis, University of Munster, 2016.

[22] H. H. Braun *et al.*, "Hadronic and electromagnetic fragmentation of ultrarelativistic heavy ions at LHC", Phys. Rev. ST Accel. Beams **17**, 021006 (2014).

[23] A. Baltz *et al.*, "The physics of ultraperipheral collisions at the LHC", Physics Reports **458**, 1 (2008).

[24] R. Bruce, D. Bocian, S. Gilardoni, and J. M. Jowett, "Beam losses from ultraperipheral nuclear collisions between Pb ions in the Large Hadron Collider and their alleviation", Phys. Rev. ST Accel. Beams **12**, 071002 (2009).

[25] S. Datz *et al.*, "Effect of nuclear size on the stopping power of ultrarelativistic heavy ions", Phys. Rev. Lett. **77**, 2925 (1996).

[26] I. Y. Tolstikhina and V. P. Shevelko, "Influence of atomic processes on charge states and fractions of fast heavy ions passing through gaseous, solid, and plasma targets", Physics-Uspekhi **61**, 247 (2018).

[27] J. Lindhard and A. H. Sorensen, "Relativistic theory of stopping for heavy ions", Phys. Rev. A **53**, 2443 (1996).

[28] C. J. Benesh and J. L. Friar, "Electromagnetic dissociation of nuclei in heavy-ion collisions", Phys. Rev. C **48**, 1285–1296 (1993).

[29] J. W. Wilson *et al.*, "NUCFRG2: An evaluation of the semiempirical nuclear fragmentation database", NASA, Langley Research Center Report No. NASA-TP-3533, 1995.

[30] J. Hüfner, K. Schäfer, and B. Schürmann, "Abrasion-ablation in reactions between relativistic heavy ions", Phys. Rev. C **12**, 1888 (1975).

[31] M. Giacomelli, L. Sihver, J. Skvarc, N. Yasuda, and R. Ilic, "Projectile-like fragment emission angles in fragmentation reactions of light heavy ions in the energy region $<$ 200-MeV/nucleon: modeling and simulations", Phys. Rev. **C69**, 064601 (2004).

[32] B. V. Carlson *et al.*, "Fermi breakup and the statistical multifragmentation model", Journal of Physics: Conference Series **312**, 082017 (2011).

[33] "MAD-X program", `http://cern.ch/mad/`, Date retrieved: 06/2019.

[34] F. Schmidt, "SixTrack. User's Reference Manual", CERN Report No. CERN/SL/94-56-AP, 1994.

[35] "Sixtrack web site", `http://sixtrack.web.cern.ch/SixTrack/`, Date retrieved: 04/2019.

[36] R. D. Maria *et al.*, "Recent Developments and Future Plans for SixTrack", in *Proc. of the 4th Int. Particle Accelerator Conf., Shanghai, China*, 2013.

[37] P. Hermes, R. Bruce, and R. D. Maria, "Symplectic tracking of multi-isotopic heavy-ion beams in SixTrack", in *Proc. of the 7th Int. Particle Accelerator Conf., Busan, Korea*, p. 1450, 2016.

[38] G. Robert-Demolaize, R. Assmann, S. Redaelli, and F. Schmidt, "A new version of sixtrack with collimation and aperture interface", in *Proc. of the Particle Accelerator Conf., Knoxville, USA*, p. 4084, 2005.

[39] R. Bruce *et al.*, "Simulations and measurements of beam loss patterns at the CERN Large Hadron Collider", Phys. Rev. ST Accel. Beams **17**, 081004 (2014).

[40] A. Ferrari, P. Sala, A. Fassò, and J. Ranft, "FLUKA: a multi-particle transport code", CERN Report No. CERN-2005-10, 2005.

[41] A. Fasso *et al.*, "The physics models of FLUKA: status and recent developments", in *Proc. of the Computing in High Energy and Nuclear Physics Conf., La Jolla, USA*, 2003.

[42] A. Mereghetti, V. Boccone, F. Cerutti, R. Versaci, and V. Vlachoudis, "The FLUKA Linebuilder and Element Database: Tools for Building Complex Models of Accelerators Beam Lines", in *Proc. of the 3rd Int. Particle Accelerator Conf., New Orleans, USA*, p. 2687, 2012.

[43] A. Mereghetti *et al.*, "Sixtrack-FLUKA active coupling for the upgrade of the SPS scrapers", in *Proc. of the 4th Int. Particle Accelerator Conf., Shanghai, China*, p. 2657, 2013.

[44] P. Hermes *et al.*, "Measured and simulated heavy-ion beam loss patterns at the CERN Large Hadron Collider", Nucl. Instrum. Methods Phys. Res. A **819**, 73 (2016).

[45] P. Hermes *et al.*, "Simulation of Heavy-Ion Beam Losses with the SixTrack-FLUKA Active Coupling", in *Proc. of the 7th Int. Particle Accelerator Conf., Busan, Korea*, 2016.

[46] N. Fuster-Martínez *et al.*, "Cleaning performance of the collimation system with Xe beams at the Large Hadron Collider", in *Proc. of the 9th Int. Particle Accelerator Conf., Vancouver, Canada*, p. 176, 2018.

[47] L. Nevay *et al.*, "BDSIM: An accelerator tracking code with particle–matter interactions", Comput. Phys. Commun. **252**, 107200 (2020).

[48] S. Agostinelli *et al.*, "Geant4—a simulation toolkit", Nucl. Instrum. Methods. Phys. Res. A **506**, 250 (2003).

[49] J. Allison *et al.*, "Recent developments in Geant4", Nucl. Instrum. Methods. Phys. Res. B **835**, 186 (2016).

[50] J. Allison *et al.*, "Geant4 developments and applications", IEEE Trans. Nucl. Sci. **53**, 270 (2006).

[51] I. Antcheva *et al.*, "ROOT — a C++ framework for petabyte data storage, statistical analysis and visualization", Comput. Phys. Commun. **180**, 2499 (2009).

[52] O. S. Brüning *et al.*, "LHC design report v.1 : The LHC main ring", CERN Report No. CERN-2004-003-V1, 2004.

[53] R. Steerenberg *et al.*, "Operation and performance of the CERN Large Hadron Collider during proton Run 2", in *Proc. of the 10th Int. Particle Accelerator Conf., Melbourne, Australia*, p. MOPMP031, 2019.

[54] J. Jowett *et al.*, "The 2018 heavy-ion run of the LHC", in *Proc. of the 10th Int. Particle Accelerator Conf., Melbourne, Australia*, p. WEYYPLM2, 2019.

[55] ATLAS collaboration, "Observation of a new particle in the search for the standard model higgs boson with the ATLAS detector at the LHC", Phys. Lett. B **716**, 1 (2012).

[56] CMS Collaboration, "Observation of a new boson at a mass of 125 GeV with the CMS experiment at the LHC", Phys. Lett. B **716**, 30 (2012).

[57] S. Holmes, R. S. Moore, and V. Shiltsev, "Overview of the Tevatron collider complex: goals, operations and performance", J. Instrum. **6**, T08001 (2011).

[58] ATLAS Collaboration, "The ATLAS experiment at the CERN Large Hadron Collider", J. Instrum. **3**, S08003 (2008).

[59] ALICE Collaboration: F. Carminati *et al.*, "ALICE: Physics performance report, volume I", J. Phys. G **30**, 1517 (2004).

[60] CMS Collaboration, "The CMS experiment at the CERN LHC", J. Instrum. **3**, S08004 (2008).

[61] LHCb Collaboration, "The LHCb detector at the LHC", J. Instrum. **3**, S08005 (2008).

[62] M. Giovannozzi and F. F. Van der Veken, "Description of the luminosity evolution for the CERN LHC including dynamic aperture effects. Part I: the model", Nucl. Instrum. Methods Phys. Res., A **905**, 171 (2018).

[63] M. S. Camillocci, "LHC nominal cycle", in *Proc. of the 6th Evian Workshop on LHC beam operation, Evian, Switzerland*, pp. 45–48, 2016.

[64] R. Alemany, M. Lamont, and S. Page, "LHC modes", CERN Report No. LHC-OP-ES-0005-10-10, 2009.

[65] S. Redaelli *et al.*, "Combined ramp and squeeze at the Large Hadron Collider", in *Proc. of the 3rd Int. Particle Accelerator Conf., New Orleans, USA*, p. MOPPC016, 2012.

[66] L. Rossi, "The LHC Superconducting Magnets", CERN Report No. LHC-Project-Report-660, 2003.

[67] L. Rossi, "Superconducting magnets for the LHC main lattice", IEEE Trans. Appl. Supercond. **14**, 153 (2004).

[68] AC Team, "Diagram of an LHC dipole magnet. Schéma d'un aimant dipôle du LHC", 1999, CERN-DI-9906025.

[69] J. B. Jeanneret *et al.*, "Quench levels and transient beam losses in LHC magnets", CERN Report No. LHC-Project-Report-44, 1996.

[70] B. Auchmann *et al.*, "Testing beam-induced quench levels of LHC superconducting magnets", Phys. Rev. ST Accel. Beams **18**, 061002 (2015).

[71] A. Lechner *et al.*, "Validation of energy deposition simulations for proton and heavy ion losses in the CERN Large Hadron Collider", Phys. Rev. Accel. Beams **22**, 071003 (2019).

[72] B. Goddard, V. Kain, V. Mertens, J. Uythoven, and J. Wenninger, "TT40 Damage during 2004 High Intensity SPS Extraction", CERN Report No. CERN-AB-Note-2005-014, 2005.

[73] V. Kain, J. Ramillon, R. Schmidt, K. Vorderwinkler, and J. Wenninger, "Material damage test with 450-GeV LHC-type beam", in *Proc. of the Particle Accelerator Conf, Knoxville, USA*, p. 1607, 2005.

[74] R. Schmidt *et al.*, "Protection of the CERN Large Hadron Collider", New J. Phys. **8**, 290 (2006).

[75] S. Redaelli, "Beam Cleaning and Collimation Systems", CERN Yellow Reports **2**, 403 (2016).

[76] M. Santana-Leitner *et al.*, "Energy Deposition Studies for the Betatron Cleaning Insertion (IR7) of LHC", CERN Report No. LHC-Project-Report-825, 2005.

[77] C. Bracco, "Commissioning Scenarios and Tests for the LHC Collimation System", PhD thesis, EPFL, 2009.

[78] R. W. Assmann, "Preliminary Beam-based specifications for the LHC collimators", CERN Report No. LHC-PROJECT-NOTE-277, 2002.

[79] R. W. Assmann *et al.*, "LHC Collimation : Design and Results from Prototyping and Beam Tests", CERN Report No. LHC-Project-Report-850, 2005.

[80] R. W. Assmann *et al.*, "The Final Collimation System for the LHC", in *Proc. of the European Particle Accelerator Conference, Edinburgh, Scotland*, p. 986, 2006.

[81] R. Bruce *et al.*, "Reaching record-low β^* at the CERN Large Hadron Collider using a novel scheme of collimator settings and optics", Nucl. Instrum. Methods Phys. Res. A **848**, 19 (2017).

[82] R. Bruce *et al.*, "Sources of machine-induced background in the ATLAS and CMS detectors at the CERN Large Hadron Collider", Nucl. Instrum. Methods Phys. Res. A **729**, 825 (2013).

[83] R. Bruce *et al.*, "Collimation-induced experimental background studies at the CERN Large Hadron Collider", Phys. Rev. Accel. Beams **22**, 021004 (2019).

[84] B. Salvachua *et al.*, "Handling 1 MW Losses with the LHC Collimation System", in *Proc. of 5th the Int. Particle Accelerator Conf., Dresden, Germany*, 2014.

[85] A. Bertarelli *et al.*, "The Mechanical Design for the LHC Collimators", CERN Report No. LHC-Project-Report-786, 2004.

[86] LHC collimation project, Pictures of LHC Collimators, `http://lhc-collimation-project.web.cern.ch/`, Retrieved: 02/2020, 2012.

[87] E. Quaranta, "Investigation of collimator materials for the High Luminosity Large Hadron Collider", PhD thesis, Politecnico Di Milano, 2017.

[88] J. B. Jeanneret, "Optics of a two-stage collimation system", Phys. Rev. ST Accel. Beams **1**, 081001 (1998).

[89] LHC Construction Canadian Collaboration, N. Catalan-Lasheras *et al.*, "Proton Collimation in TeV Colliders", CERN Report No. LHC-Project-Report-156, 1997.

[90] G. Apollinari *et al.*, *High-Luminosity Large Hadron Collider (HL-LHC): Technical Design Report V. 0.1*, CERN Yellow Reports: Monographs. CERN-2017-007-M (CERN, 2017).

[91] J. Coupard *et al.*, "LHC Injectors Upgrade, Technical Design Report, Vol. I: Protons", CERN Report No. CERN-ACC-2014-0337, 2014.

[92] J. Coupard *et al.*, "LHC Injectors Upgrade, Technical Design Report, Vol. II: Ions", CERN Report No. CERN-ACC-2016-0041, 2016.

[93] S. Redaelli *et al.*, "Collimation upgrades for HL-LHC", in *Proc. of the LHC Performance Workshop, Chamonix, France*, 2014.

[94] R. Bruce, A. Marsili, and S. Redaelli, "Cleaning Performance with 11T Dipoles and Local Dispersion Suppressor Collimation at the LHC", in *Proc. of the 5th Int. Particle Accelerator Conf., Dresden, Germany*, p. 170, 2014.

[95] J. Jowett and M. Schaumann, "Dispersion suppressor collimators for heavy-ion operation", Presentation at the LHC Collimation Review, 2013, `https://indico.cern.ch/event/251588/` Date retrieved: 11/2019.

[96] D. Mirarchi, "Crystal Collimation for LHC", PhD thesis, Imperial College, London, 2015.

[97] W. Scandale *et al.*, "Observation of channeling for 6500 GeV/c protons in the crystal assisted collimation setup for LHC", Phys. Lett. B **758**, 129 (2016).

[98] D. Mirarchi, G. Hall, S. Redaelli, and W. Scandale, "Design and implementation of a crystal collimation test stand at the Large Hadron Collider", Eur. Phys. J. C **77**, 424 (2017).

[99] G. Stancari *et al.*, "Conceptual design of hollow electron lenses for beam halo control in the Large Hadron Collider", Report No. CERN-ACC-2014-0248, 2014.

[100] D. Mirarchi *et al.*, "Hollow electron-lens assisted collimation and plans for the LHC", in *Proc. of the 61st ICFA Advanced Beam Dynamics Workshop on High-Intensity and High-Brightness Hadron Beams, Daejeon, Korea*, p. TUP1WE02, 2018.

[101] C. Zanoni, G. Gobbi, D. Perini, and G. Stancari, "Preliminary mechanical design study of the hollow electron lens for HL-LHC", J. Phys. Conf. Ser. **874**, 012102 (2017).

[102] N. Fuster-Martínez *et al.*, "Simulations of heavy-ion halo collimation at the Large Hadron Collider (LHC): benchmark with measurements and cleaning performance evaluation", Manuscript submitted for publication (2020).

[103] N. Fuster-Martínez *et al.*, "Performance of the collimation system during the 2018 lead ion run at the Large Hadron Collider", in *Proc. of the 10th Int. Particle Accelerator Conf., Melbourne, Australia*, p. MOPRB050, 2019.

[104] P. Hermes *et al.*, "LHC Heavy-Ion Collimation Quench Test at 6.37Z TeV", CERN Report No. CERN-ACC-NOTE-2016-0031, 2016.

[105] E. B. Holzer *et al.*, "Beam Loss Monitoring for LHC Machine Protection", Physics Procedia **37**, 2055 (2012).

[106] M. Stockner, "Beam loss calibration studies for high energy proton accelerators", PhD thesis, Vienna, Tech. U., 2007.

[107] E. Nebot Del Busto *et al.*, "Handling of BLM abort thresholds in the LHC", in *Proc. of the 2nd Int. Particle Accelerator Conf., San Sebastian, Spain*, p. WEPC170, 2011.

[108] V. Moens, R. Bruce, S. Redaelli, B. Salvachua, and G. Valentino, "Comparison of LHC Beam Loss Maps using the Transverse Damper Blow up and Tune Resonance

Crossing Methods", in *Proc. of the 4th Int. Particle Accelerator Conf., Shanghai, China*, p. 1008, 2013.

[109] R. Billen and C. Roderick, "The LHC Logging Service: Capturing, storing and using time-series data for the world's largest scientific instrument", CERN Report No. AB-Note-2006-046, 2006.

[110] N. Fuster-Martínez, "Loss map validation YETS 2018", Presentation at the LHC Collimation Working Group, 2018, `https://indico.cern.ch/event/726453/`, Date retrieved: 12/2019.

[111] N. Fuster-Martínez, "Heavy ions run loss maps qualification", Presentation at the LHC Collimation Working Group, 2018, `https://indico.cern.ch/event/774200`, Date retrieved: 12/2019.

[112] M. Benedikt, P. Collier, V. Mertens, J. Poole, and K. Schindl (editors), "LHC design report v.3 : The LHC injector chain", CERN Report No. CERN-2004-003-V3, 2004.

[113] S. Walker, "Development of an LHC model in BDSIM to study collimation cleaning and beam-induced backgrounds at ATLAS", PhD thesis, Royal Holloway Unversity of London, 2019.

[114] "Geant4 book for application developers", `http://geant4-userdoc.web.cern.ch/geant4-userdoc/UsersGuides/ForApplicationDeveloper/fo/BookForApplicationDevelopers.pdf`, Date retrieved: 11/2019.

[115] A. Abramov, S. Boogert, L. Nevay, and S. Walker, "First Studies of Ion Collimation for the LHC Using BDSIM", in *Proc. of the 9th Int. Particle Accelerator Conf., Vancouver, Canada*, p. MOPMF090, 2018.

[116] J. Wenninger, "Operation and Configuration of the LHC in Run 2", CERN Report No. CERN-ACC-NOTE-2019-0007, 2019.

[117] S. Walker *et al.*, "Precision Modelling of Energy Deposition in the LHC using BDSIM", in *Proc of the 10th Int. Particle Accelerator Conf., Melbourne, Australia*, p. MOPRB064, 2019.

[118] S. Boogert *et al.*, "Pyg4ometry : A Tool to Create Geometries for Geant4, BDSIM, G4Beamline and FLUKA for Particle Loss and Energy Deposit Studies", in *Proc. of the 10th Int. Particle Accelerator Conf., Melbourne, Australia*, p. WEPTS054, 2019.

[119] "LHC beam loss monitoring system", http://cern.ch/blm, Date retrieved: 02/2020.

[120] M. Stockner, B. Dehning, C. Fabjan, G. Ferioli, and E. Holzer, "Measurements and simulations of ionization chamber signals in mixed radiation fields for the lhc blm system", IEEE Nuclear Science Symposium conference record. Nuclear Science Symposium **3**, 1342 (2006).

[121] L. Sarchiapone *et al.*, "FLUKA Monte Carlo simulations and benchmark measurements for the LHC beam loss monitors", Nucl. Instrum. Methods Phys. Res. A **581**, 511 (2007).

[122] FCC, A. Abada *et al.*, "FCC-ee: The Lepton Collider", Eur. Phys. J. ST **228**, 261 (2019).

[123] M. Benedikt *et al.*, "Future Circular Collider - European Strategy Update Documents", CERN Report No. CERN-ACC-2019-0007, 2019.

[124] M. Schaumann, "Heavy ions at FCC-hh", Presentation at FCC Week 2019, Brussels, Belgium, 2018,
https://indico.cern.ch/event/727555/ Date retrieved: 01/2020.

[125] L. Bottura, "Expected performance of 11T and MB dipoles considering the cooling performance", Presentation at 8th HL-LHC collaboration meeting, 2018,
https://indico.cern.ch/event/742082/contributions/3085134/ Date retrieved: 01/2020.

[126] L. Bottura and D. Tommasini, private communication, 2019.

[127] I. Bellafont *et al.*, "Design of the future circular hadron collider beam vacuum chamber", Phys. Rev. Accel. Beams **23**, 033201 (2020).

[128] M. Brice, "FCC-hh beam screen prototype", 2016, CERN-PHOTO-201604-074, https://cds.cern.ch/record/2145407 Date retrieved: 02/2020.

[129] R. Bruce *et al.*, "Collimation system studies for the FCC-hh", J. Phys. Conf. Ser. **1350**, 012009 (2019).

[130] R. Bruce and J. Molson, "Preliminary collimation system design concept and performance estimate: Deliverable D2.6", CERN Report No. CERN-ACC-2019-0034, 2019.

[131] S. Arsenyev, O. Boine-Frankenheim, and D. Schulte, "FCC-hh transverse impedance budget", in *Proc. of the 9th Int. Particle Accelerator Conf, Vancouver, Canada*, p. MOPMF029, 2018.

[132] "FCC optics repository", `https://gitlab.cern.ch/fcc-optics/FCC-hh-lattice`.

[133] R. Bruce, private communication, 2020.

[134] FCC, A. Abada *et al.*, "HE-LHC: The High-Energy Large Hadron Collider", Eur. Phys. J. ST **228**, 1109 (2019).

[135] F. Zimmermann *et al.*, "High-Energy LHC Design", J. Phys. Conf. Ser. **1067**, MOPMF064 (2018).

[136] M. Benedikt and F. Zimmermann, "Status of the Future Circular Collider Study", in *25th Russian Particle Accelerator Conference, Saint Petersburg, Russia*, p. TUYMH01, 2016.

[137] M. Benedikt *et al.*, "Future Circular Collider", CERN Report No. CERN-ACC-2018-0058, 2018, Published in Eur. Phys. J. ST.

[138] J. Keintzel *et al.*, "HE-LHC optics design options", in *Proc. of the 10th Int. Particle Accelerator Conf., Melbourne, Australia*, p. MOPMP026, 2019.

[139] M. Hofer *et al.*, "Integrated Full HE-LHC Optics and Its Performance", in *Proc. of the 9th Int. Particle Accelerator Conf., Vancouver, Canada*, p. MOPMK002, 2018.

[140] V. Baglin, G. Bregliozzi, J. M. Jimenez, and G. Lanza, "Synchrotron Radiation in the LHC Vacuum System", in *Proc. of the 2nd Int. Particle Accelerator Conf., San Sebastian, Spain*, p. TUPS019, 2011.

[141] R. Bruce, A. Marsili, and S. Redaelli, "Cleaning performance with 11T dipoles and local dispersion suppressor collimation at the LHC", in *Proc. of the 5th Int. Particle Acclerator Conf., Dresden, Germany*, p. 170, 2014.

[142] T. Risselada, "Survey offsets, IR3 & 7 layouts, DS changes for TCLDs", Presentation at 35th HE-LHC design meeting, CERN, Geneva Switzerland, 2018, `https://indico.cern.ch/event/774203` Date retrieved: 12/2019.

[143] E. Shaposhnikova *et al.*, "LHC Injectors Upgrade (LIU) Project at CERN", in *Proc. of the 7th Int. Particle Accelerator Conf., Busan, Korea*, p. MOPOY059, 2016.

[144] S. A. Antipov *et al.*, "Low-Impedance Collimators for HL-LHC", in *Proc. of the 9th Int. Particle Accelerator Conf., Vancouver, Canada*, p. 1794, 2018.

[145] E. Quaranta *et al.*, "Towards Optimum Material Choices for HL-LHC Collimator Upgrade", in *Proc. of the 7th Int. Particle Accelerator Conf., Busan, Korea*, p. WEPMW031, 2016.

[146] R. Bruce *et al.*, "Updated parameters for HL-LHC aperture calculations for proton beams", CERN Report No. CERN-ACC-2017-0051, 2017.

[147] A. Abramov *et al.*, "Collimation of heavy-ion beams in the HE-LHC", J. Phys. Conf. Ser. **1350**, MOPRB059 (2019).

[148] M. Crouch, "Status of the HE-LHC Betatron Collimation System", Presentation at the 21st FCC collimation design meeting, CERN, Geneva Switzerland, 2018, `https://indico.cern.ch/event/758463/` Date retrieved: 02/2020.

[149] R. Bruce *et al.*, "Beam losses, lifetime and collimator hierarchy", in *Proc. of the 8th LHC Operations Evian Workshop, Evian, France*, 2019.

[150] R. Bruce, , R. W. Assmann, L. Luisella, and S. Redaelli, "Collimator hierarchy limits: assumptions and impact on machine protection and performance", in *Proc. of the MPP Workshop, Annecy, France*, 2013.

[151] J. Alonso, R. Force, M. Tekawa, and H. Grunder, "Acceleration of Partially Stripped Ions at the BEVALAC", IEEE Trans. Nucl. Sci. **24**, 1015 (1977).

[152] G. Arduini *et al.*, "Lead ion beam emittance and transmission studies in the PS-SPS complex at CERN", in *Proc. of the 5th European Particle Accelerator Conference, Sitges, Spain*, p. 380, 1996.

[153] C. Gardner *et al.*, "Operation of the RHIC Injector Chain with Ions from EBIS", in *Proc. of the 6th Int. Particle Accelerator Conf., Richmond, USA*, p. THPF046, 2015.

[154] Lead Ion Accelerating Facility Collaboration, H. Haseroth, "The CERN heavy ion accelerating facility", in *Proc. of the 16th Biennial Particle Accelerator Conference and International Conference on High-Energy Accelerators, Dallas, USA*, p. 411, 1995.

[155] FAIR Collaboration, "FAIR Baseline Technical Report (Volume 2)", GSI Report No. GSI-2013-04791, 2006.

[156] W. F. Henning, "FAIR: Recent developments and status", Nucl. Phys. A **805**, 502 (2008).

[157] M. Krasny *et al.*, "The CERN Gamma Factory Initiative: An Ultra-High Intensity Gamma Source", in *Proc. of the 9th Int. Particle Accelerator Conf., Vancouver, Canada*, p. WEYGBD3, 2018.

[158] S. Hirlaender *et al.*, "Lifetime and Beam Losses Studies of Partially Strip Ions in the SPS ($^{129}Xe^{39+}$)", in *Proc. of the 9th Int. Particle Accelerator Conf., Vancouver, Canada*, p. THPMF015, 2018.

[159] V. Shevelko, Y. A. Litvinov, T. Stöhlker, and I. Y. Tolstikhina, "Lifetimes of relativistic heavy-ion beams in the high energy storage ring of fair", Nucl. Instrum. Methods. Phys. Res. B **421**, 45 (2018).

[160] I. Tolstikhina, I. Tupitsyn, S. Andreev, and V. Shevelko, "Influence of relativistic effects on electron-loss cross sections of heavy and superheavy ions colliding with neutral atoms", J. Exp. Theor. Phys. **119**, 1 (2014).

[161] V. P. Shevelko, O. Rosmej, H. Tawara, and I. Y. Tolstikhina, "The target-density effect in electron-capture processes", J. Phys. B **37**, 201 (2003).

[162] I. Y. Tolstikhina and V. P. Shevelko, "Collision processes involving heavy many-electron ions interacting with neutral atoms", Physics-Uspekhi **56**, 213 (2013).

[163] V. Shevelko *et al.*, "Charge-changing processes in collisions of heavy many-electron ions with neutral atoms", Nucl. Instrum. Methods. Phys. Res. B **269**, 1455 (2011).

[164] J. Sabin and J. Oddershede, "Theoretical stopping cross sections of CH, CC and C=C bonds for swift protons", Nucl. Instrum. Methods. Phys. Res. B **27**, 280 (1987).

[165] "Geant4 physics reference manual", `http://geant4-userdoc.web.cern.ch/geant4-userdoc/UsersGuides/PhysicsReferenceManual/BackupVersions/V10.5-2.0/fo/PhysicsReferenceManual.pdf`, Date retrieved: 03/2020.

[166] C. Curatolo, W. Placzek, M. Krasny, L. Serafini, and M. Zanetti, "Novel high intensity gamma-source at cern: the gamma factory initiative", in *Sixth Annual Conference on Large Hadron Collider Physics*, p. 89, 2018.

[167] M. W. Krasny, "Gamma Factory for CERN", Presentation at the Input to the European Particle Physics Strategy Update meeting, CERN, Geneva Switzerland, 2018,
`https://indico.cern.ch/event/765096/` Date retrieved: 03/2020.

[168] Gamma Factory Study Group Collaboration, M. W. Krasny *et al.*, "Gamma Factory Proof-of-Principle Experiment", CERN Report No. CERN-SPSC-2019-031. SPSC-I-253, 2019.

[169] M. Schaumann *et al.*, "First partially stripped ions in the LHC (208pb81+)", J. Phys. Conf. Ser. **1350**, 012071 (2019).

[170] A. Gorzawski *et al.*, "Collimation of partially stripped ions in the CERN Large Hadron Collider", Manuscript submitted for publication (2020).

[171] A. Abramov *et al.*, "Collimation of partially stripped ion beams in the LHC", in *Proc. of the 10th Int. Particle Accelerator Conf., Melbourne, Australia.*

[172] "MAD-8 physics reference manual", `http://mad8.web.cern.ch/mad8/doc/phys_guide.pdf`, Date retrieved: 04/2020.